Observation of $\nu_\mu \to \nu_e$ oscillation in the T2K experiment

Kei Ieki

February, 2014

Department of Physics, Graduate School of Science
Kyoto University

Observation of $\nu_\mu \to \nu_e$ oscillation in the T2K experiment

A dissertation
submitted in partial fulfillment of the requirements
for the Degree of Doctor of Science
in the Graduate School of Science, Kyoto University

Kei Ieki

Department of Physics, Graduate School of Science
Kyoto University
February, 2014

Dissertation Committee:

Tsuyoshi Nakaya
Atsuko K. Ichikawa
Koji Tsumura
Masayuki Niyama
Takeshi Go Tsuru

Abstract

The T2K experiment is an accelerator based long baseline neutrino oscillation experiment. The ν_μ beam is produced at J-PARC in Tokai, and detected 295 km away from the production target by the Super-Kamiokande (SK) detector. In this thesis, we present the $\nu_\mu \to \nu_e$ oscillation measurement from the T2K experiment that clearly demonstrates, at the 7.3σ significance, evidence for ν_e appearance. The measurement of $\nu_\mu \to \nu_e$ oscillations is of a particular interest because this mode is sensitive to both mixing angle θ_{13} and CP phase $\delta_{\rm CP}$ of the mixing matrix. Precision measurement of $\nu_\mu \to \nu_e$ allows to explore the CP violation in the lepton sector, which is yet to be observed.

The identification of neutrino interaction modes is important in the measurement. In T2K, we select CCQE interaction ($\nu + n \to l + p$) as a signal, while the main background for CCQE is CC1π interaction ($\nu + N \to l + N' + \pi$). A full-active fine-grained detector (FGD) is capable of identifying the interaction modes by detecting the short pion tracks in the final state.

The interaction of pions with nuclei significantly affects the identification of neutrino interaction modes. For example, when the pion absorbed by a nucleus before being detected, CC1π interaction is misidentified as CCQE interaction. The uncertainty of the pion-nucleus interaction is one of the dominant systematic error sources in the T2K $\nu_\mu \to \nu_e$ measurement. We performed a pion-nucleus interaction measurement at the TRIUMF pion beamline, using a finely-segmented scintillator fiber detector. The sum of pion absorption and charge exchange interaction cross sections on carbon is measured with uncertainty of $\sim$6.5%, which is roughly half of the error of the past experiments. Using our new data set together with other external data sets, we improved the pion-nucleus interaction model used in T2K. The uncertainty of the pion-nucleus interaction was reduced to $\sim$1/4. The improved model is not used in the oscillation analysis yet, but the pion-nucleus uncertainty will become negligible in the future once we use the improved model.

The main topic of this thesis is the measurement of $\nu_\mu \to \nu_e$ oscillation. There are 28 ν_e candidate events observed at SK, with the T2K beam data collected from Jan. 2010 to May. 2013 (corresponding to 6.57×10^{20} protons on target). Using the momentum and angular distribution of the outgoing electrons observed at SK, we performed a maximum likelihood fit to measure the oscillation parameters. Assuming $\delta_{\rm CP} = 0$ and normal (inverted) hierarchy, we obtain a best fit value of $\sin^2 2\theta_{13} = 0.136^{+0.044}_{-0.033}$ ($0.166^{+0.051}_{-0.042}$). In the fit, the uncertainty of $\sin^2\theta_{23}$ and Δm^2_{32} are taken into account using the constraints from T2K published ν_μ disappearance measurement. The significance to exclude $\theta_{13} = 0$ is 7.3σ. This is the first measurement to discover the $\nu_\mu \to \nu_e$ with more than 5σ. Furthermore, this is the first discovery of the appearance of different neutrino flavour from neutrinos of another flavour with $>5\sigma$ significance. We obtain the 90% exclusion region for $\delta_{\rm CP}$ by combining the T2K result with the world average value of θ_{13} from reactor experiments.

$$\begin{aligned} &\text{Normal hierarchy:} && 0.604 \sim 2.509 \\ &\text{Inverted hierarchy:} && -3.142 \sim -3.043,\ -0.132 \sim 3.142 \end{aligned}$$

Although the constraint on $\delta_{\rm CP}$ is still weak to claim a discovery of non-zero $\delta_{\rm CP}$, this result is an important step towards the discovery of CP violation in the lepton sector.

Acknowledgements

For the six years of my life as a graduate student, I was extremely lucky to have supports of many people. Without their help, I could not realize this thesis.

First of all, I would like to express my gratitude to Tsuyoshi Nakaya, for always leading me to the right way. He also gave me a lot of opportunities to have precious experiences. His advice and attitude made me rethink my own stance and attitude as a researcher. I also want to express my thanks to Atsuko Ichikawa. She gave me a lot of advices at the meeting, which were often very crucial and productive. I also want to express my gratitude to Akihiro Minamino who gave me a lot of advice for my analysis.

I would like to give special thanks to the member of the DUET experiment. I owe a big thanks to Motoyasu Ikeda, who helped me not only in the research but also in the private life. I would like to thank him for his patience over the years supporting me and leading the DUET experiment. I would like to thank Takahiro Yamauchi for being a core member of PIAνO team. I owe a great deal of thanks to Hirohisa A Tanaka and Michael Wilking, who helped me not only as the DUET collaborators, but also as the member of the FGD group. I would like to give many thanks to Kendall Mann, for supporting me in DUET, in the oscillation analysis and in the life in Vancouver. I am also grateful to everyone who helped me in the DUET experiment including Masashi Yokoyama, Yoshinari Hayato, Yasutaka Kanazawa, Patrick de Perio, Elder Pinzon, Sampa Bhadra, Charles Cao and Matt Gottshalk.

My work in T2K started in 2008. Especially in the first two years, I spent a lot of time working with people from Canadian group. I am really glad to have been able to work with them. I would like to thank Scott Oser, Thomas Lindner, Fabrice Retiere, Akira Konaka, Nicholas Hastings, Daniel Brook Roberge, Caio Licciardi, Brian Kirby, Shimpei Tobayama, Jiae Kim and all other people who worked with me. I never forget the taste of Hitachi beef which we had at the collaboration meeting in 2014. I hope to have chance to work with you again in the future.

I owe a huge thanks to Christophe Bronner and Ken Sakashita, who worked with me for the oscillation analysis. I learned a lot from the discussion with them, and it was my honour and great pleasure to work with such bright and talented people. I would like to also thank Yasuhiro Nishimura and Joshua Hignight for the discussion of the ν_e analysis results. My work on the oscillation analysis is directly dependent upon the hard work of the oscillation analysis group. I want to express my gratitude to all the T2K members and people in the J-PARC, KEK and SK group.

Living in Tokai with T2K collaborators was really fun. I would like to thank Akira Murakami, Kento Suzuki, Shota Takahashi, Tatsuya Kikawa and Kunxian Huang staying at Ohta-danchi with me. It was nice to have Nabe party with sake and games with you. I enjoyed both physics discussion and meaningless discussions. I wish to extend my thanks to Masashi Otani, Hajime Kubo, Kodai Matsuoka, Takatomi Yano, Takahiro Hiraki, Seiko Hirota, Megan Friend, Ryoske Ohta and Phillip Litchfield.

Kyoto University is the place I've spent most of the time in the last years. I must thank all the other members in our laboratory: Masaya Ishino, Tadashi Nomura, Hajime Nanjo, Toshi

Sumida, Saki Yamashita, Naoki Kawasaki, Takahiko Masuda, Daichi Naito, Yosuke Maeda, Shigeto Seki, Takuya Tashiro, Tokio Nagasaki, Shinichi Akiyama, Naoyuki Kamo, Keiji Tateishi, Takaki Hineno, Yuuki Ishiyama, Ichinori Kamiji, Takuto Kunigo, Jiang Miao, Kota Nakagiri, Keigo Nakamura, Tatsuya Hayashino and Kento Yoshida.

I would like to acknowledge supports from the Japan Society for Promotion of Science (JSPS) and the global COE program.

Finally, I would like to send my best thanks to my family.

Kei Ieki
Kyoto, Japan
February, 2014

Contents

I Neutrino oscillation **1**

1 Introduction **2**
1.1 Neutrino oscillation . . . 2
1.1.1 Three flavours of neutrinos . . . 2
1.1.2 Discovery of neutrino oscillation . . . 3
1.1.3 Theory of neutrino oscillation . . . 3
1.2 Current knowledge of neutrino physics . . . 6
1.2.1 Oscillation parameters . . . 6
1.2.2 Unanswered questions . . . 8
1.3 Motivation of $\nu_\mu \to \nu_e$ measurement . . . 11
1.4 Outline of this thesis . . . 12

II T2K experiment **14**

2 Overview of the T2K experiment **15**
2.1 J-PARC neutrino beam line . . . 16
2.1.1 Controlling the primary proton beam . . . 16
2.1.2 Off-Axis method . . . 18
2.2 Monitoring of the secondary beam . . . 19
2.2.1 Muon monitor . . . 21
2.2.2 INGRID . . . 21
2.3 ND280 and Super-Kamiokande . . . 22
2.3.1 Neutrino detection at ND280 and SK . . . 22
2.3.2 ND280 . . . 23
2.3.3 Far detector (Super-Kamiokande) . . . 25
2.4 Summary of the beam data taking . . . 25

3 The Fine-Grained Detector **28**
3.1 FGD and neutrino interaction . . . 28
3.2 Fine-Grained Detector . . . 29
3.2.1 Overview of the design . . . 29
3.2.2 Readout electronics . . . 30
3.2.3 MPPC (Multi-Pixel Photon Counter) . . . 32
3.2.4 Detector calibration . . . 33
3.3 Reconstruction of particle trajectories . . . 35

III Pion interaction in the neutrino interaction model **40**

4 Measurement of pion interaction **41**
4.1 Motivation of the measurement . . . 41
4.2 Overview of the experimental setup . . . 42
4.3 Detector configuration . . . 43
4.3.1 Fiber tracker . . . 44
4.3.2 NaI detector and Harpsichord detector . . . 48
4.3.3 Summary of Data-taking . . . 49

5 Extraction of pion absorption and charge exchange cross section **50**
5.1 Event reconstruction . . . 50
5.2 Event selection . . . 52
5.3 Simulation of the detector and pion interaction . . . 53
5.3.1 Physics model . . . 54
5.3.2 Detector and beam . . . 55
5.4 Extraction of the cross section . . . 56

6 Improvement of pion interaction model **62**
6.1 Cascade model . . . 62
6.2 Fit to the pion cross section data sets . . . 64

IV Analysis of $\nu_\mu \to \nu_e$ oscillation **73**

7 Overview of the oscillation analysis **74**

8 Monte Carlo simulation **76**
8.1 Flux prediction with systematic uncertainties . . . 76
8.2 Neutrino interaction model and constraints . . . 77
8.2.1 Neutrino interaction model . . . 78
8.2.2 Cross section parameters . . . 81

9 Near detector measurement **84**
9.1 Event reconstruction . . . 84
9.2 Event selection . . . 86
9.3 Systematic uncertainties . . . 90
9.4 Constraining the neutrino flux and cross section . . . 91

10 Far detector measurement **95**
10.1 ν_e event selection . . . 95
10.2 Systematic uncertainties . . . 98

11 Oscillation analysis and results **100**
11.1 Overview . . . 100
11.2 Fit procedure . . . 101
11.2.1 Definition of the likelihood . . . 101
11.2.2 Likelihood marginalization . . . 103
11.3 Prediction of SK observables . . . 103
11.4 Systematic uncertainties . . . 104
11.4.1 Description and implementation of the systematic errors . . . 104
11.4.2 Effect of systematic uncertainties . . . 108

11.5 Sensitivity . . . 113
11.6 Fit results for Run1-4 data . . . 115
11.6.1 Fit to Run1-4 data . . . 115
11.6.2 Fit with different $\sin^2\theta_{23}$ values . . . 116
11.7 Results using the reactor measurements . . . 123
11.7.1 Constraint term and marginalization . . . 123
11.7.2 Fit results with θ_{23} and Δm^2_{32} varied . . . 124
11.7.3 Fit results with reactor measurements . . . 124
11.8 Summary . . . 128

V Conclusion 132

12 Conclusion 133

A Simulation and the systematic errors in the pion interaction measurement 135
A.1 Detector . . . 135
A.2 Beam . . . 137
A.3 Estimation of the systematic errors . . . 140

B Neutrino flux and cross section uncertainties 146
B.1 Flux tuning and errors . . . 146
B.1.1 Hadronic interactions . . . 146
B.1.2 Proton beam, alignment and off-axis angle . . . 149
B.1.3 Horn current & field . . . 150
B.2 Constraints on the cross section parameters . . . 150
B.2.1 CCQE model uncertainty . . . 150
B.2.2 CC1π, NC1π^0 resonance interaction model uncertainty . . . 150
B.2.3 Other interaction channels . . . 151

C ND280 data fit 153
C.1 Parameters for the fit . . . 153
C.2 Definition of the likelihood . . . 154

D SK efficiency error 156

E Comparison with 2012 ν_e appearance analysis 159

List of Tables 167

List of Figures 169

Part I

Neutrino oscillation

Chapter 1

Introduction

The standard model (SM) of particle physics was born in 1970s, and it has successfully explained almost all experimental results in the last 40 years. The last piece of the SM was the Higgs boson, which was finally discovered at the LHC in 2012. Arguably it has been one of the most successful theory in the particle physics, but it is not perfect. For example:

- Gravity is not included in SM in a consistent quantum mechanical way
- SM contains too many parameters, and do not explain the origin of masses and mixing pattern of particles
- Matter-antimatter asymmetry in the universe is not explained
- Dark matter and dark energy are not explained

Neutrino physics is one of the key to explore the physics beyond SM. The SM assumes mass-less neutrinos and no flavour mixing in the lepton sector, but the discovery of neutrino oscillation in 1998 by the Super-Kamiokande collaboration [1] shows that they have non-zero mass. This discovery gives a first hint of the physics beyond SM. Furthermore, the measurements of the neutrino oscillations are important for investigating the origin of the mixing pattern of leptons. Neutrino physics can also be a key to solve the problem of the matter-antimatter asymmetry. In the leptogenesis scenario [2], which is one of the most plausible explanation of the matter-antimatter asymmetry, the asymmetry arises from the decay of heavy right handed neutrinos which do not exist in the SM.

1.1 Neutrino oscillation

1.1.1 Three flavours of neutrinos

Neutrino is a neutral elementary particle which was first postulated by W. Pauli in 1930, in his famous "Dear Radioactive Ladies and Gentlemen" letter. In order to explain the energy spectrum of the electron from the beta-decay which seemed to indicate that energy was not conserved in the process, he postulated an existence of a new neutral particle. The new particle was originally called "neutron", but it was named "neutrino" by E. Fermi in 1931.

Neutrino was first detected by Reines and Cowan in 1953 [3]. They observed electron anti-neutrinos produced in the reactors, by detecting the inverse β-decay ($\overline{\nu}_e + p \rightarrow n + e^+$) on a $CdCl_2$-loaded scintillator target. In 1962, it was showed by L.M. Lederman, M. Schwartz and J. Steinberger [4] that there were more than one type of neutrino. They detected muon neutrinos from the decay of pions at the Brookhaven's AGS (Alternating Gradient Synchrotron). Evidence that there are three active neutrino species comes from the Z^0 width measurement at the CERN

LEP collider [5]. Nowadays, three types or "flavours" of neutrinos are known to exist: electron neutrino (ν_e), muon neutrino (ν_μ) and tau neutrino (ν_τ). Transmission from the neutrino in one flavor to an another flavour is not allowed in the SM.

1.1.2 Discovery of neutrino oscillation

Neutrino oscillation is a phenomena that neutrino flavour (e, μ, τ) changes back and forth periodically as neutrino travels through space. It was initially indicated from the measurement of solar neutrinos. Solar neutrinos are the neutrinos generated from nuclear fusion process in the sun. The first solar neutrino experiment was the Homestake experiment [6] in late 1960s. The measured solar neutrino flux was found to be only 1/3 of neutrinos predicted by the Standard Solar Model. This deficit of the solar neutrino flux was called "solar neutrino problem".

The deficit was also observed by the Kamiokande experiment [7], GALLEX (Gallium experiment) [8, 9], GNO (Gallium Neutrino Observatory) [10] and SAGE (Soviet-American Gallium Experiment) [11]. The Kamiokande experiment was able to confirm that the neutrinos are coming from the sun, by measuring the direction of electrons in the neutrino interactions ($\nu_e + n \to p + e^-$) by using water Cherenkov detector. The gallium experiments were able to measure with a lower energy threshold, by measuring radio-chemical interaction ($\nu_e + {}^{71}\mathrm{Ga} \to {}^{71}\mathrm{Ge} + e^-$). The simplest explanation for the deficit was that the solar model was wrong, but the neutrino oscillation was another possible explanation. In 1950, when the muon neutrino was not discovered yet, Pontecorvo postulated $\nu_e \leftrightarrow \overline{\nu}_e$ oscillation [12]. Later in 1962, after the discovery of ν_μ, Maki, Nakagawa and Sakata proposed [13] that neutrino could oscillate between different flavours*. At that time, people did not reach the conclusion whether the deficit is due to wrong solar neutrino model or the neutrino oscillation.

In 1998, the Super-Kamiokande (SK) collaboration reported [1] the first evidence of neutrino oscillation by measuring the atmospheric neutrinos at SK. SK is a water Cherenkov detector about ten times larger than Kamiokande. The atmospheric neutrinos are generated as decay products of hadrons produced in collisions of cosmic rays with nuclei in the atmosphere. The travel distance between the atmosphere and SK depends on the direction of incoming neutrinos at SK. The distance is long for the neutrinos which comes from the opposite side of the earth. The SK collaboration observed a zenith angle dependent deficit in atmospheric neutrino flux, which was consistent with the two-flavour $\nu_\mu \leftrightarrow \nu_\tau$ oscillation. The first evidence of the oscillation of solar neutrinos came in 2001 from the solar neutrino measurement by SNO (Sudbury Neutrino Observatory) [15] combined with the SK result [16]. Using a D_2O target, they were able to measure both charged current interaction ($\nu_e + d \to e + p + p$) and neutral current interaction ($\nu + d \to \nu + p + n$). The charged current (CC) interaction is an interaction mediated by $W^\pm$ bosons, and the neutral current (NC) interaction is an interaction mediated by Z boson. The CC interaction happens only when the energy of neutrino is sufficiently large to produce the charged lepton in the final state. While at low energy the CC interaction mode is only sensitive to ν_e, the NC interaction mode is also sensitive to the other type of neutrinos, so measuring both CC and NC interactions made it possible to confirm that neutrinos are oscillating to different flavour.

1.1.3 Theory of neutrino oscillation

Oscillation in vacuum

Neutrino oscillation arises from a mixture between the flavour and mass eigenstates of neutrinos. When there is a mixture, neutrino flavour eigenstates $|\nu_\alpha\rangle$ ($\alpha = e, \mu, \tau$) are described by a linear

*There is also an other paper from Katayama, Matsumoto, Tanaka and Yamada which proposed two flavour oscillation [14]

combination of the mass eigenstates $|\nu_i\rangle$ $(i = 1, 2, 3)$.

$$|\nu_\alpha\rangle = \sum_i U_{\alpha i}|\nu_i\rangle, \tag{1.1}$$

where $U_{\alpha i}$ is an element of 3×3 unitary matrix which is often called Pontecorvo-Maki-Nakagawa-Sakata (PMNS) matrix. PMNS matrix is expressed as follows.

$$\begin{aligned} U &= \begin{pmatrix} 1 & 0 & 0 \\ 0 & c_{23} & s_{23} \\ 0 & -s_{23} & c_{23} \end{pmatrix} \begin{pmatrix} c_{13} & 0 & s_{13}e^{-i\delta_{\rm CP}} \\ 0 & 1 & 0 \\ -s_{13}e^{i\delta_{\rm CP}} & 0 & c_{13} \end{pmatrix} \begin{pmatrix} c_{12} & s_{12} & 0 \\ -s_{12} & c_{12} & 0 \\ 0 & 0 & 1 \end{pmatrix} \\ &= \begin{pmatrix} c_{12}c_{13} & s_{12}c_{13} & s_{13}e^{-i\delta_{\rm CP}} \\ -s_{12}c_{23} - c_{12}s_{13}s_{23}e^{i\delta_{\rm CP}} & c_{12}c_{23} - s_{12}s_{23}s_{13}e^{i\delta_{\rm CP}} & c_{13}s_{23} \\ s_{12}s_{23} - c_{12}s_{13}c_{23}e^{i\delta_{\rm CP}} & -c_{12}s_{23} - s_{12}s_{23}s_{13}e^{i\delta_{\rm CP}} & c_{13}c_{23} \end{pmatrix}, \end{aligned} \tag{1.2}$$

where s_{ij} and c_{ij} represent $\sin\theta_{ij}$ and $\cos\theta_{ij}$, respectively. Three θ_{ij} are referred to as the mixing angles, and $\delta_{\rm CP}$ is the CP-violating phase. When a neutrino travel in vacuum, evolution of the mass eigenstate $|\nu_i\rangle$ after traveling time t is derived from Schrödinger equation.

$$i\frac{d}{dt}|\nu_i(t)\rangle = H|\nu_i(t)\rangle = E_i|\nu_i(t)\rangle, \tag{1.3}$$

$$|\nu_i(t)\rangle = e^{-E_i t}|\nu_i\rangle, \tag{1.4}$$

where H is the Hamiltonian, E_i is the energy of the mass eigenstate. Then, the flavour state at time t is written as:

$$|\nu_\alpha(t)\rangle = \sum_i U_{\alpha i}e^{-E_i t}|\nu_i\rangle, \tag{1.5}$$

Because neutrino masses are small, we can use following approximation.

$$E_i = \sqrt{p^2 + m_i^2} \simeq p + m_i^2/2p \simeq p + m_i^2/2E, \tag{1.6}$$

where p and m_i are the momentum and mass of the neutrino eigenstates. With this approximation, Equation 1.5 is written as:

$$|\nu_\alpha(t)\rangle = \sum_i U_{\alpha i}e^{-ipt}e^{-i\frac{m_i^2}{2E}t}|\nu_i\rangle \tag{1.7}$$

This equation indicates that the flavour state $|\nu_\alpha(t)\rangle$ changes as a function of t, because the time propagation of three mass eigenstates $|\nu_i\rangle$ are different from each other due to $e^{-im_i^2 t/(2E)}$ term. Therefore, an observation of neutrino oscillation indicates that neutrinos have masses.

The phase factor e^{-ipt} can be omitted in the calculation of oscillation probability, because it only changes the overall phase. Right hand side of Equation 1.7 can be re-written by converting the mass eigenstates to flavour eigenstates.

$$|\nu_\alpha(t)\rangle = \sum_{i,\beta} U_{\alpha i}e^{-i\frac{m_i^2}{2E}t}U_{\beta i}^*|\nu_\beta\rangle, \tag{1.8}$$

The probability $P(\nu_\alpha \to \nu_\beta)$ that ν_β is observed after ν_α traveling the distance L is given by:

$$P(\nu_\alpha \to \nu_\beta) = |\langle\nu_\beta|\nu_\alpha(t)\rangle|^2 \tag{1.9}$$

$$= \left|\sum_i U_{\alpha i}e^{-i\frac{m_i^2}{2E}t}U_{\beta i}^*\right|^2 \tag{1.10}$$

$$= \sum_{i,j} U_{\alpha i}^* U_{\beta i} U_{\alpha j} U_{\beta j}^* e^{-i\frac{(m_i^2 - m_j^2)}{2E}t}. \tag{1.11}$$

The time t can be replaced with the travel distance $L(= ct)$ since neutrinos are relativistic. Using the unitarity condition $\sum_i U^*_{\alpha i} U_{\beta_i} = \delta_{\alpha\beta}$, Equation 1.11 can be written as follows.

$$P(\nu_\alpha \to \nu_\beta) = \delta_{\alpha\beta} - 4\sum_{i>j} \mathrm{Re}(U^*_{\alpha i} U_{\beta i} U_{\alpha j} U^*_{\beta j}) \sin^2\left(\frac{\Delta m^2_{ij} L}{4E}\right) - 2\sum_{i>j} \mathrm{Im}(U^*_{\alpha i} U_{\beta i} U_{\alpha j} U^*_{\beta j}) \sin\left(\frac{\Delta m^2_{ij} L}{2E}\right), \quad (1.12)$$

where $\Delta m^2_{ij} = m^2_i - m^2_j$.

Let's derive $P(\nu_\mu \to \nu_e)$, which is relevant to the analysis described in this thesis. From the past experimental results, we know that $|\Delta m^2_{23}| \simeq |\Delta m^2_{31}| \gg |\Delta m^2_{21}|$. Therefore, the effect on the neutrino oscillation due to Δm^2_{12} can be disregarded when $E/L \gg \Delta m^2_{21}$. In this case, an approximated formula for $P(\nu_\mu \to \nu_e)$ can be derived from Equation 1.12 as follows.

$$P(\nu_\mu \to \nu_e) \simeq \sin^2 2\theta_{13} \sin^2\theta_{23} \sin^2\left(\frac{\Delta m^2_{31} L}{4E}\right) \quad (1.13)$$

Oscillation in matter

In case of accelerator-based neutrino oscillation experiments, neutrinos are detected after traveling through matter. The neutrino oscillation probability with the matter is different from the probability in vacuum, due to the coherent scatterings in matter [17]. Figure 1.1 shows the coherent forward scatterings in the matter through neutral current (NC) and charged current (CC). The NC interaction is relevant for all flavours (ν_e, ν_μ and ν_τ), but the CC coherent forward scattering with electrons in the matter is only relevant for ν_e. Therefore, ν_e feels extra interaction potential in the matter. This is called "matter effect".

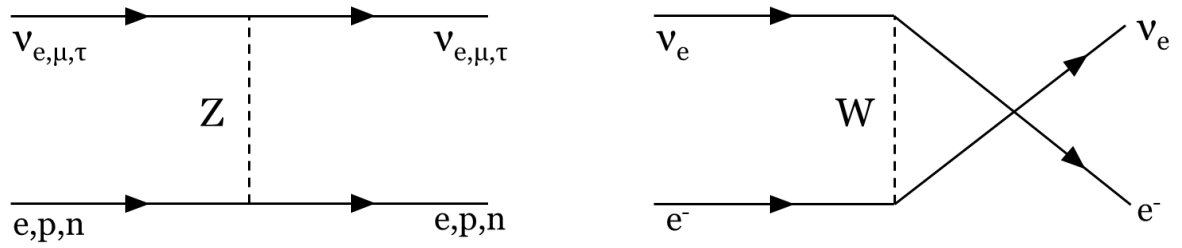

(a) Neutral current

(b) Charged current

Figure 1.1: Coherent forward scattering in matter.

The matter effect is taken into account by adding V in the Schrödinger equation.

$$i\frac{d}{dt}|\nu_\alpha(t)\rangle = (H_{\mathrm{vac}} + V)|\nu_\alpha(t)\rangle, \quad (1.14)$$

where H_{vac} is a Hamiltonian in case of vacuum. Note that this equation is written with flavor eigenstates, while in Equation 1.1 it was written with mass eigenstates. According to Equation 1.8, H_{vac} can be written as follows.

$$H_{\mathrm{vac}} = \frac{1}{2E} U \begin{pmatrix} m^2_1 & 0 & 0 \\ 0 & m^2_2 & 0 \\ 0 & 0 & m^2_3 \end{pmatrix} U^*. \quad (1.15)$$

V can be written as follows.

$$V = \begin{pmatrix} \sqrt{2}G_F n_e & 0 & 0 \\ 0 & 0 & 0 \\ 0 & 0 & 0 \end{pmatrix}, \tag{1.16}$$

where G_F is the Fermi constant, n_e is the matter electron density.

Probability of $\nu_\mu \to \nu_e$ oscillation

Including the first order of the matter effect, $P(\nu_\mu \to \nu_\mu)$ is written as [18]:

$$\begin{aligned} P(\nu_\mu \to \nu_e) &= 4c_{13}^2 s_{13}^2 s_{23}^2 \cdot \sin^2 \Phi_{31} \\ &+ 8c_{13}^2 s_{12} s_{13} s_{23} (c_{12} c_{23} \cos\delta_{\rm CP} - s_{12} s_{13} s_{23}) \cdot \cos\Phi_{32} \sin\Phi_{31} \sin\Phi_{21} \\ &- 8c_{13}^2 c_{12} c_{23} s_{12} s_{13} s_{23} \sin\delta_{\rm CP} \cdot \sin\Phi_{32} \sin\Phi_{31} \sin\Phi_{21} \\ &+ 4s_{12}^2 c_{13}^2 (c_{12}^2 c_{23}^2 + s_{12}^2 s_{23}^2 s_{13}^2 - 2c_{12} c_{23} s_{12} s_{13} \cos\delta_{\rm CP}) \cdot \sin^2 \Phi_{21} \\ &- 8c_{13}^2 c_{13}^2 s_{23}^2 \cdot \frac{aL}{4E} (1 - 2s_{13}^2) \cdot \cos\Phi_{32} \sin\Phi_{31} \\ &+ 8c_{13}^2 s_{13}^2 s_{23}^2 \frac{a}{\Delta m_{31}^2} (1 - 2s_{13}^2) \cdot \sin^2 \Phi_{31}, \end{aligned} \tag{1.17}$$

where

$$\Phi_{ij} \equiv \frac{\Delta m_{ij}^2 L}{4E} = 1.27 \frac{\Delta m_{ij}^2\ [\mathrm{eV}^2]\ L\ [\mathrm{km}]}{E\ [\mathrm{GeV}]}, \tag{1.18}$$

$$a \equiv 2\sqrt{2} G_F n_e E = 7.56 \times 10^{-5} \times \rho\ [\mathrm{g/cm}^3] \times E, \tag{1.19}$$

a represents the factor associated with the matter effect, and ρ represents the density of the earth. $P(\overline{\nu}_\mu \to \overline{\nu}_e)$ is derived by replacing $\delta_{\rm CP}$ to $-\delta_{\rm CP}$ and a to $-a$. The first term is the leading term, and it is equivalent to Equation 1.13. The second term which contains $\cos\delta_{\rm CP}$ is called CP conserving (CPC) term, while the third term which contains $\sin\delta_{\rm CP}$ is called CP violating (CPV) term. The fourth term which contains s_{12}^2 is called solar term (as we describe later, s_{12} is measured by solar neutrino experiments and reactor neutrino experiments). The last two terms represents the corrections by the matter effect. Figure 1.2 shows the $\nu_\mu \to \nu_e$ and $\overline{\nu}_\mu \to \overline{\nu}_e$ oscillation probability as a function of neutrino energy, calculated assuming $\Delta m_{12}^2 = 7.58 \times 10^{-5}$ eV^2, $\Delta m_{32}^2 = 2.35 \times 10^{-3}$ eV^2, $\sin^2\theta_{12} = 0.312$, $\sin^2\theta_{23} = 0.420$ and $\sin^2\theta_{13} = 0.0251$ [19].

1.2 Current knowledge of neutrino physics

1.2.1 Oscillation parameters

Since the discovery of neutrino oscillations, there have been a lot of experiments to measure neutrino oscillation parameters: three mixing angles $\theta_{12}, \theta_{23}, \theta_{13}$, mass-splittings $\Delta m_{23}^2, \Delta m_{12}^2, \Delta m_{31}^2$ ($\Delta m_{23}^2 + \Delta m_{12}^2 + \Delta m_{31}^2 = 0$, by definition) and the CP phase $\delta_{\rm CP}$. Except for $\delta_{\rm CP}$, all of them have been already measured. Table 1.1 shows the summary of the measured oscillation parameters from PDG 2012 [19]. They are measured in the following ways.

Measurements of θ_{12} and Δm_{21}^2

These parameters are sometimes referred to as the solar mixing angle and the mass splittings ($\theta_\odot, \Delta m_\odot^2$), because in solar neutrino experiments the oscillation probability $P(\nu_e \to \nu_e)$ is dominantly determined by these parameters. The Kamland experiment is a reactor neutrino

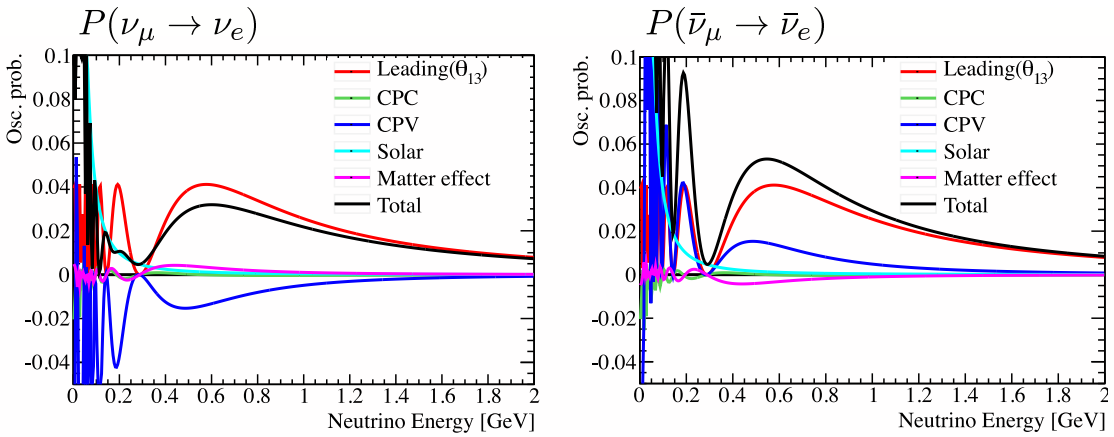

Figure 1.2: The $\nu_\mu \to \nu_e$ and $\overline{\nu}_\mu \to \overline{\nu}_e$ oscillation probability as a function of neutrino energy, with $\sin^2 2\theta_{13} = 0.098$, $\delta_{\rm CP} = \pi/2$, $\sin^2 2\theta_{23} = 0.97$, $|\Delta m^2_{32}| = 2.35 \times 10^{-3}{\rm eV}^2$, normal hierarchy and baseline of 295 km.

experiment which also measures these parameters. They measure $P(\overline{\nu}_e \to \overline{\nu}_e)$ for the anti-electron neutrinos from the reactors in nuclear fission process. Typical neutrino energy is $\mathcal{O}(1)$ MeV for both solar and reactor experiments. The best fit values of the parameters given in PDG 2012 are $\sin^2 2\theta_{12} = 0.857^{+0.023}_{-0.025}$ and $\Delta m^2_{12} = 7.50^{+0.19}_{-0.20} \times 10^{-5}$ eV^2 [20].

Measurements of θ_{23} and $|\Delta m^2_{32}|$

These parameters are called the atmospheric mixing angle and mass splittings ($\theta_{atm}, |\Delta m^2_{atm}|$) because the effect of these parameters is dominant in atmospheric neutrino experiments. The accelerator experiments also measure these parameters. They measure $P(\nu_\mu \to \nu_\mu)$ with ν_μ from the decay of pions, where the pions are generated by a proton beam. The energy of neutrinos are typically $\mathcal{O}(1)$ GeV for both atmospheric and accelerator neutrinos.

In PDG 2012, the Super-Kamiokande atmospheric neutrino measurement [21] provided the best measurement of θ_{23} ($0.95 < \sin^2 2\theta_{23} < 1$) with their high statistic data. The latest results from the T2K experiment also shows the measurement of θ_{23} with similar accuracy [22]. In the atmospheric neutrino experiments, there is ambiguity in the neutrino travel distance, which results in large systematic error on Δm^2_{32}. Therefore, the best value of Δm^2_{32} in PDG 2012 ($|\Delta m^2_{32}| = 2.32^{+0.12}_{-0.08}$ eV^2) is provided by the accelerator experiment (MINOS [23]), which measured the neutrino oscillation at the fixed distance. The sign of Δm^2_{32} is not known yet.

Measurements of θ_{13}

This parameter was not precisely measured until 2012. The first indication of non-zero θ_{13} was reported in 2011 [24] by an accelerator neutrino experiment, T2K. They (we) measured $P(\nu_\mu \to \nu_e)$ with the ν_μ beam ($E \sim 0.6$ GeV) and observed six ν_e candidate events at Super-Kamiokande ($L = 295$ km). The significance to exclude $\theta_{13} = 0$ was 2.5σ. Until then, only the upper limit of θ_{13} ($\sin^2 2\theta_{13} < 0.15$) was given by the Chooz reactor experiment [25]. In March 2012, Daya Bay [26] and RENO [27] reactor experiments reported an observation of non-zero θ_{13} with more than 5σ significance by measuring $P(\overline{\nu}_e \to \overline{\nu}_e)$.

The best fit value in PDG 2012 is $\sin^2 2\theta_{13} = 0.098 \pm 0.013$. It is an average of the results from three reactor experiments, Daya Bay, RENO and Double Chooz [28]. The T2K result was updated in 2012 summer, excluding $\theta_{13} = 0$ with 3.1σ significance [29–31]. Furthermore, as we

describe later in this thesis, we reported an updated results from T2K in 2013 [32] with 7.3σ significance.

Table 1.1: Best fit values of the oscillation parameters from PDG 2012.

Parameter	Best fit value
Δm^2_{21}	$7.50^{+0.19}_{-0.20} \times 10^{-5}$ eV^2
$\lvert\Delta m^2_{32}\rvert$	$2.32^{+0.12}_{-0.08} \times 10^{-3}$ eV^2
$\sin^2 2\theta_{12}$	$0.857^{+0.023}_{-0.025}$
$\sin^2 2\theta_{23}$	> 0.95
$\sin^2 2\theta_{13}$	0.098 ± 0.013

1.2.2 Unanswered questions

The last mixing angle, θ_{13}, was finally measured in 2012. However, there are still many questions in neutrino physics that have not been answered yet.

- What is the value of $\delta_{\rm CP}$?
- How are the mixing parameters determined? Is there physics behind it?
- Is $\Delta m^2_{32} > 0$ or $\Delta m^2_{32} < 0$?
- Does sterile neutrino exist?
- What are the absolute mass of neutrinos?
- Why are the neutrino masses so small? Are they the Majorana type or the Dirac type?

The first question is directly related to the motivation of the $\nu_\mu \to \nu_e$ measurement that we report in this thesis, and it is explained in the next section. The others are explained below.

Physics behind the mixing matrix

The standard model contains 19 free parameters. When the neutrino masses are not zero, we need to add 7 more parameters (3 masses + 3 mixing angles + 1 Dirac CP phase). It is natural to expect physics beyond the standard model to predict these parameters. Ten of the parameters in SM comes from the mass and mixing of the quarks. A mixing matrix in the quark sector, which is similar to the PMNS matrix in the lepton sector, is called CKM (Cabibbo-Kobayashi-Maskawa) matrix. The CKM elements are measured as follows [19]:

$$|V_{\rm CKM}| = \begin{pmatrix} |V_{ud}| & |V_{us}| & |V_{ub}| \\ |V_{cd}| & |V_{cs}| & |V_{cb}| \\ |V_{td}| & |V_{ts}| & |V_{tb}| \end{pmatrix} = \begin{pmatrix} 0.97427 \pm 0.00015 & 0.22534 \pm 0.00065 & 0.00351^{+0.00015}_{-0.00014} \\ 0.22520 \pm 0.00065 & 0.97344 \pm 0.00016 & 0.0412^{+0.0011}_{-0.0005} \\ 0.00867^{+0.00029}_{-0.00031} & 0.0404^{+0.0011}_{-0.0005} & 0.999146^{+0.000021}_{-0.000046} \end{pmatrix}. \tag{1.20}$$

On the other hand, the PMNS matrix is measured as follows with the parameters shown in Table 1.1 (assuming $\sin^2 2\theta_{23} = 1$ and $\delta_{\rm CP} = 0$).

$$U_{\rm PMNS} = \begin{pmatrix} 0.81 \sim 0.83 & 0.54 \sim 0.57 & 0.15 \sim 0.17 \\ -0.53 \sim -0.44 & 0.44 \sim 0.61 & 0.61 \sim 0.77 \\ 0.23 \sim 0.37 & -0.73 \sim -0.56 & 0.62 \sim 0.77 \end{pmatrix}. \tag{1.21}$$

The elements of the PMNS matrix are found to be very different from the elements in the CKM matrix. The mixing angles in lepton sector ($\theta_{12} \sim 33.9,\ \theta_{23} \sim 45.0,\ \theta_{13} \sim 9.1$ degrees) are much larger than the mixing angles in the quark sector ($\theta_{12}^{\rm CKM} \sim 13.0,\ \theta_{23}^{\rm CKM} \sim 2.4,\ \theta_{13}^{\rm CKM} \sim 0.2$ degrees). Especially, θ_{23} is large; $\theta_{23} = 45$ degrees corresponds to maximal $\nu_\mu \to \nu_\tau$ oscillation ($P(\nu_\mu \to \nu_\tau) \simeq \sin^2 2\theta_{23} \sin^2 \Phi_{23}$).

There are many physics models that predict the mixing angles in the lepton sector. One of the famous approach is to explain the mixing pattern as a special mixing pattern, such as "Tri-bimaximal" (TB) mixing [33].

$$U_{\rm TB} = \begin{pmatrix} \sqrt{2/3} & 1/\sqrt{3} & 0 \\ -1/\sqrt{6} & 1/\sqrt{3} & 1/\sqrt{2} \\ 1/\sqrt{6} & -1/\sqrt{3} & 1/\sqrt{2} \end{pmatrix} = \begin{pmatrix} 0.816 & 0.577 & 0 \\ -0.408 & 0.577 & 0.707 \\ 0.408 & -0.577 & 0.707 \end{pmatrix} \tag{1.22}$$

This mixing pattern assumes tri-maximal mixing in ν_2 (second row) and bi-maximal mixing in ν_3 (third row). The TB mixing pattern can be derived by assuming flavour symmetry [†]. Flavour symmetry is obtained by requiring the Lagrangian to be invariant under following transformations.

$$L_L \to X_L L_L, \quad \nu \to X_\nu \nu, \tag{1.23}$$

where L_L represents three generations of left-handed lepton doublets and ν is right-handed Majorana neutrinos. X_L and X_ν are the unitary matrices which belong to a representation of some symmetry group. For example, S_3 symmetry group is a symmetry under exchange of three objects. In this case X can be written as follows.

$$X = \begin{pmatrix} 1 & 0 & 0 \\ 0 & 0 & 1 \\ 0 & 1 & 0 \end{pmatrix}, \begin{pmatrix} 0 & 1 & 0 \\ 0 & 0 & 1 \\ 1 & 0 & 0 \end{pmatrix} \tag{1.24}$$

Some of the discrete family symmetries used in the literature are: A_4, S_3, S_4 and so on. A_4 is known as one of the good candidate for describing the symmetry of the three families observed in the nature, because it contains 3-dimensional representation.

The TB mixing pattern in Equation 1.22 seems to agree well with the measured values in Equation 1.21, except for the right top element ($= s_{13}e^{-i\delta_{\rm CP}}$ in Eq. 1.2) which is supposed to be zero in the case of the TB mixing but it is found to be non-zero according to the measurements of θ_{13}. Therefore, the exact TB mixing pattern is already ruled out. However, there are some approaches to view TB as a leading order patterns only, and to apply corrections to it [34].

The other famous model is called "Anarchy" model [35], which assumes no structure and no symmetry in the lepton sector. This model suggests that the mixing matrix is defined as a result of a random draw from an unbiased distribution of unitary three-by-three matrices. In this case it is plausible that the resulting mixing angles are large.

In order to identify the correct model, it is necessary to measure the mixing angles precisely, especially the unknown parameter $\delta_{\rm CP}$.

Mass hierarchy

The sign of Δm^2_{23} is not known yet, and the ordering of mass can be either $m_3 > m_1, m_2$ or $m_3 < m_1, m_2$ (see Fig. **??**). The former case is called "normal hierarchy", and the latter case is called "inverted hierarchy". Long baseline experiments at accelerators, which look for $\nu_\mu \to \nu_e$ oscillations, such as T2K and NOνA experiments are sensitive to the mass hierarchy through matter effects. NOνA is more sensitive to the mass hierarchy than T2K because the baseline is longer ($L \sim 810$ km) and the matter effect is more significant.

[†]Furthermore, in order to obtain the TB mixing pattern, the addition of extra Higgs scalars with non-zero vacuum expectation values that break the family symmetry is usually required.

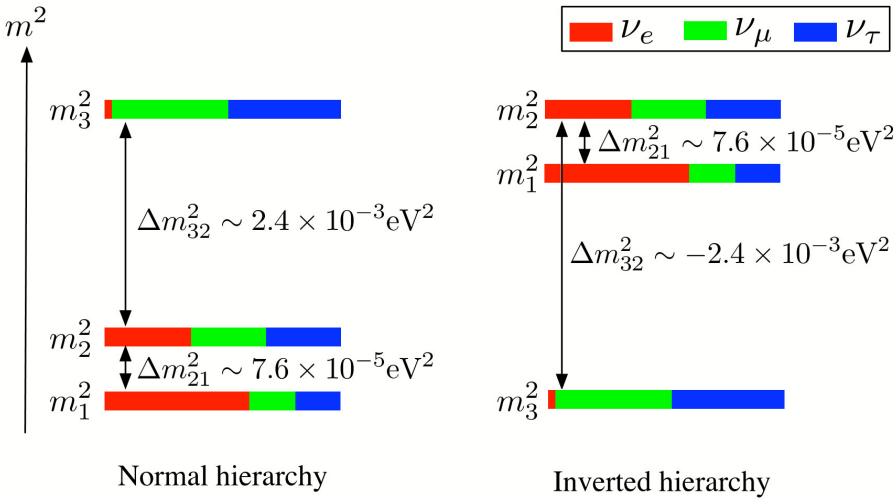

Figure 1.3: Neutrino mass hierarchy.

Sterile neutrino

As explained in Section 1.1, the number of neutrino flavours is measured to be three. However, there could be a fourth (or fifth, sixth, ...) generation of neutrinos which do not interact via weak interaction. If they exist, the active three neutrinos may oscillate to those sterile neutrinos. There are several experiments that indicate the existence of sterile neutrinos [36–39]. For example, the LSND experiment observed 3.8σ event excess in $\overline{\nu}_\mu \to \overline{\nu}_e$ signal. A possible explanation of the signal is the neutrino oscillation through sterile neutrino ν_s with $\Delta m^2 \sim$1 eV^2 ($\nu_\mu \to \nu_s \to \nu_e$). However, there are also several experiments which show the negative indication for the existence of sterile neutrinos and give a constraint in the allowed parameter space [40–42]. The existence of sterile neutrinos is not yet confirmed, and there are many experiments to measure sterile neutrinos.

Absolute mass measurement

Although the mass squared difference (Δm^2) are measured in neutrino oscillation experiments, the absolute masses are not measured yet. The upper limit for neutrino masses in PDG 2012 is summarized in Table 1.2. The upper limit of sum of the mass for three types of neutrinos is

Table 1.2: Upper limits for neutrino mass.

Neutrino type	Mass limit	Measurement method
$\overline{\nu}_e$	2 eV	Tritium decay
ν_μ	0.19 MeV	π decay at rest
ν_τ	18.2 MeV	τ decay

also obtained from cosmology (cosmic microwave background measurements and others, model dependent): $m_{\nu_e} + m_{\nu_\mu} + m_{\nu_\tau} <\sim 0.5$ eV. There are also several experiments (KATRIN, MARE, Project8 and so on) to measure the mass directly.

Majorana and see-saw model

The neutrino masses are very small compared to the other elementary particles. A see-saw mechanism is a possible explanation for the tiny neutrino masses. The original see-saw mechanism (type-I) extends the SM by assuming two or more additional right handed neutrino fields. In this case, the neutrino mass term in the Lagrangian can be written as follows.

$$\begin{aligned} \mathcal{L}_{\text{mass}} &= \mathcal{L}^{D}_{\text{mass}} + \mathcal{L}^{M}_{\text{mass}}, \\ \mathcal{L}^{D}_{\text{mass}} &= -m\overline{\nu}_L\nu_R + h.c., \qquad (1.25) \\ \mathcal{L}^{M}_{\text{mass}} &= -\frac{1}{2}M\overline{\nu}^c_R\nu_R + h.c., \qquad (1.26) \end{aligned}$$

where $\mathcal{L}^{D}_{\text{mass}}$ and $\mathcal{L}^{M}_{\text{mass}}$ are Dirac and Majorana mass terms. The Majorana mass term is constructed from ν_R or ν_L alone. It mixes neutrino and anti-neutrino, and violates lepton number. Quarks and charged leptons can not have the Majorana mass term because the conservation of electric charge will be violated if fermions and anti-fermions are mixed.

The mass term can be rewritten as follows:

$$\mathcal{L}_{\text{mass}} = -\frac{1}{2}(\overline{\nu}^c_L, \overline{\nu}_R)M_{mass}\begin{pmatrix}\nu_L \\ \nu^c_R\end{pmatrix} + h.c., \qquad (1.27)$$

where the mass matrix M_{mass} is

$$M_{mass} = \begin{pmatrix}0 & m \\ m & M\end{pmatrix}. \qquad (1.28)$$

The physical masses are the eigenvalues of the diagonalized mass matrix. If $m/M \ll 1$, these masses are obtained as m^2/M and M. We usually assume that m is the mass scale associated with the SM, and the scale M is provided by models extended beyond the SM. Because m^2/M is very small, it naturally explains the small mass of neutrinos. It also introduces heavy right handed neutrinos.

Whether the neutrinos are Majorana or not is important to understand the baryon asymmetry in the universe. In the leptogenesis scenario proposed by Fukugita and Yanagida [2], the matter-antimatter asymmetry is originated from the see-saw Majorana neutrinos. Majorana right handed neutrino N can decay to either leptons or anti-leptons

$$N \to l + H, \quad N \to \bar{l} + \overline{H}, \qquad (1.29)$$

where H represents the charged Higgs. If the CP is violated in the lepton sector, the probability for decaying to lepton and anti-lepton will be different. This lepton asymmetry is then converted to baryon asymmetry by the SM process called sphaleron [43], which happens at very high energy in the early universe. This could explain the baryon asymmetry in our universe.

Whether the neutrinos are Majorana or not can be tested by an observation of neutrinoless double beta decay (Fig. 1.4).

$$(Z, A) \to (Z + 2, A) + 2e^- \qquad (1.30)$$

This process is not forbidden if the neutrinos are Majorana. It is being searched by many experiments such as GERDA [44], CUORICINO [45], EXO-200 [46], Kamland-Zen [47] and so on.

1.3 Motivation of $\nu_\mu \to \nu_e$ measurement

In this thesis, we report a measurement of $\nu_\mu \to \nu_e$ oscillation in the T2K experiment. This oscillation mode is of particular interest because, as shown in Equation 1.17, this mode is sensitive

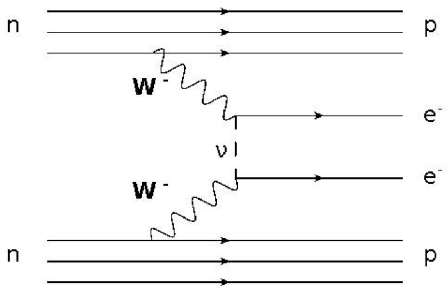

Figure 1.4: Feynman diagram of double beta decay.

to θ_{13} and $\delta_{\rm CP}$. As we explain in the previous section, the non-zero θ_{13} was first indicated by T2K in 2011, and confirmed by the reactor experiments. The reactor measurements provided the precise value of $\sin^2 2\theta_{13}$, but the $\delta_{\rm CP}$ is not measured yet.

The oscillation provability $P(\nu_\mu \to \nu_e)$ depends not only on θ_{13}, but also on $\delta_{\rm CP}$. On the other hand, the reactor experiments measures a disappearance of $\overline{\nu}_e$ ($P(\overline{\nu}_e \to \overline{\nu}_e)$).

$$P(\overline{\nu}_e \to \overline{\nu}_e) \simeq 1 - \sin^2 2\theta_{13} \sin\left(\frac{\Delta m^2_{31} L}{4E}\right). \tag{1.31}$$

This probability purely depends on θ_{13}, but not on $\delta_{\rm CP}$. In order to measure $\delta_{\rm CP}$, we need to measure the neutrino appearance mode $P(\nu_\alpha \to \nu_\beta)$. Disappearance mode ($P(\nu_\alpha \to \nu_\alpha)$) has been measured by many experiments, but there has not been an explicit observation of the appearance mode. In the T2K ν_e appearance analysis in 2012, we measured $P(\nu_\mu \to \nu_e)$ with 3.1σ significance. This thesis presents new results from the T2K experiment that establish, at greater than 5σ, the observation of ν_e appearance.

Since the value of θ_{13} is precisely measured by the reactor experiments, it is possible to measure $\delta_{\rm CP}$ by combining T2K $\nu_\mu \to \nu_e$ measurement with the result of $\sin^2 2\theta_{13}$ measurement from the reactor experiments, as we describe later in this thesis. The CPV term in Equation 1.17 is a second dominant term, and it can be as large as 27% of the leading term. The CP violation in lepton sector is never observed in the past, although it is already observed in the quark sector. Observations of the symmetry violations, such as discovery of P violation in 1957 [48] and discovery of CP violation in quark sector in 1964 [49], were very important in understanding the weak interactions. The observation of CP violation in the lepton sector is essential for understanding the mixing of leptons and quarks. It is also worth mentioning that even though the size of the CP phase that we measure in neutrino oscillation is not directly related to the CP phase in leptogenesis in a model independent way, the observation of non-zero $\delta_{\rm CP}$ would be a indication, even not a proof, of leptogenesis.

1.4 Outline of this thesis

We report the updated T2K ν_e appearance analysis using the neutrino beam data collected from Jan. 2010 to May. 2012.

First, we describe the overview of the T2K experiment in Chapter 2, which includes description of the neutrino beamline, the near detector and the far detector. In order to measure the neutrino oscillation with high precision, it is important to reduce the neutrino cross section and beam flux uncertainties. Those are measured by the near detector complex, which consists of several types of detectors. Especially the detector called FGD is important in the neutrino interaction measurement, and it is described in detail in Chapter 3.

Second, we describe the measurement of pion-nucleus cross section in Chapter 4 to 6. The pions are often generated in the neutrino interactions, and the uncertainty in the pion-nucleus interaction cross section is one of the important systematic error source in the neutrino oscillation experiment. Therefore, we performed a pion-nucleus cross section measurement at pion secondary beam line at TRIUMF. The detail of this measurement and the improvement in pion-nucleus interaction model are discussed.

Finally in Chapter 7∼11, we describe the ν_e appearance analysis. The overview of the analysis is given in Chapter 7. Because the ν_e appearance analysis relies on the simulation of neutrino beam and interaction in the analysis, we describe the details in Chapter 8. Then in Chapter 9 and 10, we describe the measurement at near and far detectors. Using the output of those measurements, we fit the data to extract the oscillation parameters in Chapter 11. The conclusions are given in Chapter 12.

Part II

T2K experiment

Chapter 2

Overview of the T2K experiment

The T2K experiment is an accelerator based long baseline neutrino oscillation experiment started physics data taking in 2010. The intense ν_μ beam is produced by J-PARC (Japan Accelerator Research Complex) proton accelerator at Tokai. We detect the neutrinos at both the near detector "ND280" and the far detector "Super-Kamiokande" (SK) (Fig. 2.1). Neutrino oscillation probability is determined by measuring the neutrino beam before and after oscillation at the near and far detectors, respectively.

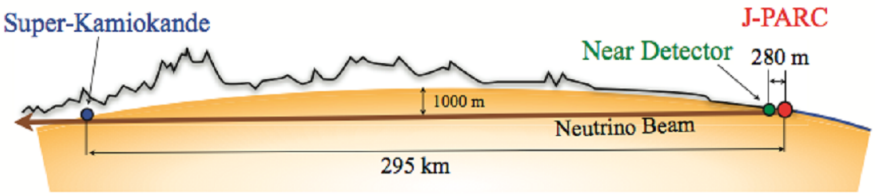

Figure 2.1: The overview the of T2K experiment [50].

The main goals of the T2K experiment are as follows:

Discovery of $\nu_\mu \to \nu_e$ oscillation

Before the discovery of non-zero θ_{13} in 2012, our primary goal was to extend the θ_{13} search down to $\sin^2 2\theta_{13} \sim 0.008$ by the measurement of $\nu_\mu \to \nu_e$. Nowadays, θ_{13} is already measured to be $\sin^2 2\theta_{13} = 0.098 \pm 0.013$ [51]. Then, in order to determine the value of δ_{CP}, the precise measurement of $\nu_\mu \to \nu_e$ become more important. Currently, our motivation of this measurement is to discover $\nu_\mu \to \nu_e$ with more than 5σ significance, and to measure δ_{CP}.

Precise measurement of oscillation parameters in $\nu_\mu \to \nu_\mu$ oscillation

Our goal of the $\nu_\mu \to \nu_\mu$ measurement is to determine the values of θ_{23} and Δm^2_{32} with an accuracy of 1% and 3%, respectively. This is important not only to explore the physics behind the mixing pattern, but also for the measurement of δ_{CP} because the CPV term in $P(\nu_\mu \to \nu_e)$ is proportional to $\sin\theta_{13}\sin\theta_{23}\sin\theta_{12}\sin\delta_{\mathrm{CP}}$. In our current best knowledge, the uncertainty of θ_{23} is the largest among three mixing angles.

The main feature of the T2K experiment is that we use high intensity neutrino beam and gigantic water Cherenkov detector (SK) which provides high statistics of neutrino events. The other important feature is that we use "off-axis beam" which enables to obtain a neutrino beam with sharp energy spectrum peaked at the energy which maximizes the neutrino oscillation probability. In the following sections, we describe those important features while explaining the overview of the T2K beamline and detector configurations.

2.1 J-PARC neutrino beam line

The layout of the J-PARC accelerators is shown in Fig. 2.2. The protons are accelerated through linear accelerator (LINAC), 3 GeV proton-synchrotron (RCS), and main ring (MR). The proton beam is extracted from the MR to the neutrino beam line. In the neutrino beamline, the beam is shaped by 11 normal conducting magnets, bent to the direction of SK by 14 superconducting magnets, and transported to the neutrino production target by 10 normal conducting magnets. The protons generates the pions by the interaction on target, and the pions decay to μ and ν_μ to produce a ν_μ beam.

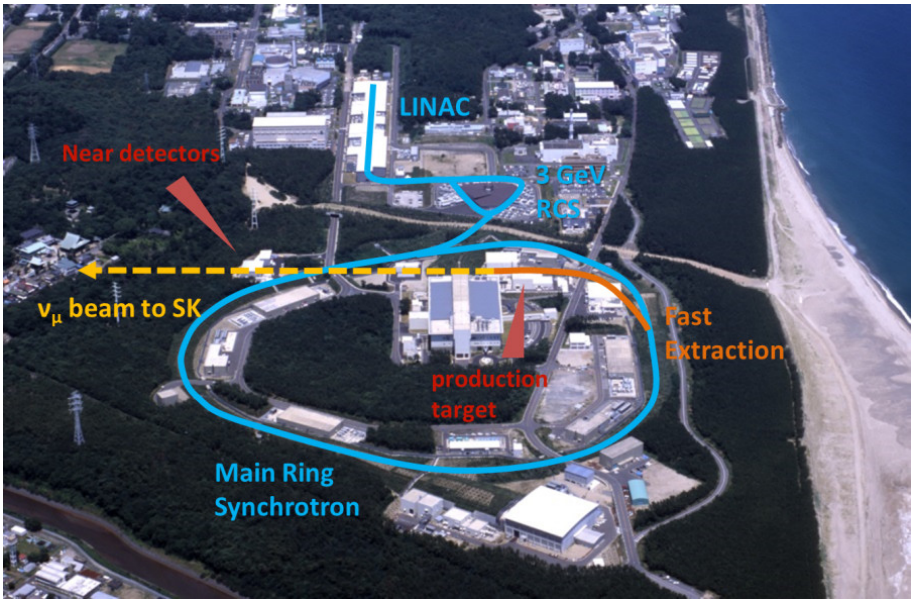

Figure 2.2: Bird's eye view of J-PARC.

Figure 2.3 shows the overview of the neutrino beam line and the near detectors. The protons smashes the graphite target and produces secondary pions. The directions of pions are focused by three electro-magnetic horns [52]. The target sits inside the first horn, and the second and third horns are placed at the downstream of the target. The positive pions are focused to the forward direction (Fig. 2.4), while the negative pions are de-focused. Then the pions decay to neutrinos in the 94 m long decay region ($\pi \rightarrow \mu + \nu_\mu$). At the end of the decay volume, the remaining protons and pions are absorbed by the beam dump. Only the neutrinos and high energy muons will penetrate the beam dump. The muon monitor sits at the 118 m downstream of the beam target and measures the muon beam flux and direction. The near detectors called "ND280" and "INGRID" measure the neutrino beam at 280 m downstream of the target. As we explain in Section 2.1.2, the direction of SK is shifted by 2.5 degree from the direction of the proton beam, because we use the "off-axis" method.

The T2K beam parameters are listed in Table (2.1). The current beam power is 220 kW, while the designed value is 750 kW. The beam power will increase in the future by increasing the number of protons per bunch and the repetition rate, by upgrading the LINAC, the MR magnet power supply and the MR RF core.

2.1.1 Controlling the primary proton beam

The proton beam is controlled by using many beam monitors which are placed in the beamline. Figure 2.5 shows the locations of the beam monitors. The beam intensity, position, profile and

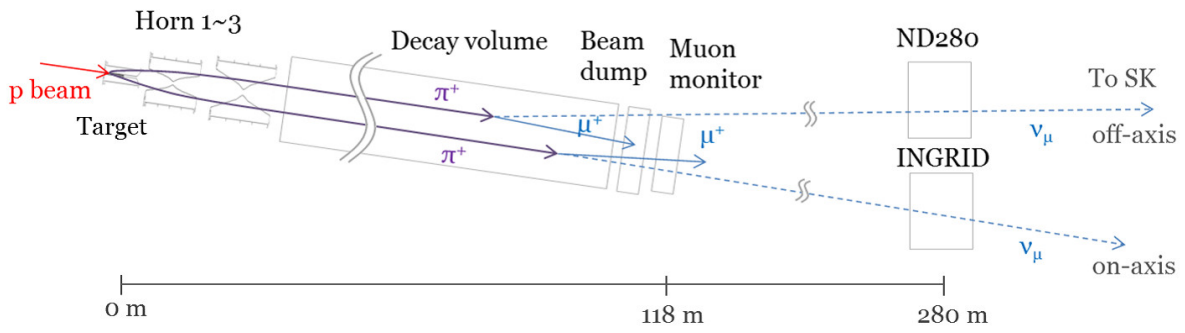

Figure 2.3: Neutrino beam line and the near detectors.

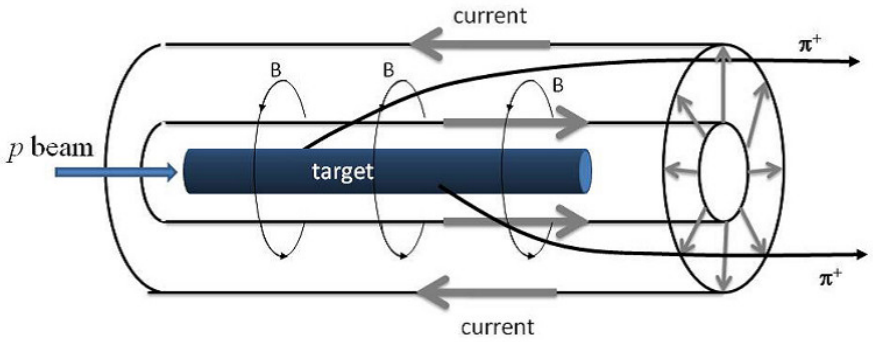

Figure 2.4: Illustration of the first horn. The graphite target sits inside the first horn. The positively charged particles produced by the proton beam are focused in the forward direction due to the magnetic field.

loss are monitored by the current transformers (CT), electro-static monitors (ESM), segmented secondary emission monitors (SSEM) and beam loss monitors (BLM), respectively. The optical transition radiation (OTR) monitor which is placed just upstream of the target measures the beam profile. Figure 2.6 shows the illustrations of CT, ESM, SSEM and OTR. We describe each of the monitor below.

Current transformer (CT)

The CT is a 50-turn toroidal coil around a cylindrical ferromagnetic core. It measures the current induced by the toroidal magnetic field induced by the proton beam. The beam intensity is measured by CT with 2% accuracy.

Electro-static monitor (ESM)

The ESM has four segmented cylindrical electrodes surrounding the proton beam. By measuring the induced current, it measures the beam position with better than 450 μm accuracy.

Segmented secondary emission monitor (SSEM)

The SSEM is made of 5 μm titanium foil strips oriented in horizontal and vertical directions. The interaction of protons with the foil produces secondary electrons which induce currents on strips that can then be measured. Since they cause a beam loss, they are inserted only during the beam tuning and removed in the physics data taking except for the one which is placed at most downstream of the beam line.

Parameter	Design value	Present value in May 2013
Beam energy	50 GeV	30 GeV
Beam power	0.75MW	0.22 MW
Spill interval	~3.3 sec	2.48 sec
Number of protons	3.3×10^{14}/spill	1.2×10^{14}/spill
Number of bunches	8 bunches/spill	8 bunches/spill
Bunch interval	581 nsec	581 nsec
Bunch width	58 nsec	58 nsec

Table 2.1: Summary table of beam parameters

Beam loss monitors (BLM)

The BLM is a gas filled proportional counters. The beam abort signal is fired when the beam loss become too large.

Optical transition radiation monitor (OTR)

The OTR [53] measures the beam profile with 50 μm thick titanium alloy foil placed at 45 degrees to the incident proton beam. The beam crossing the foil produces transition radiation. Profile of the proton beam is measured by imaging the light using a system of parabolic mirrors and camera.

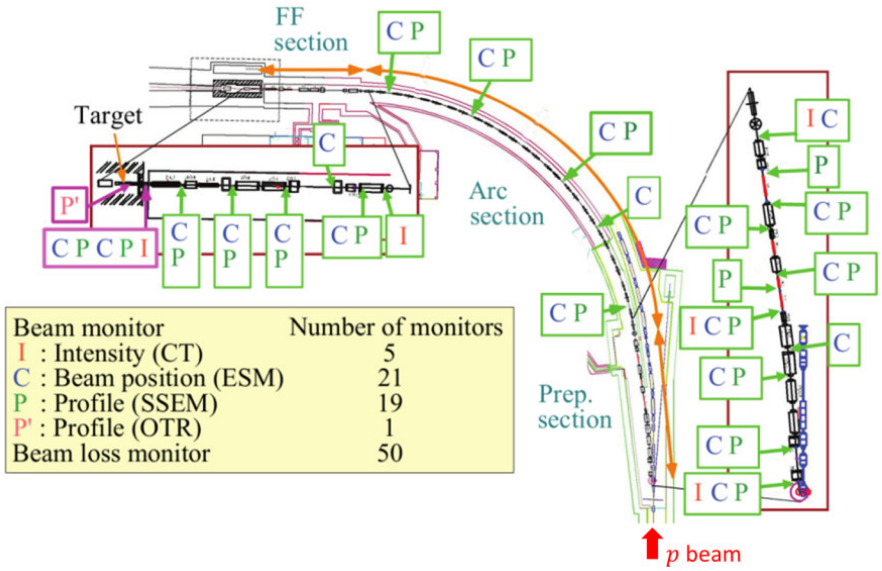

Figure 2.5: Locations of the beam monitors [50].

2.1.2 Off-Axis method

One of the important features of T2K is the off-axis beam. As shown in Fig. 2.3, the direction of neutrino beam is shifted by ~2.5 degree from the direction of SK. The direction of proton beam is called "on-axis", while the direction of SK is called "off-axis".

When a neutrino is produced from the decay of a pion $\pi \to \mu + \nu_\mu$ in the direction of off-axis angle θ_{OA} with respect to the initial pion direction, the energy of the neutrino can be derived

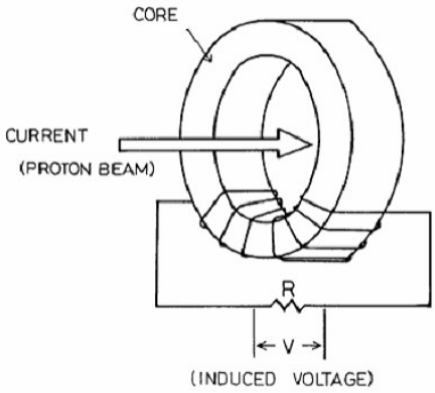

(a) CT

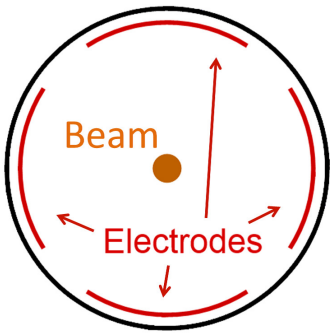

(b) ESM

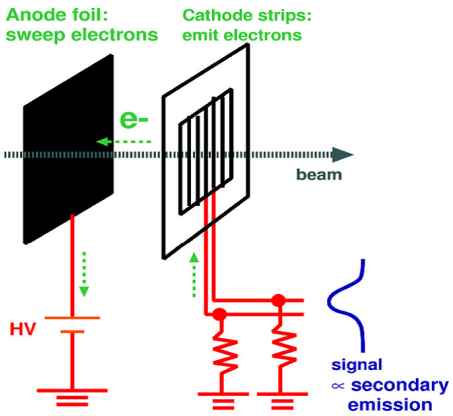

(c) SSEM

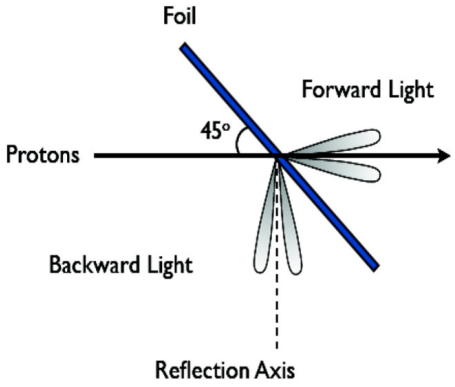

(d) OTR

Figure 2.6: Illustrations of the beam monitors.

from following equation:

$$E_\nu = \frac{m_\pi^2 - m_\mu^2}{2(E_\pi - P_\pi \cos\theta_{OA})}. \tag{2.1}$$

With a finite off-axis angle, the neutrino energy becomes almost independent of parent pion momentum (Fig. 2.7). Figure 2.8 shows the simulated neutrino energy spectrum with different off-axis angles and the oscillation probability as the function of neutrino energy. By using the off-axis method and adjusting the off-axis angle, we can maximize the signal to background ratio by making the narrow neutrino energy spectrum with a peak at the oscillation maximum, while reducing the backgrounds from high energy neutrino interactions. However, this method requires to carefully monitor the beam angle because the beam energy strongly depends on the beam direction.

2.2 Monitoring of the secondary beam

The direction and intensity of the neutrino beam are monitored by the muon monitor [54] and the INGRID detector [55], to ensure high quality neutrino beam.

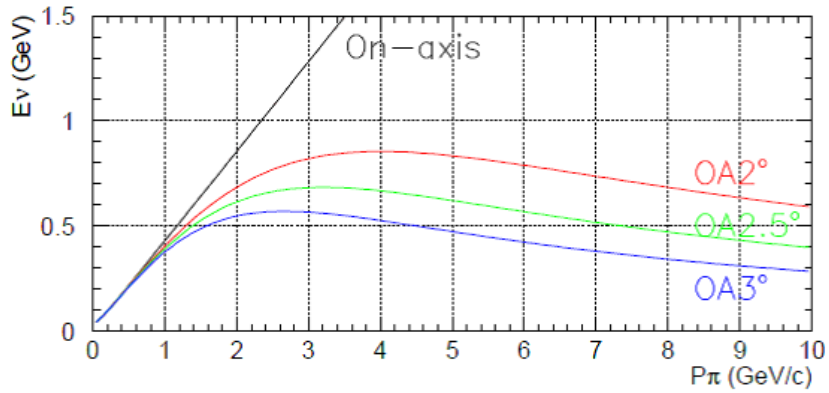

Figure 2.7: Neutrino energy in the function of the momentum of parent pion, for different off-axis angles.

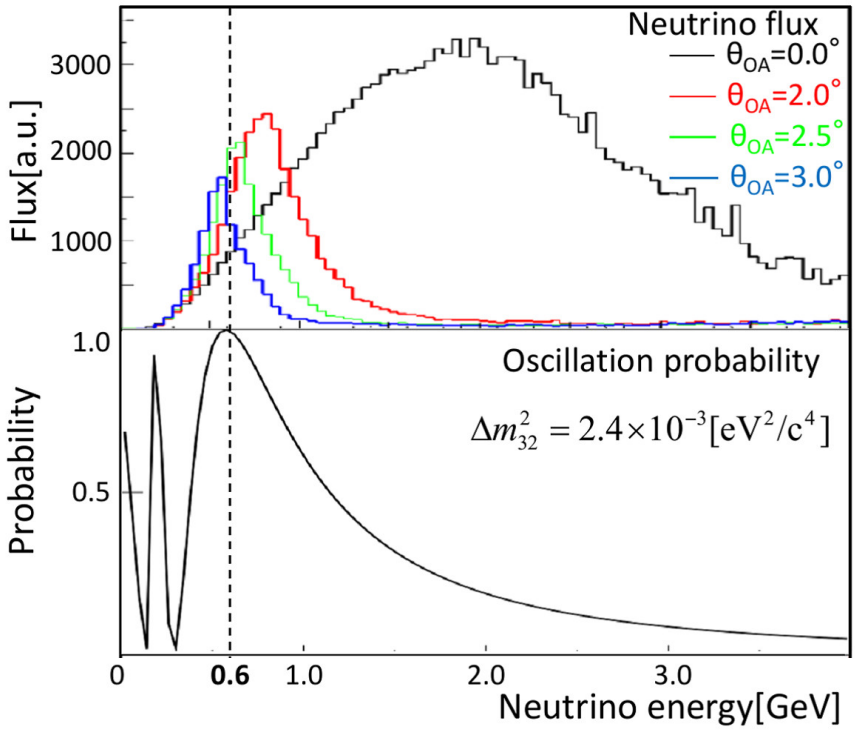

Figure 2.8: The neutrino energy spectrum for different off-axis angles (top) and the oscillation probability in the function of neutrino energy (bottom).

2.2.1 Muon monitor

The muons which penetrates the beam dump are measured by the muon monitor (MUMON), which is placed just behind the beam dump. While the INGRID monitors the neutrino beam by directly measuring it, MUMON indirectly monitor the neutrino beam by detecting muons which are produced together with neutrinos. The advantage of measuring the muon beam is that it makes it possible to monitor the neutrino beam direction in spill-by-spill basis, while the INGRID can only measure the beam direction in day-by-day basis at the designed beam power.

The MUMON monitors the intensity, profile and direction of the muon beam with the combination of ionization chambers array and silicon PIN photo-diodes array (Fig. 2.9). In each array, there are 7×7 sensors at 25 cm intervals. The ionization chambers are suitable to the muon beam measurement because they are made out of radiation tolerant material. However, it requires fine control of the gas quality to have a stable response. On the other hand, the silicon diodes are easy to handle, but the stability of the response is affected by the radiation. Therefore, the combination of two types of detectors provides complementary measurements. The precisions of muon flux intensity and direction measurement is estimated to be ~ 0.1 % and 0.25 mrad, respectively.

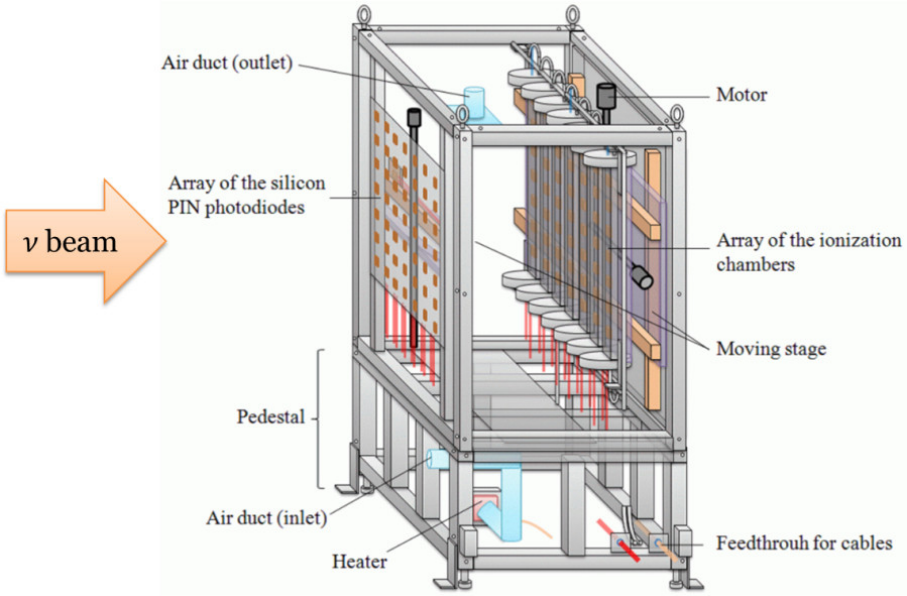

Figure 2.9: Schematic view of MUMON. Neutrino beam comes from the left side of the figure.

2.2.2 INGRID

The initial beam properties are measured by the near detectors, located at 280 m downstream from the neutrino production target, $\sim$ 30 m underground in the pit. The near detector consists of the on-axis detector INGRID and the off-axis detector ND280 (Fig. 2.10). The INGRID detects neutrino interactions to measure the neutrino beam direction and the stability of the beam.

The RMS width of the neutrino beam at the near detector pit is $\sim$5 meters. In order to monitor the neutrino beam, INGRID is designed to cover a wide region with large mass. Figure 2.11 shows the schematic view of the INGRID. It consists of 16 identical modules: seven horizontal modules, seven vertical modules and two off-cross modules. The total width $\times$ total height is $\sim$10 m $\times$ 10 m. The beam direction is obtained by measuring the profile center of

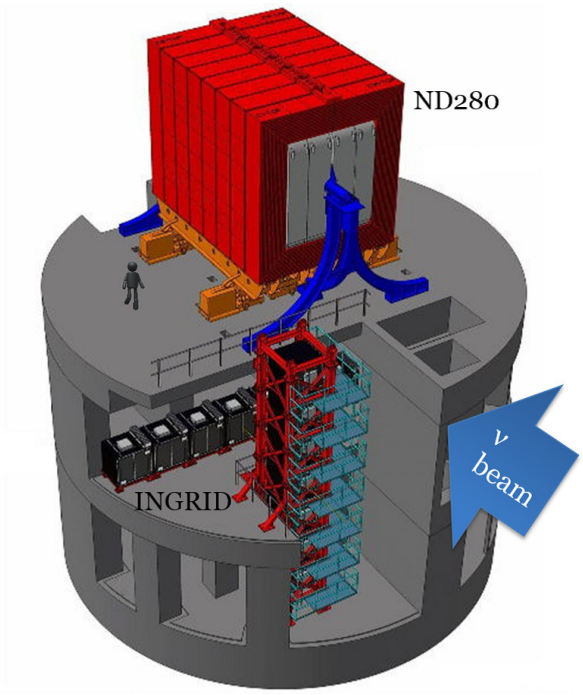

Figure 2.10: The near detectors located at 280 m downstream from the neutrino production target.

the neutrino beam. Each module is made of alternating plastic scintillators tracking planes and irons plates. The total iron mass serving as a neutrino target is 7.1 tons per module and ∼114 tons for all the modules.

The light signals from the scintillators are read out by a photon sensor called MPPC (Multi-Pixel Photon Counter). There are in total 9592 channel of MPPCs used in the INGRID, and they are also used in the ND280 detector. The detail of the MPPC is described in Chapter 3.

2.3 ND280 and Super-Kamiokande

The ND280 detector measures the neutrino interactions before oscillations, while the SK measures the neutrino interactions after oscillations.

2.3.1 Neutrino detection at ND280 and SK

Before explaining the detail of the ND280 and SK, we describe the neutrino interaction modes which are relevant to the measurements in T2K. When we measure the neutrino beam at ND280 and SK, the flavour of neutrino is identified from the type of leptons (l) in the final state of neutrino-nucleus charged current (CC) interaction. For example, the following interaction is called CCQE (Charged Current Quasi-Elastic) interaction.

$$\nu_l + n \to l^- + p \tag{2.2}$$

There are also other interaction modes. For example:

$$\nu_l + n \to l^- + n + \pi^+ \tag{2.3}$$
$$\nu_l + n \to \nu_l + n + \pi^0 \tag{2.4}$$

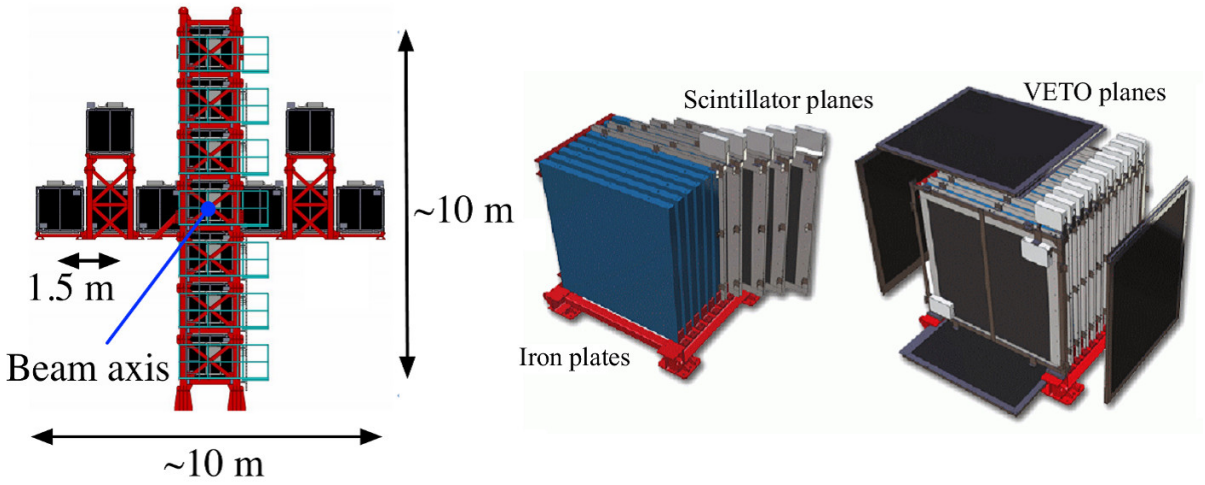

Figure 2.11: The INGRID detector.

The first one is called CC1π (Charged Current 1 pion) interaction, and the second one is called NC1π^0 (Neutral current 1 π^0) interaction. As we describe in Chapter 3 and 7, we select CCQE interaction as a signal, and the CC1π and NC1π^0 interactions are the main background interaction modes. The uncertainty of the cross sections for each interaction mode must be constrained by measuring these interactions at the ND280 detector.

2.3.2 ND280

The ND280 (Near Detector at 280 m) is designed to measure the initial neutrino beam flux, energy spectrum and the neutrino-nucleus cross sections for several different interaction modes. It consists of various types of detectors suited inside the magnet (Fig. 2.12).

- Magnet
  ND280 uses the magnet which was donated from the UA1 experiment at CERN. It supplies a magnetic field of 0.2 T to measure the momenta and charges of the charged particles produced in neutrino interactions. The inner size of the magnet is 3.5 m $\times$ 3.6 m $\times$ 7.0 m. The magnetic coils are made of aluminum bars with 5.45 cm $\times$ 5.45 cm square cross sections. They are mechanically supported by the C-shaped yokes which stands on movable carriages.

- Tracker (FGD+TPC)
  The tracker consists of two FGDs (Fine-Grained Detectors) [56] and three TPCs (Time Projection Chambers) [57]. These detectors are particularly important because they measure the charged current (CC) interactions, which are the signal mode for T2K.
  The FGDs are made of fine-grained scintillator bars. The second FGD also contains water targets to measure the neutrino interaction on water, because the water is the neutrino interaction target in SK. The FGD provides the target mass while detecting the short-ranged particles around the interaction vertex. Detecting the short tracks in the FGD is important for identifying the neutrino interaction modes. The detail of the FGD is explained in the Chapter 3.
  The long tracks, especially the leptons in the final state of the CC interaction, are detected by the TPCs. Using the TPCs, the 3-momenta of charged particles is measured from the track curvature in the magnetic field. We perform the particle identification (PID) by measuring the energy loss in the gas. The transverse momentum resolution is ~10 %, and

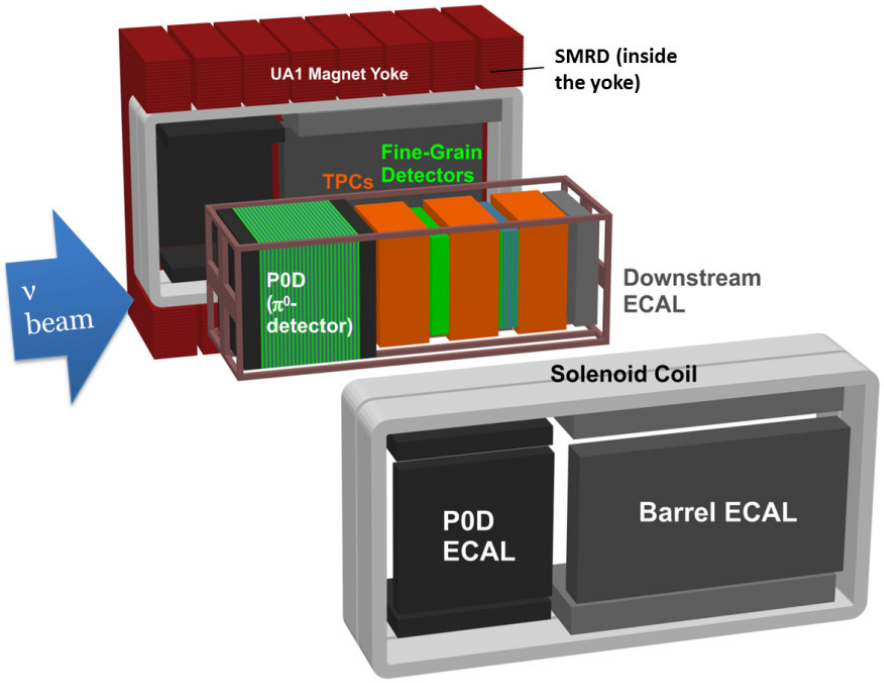

Figure 2.12: Schematic view of ND280 detectors. In this figure, the magnet yoke and the inner detectors are drawn separately, but they are combined in the actual detector, as shown in Fig. 2.10.

the resolution of energy loss per length (dE/dx) is 7.8% for a minimum ionizing particle. Figure 2.13 shows a schematic view of the TPC detector. Each of the three TPCs consists of an inner box filled with a gas mixture of Ar:CF_4:iC_4H_{10} (95%:3%:2%). The cathode panel at the center of the inner box and the copper strips that line inside the box produces a uniform electric field in a horizontal direction aligned with the magnetic field direction, perpendicular to the beam axis. When the charged particles pass through the gas, the ionized electrons drift towards the readout plane on each side of TPCs (Fig. 2.14). The readout planes are formed from micro-mesh gaseous detectors (micromegas [58]), which amplify the electrons in a high electric field ($\sim$ 27 kV/cm) and then measure the ionization produced.

- P0D (Pi-zero detector)
  P0D [59] locates at the upstream side of the inner magnet. It is optimized to measure the π^0 generated by neutral current interaction. The P0D consists of plastic scintillators, brass sheets and water target bags. The detector can be run with the water bags filled or empty, enabling subtraction method to determine the water target cross sections.

- ECAL (Electro-magnetic CALolimeter)
  ECAL [60] surrounds the Tracker and P0D. The ECAL consists of the plastic scintillator layers interleaved with Pb foils. Its main purpose is to measure the γ-rays from π^0 decays which did not convert in the inner detectors. It also detects the electrons generated from the CC interaction of ν_e.

- SMRD (Side Muon Range Detector)
  SMRD [61] consists of the scintillator pads which are inserted in the gaps of magnet iron

yokes. The SMRD measures the range of muons from neutrino interactions that go in the side ways and missed the TPCs. It also provides the cosmic-ray triggers used for calibrating the detectors.

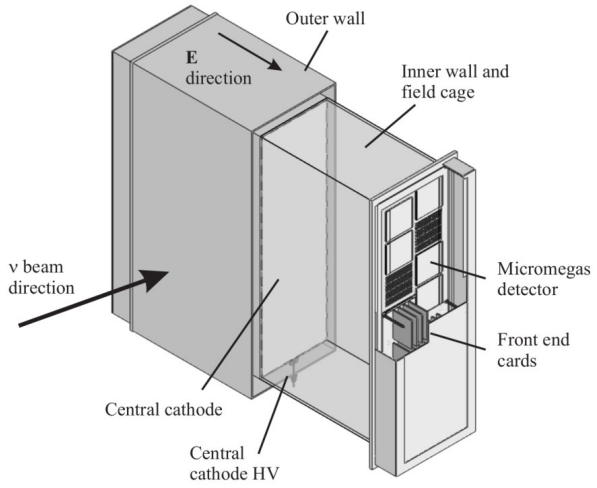

Figure 2.13: The TPC detector [57].

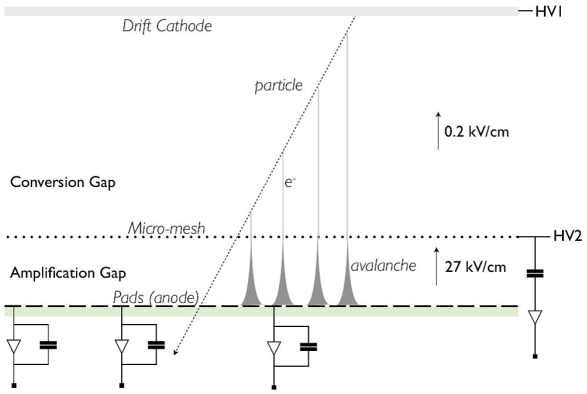

Figure 2.14: TPC micromegas readout.

All of these detectors except for the TPCs are made of plastic scintillator bars alternating with target materials such as water panel, lead foils or iron. The light from the scintillator bars are read out by the MPPCs. There are in total ∼50000 MPPCs used in ND280.

2.3.3 Far detector (Super-Kamiokande)

An important feature of the T2K experiment is that we use SK, the gigantic water Cherenkov detector, for the far detector [62]. SK is 50 kton water Cherenkov detector which is located at 295 km away from J-PARC, 1000 m underground of Kamioka mine in Gifu prefecture (Fig. 2.15). The cylindrically shaped water tank is optically separated to make two concentric detectors: an inner detector (ID) and an outer detector (OD). The ID contains 11129 inward-looking 20-inch photo-multipliers (PMTs), and the OD contains 1885 outward-facing 8-inch PMTs. The ID has $\sim$ 40 % of its surface covered by the PMTs.

The charged particles above the Cherenkov threshold produces rings of light which is detected by the PMTs. It is possible to identify the particle types from the topological pattern of the light. For example, an electron produces a fuzzy ring pattern because it undergoes large multiple scattering and induce electromagnetic showers. In contrast, a muon produces sharp ring because it is resilient to changes in its momentum due to its relatively large mass.

The trigger signal is sent from J-PARC to SK via private network connection, with the information of GPS (Global Positioning System) time of the spill. The beam arrival time at SK is computed by correcting the neutrino time-of-flight and the delay of electronics. The data within $\pm$500 μsec of the arrival time is recorded. The time synchronization between the J-PARC site and the Kamioka site is done by using GPS with a precision of $\sim$ 150 nsec.

2.4 Summary of the beam data taking

T2K started physics data taking in January 2010. For the analysis presented in this thesis, we use the data collected from Jan 2010 to May 2013. There are four data taking periods called Run1∼4, as summarized in Table 2.2.

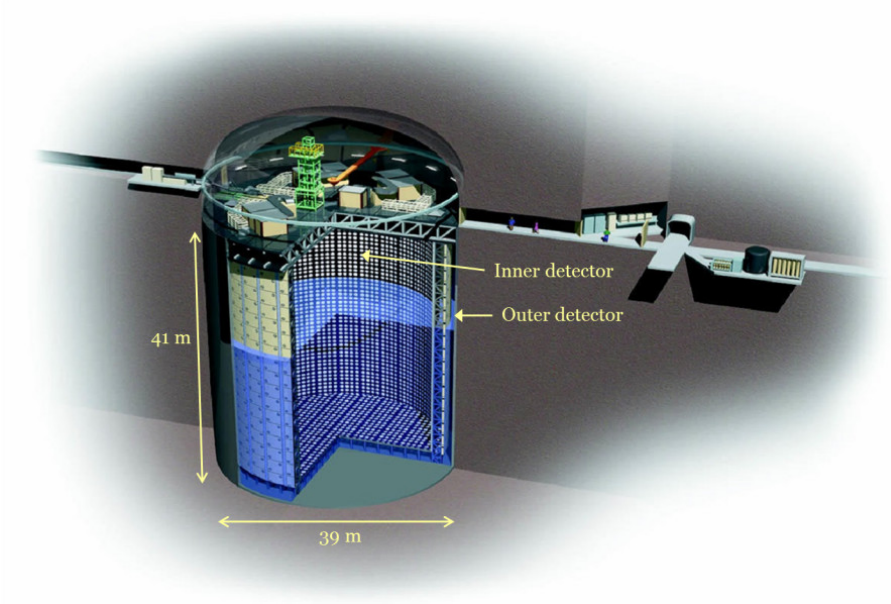

Figure 2.15: Super Kamiokande detector.

Run	Period	POT
Run 1	Jan. 2010 – Jun. 2010	0.32×10^{20}
Run 2	Nov. 2010 – Mar. 2011	1.11×10^{20}
Run 3	Mar. 2012 – Jun. 2012	1.58×10^{20}
Run 4	Oct. 2012 – May. 2013	3.56×10^{20}

Table 2.2: Summary of data taking periods

Figure 2.16 shows the history of the number of protons delivered to the neutrino facility. The total number of protons on target (POT) for whole run period is 6.57×10^{20} POT. The number of protons per pulse is also shown in the plot. The proton beam power is steadily increased and reached to 220 kW continuous beam operation with a world record of 1.2×10^{14} protons per pulse. We suffered from the 7.3-magnitude earthquake in Apr. 2011, but thanks to tremendous amount of work mainly by people in the J-PARC/KEK group, we restarted the beam operation in one year.

Figure 2.17 shows the stability of the neutrino event rate per POT at INGRID, and the stability of the beam direction measured by INGRID and MUMON. The neutrino event rate per POT is stable within 0.7 %, except for the period in the beginning of Run 3. The nominal value of horn current is 250 kA, while it was 205 kA in the beginning of Run 3 because of the trouble in the horn power supply. The stability of the beam direction is much better than the requirement (1 mrad) during whole run period.

The first result from the T2K ν_e appearance measurement [24] was reported in 2011. The data sets for that analysis was Run 1 and 2 (1.43×10^{20} POT). There were six ν_e candidate events observed, and the significance was 2.5 σ. For the second result which we reported in 2012 [29], we used the data sets from Run 1 to 3 (3.01×10^{20} POT), and there were 11 ν_e candidate events observed. The significance was 3.1σ. For the analysis we present in this thesis, the total POT in our data set is increased to 6.57×10^{20} POT, which is $\sim$2.2 times larger compared to the previous report, and $\sim$ 8.4% of the T2K goal. The expected significance is above 5 σ.

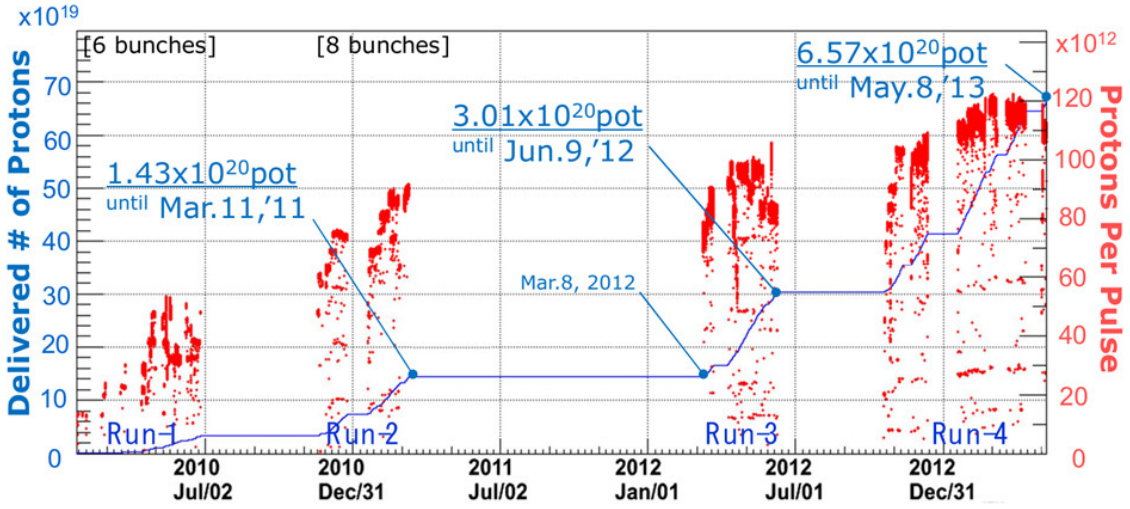

Figure 2.16: Delivered POT to neutrino facility.

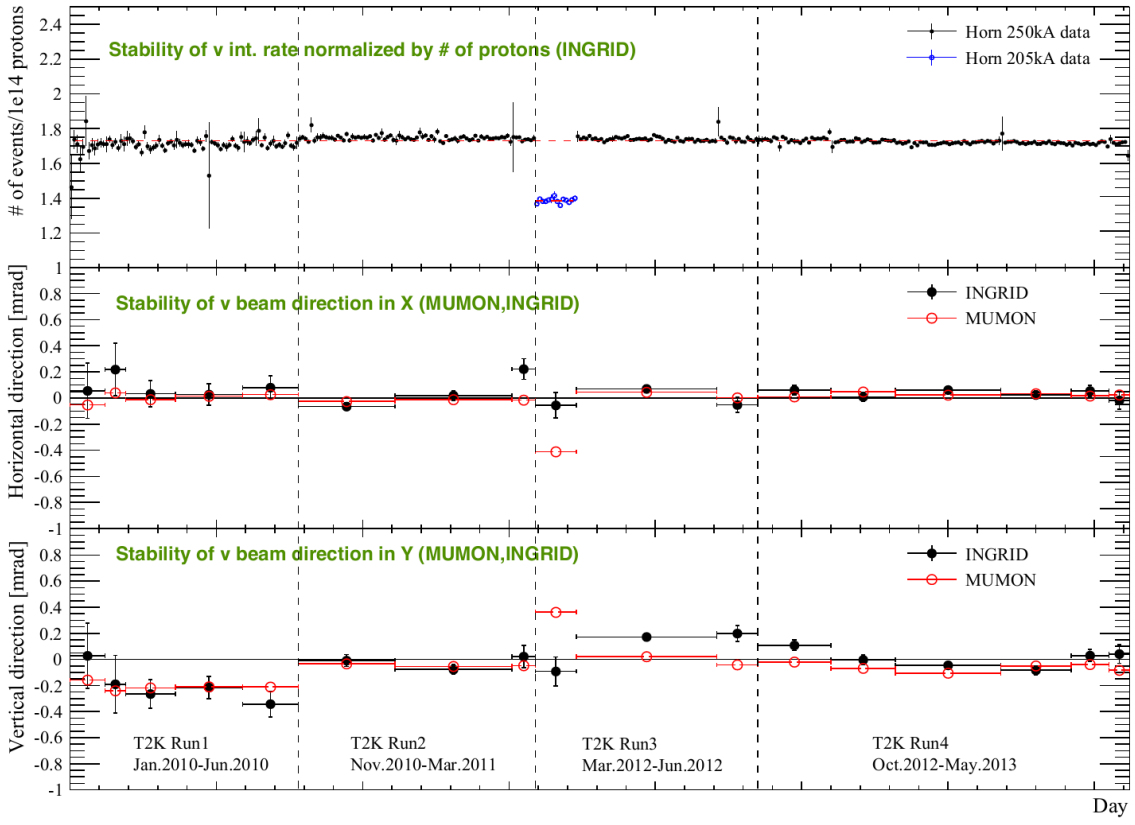

Figure 2.17: Stability of neutrino event rate normalized by POT in INGRID (top), and the stability of neutrino beam direction measured by INGRID and MUMON (middle, bottom).

Chapter 3

The Fine-Grained Detector

The FGD (Fine-Grained Detector) is a part of the ND280 tracker system. It is made of finely segmented scintillator bars, and acts as the neutrino interaction target as well as a tracking detector. The identification of neutrino interaction types in FGD is important in the neutrino beam measurement at ND280. In this chapter, we report the design, calibration and track reconstruction of FGD.

3.1 FGD and neutrino interaction

The ND280 Tracker is composed of three TPCs (Time Projection Chambers) alternating with two FGDs (Fig. 3.1). The Tracker is designed to detect the charged current (CC) interactions in order to measure the neutrino beam flux, energy spectrum and the neutrino-nucleus interaction. The main signal of the measurement is the CCQE interaction ($\nu_l + p \rightarrow l + n$), which is the most common interaction in T2K's beam energy. Because CCQE is a 2-body interaction and the direction of the neutrino beam is known, the energy of the initial neutrino can be reconstructed from the energy and direction of the final lepton.

$$E_\nu^{\mathrm{rec}} = \frac{m_p^2 - (m_n - E_b)^2 - m_l^2 + 2(m_n - E_b)E_l}{2(m_n - E_b - E_l + p_l \cos\theta_l)}, \tag{3.1}$$

where m_p, m_n and m_l are the mass of proton, neutron and lepton. E_b is the neutron binding energy in the nucleus. p_l, E_l and θ_l are the momentum, energy and angle (with respect to beam axis) of the lepton. However, there exist many other background processes. For example, the CC1π ($\nu_l + p \rightarrow l + n + \pi$) process has an additional pion, thus the initial neutrino energy is miss-reconstructed using Equation 8.1. In SK, only the lepton in the final state has the momentum above the Cherenkov threshold in many cases, and it is hard to distinguish the CC1π background events from CCQE events. Therefore we need to measure the background event rates as well as CCQE interaction rate in the near detector.
To distinguish the types of neutrino interactions, it is important to detect the short pion tracks around the neutrino interaction vertex. In the ND280 Tracker, the FGDs acts as both neutrino interaction target and the tracking detector. The FGDs are designed to measure the short tracks. Long tracks such as those of muons will reach the TPCs, where its momentum and charge are measured from the curvature of the particle trajectory in the magnetic field (Fig. 3.1). Results of the neutrino beam measurement is described in Chapter 9.

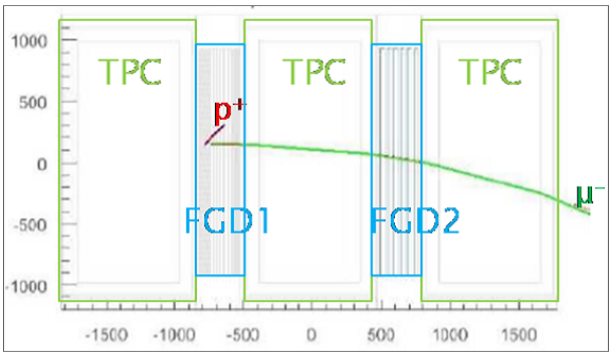

Figure 3.1: Example event display of ND280 tracker. CCQE interaction is simulated.

3.2 Fine-Grained Detector

3.2.1 Overview of the design

The FGDs are composed of planes of scintillator bars which are oriented in either the x or y direction, perpendicular to the beam direction (Fig. 3.2). Each plane consists of 192 bars and

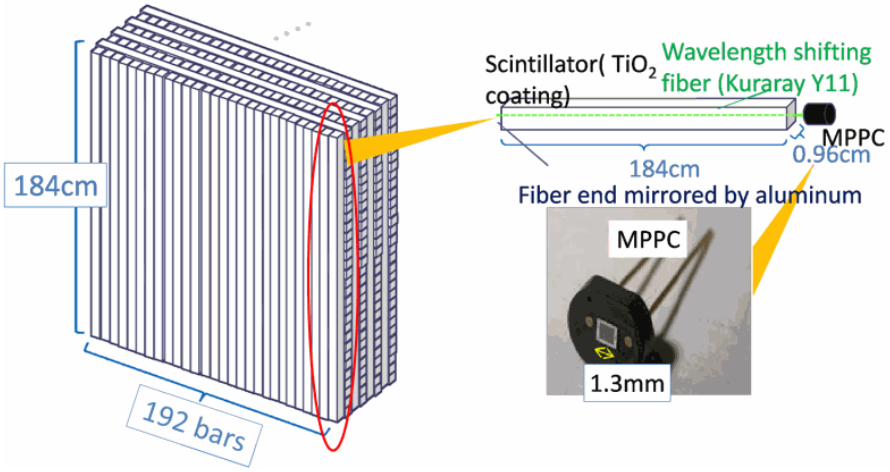

Figure 3.2: FGD architecture.

has dimensions of 184.3 cm (H)×184.3 cm (W)×0.96 cm (D). The combination of the X planes (vertical bars) and Y planes (horizontal bars) forms an "XY module". The first FGD (FGD1) which locates upstream contains 15 XY modules. The second FGD (FGD2) contains 7 XY modules alternating with 6 water modules.

The water module is made of 25 mm thick polycarbonate (Lexan©) hollow panel, in which the water is filled. The interior of the panel is divided into 12.5 mm × 25.4 mm rectangular shells, which is further subdivided by a thin curved wall (Fig. 3.3). This structure provides enough strength with minimum amount of plastic material. The water pressure in the module is kept below atmospheric pressure by a pump, so that the water do not leak even if there is any pinholes or hairline cracks.

The scintillator bars are 184.3 cm long and 0.96 cm×0.96 cm in the cross-section. Each bar is coated with TiO_2 for light reflection and has a hole at the center of the cross section. A wavelength shifting fiber is inserted in the hole (Fig. 3.4). The bars are glued together with 0.25 mm thick G10 sheets to add mechanical rigidity and allow for easier handling. For the glue

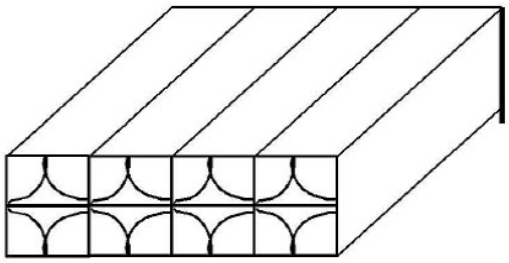

Figure 3.3: Cross-sectional view of the water panel [56].

we used Plexus MA590. The scintillation light is not produced when a charged particle pass the TiO_2 coating region. Hence, the efficiency to detect charged particles passing through the scintillator plane is evaluated as a function of the distance from the center axis of the bar (Fig. 3.5). The light yield for typical minimum ionizing particle is ∼30 p.e., while the threshold we use to find the hits in the analysis is 5 p.e.

Photons from each scintillator bar are collected and transmitted to the end of the bar by a blue-to-green double-clad wavelength shifting (WLS) fiber inserted in the scintillator bars. The Kuraray Y11 (200) S-35 fiber was selected. The MPPCs (Multi-Pixel Photon Counters) detect photons from the scintillator bars via WLS fibers at the end of the bars. The other end of the fibers are mirrored with vacuum deposition of aluminum which increased the light yield by 30-40%. The FGDs contains 8448 channels (8448 bars and 8448 MPPCs) in total.

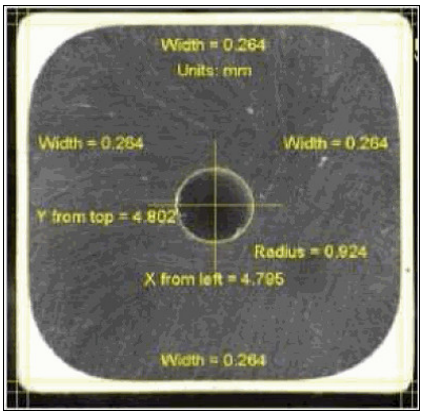

Figure 3.4: Cross-sectional view of the scintillator bar [56].

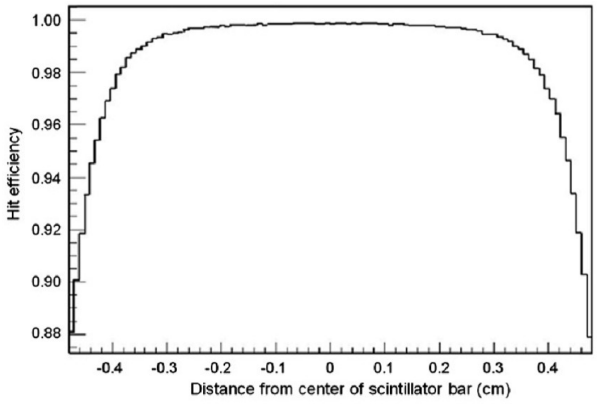

Figure 3.5: Hit finding efficiency as a function of the distance from the center axis of the bar [56].

The XY modules and the water modules hang inside the light-tight box called “dark box”, which is made by aluminum. The read out electronics are mounted on the four sides of the FGDs, outside the dark box. In this way the heat-producing elements are separated from the MPPCs, which are sensitive to temperature. The cooling water lines run through the four sides of the FGDs to keep the temperature stable.

The specification of the FGD is summarized in Table 3.1

3.2.2 Readout electronics

The overview of the readout system is summarized in Fig. 3.6. The MPPCs are mounted on the “bus-boards”. Each bus-board contains 16 MPPCs, 2 temperature sensors and 16 LEDs

Structure	
Dimensions	184 cm×184 cm×33.6 cm for each FGD
Weight (FGD1)	1 ton
(FGD2)	0.56 ton(Scintillator) + 0.44 ton(Water modules)
Number of channels	5760(FGD1), 2688(FGD2)
Scintillator	
Material	Polystyrene, PPO(1%), POPOP(0.03%)
Reflector material	TiO_2(15%) infused in polystyrene
Dimensions	0.96 cm × 0.96 cm × 184.3 cm
WLS fiber	
Type	Kuraray Y11(200) S-35
Absorption peak wavelength	430 nm
Emission peak wavelength	476 nm
Diameter	1 mm
Length	∼2 m
Attenuation length	350 cm
Reflective coating	Coated by aluminum sputtering at the end
Refractive index	1.59(outer clad)/1.49(middle clad)/1.42(core)
Decay time	∼7 ns
MPPC	
Active area	1.3 mm × 1.3 mm
Pixel size	50 × 50 μm^2
Number of pixels	667
Operation voltage	70 V (typ.)
Photon detection efficiency	>15% (for 550 nm light)
Dark noise rate	few hundred kHz (at $V_{over} = 0.8V$)

Table 3.1: Specifications for the FGDs

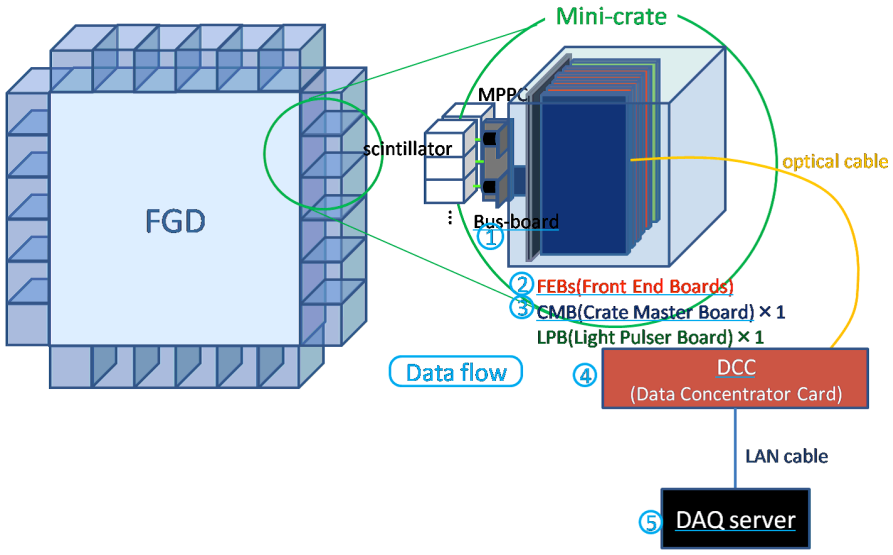

Figure 3.6: The overview of read out system for the FGDs.

for calibration. The MPPCs are controlled and read out by the "Mini-crates". There are six mini-crates installed at each side of the FGD. Each mini-crates contains following boards.

Front-End Board (FEB)
The FEBs sets the bias voltage for the MPPCs (64 channels/board). It contains the AFTER ASIC chip [63] which shapes and stores the signal with the Switched Capacitor Array (SCA). The SCA records the MPPC waveform at 50MHz for 10 μs, so it is capable of recording delayed electron signal, originated from $\pi \to \mu \to e$ decay. This helps to distinguish the CC1π interaction from CCQE interaction. In order to have wide dynamic range, it contains low and high attenuation channel for each MPPC. The low (high) attenuation channel measures the signals between 0.2 to 80 p.e. (2 to 700 p.e.).

Crate Master Board (CMB)
The CMB controls data acquisition process using a FPGA chip and transfer the data from the FEBs to the rest of the DAQ.

Light Pulser Board (LPB)
The LPB controls the LEDs on the bus-boards.

There are four (two) FEBs, one CMB and one LPB installed for each mini-crate in FGD1 (FGD2). The data from the mini-crates are transmitted to the back-end electronics module called DCC (Data Concentrator Card), which are located outside the magnet.

The FGD electronics is also capable of generating cosmic-ray triggers for calibration. In order to detect the cosmic-rays which pass both FGD1 and FGD2, the Cosmic Trigger Module (CTM) generate the cosmic trigger when it receive the trigger signal from the mini-crates in both horizontal and vertical row, from both FGD1 and FGD2. The triggers from the mini-crates are generated when the CMB receive at least two "ASUM" signal, which is the analog sum of charges from groups of eight MPPCs.

3.2.3 MPPC (Multi-Pixel Photon Counter)

The MPPC is a photon counting device manufactured by Hamamatsu photonics. It consists of many small avalanche photo-diodes (APDs) in an area of typically 1 mm^2. Each APD pixel outputs a pulse signal when it detects one photon. The sum of the output of each APD pixels forms the MPPC output. The MPPCs are used in all of the ND280 detectors except for the TPCs. It satisfies the following requirements:

- Counting photons down to one photo-electron level.
- Works inside the 0.2 T magnetic field.
- Compact enough to fit in a very tight space constraint.

We use the special type of MPPC, with a sensitive area of 1.3×1.3 mm^2 containing 667 pixels with 50×50 μm^2 size each, which was developed for the T2K experiment. The FGDs use 8448 channels of MPPCs. Their basic features were measured by the Kyoto group [64]. All of the measured features fulfilled the requirements for the ND280 detectors.

There are some features which are relevant to the calibration of the MPPC signal.

- Dark noise
  The MPPC generates dark noise signals that correspond to 1 p.e., 2 p.e. ... even if there are no input photoelectrons. The rate of dark noise is typically several hundred kHz.

- Breakdown voltage and the temperature dependence
  When the bias voltage for the MPPC is higher than the specific voltage called the "breakdown voltage" V_{bd}, the output charge of the 1 p.e. signal linearly increases as follows:
  $$\text{Output charge} = C(V_{bias} - V_{bd}),$$
  where C is the capacitance of each APD pixel and V_{bias} is the bias voltage. The voltage above the breakdown voltage is called as "overvoltage" V_{over}. The typical breakdown voltage is ∼70 V. The V_{bd} increases by ∼0.05 V as the temperature increase.

- Crosstalk + Afterpulsing
  Crosstalk: Photon from an avalanche generates another avalanche in a neighbor pixel.
  Afterpulsing: Electron from an avalanche is trapped in the lattice defect, re-emitted later, and makes a second avalanche in the same pixel.
  These effects makes the output signal bigger than originally it was, so we need to correct these effects in the calibration to extract the actual charge.

Because the gain, photon detection efficiency (PDE), dark noise rate and the crosstalk + afterpulsing increases as the V_{over} increase, it is important to set the V_{over} uniform over all MPPC channels.

3.2.4 Detector calibration

Bias voltage setting

In order to make detector response become uniform, we set the overvoltage same for all of the MPPCs. We adjust the bias voltage so that the pulse height of the 1 p.e. signal become ∼40 ADC for all of the channels. This is equivalent to setting the overvoltage to ∼ 0.8 V. Figure 3.7 shows an example of the pulse height distribution of the MPPC dark noise. The largest peak at ∼40 ADC count corresponds to the 1 p.e. pulse height.

Temperature correction

The breakdown voltage changes as the temperature change, and the temperature changes by ∼ ±2°C around the MPPCs, during the long term detector operation. To compensate this effect, we adjust the bias voltage for roughly every month.

We also apply a correction in the analysis. We define the conversion factor $\langle PH_1 \rangle$ to convert from ADC count to photo-electrons depending on the temperature. The $\langle PH_1 \rangle$ is equivalent to ADC count of the pulse height of 1 p.e. signal. The left plot in Fig. 3.8 shows an example of 1 p.e. pulse height as a function of bias voltage, measured for a typical MPPC at several different temperature. The $\langle PH_1 \rangle$ is expected to vary in proportion to the overvoltage, but the quadratic dependence provided a better description of the measured variation. Therefore, we derive the $\langle PH_1 \rangle$ from the following formula:

$$V_{bias} - C_T(T - T_0) = V_{bd} + (1/G)\langle PH_1 \rangle + C_G \langle PH_1 \rangle^2, \tag{3.2}$$

where C_T corresponds to the temperature dependence of the breakdown voltage, which is empirically defined to be 57±3 mV/deg. The parameter $1/G$ and C_G are the coefficients in the quadratic relationship, which are determined separately for each MPPC. Fig. 3.8 right plot shows the relationship between $\langle PH_1 \rangle$ and voltage after temperature correction.

Conversion from pulse height to energy deposit

The energy deposit of the charged particles in the FGD scintillator is calculated from the measured pulse height (PH) of the MPPC signal as follows.

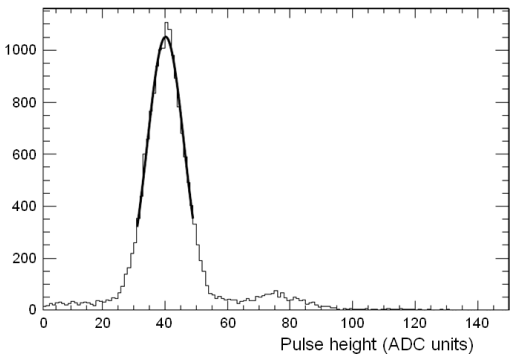

Figure 3.7: Example of pulse height distribution for MPPC dark noise. The peak around 40 ADC corresponds to the 1 p.e. signal [56].

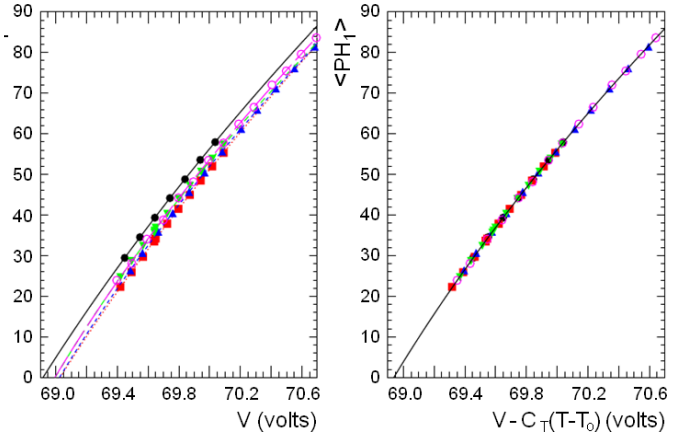

Figure 3.8: The 1 p.e. pulse height vs. Bias voltage before (left) and after (right) the temperature correction for typical MPPC. The different colors corresponds to the different temperature [56].

1. Conversion from PH to the number of detected photo-electrons N_{pe1} ("charge")
$$N_{pe1} = PH / \langle PH_1 \rangle .$$

2. Correction for Crosstalk + Afterpulse and PDE
These effects increases approximately in proportion to the overvoltage, which is proportional to the 1 p.e. pulse height. Therefore, we define the correction factor for these effects as a function of the 1 p.e. pulse height. The corrected number of photo-electrons N_{pe2} is calculated as follows:
$$N_{pe2} = N_{pe}/(C_0 + C_1 \langle PH_{corr} \rangle),$$
where $\langle PH_{corr} \rangle$ is the 1 p.e. pulse height corrected for capacitance of its bus-board trace. The empirical correction factor C_0 and C_1 are determined to be -0.0885 and 0.0338 from the beam test.

3. Correction for saturation in MPPC
Because of the finite number of pixels in each MPPC (667 pixels), the pulse height is saturated at high light levels. The number of photo-electrons that we observe can be written in the analytic formula below:
$$N_{pe2} = N_{\mathrm{pix\_eff}}(1 - e^{-N_{pe3}/N_{\mathrm{pix\_eff}}}),$$
where N_{pe3} is the expected number of detected photons when there are no saturation, which can be obtained by inverting this formula. $N_{\mathrm{pix\_eff}} = 396$ is the effective number of pixels illuminated by the fiber for typical MPPC.

4. Correction for the bar-to-bar variations
The variations in the light yield from bar-to-bar are caused by the fiber/MPPC coupling, scintillator material, fiber mirroring etc. The correction factor C_{bar} is determined from the cosmic ray data. The variation of C_{bar} is $\sim$7%.

5. Correction for the fiber attenuation
The attenuation of the light in the fiber is corrected using a correction factor defined as follows.

$$C_{att} = \left(1 - \frac{1}{2}e^{-x/M} - \frac{1}{2}e^{-(D-x)/M)}\right)\left(e^{-(x+A)/S} + Be^{-(x+A)/L)}\right),$$

where x represents the distance of the hit from the end of the bar closest to the MPPC. The first set of parentheses represents an exponential decrease in the very end of the bars with length scale $M = 21.55 \pm 0.28$ mm, due to light leaking out the uncovered end of the bar before it is all absorbed in the fiber. $D = 1864.3$ mm represents the length of the bar. The second factor represents the light attenuation of the fiber. $A = 41.0$ mm is the extra length of fiber between the end of the bar and MPPC, $S = 410 \pm 60$ mm and $L = 23,600 \pm 2900$ mm are the short and long attenuation length. The values of these parameters are determined from cosmic ray data. Fig. 3.9 shows the number of photo-electrons normalized by the path length of the cosmic ray as a function of the hit position. The solid line corresponds to the attenuation curve which is determined from the correction factor.

6. Conversion from scintillating photons to energy deposit
   The energy deposit by charged particles in the scintillator is calculated from the number of photo-electrons after all these corrections. The conversion factor is determined using the cosmic-ray data (about 21 p.e. per MeV). We apply a factor of $1/(1 + C_B \cdot dE/dx)$ to correct the non-linearity in the scintillator response. The Birk's constant $C_B = 0.0208$ cm/MeV is measured by the K2K-SciBar group [65], using the scintillator bar of the same material as the FGD bars.

The response of MPPC, attenuation of the light in the fiber and the response of scintillator are implemented in the simulation so that it reproduces data. Figure 3.10 shows the charge distribution of cosmic data and simulated cosmic data after all of the calibration chain. The simulated distribution in shows a good agreement with data. Figure 3.11 shows the deposited energy vs. stopping range in FGD1, for the particle trajectories measured in neutrino beam data. The data and expectation agree well. The stopping range and energy deposit are used for identifying particle types, as we explain in Chapter 9

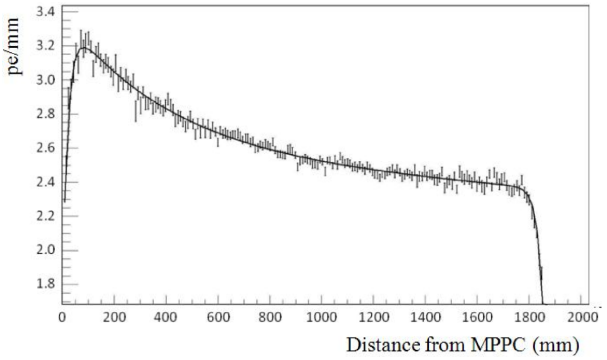

Figure 3.9: The number of photo-electrons normalized by the path length, as a function of the hit position. The data points are derived from cosmic-ray measurement. The line represents the empirical attenuation formula [56].

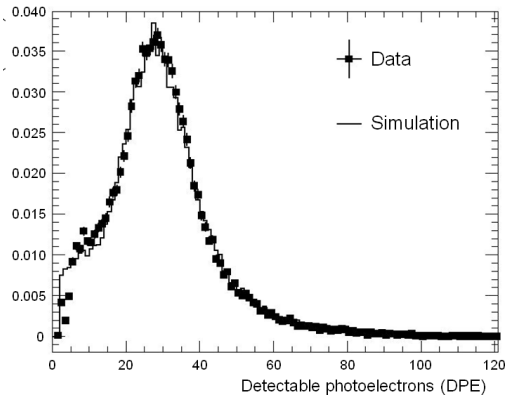

Figure 3.10: Charge distribution after correction, compared with simulation [56].

3.3 Reconstruction of particle trajectories

Identification of neutrino interaction type is important in neutrino oscillation measurement. Compared to the previous ν_e appearance analysis in 2012, one of the main changes in the ν_e

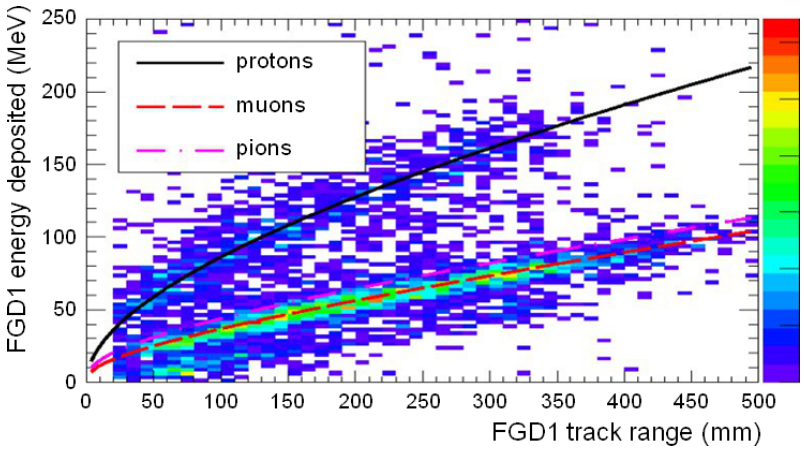

Figure 3.11: Deposited energy vs. stopping range for FGD1. The scatter-plot shows stopping particles in neutrino beam data, while the curves show the MC expectations for protons, muons, and pions [56].

appearance analysis in this thesis is the improvement of the neutrino interaction measurement in ND280. The uncertainty of CC1π cross section is significantly reduced by using a CC1π enhanced sample, which is newly added (see Chapter 9). The CC1π events are selected by requiring a π^+ in the final state. Because the pions do not always reach the TPCs, reconstruction of the pion trajectories in the FGD is important. A new algorithm to reconstruct particle trajectories is developed to improve the reconstruction efficiency.
The particle trajectories in FGD are reconstructed in the following procedure.

1. Reconstruction of FGD-TPC matched tracks
   The trajectories which reached the TPCs are reconstructed by extrapolating the TPC tracks to FGD, by using Kalman-Filter algorithm implemented in the RecPack toolkit [66].

2. Reconstruction of FGD only track
   The hits which were not associated with FGD-TPC matched tracks are used in this procedure to reconstruct the FGD-only track. The tracks in XZ and YZ projections are reconstructed separately from the hits in X and Y layers. Then the tracks in two projections are combined to form a 3D track.

For step 2, we need an algorithm to identify the particle tracks from the topological pattern of the hits. Followings are the example of existing algorithms that have been used for this procedure:

- SBCAT (SciBar Cellular AuTomaton) [67]:
  This is the method which was used in FGD before the new method is developed. It was also used in the K2K experiment and the SciBoonNE experiment. Because this method uses an algorithm which has a layer-based structure, the efficiency to reconstruct the tracks depends on the angle of the tracks. The efficiency is worse for large angle tracks.

- Hough transform [68]:
  This method is commonly used, but it is not perfect because it does not take into account the size of the scintillator bars. For example, in case of a track shown in Fig. 3.12, it tends to find wrong tracks like in Fig. 3.13, due to its preference for tracks that pass through the center of the bar.

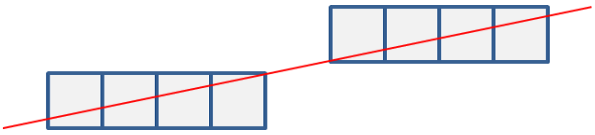

Figure 3.12: Example of the hit bars for a given particle, following the true trajectory in red.

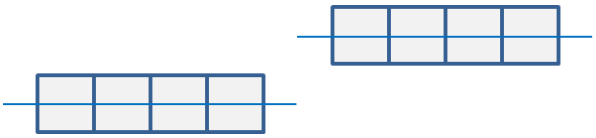

Figure 3.13: Example of the tracks (blue lines), reconstructed by Hough transform method.

In order to improve the efficiency to reconstruct the tracks, we have developed a new algorithm based on the idea of Radon transform. Radon transform is a mathematical transformation from a 2D distribution $f(x, y)$ to an integral over a straight line $g(r, \theta)$.

$$g(r, \theta) = \int\int f(x, y)\delta(x\cos\theta + y\sin\theta - r)dxdy, \tag{3.3}$$

where r represents the distance from the origin to the line, and θ represents the angle of the line. The inverse Radon transform is used in CT scan, to extract a 2D human body cross section image from X-ray scan data from many different angles.

For the actual implementation in FGD, we draw many lines in the 2D hit map, and transform the 2D hit map in the (x, y) space to the distribution in the Radon space (r, θ), as illustrated in Fig 3.14. A point in the Radon space corresponds to a line in the 2D space, and the color of the point represents the number of hits on that line. For each line, we count the number of scintillator bars with hits greater than 5 p.e. After drawing many lines, we can identify a particle trajectory from the point in Radon space which have largest number of hits.

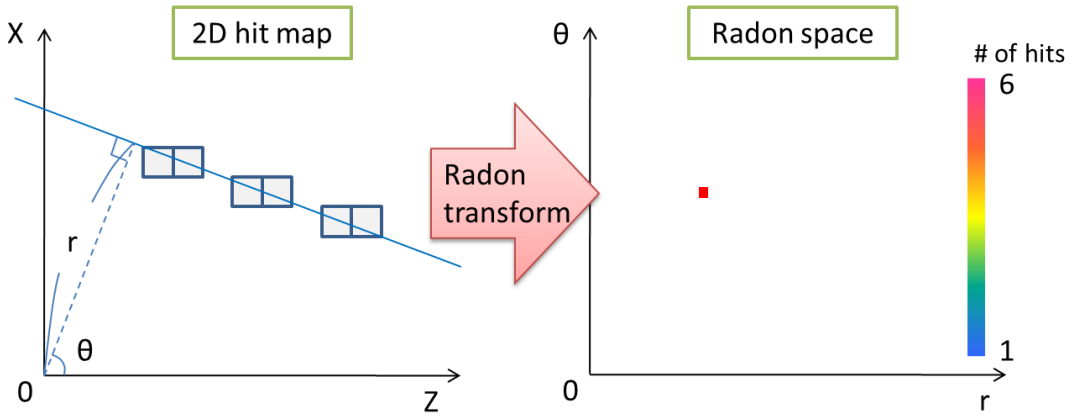

Figure 3.14: Illustration of Radon transform in FGD reconstruction.

This method is better than SBCAT or Hough transform, because it is expected to have similar efficiency in all directions, and because it takes into account the size of the scintillator bars. However, it may require longer CPU time for drawing many lines. Great care was taken in the coding to minimize the CPU time, by making the data format as simple as possible, and by minimizing the number of lines to draw.

The following is the flowchart of the track reconstruction with Radon transform.

1. Pre-selection of the hits
   We cluster the hits in time. Hits greater than 5 p.e. are selected in this procedure. These hits are selected as a cluster if there are more than or equal to two hits found within 100 nsec. Then, at least one of the hits is required to be larger than 10 p.e.

2. Radon transform
   We draw many straight lines and count the number of hits on the lines. The Radon space is sampled in 2.5 mm step in r and 25 mrad step in θ. In order to save time, the lines are not drawn if $r > R_{max}$, where R_{max} is determined from the distance between the origin and the hit which is farthest from the origin. The line is selected as a track candidate, if there are more than or equal to three hits found on the line. The track is not selected if there is a gap in the track without hits, for more than 1 layer or more than 1 bar in one layer.

3. Connecting the track candidates
   Because of the magnetic field, the tracks may have a curvature. The long tracks are reconstructed as multiple tracks, if we only assume straight tracks. We reconstruct those long curved tracks by connecting multiple straight tracks. When we connect the tracks, we require the original track length to be greater than 100mm, and require an overlap of the hits ($\geq$ 3 hits for FGD1, $\geq$ 2 hits for FGD2). We also require the angles of the tracks to be close to each other. The allowed difference in the angle is defined as a function of track length (0.04 deg/mm).

4. Selection of final candidates
   The final candidate tracks are selected based on the number of hits in the track. From all of the candidate tracks, we find the best candidate track which have maximum number of hits. After selecting the first track, we remove the tracks which overlap with the first track. The second candidate track is searched from the remaining tracks. We repeat this procedure as long as the candidates exist.

The performance of this new algorithm is tested by using MC simulation. In this study, the reconstruction of the TPC-FGD matched track is not applied to see the effect of FGD-only reconstruction. Figure 3.15 shows an example of the neutrino event in MC, after track reconstruction. The circles (squares) represent the hit above 5 p.e. The thick lines represent the reconstructed tracks, while the thin lines represent the true trajectories.

A true trajectory A is assumed to be "reconstructed" to track B if the following criteria are both satisfied:

- Track is "complete": More than 80% of the hits in the true trajectory A are included in the reconstructed track B.

- Track is "clean": More than 80% of the hits in the reconstructed track B are originated from the true trajectory A.

Figure 3.16 shows the efficiency to reconstruct the tracks vs. the number of tracks, compared to SBCAT (tracks with <3 hits are not counted in the efficiency calculation). The new algorithm shows significantly better efficiency compared to SBCAT, especially when the number of tracks is greater than 1. Reconstruction efficiency for multiple tracks is important for reconstructing the pion track in the CC1π interaction.

Track reconstruction may fail in the following condition, which happens more often as the number of tracks increase.

- Track length is short (<3 hits).

- Tracks are overlapped to each other.

- The opening angle of two tracks is $\sim$180 deg.

- Too many tracks are generated in one event.

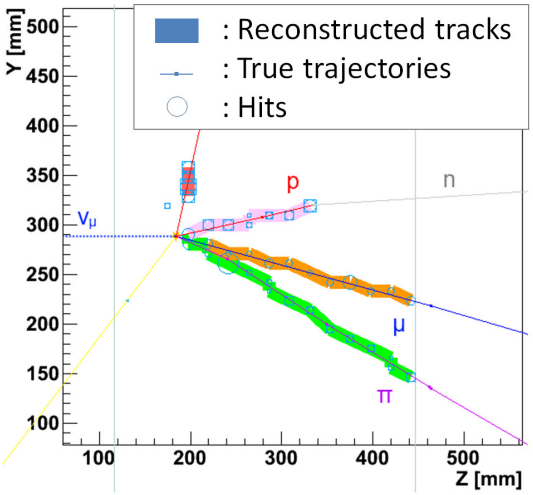

Figure 3.15: Example of the neutrino event after track reconstruction (MC).

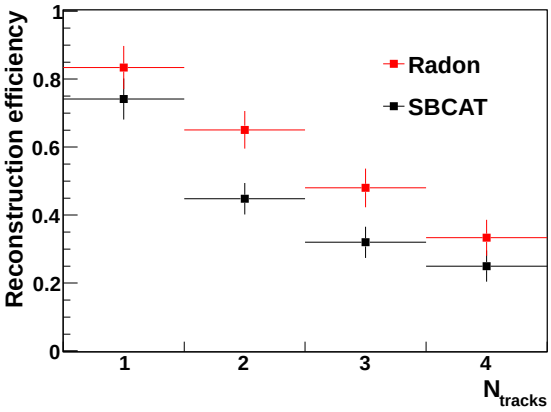

Figure 3.16: Reconstruction efficiency vs. Number of tracks

These type of tracks are very difficult to identify, even if we look them by eye.

The CPU time for running Radon code is measured to be $\sim$ 1.5 times longer than the SBCAT case. SBCAT is a simple and fast method, but Radon is still comparable in the CPU time, thanks to a great effort for minimizing the calculation time.

Part III

Pion interaction in the neutrino interaction model

Chapter 4

Measurement of pion interaction

4.1 Motivation of the measurement

As explained in the previous chapter, identifying the neutrino interaction types is important in the neutrino oscillation measurement. In order to distinguish CC1π interaction from CCQE, a pion in the final state needs to be detected. The FGD is suitable for this measurement, because it is full active and finely segmented. The new track reconstruction algorithm also improved the efficiency to reconstruct the pion tracks. However, pions are often absorbed by nuclei before making a track in the detector. When the pions from CC1π interaction is absorbed by a nuclei and not detected, the event is misidentified as CCQE. Because we select CCQE for a ν_e signal in SK, the uncertainty in the pion absorption cross section results in an uncertainty for the number of ν_e events.

These kind of interactions of hadrons in the final state of neutrino interaction are called FSI (Final State Interaction) or SI (Secondary Interaction). When the hadrons are generated inside the nucleus and interacted before they escape the nucleus, that effect is called FSI. When the hadrons escape from the nucleus and interact with the other nucleus, that effect is called SI. FSI and SI for pions make a big effect in our measurement. For few hundred MeV pions, there are three main interaction modes: 1) Scattering (SCAT), 2) Absorption (ABS) and 3) Charge exchange (CX) (Fig. 4.1). The SCAT includes both elastic and inelastic (quasi-elastic) scattering. Among these interactions, ABS and CX are important because the charged pion disappears in the final state.

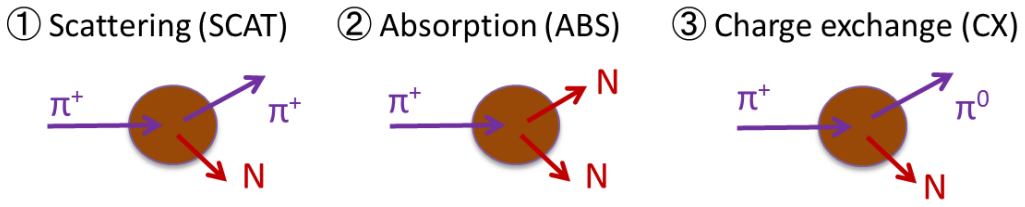

Figure 4.1: Pion interactions on nuclei.

Figure 4.2 shows the π^+-C ABS and CX cross section data from past experiments. The lines represent the prediction from the NEUT cascade model [69] (see Chapter 6). The momentum distribution of π^+ from CC1π interaction is peaked around 200 MeV/c, so the ABS + CX cross section is ~200 mbarn. This means that the ABS + CX interaction probability per path length is ~1%/cm in the plastic scintillator. Also, roughly half of the positive pions from CC1π do not even escape the nuclei, due to ABS and CX. Therefore, the measurement of CC1π (and

CCQE) interaction is significantly affected by pion ABS and CX. However, the uncertainty of the cross section from the past experiments is large. The uncertainty is typically ∼25% for ABS, and ∼50% for CX. In 2012 ν_e appearance analysis, the effect of those FSI and SI error to the uncertainty of number of ν_e candidate events in SK is estimated to be 2.3% (2.9%) in case of $\sin^2 2\theta_{13} = 0.1$ (0.1), while the total systematic error is 9.9% (13.0%). Other systematic error are related to neutrino beam flux, $\nu - N$ cross section and detector response. As we see in Chapter 11, the neutrino beam flux and cross section uncertainty could reduce by the further neutrino beam measurement in T2K. Also the SK detector response error could reduce by an atmospheric neutrino measurement at SK. However, it is difficult to reduce FSI+SI systematic error by a measurement in T2K. Therefore, we measured the pion interaction in a independent experiment, using the pion secondary beam line at TRIUMF (Canada's National Laboratory for Particle and Nuclear Physics).

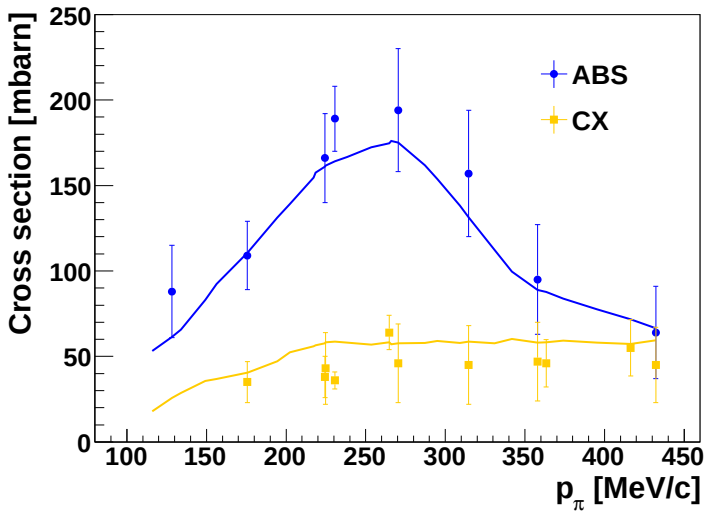

Figure 4.2: π^+-C absorption and charge exchange cross sections from past experiments [70–76] The lines represent the prediction from the NEUT cascade model.

We performed $\pi - N$ cross section measurement at the TRIUMF secondary beam line. Our goal was to measure the absorption and charge exchange cross section with better than 10% uncertainty. The overview of the experiment is explained in Section 4.2. The detail of the detector setup is described in Section 4.3. The analysis to derive ABS and CX cross section is explained in Chapter 5, and the improvement of FSI model in T2K is discussed in Chapter 6.

4.2 Overview of the experimental setup

The experiment took place in M11 secondary beam line at the TRIUMF. Figure 4.3 shows the overview of the M11 beam line area. The primary beam is 500 MeV proton beam which comes from the TRIUMF main cyclotron. The beam hits the production target which is 1 cm thick carbon. The momenta and charge of the secondary beam is controlled by two user-controlled dipole magnets (B1 and B2). The beam is focused by a series of six quadrupole magnets. We took the beam data for positive pions in the momentum range of 150 ∼ 350 MeV/c, by changing the momentum settings in 25 MeV/c step.

Figure 4.4 shows the overview of the detector setup. Our detectors are called PIAνO and Harpsichord. PIAνO consists of the scintillation fiber tracker and NaI crystals, and Harpsichord consists of scintillation bars and lead plates. The detail of those detectors are explained in

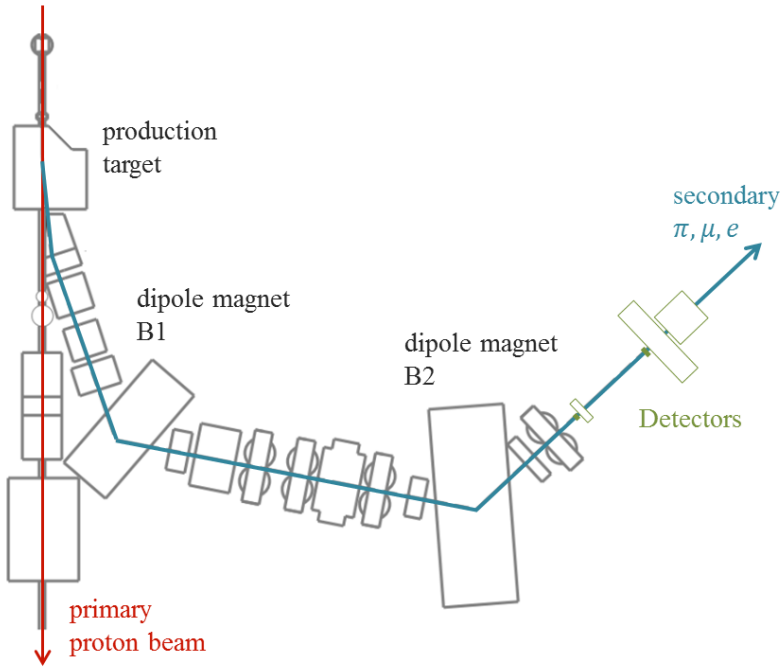

Figure 4.3: Overview of the M11 beam line.

the next section. The beam was triggered by two trigger counters, named S0 and S1. They were made of thin scintillator squares and read out by photomultiplier tubes (PMTs). The cross-sectional areas of the counters are 2 cm × 2 cm and 4 cm × 5 cm, respectively.

The secondary beam consists of pions, muons and electrons. The pions are selected by measuring Time Of Flight (TOF) and Cherenkov light. The TOF of the secondary particles was calculated from the difference of the signal timing between the S1 counter and the Current Transformer (CT) counter. CT is placed near the production target, where the distance from S1 was ∼15 m. The Cherenkov detector was placed at 11 cm downstream of S0 counter. It was a 3.5 cm × 3.5 cm × 20 cm bar of ultra-violet transmitting acrylic plastic bar fabricated from Bicron, and readout by a PMT attached to each end. The refractive index of the acrylic bar was 1.49, so muons with momentum larger than ∼250 MeV/c produce Cherenkov light at angles that are totally internally reflected within the bar, whereas pions of the same momentum would produce Cherenkov light at an angle that was largely transmitted (see Fig. 4.5). Figure 4.6 shows the example of Cherenkov light vs. TOF distribution for $p_\pi = 250$ MeV/c. The electron, muon and pion signals are clustered around left top, middle and right bottom of the plot. The pions are selected by requiring the data point to be below the threshold, which is shown as a red line in the plot. The purity of pions after this cut is estimated to be larger than 99% for all of the momentum settings that we used for the analysis.

4.3 Detector configuration

Our goal is to measure ABS and CX cross section. The ABS and CX events are identified by requiring no π^+ in the final state. Therefore, we have constructed a super-fine-grained scintillation fiber detector, which is a main detector for this experiment. It works as a interaction target (carbon) as well as a tracker, which is similar to the FGD. As it is super-fine-grained and fully active, it is capable of distinguishing ABS and CX events from scattering events, by detecting all the tracks of charged particles.

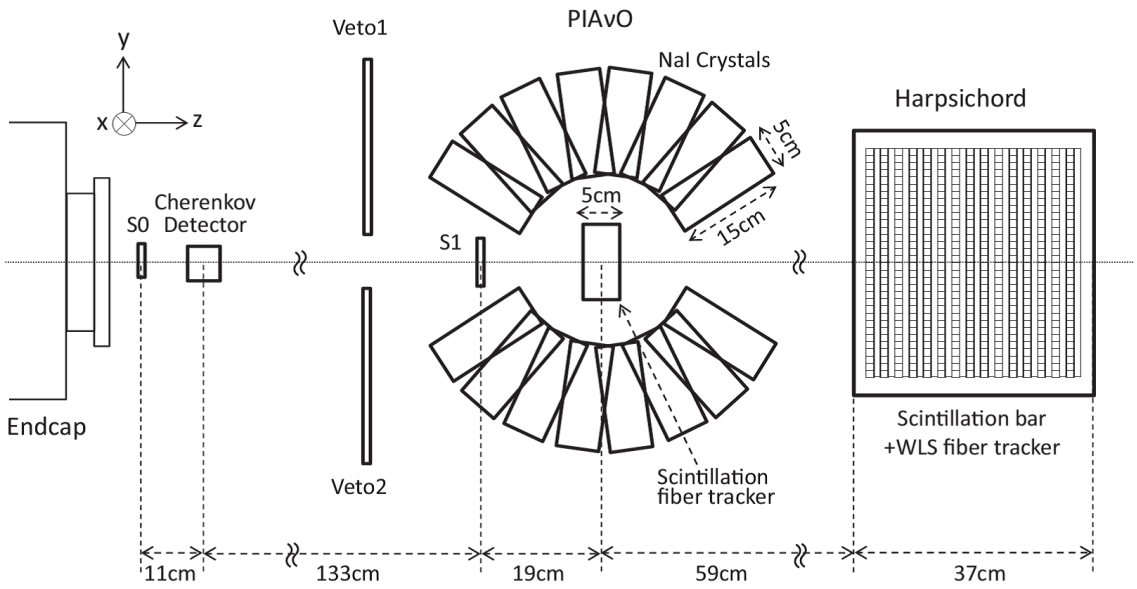

Figure 4.4: Overview of the detector setup (side view). The pion beam comes from the left side of this figure.

Figure 4.5: Illustration of light propagation in Cherenkov detector for pion (left) and muon (right).

The NaI crystals and Harpsichord detector which surrounds the fiber tracker detects the γ-rays from π^0 decay, to identify CX events. In this thesis, we only describe the measurement of ABS + CX total cross section, and do not describe the separate measurement of ABS and CX. Therefore, NaI crystals and Harpsichord detector are not used in the event selection.

In the following sections, we describe the detail of each detector component.

4.3.1 Fiber tracker

The fiber tracker consists of 1.5 mm scintillation fibers, and is read out by Multi-Anode Photo Multiplier Tubes (MAPMTs). Figure 4.7 shows the front view of the detector. The pion beam is injected to the center of the detector, where the fibers cross each other perpendicularly to form X and Y layers. The dimension of the region where the fibers cross with each other ("fiber crossing region") is $\sim 5 \times 5 \times 5$ cm^3. There are 32 fibers for each layer, and 16 X and 16 Y layers in total. The fibers are held together by fiber holders which clip the fibers, without using glues. There are 1024 fiber channels in total, read out by 16 MAPMTs. The specifications of the fiber tracker is summarized in Table 4.1.

The scintillating fibers that we used are single clad square fibers (Kuraray SCSF-78SJ), 60

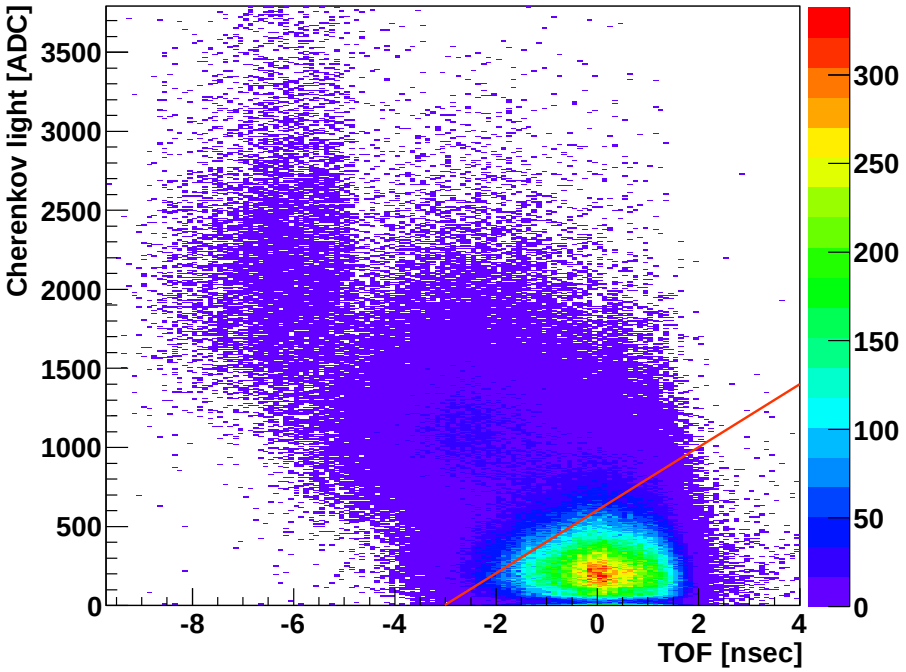

Figure 4.6: Cherenkov light vs. TOF for the beam particle at $p_\pi = 250$ MeV/c setting. The red line correspond to the threshold to distinguish pions from muons and electrons.

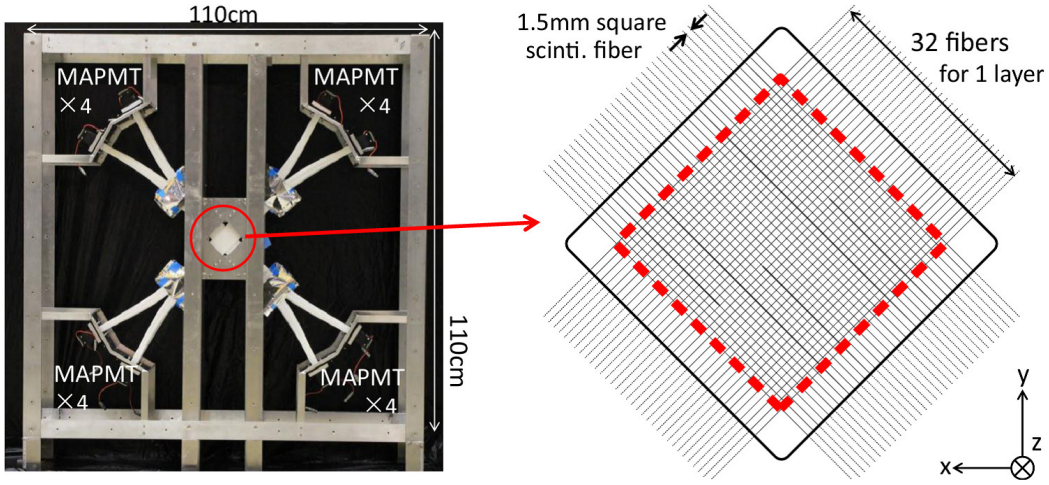

Figure 4.7: Front view of the fiber tracker detector.

Structure	
Dimensions in fiber crossing region	49 mm × 49 mm × 51 mm
Dimensions of support structure	110 cm × 110 cm × 25 cm
Number of channels	1024
Scintillating fiber	
Material	Polystyrene (core), PMMA (clad)
Reflector	EJ-510 ($\sim$ 25 μm)
Dimensions	0.149 cm × 0.149 cm × 60 cm (core + clad)
Clad thickness	2% of core + clad
Emission peak wavelength	450 nm
Decay time	2.8 ns
Attenuation length	$>$ 4 m
MAPMT	
Type	Hamamatsu H8804
Anode	8×8 pixels (pixel size: 2×2 mm^2)
Cathode	Bialkali (Sb-K-Cs)
Sensitive wavelength	300-650 nm (peak: 420 nm)
Quantum efficiency	12% at λ=500 nm
Dynode	Metal channel structure 12 stages
Gain	typical 2 × 10^6 at 900 V
Crosstalk	$\sim$2% (adjacent pixel)
Readout electronics	
Number of ADC channels	1024
ADC pedestal width	less than 0.1 p.e.

Table 4.1: Specifications of the fiber tracker

cm long, 1.5 mm × 1.5 mm in the cross section. Side of the fibers are coated with about 25 μm of reflective coating (EJ-510) which contains TiO_2, to increase the light yield and to optically separate the fibers from each other. One end of the fibers are mirrored by vacuum deposition of aluminum, which increased the light yield by a factor of 1.7.

The scintillating light from the fibers is read out by 64 channel MAPMTs (Hamamatsu H8804). The fibers are connected to MAPMTs via acrylic connector. A small fraction of the light from the fibers are injected to adjacent MAPMT channels, which generate crosstalk signals. The crosstalk probability is measured to be ∼2% for the adjacent channels. When we assembled the fibers, the adjacent fibers in a layer were connected to the MAPMT channels which are not next to each other, so that the crosstalk signals can be separated from the real signal for charged particles. The high voltage for MAPMTs is tuned in a bench test by measuring 1 p.e. signal of LED light, so that the gain of MAPMTs become uniform over all MAPMTs. The high voltage was set to ∼950 V, and the typical gain was 60 ADC / p.e. However it varies by ∼23% between MAPMT channels because the gain of 64 channels in MAPMT are not tuned individually. The measured light yield is ∼11 p.e. per fiber for minimum ionizing particle.

Readout electronics for MAPMT is recycled from the SciBar detector in the K2K experiment [77]. The schematic drawing of the MAPMT readout electronics is shown in Fig. 4.8. Each of the MAPMT is read out through a front-end board. The front-end board contains two sets of ASIC chips called VA and TA (IDEAS VA32HDR11 and TA32CG). VA has 32-channel pre-amplifier shaper circuit with multiplexer, and serializes the signal from MAPMTs. TA provides OR signal of 32 channels, but it is not used in our experiment. Signals from VA is digitized by the FADCs on the back-end modules, mounted on VME-9U crate. In this experiment, the bias voltage for MAPMTs are set to relatively large value (∼950 V) to measure the light from the fibers with a good resolution. The dynamic range of FADCs is therefore not wide (maximum ∼30 p.e.).

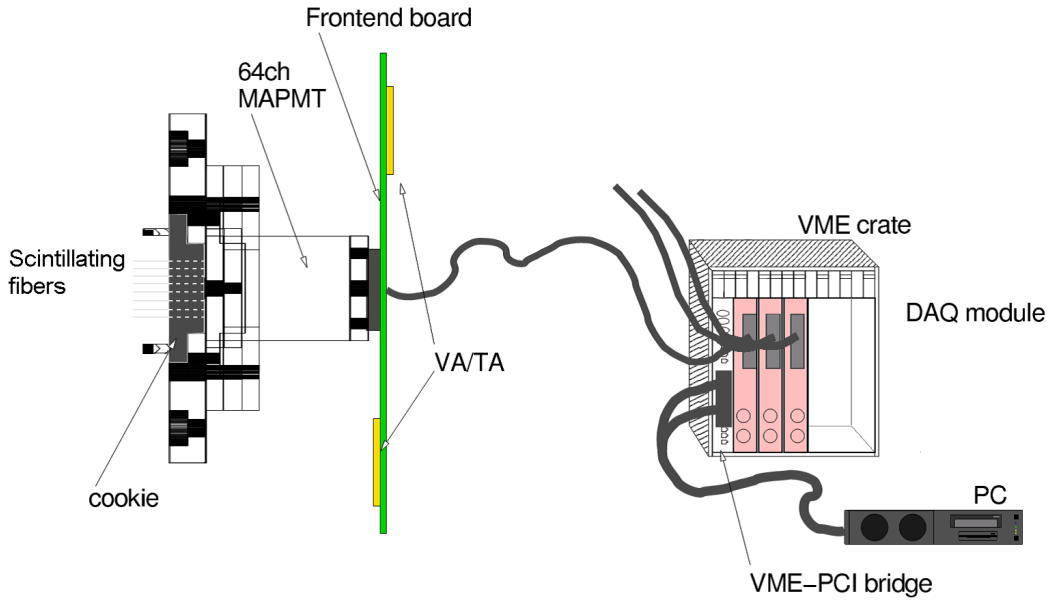

Figure 4.8: Schematic drawing of MAPMT readout electronics.

The data acquisition was controlled by using MIDAS (Maximum Integration Data Acquisition System) [78], which is developed at TRIUMF and PSI (Paul Scherrer Institute) and also used in the T2K experiment. It controls the front-end DAQ programs for each detector, and combines the data to build events. MIDAS provides a graphical interface with full control on a

web browser.

4.3.2 NaI detector and Harpsichord detector

The NaI detectors and Harpsichord detector are placed surrounding the fiber tracker, to detect γ-rays from π^0 decay, to identify CX events. Harpsichord detector is also used for measuring the beam momentum and the fraction of muons in the beam. Both NaI and Harpsichord are not used in the event selection for this ABS + CX total cross section measurement described in the following chapter.

There were two different configurations in the experiment. Figure 4.4 and 4.9 shows the setup for configuration A and B, respectively. In configuration A, we measured charge exchange cross section as well as the angular distribution of the γ-rays from the π^0 decay. There were no lead plates in the Harpsichord for this configuration. Since it is expected that the γ's are mostly emitted in the forward and backward direction, configuration B can provide more charge exchange events thanks to the larger solid angle of Harpsichord.

Each NaI detector has a 5 cm $\times$ 5 cm $\times$ 15 cm NaI crystal, connected to 38 mm (1.5 inch) PMT (Hamamatsu R580). There are 16 (15) NaI detectors used in configuration A (B). The Harpsichord is a miniature version of the FGD, with removable lead plates added in the configuration B. The length of each scintillator is 30.7 cm, which is 1/6 of the length of the bars used in FGD. There are 15 XY scintillator layers, and each layer are made of 32 bars. The total number of bars was 960. The lead plates with thickness between 1 and 2 mm are inserted between each of XY layers, so there are 14 plates in total. The scintillator bars, MPPCs and the readout electronics are the same as the FGD, except for the number of channels and the length of the bars.

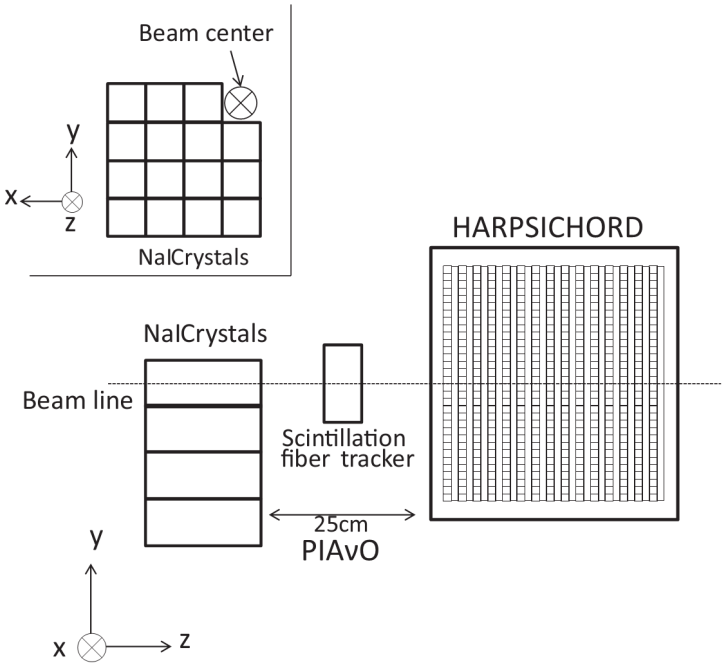

Figure 4.9: Experimental setup in configuration B.

4.3.3 Summary of Data-taking

This project started in May. 2010. The PIAνO detector was designed, constructed and tested at Kyoto University in 2010 summer. The data taking in M11 beamline took place in Oct.$\sim$ Dec. 2010, and Aug. $\sim$ Sep. 2011. For the second data taking in 2011, we used an additional water target to measure the cross section on water, but this data is not relevant to the analysis described in the following chapter. We also took calibration data in 2011, which is used for the analysis presented in this thesis.

The data set we used for the analysis we describe in the following chapter is π^+ beam data on scintillator target (carbon), for five momentum points (200, 225, 250, 275 and 300 MeV/c), taken in the configuration B setting. There was $\sim$ 1.5 Million beam triggered events recorded for each momentum settings, except for 225 MeV/c in which we only took 0.5 Million events due to limited beam time. The analysis not described in this thesis, such as the analysis of ABS and CX individual cross section measurement, will be reported in the future publications.

Chapter 5

Extraction of pion absorption and charge exchange cross section

In this chapter, we describe the measurement of the ABS + CX cross section with the PIAνO fiber detector. The ABS + CX cross section is extracted from the ratio of Data to the MC prediction of the ABS + CX events. The ABS + CX events are selected by requiring no π^+ tracks in the final state of the interaction. The reconstruction of the particle tracks, event selection cuts and simulation are described in Section 5.1, 5.2 and 5.3, respectively. The result of the ABS + CX measurement and the systematic errors are described in Section 5.4.

5.1 Event reconstruction

Figure 5.1 shows an example of an ABS candidate event in data, in the X layers (in the XZ projection). The π^+ beam is injected from the left side of the plot. The blue track is the track identified as pion ("pion-like track"). The green and pink tracks are the proton-like tracks, which are ejected from the nuclei receiving the energy of incident π^+. The tracks are reconstructed in the following procedure.

The first stage of the event reconstruction is the conversion from ADC count to the number of photo-electrons. The number of photo-electrons is derived by multiplying the ADC count by the ADC to p.e. conversion factor and applying electronics non-linearity correction. The typical number of p.e. is $\sim$ 11 p.e./hit for the minimum ionizing particles. Only the hits above 2.5 p.e. are used in the track reconstruction. The efficiency to detect a hit larger than 2.5 p.e. for the charged particles passing through the layer is $\sim$93%. The inefficiency is caused by the inactive region of the fiber. As shown in Fig. 5.1, the position of the fiber layers are shifted from each other to minimize the effect of the inactive regions.

In the track reconstruction algorithm, the usual hits and the crosstalk hits are treated in a different way. The crosstalk hits are usually small and they are associated with large hits. Therefore, when there is a large hit ($>$ 20 p.e.), the small hits ($<$ 10 p.e.) in the adjacent MAPMT channels are identified as crosstalk hits.

The tracks are reconstructed in X and Y layers individually, and then combined to make 3D tracks. The following is the reconstruction procedure.

1. Incident track search:
   The incident track is searched by tracing the hits from the most upstream layer. The hit tracing stops if the hit was not found for the path length longer than 2 fiber thickness. At least 3 hits are required to make a track. For the incident track, we search the track from the most upstream layer, and require that the track angle is horizontal (0 $\pm$ 4 degrees), and the hits are not large ($<$ 20 p.e.). In case the hits are large or identified as cross talk,

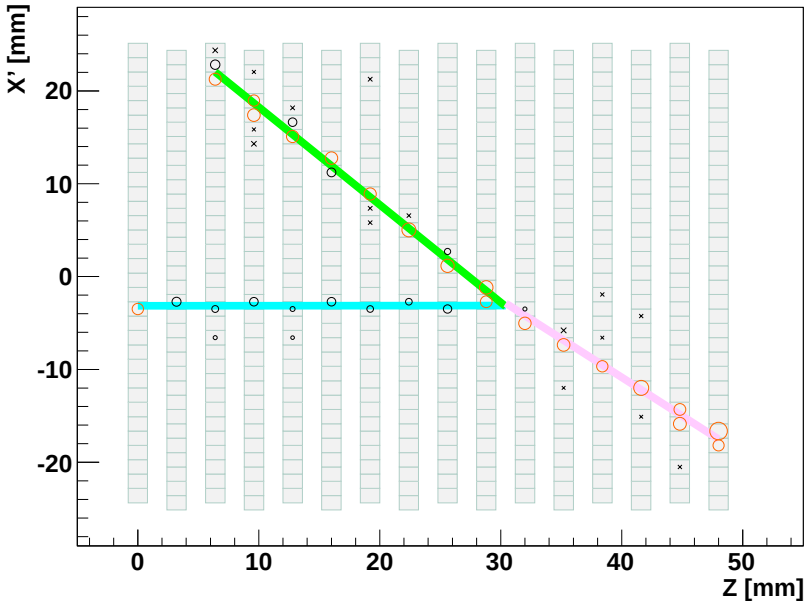

Figure 5.1: Example of ABS candidate event in data (p_π =250MeV/c). The red circles correspond to the large hits (> 20 p.e.), and the crosses correspond to the hits identified as crosstalk hits.

it is not used in the > 3 hits requirement, but the hit tracing do not stop. When there are multiple incident track candidates, the longest track which had maximum number of hits is selected.

2. Interaction vertex search:
   The end position of the incident track is selected as a temporary interaction vertex point. Then we search for a best vertex position around the temporary vertex in ± 3 layers and ± 1 fiber region. The best vertex position is defined as the position where the largest number of hits can be traced. The procedure to trace the hits is same as that for the incident track, except for the horizontal track requirement and small hit (< 20 p.e.) requirement. The tracks traced from the best vertex position are selected as final tracks.

3. Combine the 2D tracks into 3D track:
   The 2D tracks in X and Y projections are combined to form a 3D track, if the Z position (Z is the direction of beam) at the track end agree in two projections. The track end position may not agree when the particle escape from the fiber crossing region and leave the hits in only one projection. Otherwise the track end position is required to agree within ± 2 layers.

Comparing the reconstructed track with the true trajectory in MC, the position resolution of the interaction vertex is evaluated to be ∼ 1 mm in X and Y, and ∼ 2 mm in Z. The angular resolution of the reconstructed track is evaluated to be ∼ 3 degree.

For each track, we calculate deposited charge per track length, dQ/dx. The dQ/dx is used for identifying the particle types in the event selection. It is calculated by dividing total charge deposit by the total length of the track. For the large hits (∼30 p.e.), the measured charge sometimes become smaller than the actual charge, because of the electronics saturation effect. The effect of saturation become significant when the path length of the track per fiber is long

and the charge deposit per fiber is large. The path length per fiber is usually different between X and Y projection. In order to minimize the saturation effect, we calculate the dQ/dx from the projection with shorter path length per fiber.

5.2 Event selection

The ABS + CX events are selected by requiring no π^+ in the final state. The main backgrounds are elastic and inelastic pion scattering events. Figure 5.2, 5.1 and 5.3 shows the example of scattering, ABS and CX candidate events in data, respectively. Pion scattering event has scattered pion track in the final state. A recoil proton track may also exist. The ABS event typically has one or two protons in the final state, but sometimes there are more than or equal to three protons. The CX event usually has zero or one short proton track. In this analysis, we do not distinguish the ABS events from CX, so the ABS + CX events are selected by requiring a incident pion track, interaction vertex in the fiducial volume of the fiber and no π^+-like track in the final state. We define the final state track as all of the reconstructed tracks except for the incident track. With this definition, the scattered pion tracks are included in the final state track.

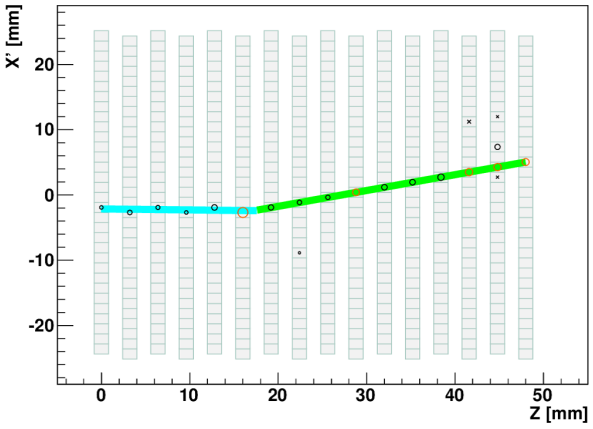

Figure 5.2: Example of pion scattering candidate event in data (p_π =250MeV/c). The blue track is identified as the incident pion track, and the green track is identified as a scattered pion track.

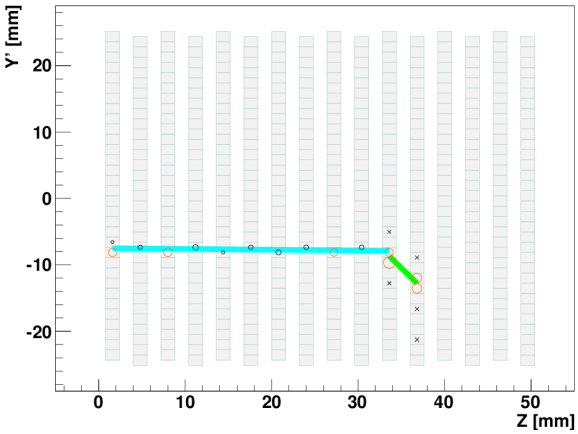

Figure 5.3: Example of CX candidate event in data (p_π =250MeV/c). The blue track is assumed to be the incident pion track, and the green track is assumed to be a proton track from CX interaction.

The ABS + CX event selection consists of the following three cuts.

1. Good incident π^+ cut
   This cut consists of three requirements. First, we require that the incident particle is pion. We apply a cut in the Cherenkov light vs. TOF distribution, as explained in Section 4.2 (except for 200 MeV/c data set, in which we used TOF distribution only).
   Second, we require that the straight incident track exist in the fiber. We require hits on first, third and fifth layers in the upstream, in the same fiber position (same X,Y position), in both X and Y projection (see Fig. 5.4). Only the horizontal straight track passes this cut, so the muons originated from the decay of pions are mostly rejected.
   Third, we require the incident track to enter the fiducial volume (FV). The FV is shown as the broken lines in Fig. 5.4 and 5.5. Figure 5.5 shows the X, Y position distribution of the incident beam. The hexagonal shape corresponds to the region where the S1 trigger

overlap with the fiber crossing region. Because the reconstruction algorithm requires at least 3 hits to reconstruct a track, the fiducial volume is defined to be ≥ 3 fibers (3 layers) inside the edge of the fiber crossing region. The X,Y position of the incident track is required to be inside the X-Y plane of the FV.

2. Vertex in FV cut
   After the *good incident* π^+ cut, $\sim$90% of the events are through going pion events. The events with pion interaction is selected by requiring a reconstructed vertex inside the FV. In this cut, we attempt to reject not only the through going event, but also the pion scattering events with very small scattering angle ("low angle" event). To identify those events, we count the number of hits inside or outside $\pm$ 2 fibers of the incident X, Y position. Because the "low angle" event look very similar to the through going pion event, those events are identified by requiring no reconstructed hits outside the 2 fiber region and $\geq$25 hits inside the 2 fiber region, with at least 2 hits in the last three layers. The events identified as "low angle" events are rejected.

3. No π^+ cut
   In this cut we require no π^+ in the final state. The pion tracks are distinguished from proton tracks by applying dQ/dx cut. Figure 5.6 shows the example of dQ/dx distributions for p_π = 250 MeV/c data and MC. There are six plots corresponding to six different angular regions ($0 < \theta < 30, 30 < \theta < 60, ...150 < \theta < 180$ deg), where θ is the angle of the reconstructed track with respect to the beam direction. The histograms for MC are normalized by number of incident pions. The color of the histograms represents the interaction types ("Elastic" and "Inelastic" corresponds to the elastic and inelastic pion scatterings). The vertical broken line represents the threshold to distinguish pions and protons. Because the dQ/dx distribution is different for different angle or different incident momentum, the different threshold is applied for different angular regions and different incident momentum data sets. If any of the reconstructed track except for the incident track is found to have dQ/dx below the threshold, then that track is identified as pion, and the event is not selected.
   The dQ/dx cut is applied not only for the 3D matched tracks but also for the 2D tracks which were reconstructed only in X or Y projection. For those tracks, the dQ/dx is calculated by using the track length projected in 2D, which is shorter than the actual 3D track length. Therefore, the dQ/dx is overestimated for 2D tracks. However, we apply same dQ/dx threshold for both 3D and 2D tracks, so that the event selection efficiency do not decrease by applying this cut.

The number of selected events after each stage of the cuts is summarized in Table 5.1. There are $\sim$7000 events in data after the event selection, except for 225 MeV/c data set in which the number of incident pions is smaller due to the limited data taking time. The efficiency to select ABS or CX events which occurred inside the fiducial volume is estimated to be $\sim$79%, and the purity of ABS + CX events in the selected sample is estimated to be $\sim$77%. The detail of the MC simulation and comparison with data after event selection are explained in the next section.

5.3 Simulation of the detector and pion interaction

Our simulation code is based on Geant4 version 9.4 patch 2 [79]. The incident beam, pion interaction in the detector and the detector response are taken into account in the simulation. In this section, we describe how the simulation code is tuned.

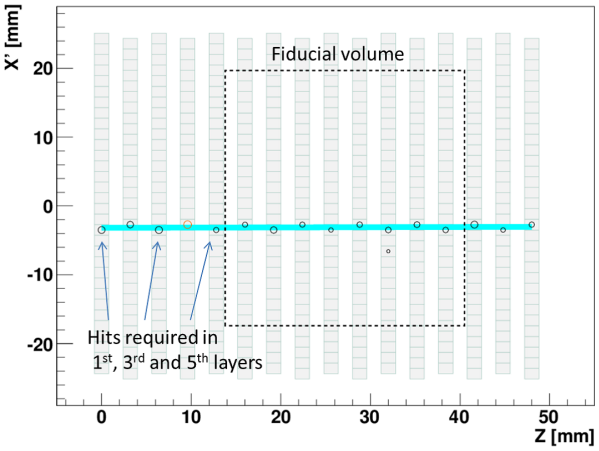

Figure 5.4: Illustration of *good incident pion* cut requirement. The black broken line represents the definition of the fiducial volume.

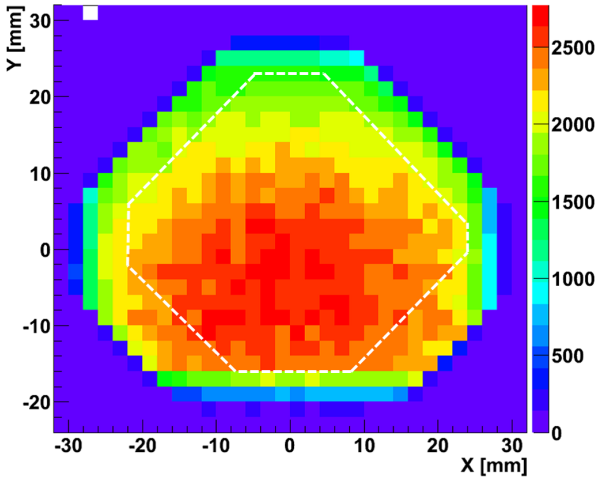

Figure 5.5: The X-Y view of incident beam position distribution. The white broken line represents the definition of the fiducial volume.

	200 MeV/c		225 MeV/c		250 MeV/c		275 MeV/c		300 MeV/c	
Cut	Data	MC	Data	MC	Data	MC	Data	MC	Data	MC
Good incident π	273625		67164		259540		238534		282611	
Vertex in FV	17521	18953.8	4833	5131.0	20548	21481.3	20572	20753.4	24332	24159.2
No π^+	6793	6298.8	1811	1706.3	7226	7138.8	6766	6991.3	7282	7528.8
Efficiency [%]	79.0		79.9		79.8		79.1		76.5	
Purity [%]	75.7		76.5		76.8		77.4		76.5	

Table 5.1: The number of events after each stage of the cut. The numbers for MC are normalized by the numbers of good incident pion events in data.

5.3.1 Physics model

The hadronic interaction of the pions with a nuclei is simulated by using the list of physics models called "QGSP-BERT". For the elastic scattering, it uses a model (called "G4LElastic") based on simple parametrization of the cross section. The inelastic processes are simulated using Bertini Cascade model [80]. The inelastic scattering (INEL), ABS and CX are included in the inelastic process. There are also other processes called double charge exchange and hadron production, but the cross sections for those interactions are negligibly small in the pion momentum range in this experiment.

We tune the cross sections of pion hadronic interactions so that they agree better with the measurements in the past. The π^+−C and π^+−H elastic cross sections and differential cross sections ($d\sigma/d\theta$) are tuned. Also, the inclusive π^+−C inelastic scattering, ABS and CX cross sections are tuned. Figure 5.7 and 5.8 shows the comparison of the cross sections between the past experiments and Geant4 default, for elastic and inelastic processes. There are disagreements between Geant4 cross section (ver9.4, QGSP-BERT) and the measurements from the past experiments, especially for π−H elastic scattering process. We tune the cross section in Geant4 code by simply interpolating the data points from past experiments. Table 5.2 summarizes the data from past experiments that we used for the tuning. The momentum of pions after inelastic scattering is also tuned, by using the NEUT cascade model because the data from past

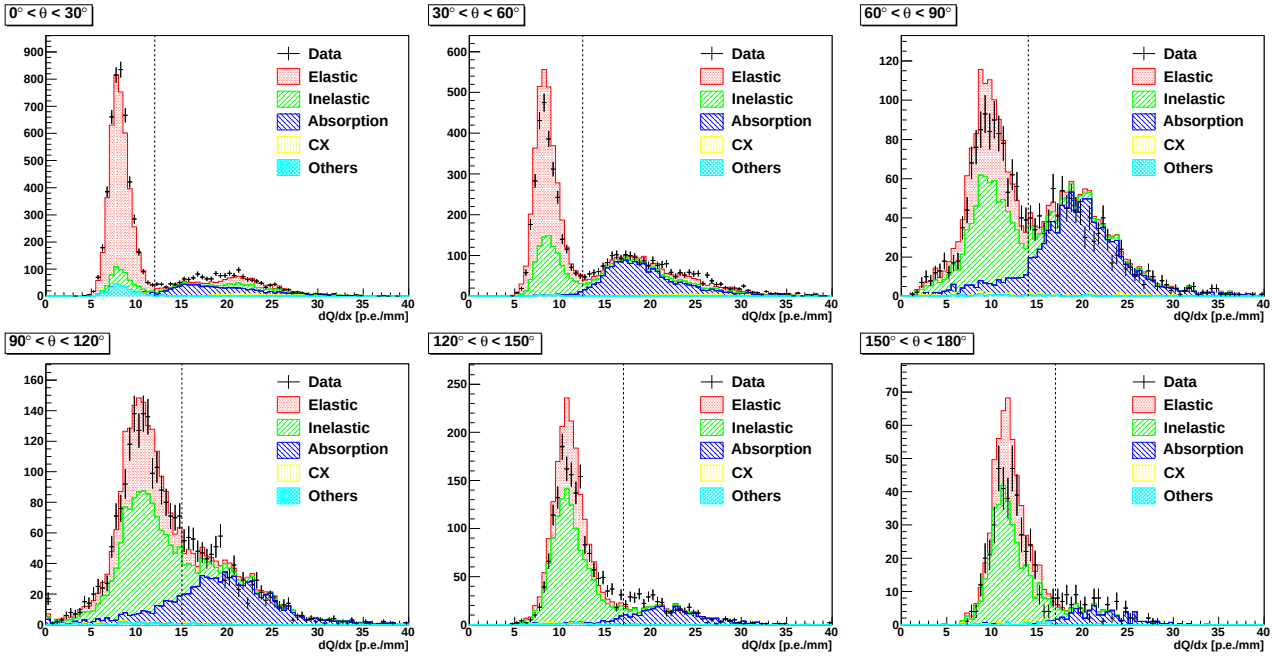

Figure 5.6: dQ/dx distribution in six different angular regions, for $p_\pi = 250$ MeV/c data and MC. The dotted vertical lines represent the threshold to distinguish pions and protons. For multiple tracks events, only the smallest value of dQ/dx among the tracks is filled in the histogram. The events in the "Others" category are mainly pion decay in flight events and Coulomb scattering events.

experiments are not available.

Figure 5.9 shows the number of tracks and angular distribution for the reconstructed tracks before and after the tuning, for $p_\pi = 250$ MeV/c data set. The *No* π^+ cut is not applied for these plots. The forward angle multiple track events increased after the tuning, mainly due to the increase of $\pi-$H elastic cross section. The agreement between data and MC is much better with the tuning, although there are still small disagreements because the linear interpolation do not perfectly reproduce the data. The difference between data and MC is included in the systematic error.

Figure 5.10 shows the angular distribution of the reconstructed tracks before and after applying *No* π^+ cut, for 200, 250 and 300 MeV/c data sets. In case there are multiple tracks in the final state, only the track with smallest value of dQ/dx is selected to fill the histograms in these plots. Figure 5.11 shows the number of tracks distribution before and after applying *No* π^+ cut. After applying *No* π^+ cut, the fraction of ABS and CX events increase, and the agreement between data and MC become worse. This is expected, because the kinematics of the final state particles for ABS and CX interactions are not tuned. The event selection efficiency is affected by this difference, so it is taken into account in the systematic error.

5.3.2 Detector and beam

The detector geometry, material and the response are included in the simulation so that it reproduce the data. The beam momentum and profile are measured in the data and implemented in the simulation. We use the pion through going data and the bench test data to tune the detector calibration parameters and the beam parameters. The detail of the tuning is described in Appendix A.1 and A.2. As an example, Figure 5.12 shows the distribution of charge deposit

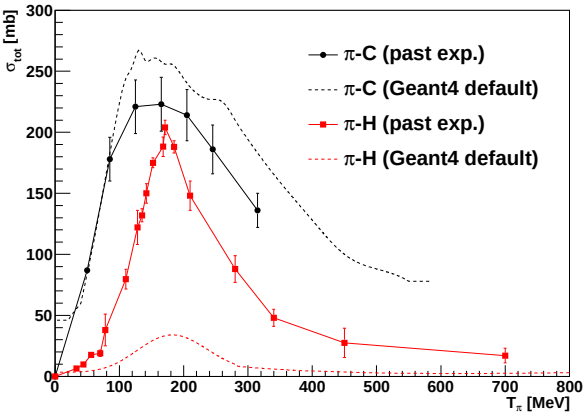

Figure 5.7: Comparison of elastic inclusive cross section between the past experiments (summarized in Table 5.2) and Geant4 default. The cross sections are plotted as a function of pion kinetic energy.

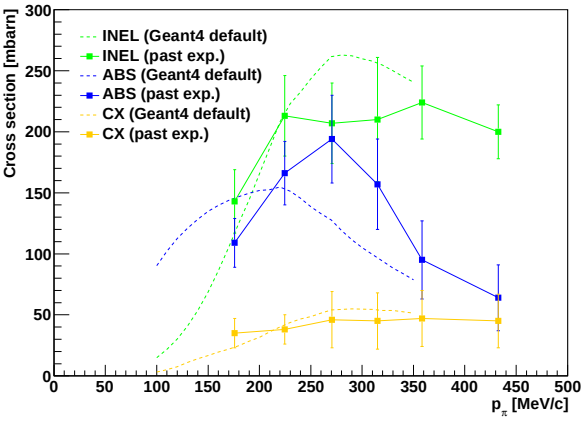

Figure 5.8: Comparison of inelastic inclusive cross sections between the past experiment [70] and Geant4 default. The cross sections are plotted as a function of pion momentum.

per fiber for 250 MeV/c data set. The MC (red) and data (black) agree well. The momentum of the incident pion for each data set is measured by using through going pion data. The momenta at the fiber are summarized in Table 5.3.

5.4 Extraction of the cross section

The ABS + CX cross section for each momentum data set is measured in the following formula.

$$\sigma(\mathrm{ABS}+\mathrm{CX}) = \sigma(\mathrm{ABS}+\mathrm{CX})_{pred} \times \frac{N_{\mathrm{data}} - N_{\mathrm{BG}}^{pred}}{N_{\mathrm{sig}}^{pred}}, \tag{5.1}$$

where σ(ABS+CX) is the predicted cross section that we measure, $\sigma(\mathrm{ABS}+\mathrm{CX})_{pred}$ is predicted cross section in MC, N_{data} is the number of events after event selection in data, N_{BG}^{pred} is the predicted number of background events in MC after event selection, N_{sig}^{pred} is the number of ABS + CX events in MC after event selection.

In the actual calculation, the fraction of muon in the beam is taken into account. Also, in order to extract the cross section on carbon, the ABS and CX cross sections on other nuclei are considered. The number of nuclei in the fiducial volume of the fiber is estimated from the material and dimension of the fibers, and summarized in Table 5.4. Because the ABS and CX interactions do not occur in π^+−H interaction, we only have to consider oxygen and titanium.

Adding the corrections for muon contamination and interaction on other nuclei, the formula to extract the cross section changes as follows.

$$\sigma(\mathrm{ABS}+\mathrm{CX}) = \sigma(\mathrm{ABS}+\mathrm{CX})_{pred} \times \frac{N_{\mathrm{data}} - N_{\mathrm{BG}}^{pred}}{N_{\mathrm{sig}}^{pred}} \times \frac{1 - R_{\mathrm{TiO}}^{data}}{1 - R_{\mathrm{TiO}}^{\mathrm{MC}}} \times \frac{1}{1 - f_\mu}, \tag{5.2}$$

where f_μ is the fraction of muons in the beam. The R_{TiO}^{data} and $R_{\mathrm{TiO}}^{\mathrm{MC}}$ are the fraction of ABS and CX events on Ti or O after event selection, for data and MC. The R_{TiO}^{data} is estimated from

Measurement	Kinetic energy (MeV)	Reference
$\pi-$C inclusive (elastic, inelastic, ABS and CX)	85, 125, 165, 205, 245, 315	D. Ashery et al. [70]
$\pi-$C elastic inclusive	49.9	M. A. Moinester et al. [81]
$\pi-$H elastic inclusive	33, 44, 56, 70	S. L. Leonard et al. [82]
	78, 110, 135	H. L. Anderson et al. [83]
	165	H. L. Anderson et al. [84]
	128, 142, 152, 171, 185	J. Ashkin et al. [85]
	210, 280, 340, 450, 700	Lindenbaum et al. [86]
$\pi-$C elastic differential	40	M. Blecher et al. [87]
	50	R. R. Johnson et al. [88]
	67.5	J. F. Amann et al. [89]
	80	M. Blecher et al. [90]
	100	L. E. Antonuk et al. [91]
	142	A. T. Oyer et al. [92]
	162	M. J. Devereux et al. [93]
	180, 200, 230, 260, 280	F. Binon et al. [94]
$\pi-$H elastic differential	29.4, 49.5, 69	J. S. Frank et al. [95]
	69	Ch. Joram et al. [96]
	87, 98, 117, 126, 139	J. T. Brack et al. [97]
	87, 98, 117, 126, 139	J. T. Brack et al. [98]
	166.0, 194.3, 214.6, 236.3, 263.7, 291.4	P. J. Bussey et al. [99]

Table 5.2: List of data sets used for cross section tuning in simulation.

Momentum setting [MeV/c]	200	225	250	275	300
Momentum at the fiber tracker [MeV/c]	201.6	216.6	237.2	265.5	295.1

Table 5.3: The measured momentum for five different data sets.

the number of Ti and O nuclei and the ABS and CX cross section for those nuclei, which was calculated by interpolating the measured cross sections in the past experiment [70].

Table 5.5 summarizes the measurements for five momentum data sets. The errors in σ(ABS+ CX) includes both statistical and systematic uncertainties. The systematic errors are originated from the uncertainties in the detector, beam and physics model. Table 5.6 shows the summary of the statistical and systematic errors. The total error is ∼6.5 % except for $p_\pi = 216.6$ MeV/c data set, which is roughly half of the errors of the past experiments [70, 71, 75]. For $p_\pi = 216.6$ MeV/c data set, the statistical error is relatively large, and the systematic error was also found to be large.

The largest contribution to the errors come from the uncertainty in the physics model which affects the event selection efficiency and the predicted number of background events. The dominant systematic error sources are estimated as follows.

- The uncertainty of the number of background events is estimated by comparing the number of background events in the control sample between data and MC. Because the backgrounds are the pion scattering events, the background control sample is produced by requiring a pion-like track in the final state.

- The efficiency to reconstruct the vertex in FV depends on the angular distribution of the protons in the final state, which is not perfectly reproduced in MC. In order to estimate the

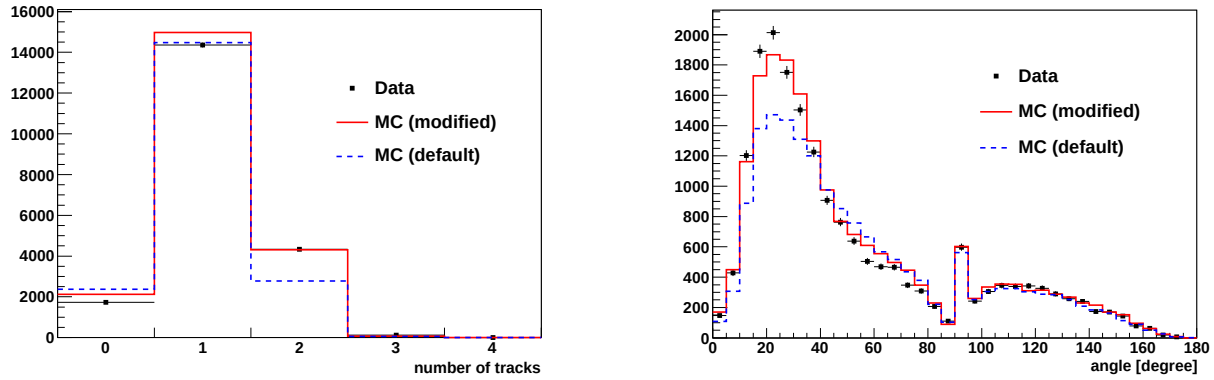

Figure 5.9: The number of tracks and angular distribution of reconstructed tracks for MC before and after tuning, and for data, for p_π =250 MeV/c data set. The *No* π^+ cut is not applied.

Nuclei	C	H	O	Ti
Number of nuclei [$\times 10^{24}$]	1.518±0.007	1.594±0.008	0.066±0.004	0.006±0.0002

Table 5.4: The number of nuclei in the fiducial volume of the fiber tracker.

error of the reconstruction efficiency, we change the proton track angle in MC to reproduce the angular distribution of the proton-like tracks in data. Then we derive the error from the difference between the efficiency in MC before and after the change.

- The error of the efficiency of the dQ/dx cut is estimated by measuring the probability to pass the dQ/dx cut in one projection (X or Y) but fail in the other projection. The efficiency error is derived from the difference of this probability between data and MC.

The detail of the systematic error estimation is described in Appendix A.3.

p_π [MeV/c]	$N_{\rm data}$	$N_{\rm BG}^{pred}$	$N_{\rm sig}^{pred}$	$R_{\rm TiO}^{data}$	$R_{\rm TiO}^{\rm MC}$	f_μ	$\sigma({\rm ABS+CX})_{pred}$ [mbarn]	$\sigma({\rm ABS+CX})$ [mbarn]
201.6	6793	1527.7	4771.1	0.0634	0.0808	0.0016	175.93	$198.1^{+11.1}_{-15.4}$
216.6	1811	401.0	1305.3	0.0636	0.0731	0.0071	194.41	$213.7^{+17.8}_{-19.1}$
237.2	7226	1658.8	5479.9	0.0624	0.0632	0.0043	214.43	$219.0^{+12.7}_{-14.0}$
265.5	6766	1583.2	5408.1	0.0603	0.0528	0.0054	235.92	$225.5^{+14.6}_{-14.1}$
295.1	7282	1773.0	5755.7	0.0591	0.0518	0.0034	219.39	$209.1^{+14.9}_{-13.6}$

Table 5.5: Summary of the measurements. In this table, p_π is the momentum of pions at the fiber tracker.

Figure 5.13 shows the result of ABS + CX cross section as a function of pion momentum, compared with the results from past experiments [70, 71]. As already mentioned, the uncertainty in our measurement is roughly half of the uncertainty in the past experiments. In these past experiments (which took place in the 80's), the ABS + CX cross section was measured by subtracting the pion scattering cross section from the total cross section. Because they did not directly select the ABS and CX events, there was large errors (typically 5 $\sim$ 10 % in [70]) assigned for the subtraction procedure. In our measurements, thanks to a fine-grained full active fiber tracker, we were able to measure the ABS + CX interaction directly.

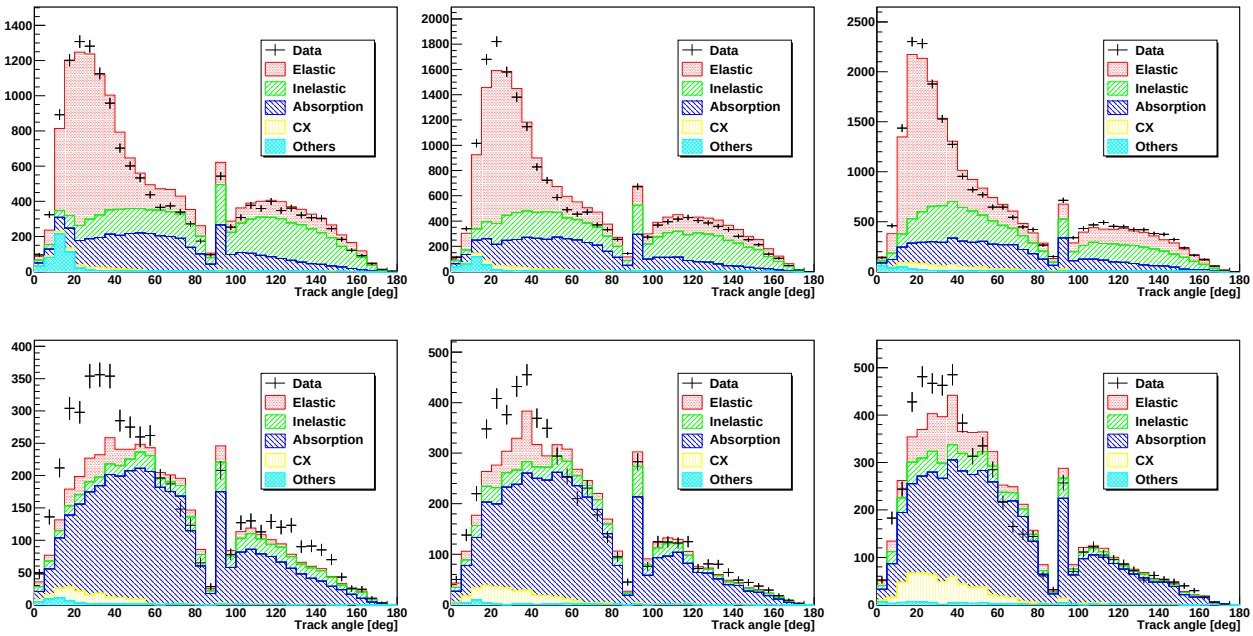

Figure 5.10: Angular distribution of the reconstructed tracks in the final state, for 200 (left), 250 (center) and 300 (right) MeV/c data sets, before (top) and after (bottom) applying *No* π^+ cut. When the true track angle is close to 90 degrees, the track reconstruction algorithm tends to reconstruct the track exactly at 90 degrees, so the number of events in the bin corresponding to 90 degrees is larger than the neighbor bins.

By using this new result, the uncertainty in the pion interaction model that we use in T2K is improved. The detail of the pion interaction model in T2K and the improvement of uncertainty for the parameters in the model are discussed in the next chapter.

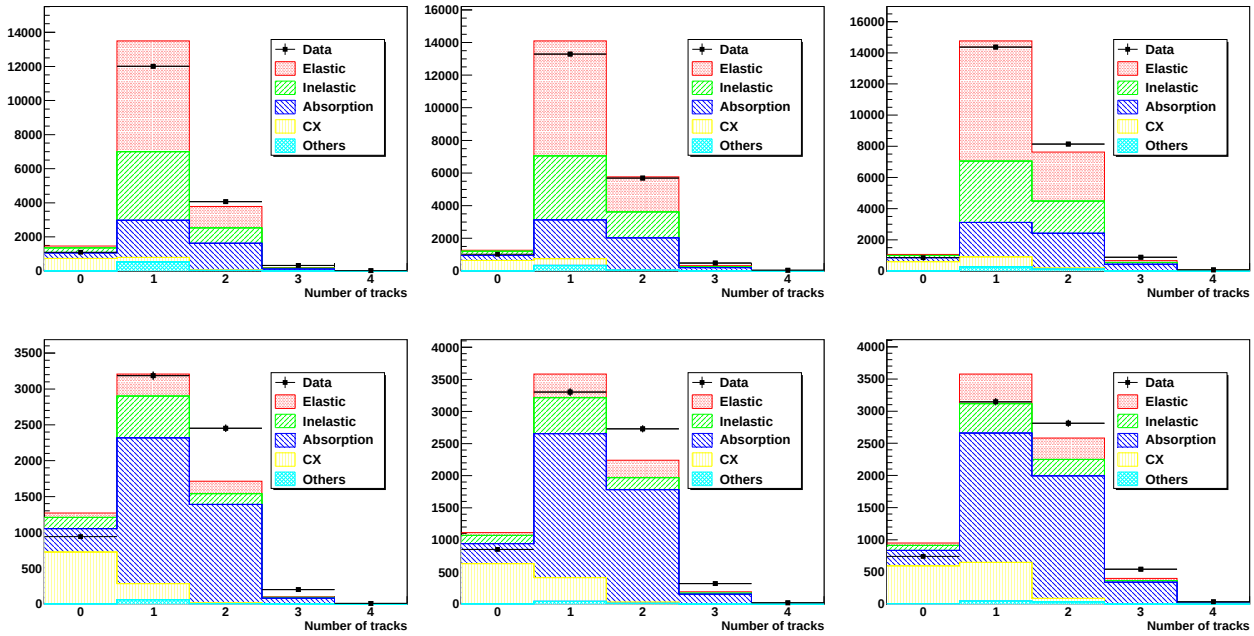

Figure 5.11: Distribution of number of reconstructed tracks in the final state, for 200 (left), 250 (center) and 300 (right) MeV/c data sets, before (top) and after (bottom) applying *No* π^+ cut.

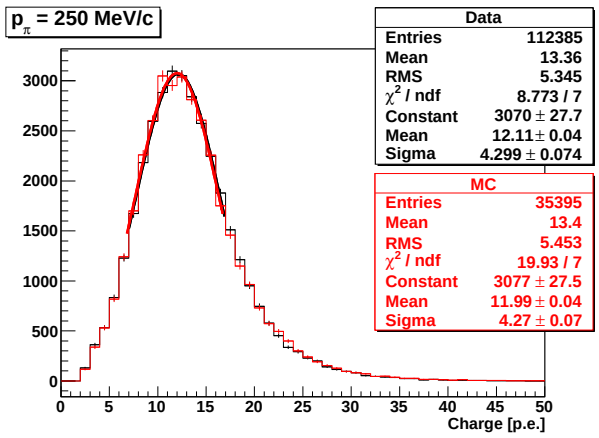

Figure 5.12: Charge distribution of through going pions in $p_\pi = 250$ MeV/c setting.

	p_π at the fiber tracker [MeV/c]				
	201.6	216.6	237.2	265.5	295.1
Systematic errors					
Beam profile	1.8	2.6	2.1	2.3	2.2
Beam momentum	1.3	2.1	1.5	1.2	0.7
Fiducial volume	1.0	1.7	1.9	0.6	1.6
Charge distribution	1.6	2.4	1.1	1.0	2.5
Crosstalk probability	1.7	1.7	1.1	1.1	2.0
Layer alignment	0.6	2.5	1.1	0.8	0.8
Hit efficiency	0.6	1.1	1.0	0.7	0.9
Muon contamination	0.5	0.8	0.9	0.3	0.2
Target material	0.8	0.9	0.9	0.8	1.0
Physics model (selection efficiency)	2.8	4.9	2.9	4.8	3.7
(background prediction) +	2.8	1.8	2.4	2.3	3.3
−	6.1	3.7	3.6	1.5	1.9
Subtotal +	5.3	7.7	5.5	6.2	6.7
−	7.6	8.4	6.1	6.0	6.1
Statistical error (data)	1.7	3.1	1.7	1.8	1.7
Statistical error (MC)	0.5	0.7	0.7	0.6	0.6
Total +	5.6	8.4	5.8	6.5	6.9
−	7.8	9.0	6.4	6.3	6.4

Table 5.6: Summary of the statistical and systematic errors in percentage.

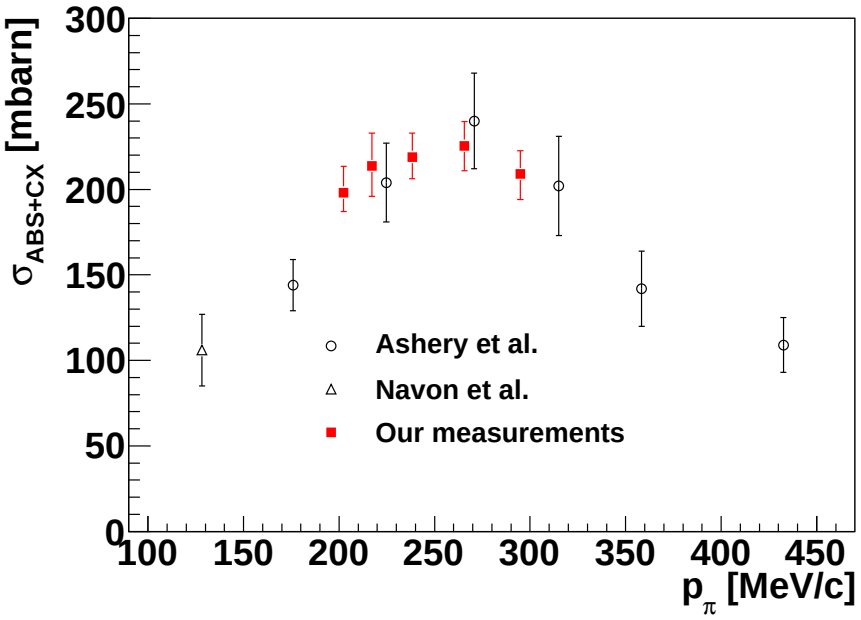

Figure 5.13: Result of ABS + CX cross section vs. Pion momentum, compared with the results from past experiments.

Chapter 6

Improvement of pion interaction model

In T2K, the interaction of pions in the final state of neutrino interaction is simulated by the NEUT cascade model [69]. The parameters used in the model are tuned by using the cross section data sets from past pion-nucleus interaction measurements. We have improved the model by tuning the parameters using the result of our measurement at TRIUMF. In Section 6.1, we describe the cascade model which we use in NEUT. Tuning of the parameters in the model and the improvement of the uncertainty in the prediction is discussed in Section 6.2.

6.1 Cascade model

NEUT simulates the neutrino-nucleus interaction and the interaction of hadrons (mainly pions and protons) in the final state. The interaction of hadrons are simulated by using the cascade model. Figure 6.1 illustrates how cascade model works. In the cascade model, pion is propagated

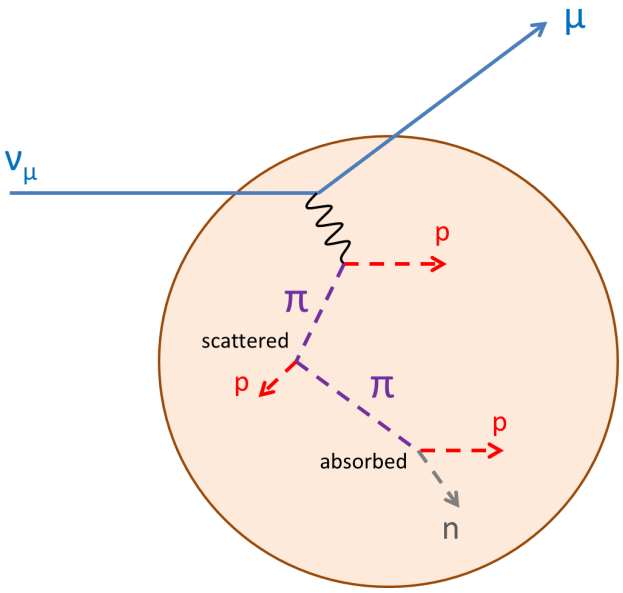

Figure 6.1: Illustration of the NEUT cascade model. The large circle represents the nuclei.

through the nuclear medium in finite steps. The interaction probability is calculated for step by

step, according to the predicted microscopic cross section from Δ-hole model [100] (for $p_\pi < 500$ MeV/c). This is a microscopic, many-body calculation, including Pauli blocking and the local density approximation of a finite nucleus.

The interaction probability depends on the nuclear density. In NEUT, we use the two-parameter Fermi model for oxygen (a Woods-Saxon potential):

$$\frac{\rho(r)}{\rho_0} = \frac{1}{1+\exp(\frac{r-c}{\alpha})}, \tag{6.1}$$

where r is the distance from the center of the nuclei, and the nuclear radius c and surface thickness α are determined from electron scattering data [101]. For nuclei other than oxygen, we use three-parameter Fermi model:

$$\frac{\rho(r)}{\rho_0} = \frac{1+w\frac{r^2}{c^2}}{1+\exp(\frac{r-c}{\alpha})}, \tag{6.2}$$

where w is also extracted from data [101]. Figure 6.2 shows the example of normalized nuclear density distributions for Pb, Fe, O and C.

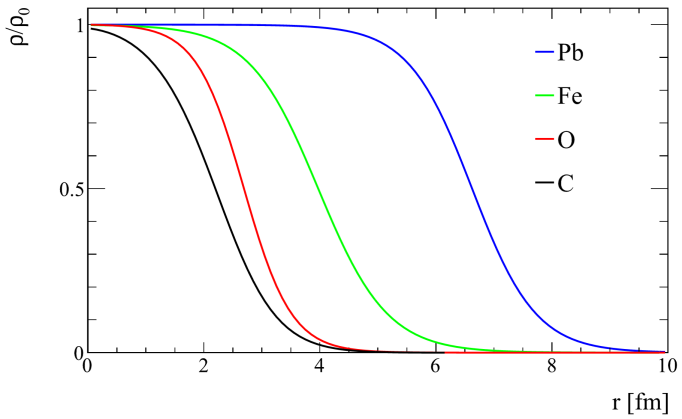

Figure 6.2: Example of normalized nuclear density distributions.

The interaction probability is calculated for oxygen as a function of p_π and r_{oxy} and provided in a table. For other nuclei, we use the same table by calculating the effective position in oxygen:

$$r_{oxy} = \alpha_{oxy} \ln\left(\frac{1+\exp(\frac{r-c}{\alpha})}{1+w\frac{r^2}{c^2}} - 1\right) + c_{oxy} \tag{6.3}$$

Figure 6.3 shows an example of interaction probability per step as a function of r, for π^+ with $p_\pi = 275$ MeV/c in ^{16}O.

The cascade process stops when the pion escape from the nuclei. The maximum distance from the center of the nucleus is determined as $R_N = 2.5c$ (~ 6 fm for carbon), which is defined so that we encompass most of the nuclear medium without wasting time in low density regions. When the distance from the center of the nucleus become larger than R_N, the cascade process stops. The step size is defined as $dx = R_N/100$, which is selected such that the probability of two or more interactions in one step is negligible.

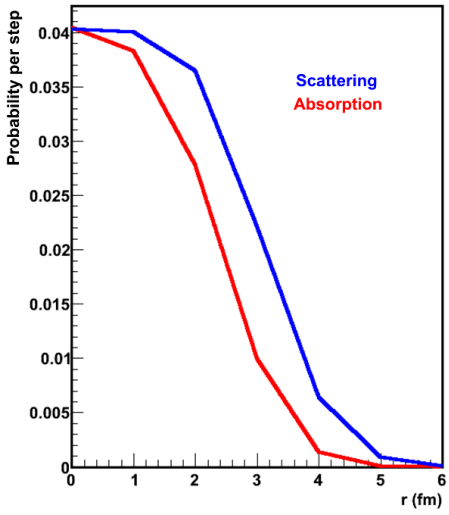

Figure 6.3: Interaction probability per step for π^+ with $p_\pi = 275$ MeV/c in ^{16}O.

6.2 Fit to the pion cross section data sets

The scaling factors for the microscopic cross section in the cascade model is tuned by using external pion-nucleus cross section data sets. Our goal in this section is to improve the uncertainty of these scaling parameters by using the result of our ABS + CX cross section measurement. There are three scaling parameters: *abs*, *qe* (quasi-elastic or inelastic scattering) and *cx*. The *abs* and *qe* define the normalization of microscopic cross section for ABS and the sum of quasi-elastic and CX interaction, while the *cx* defines the fraction of CX interaction in the sum of quasi-elastic and CX. The change in the scaling of the microscopic parameter do not simply correspond to the change in macroscopic cross section, because *abs*, *cx* and *qe* are correlated to each other. For example, when the value of *qe* increases, pions are scattered more often inside the nuclei, and the momentum of pion changes. Because the microscopic cross section for ABS depends on the momentum of pion, the absorption probability also changes.

Figure 6.4 shows π^+-C cross section for four different interaction modes, measured by past experiments. A reactive channel corresponds to ABS + CX + INEL. The lines in each interaction channels corresponds to the prediction by NEUT. There are eight lines for each interaction channels, which correspond to different value of (*qe*, *abs*,*cx*). These eight parameter sets represents 1 sigma deviation from the best fit, which was used in 2012 ν_e appearance analysis. The best fit value of the scaling parameters and their 1 sigma errors are defined by minimizing the chi-square, which is calculated from the difference between data and prediction. These eight parameter sets are then used in the oscillation analysis to evaluate the 1 sigma error for the prediction of ν_e candidate events in SK.

In the following text, we describe the improvement in the optimization of these scaling parameters and in the estimation of the errors. One of the improvement is to add ABS + CX cross section data set measured by ourselves. The other improvement is the change of the method to estimate the error.

In the original method, the chi-square was defined as follows:

$$\chi^2 = \frac{1}{n} \sum_i \sum_{\pi^+,\pi^-} \frac{(\sigma_i^{\mathrm{MC}} - \sigma_i^{\mathrm{data}})^2}{(\delta(\sigma_i^{\mathrm{data}}))^2}, \tag{6.4}$$

where n is the total number of data points across all interaction channels i and π^+ and π^- data, and δ denotes the systematic and statistical uncertainty. The best values of (*qe*, *abs*, *cx*) defined

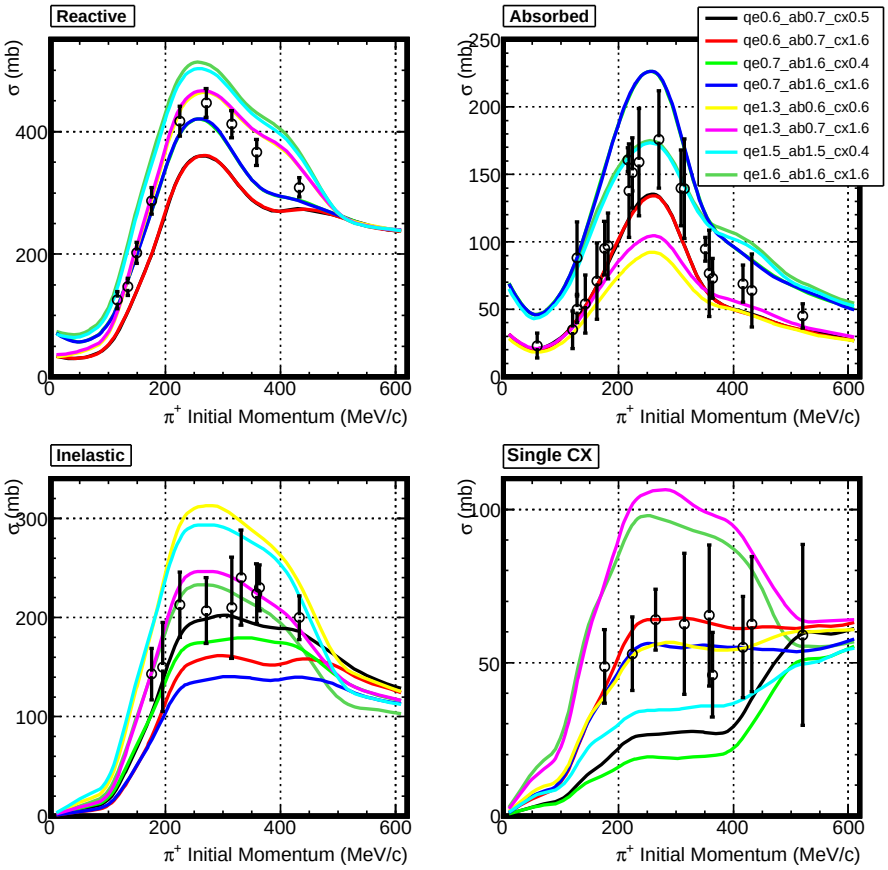

Figure 6.4: The predicted π^+-C cross section compared to measurements in the past, for four different interaction channels.

as the set of parameters which minimize the χ^2. We scan over the parameter space in 0.05 step to find the best set of parameters. Because some of the data points in the past experiments are correlated to each other, the parameters will be over-constrained if we define the χ^2 assuming that all of the data points are independent to each other. Therefore, a factor of $1/n$ is introduced in Eq. 6.2. In fact, most of the ABS data points are correlated with CX data points, because the ABS cross section measured by the past experiments are derived by measuring ABS + CX and subtracting CX cross section extracted from other experiments.

In the improved analysis, we use ABS + CX data points instead of ABS and CX separate data points, to remove the correlations. Some of the CX data points were estimated from the other CX data points, so they are also removed. Some of the INEL data points are also removed because they are correlated with the Reactive data points, and some of the ABS data points in are removed because they are found to be exclusive cross section in which more than or equal to 2 protons in the final state. Figure 6.5 shows π^+-^{12}C cross section for five different interaction channels, for nominal NEUT prediction compared with the data points newly selected from the past experiments. Figure 6.6 shows the same plots, but for π^-. For π^-, ABS and INEL cross section are not available from the past experiments, so they are not used in this study. Table 6.1 summarizes the external data sets that we used for this tuning. In the new data set, there are no correlations between the data points from different experiments, but the correlation between

data points from same experiment may exist. Therefore, we define the chi-square as follows:

$$\chi^2 = \sum_{iexpr} \chi^2_{iexpr} \tag{6.5}$$

$$\chi^2_{iexpr} = \frac{1}{n_{expr}} \sum_i \frac{(\sigma_i^{\rm MC} - \sigma_i^{\rm data})^2}{(\delta\sigma_i^{\rm data})^2}, \tag{6.6}$$

where χ^2_{expr} is the chi-square for each experiment, n_{expr} is number of data points in that experiment.

Reference	Interaction channel	Pion momentum [MeV/c]
D. Ashery et al. [70]	π^+-C Reactive, ABS+CX	175.7, 224.4, 270.4, 314.7, 358.0, 432.2
	π^--C Reactive, ABS+CX	224.4, 270.4
A. Saunders et al. [102]	π^+-C Reactive	115.9, 133.9, 149.3
E. Bellotti et al. [72]	π^+-C ABS	230.6
S. M. Levenson et al. [103]	π^+-C INEL	194.4, 331.0
M. K. Jones et al. [76]	π^+-C INEL, CX	363.3, 416.4
D. Ashery et al. [74]	$\pi^\pm$-C CX	270.4
E. Bellotti et al. [73]	π^+-C CX	230.6
I. Navon et al. [75]	$\pi^\pm$-C ABS+CX, CX	224.8
I. Navon et al. [71]	π^+-C ABS+CX	128.3
F. Binon et al. [94]	π^--C Reactive	218.5, 253.4, 287.1, 309.2, 341.8, 374.0, 395.3
H. Hilscher et al. [104]	π^--C CX	156.3
R. H. Miller et al. [105]	π^--C ABS+CX	253.4

Table 6.1: List of external data sets used for tuning the scaling parameters.

We scanned over the parameter space in 0.05 step to find the best combination of *abs*, *qe* and *cx* which minimizes the chi-square. Figure 6.7 shows the best fit point and 1 sigma allowed region of the scaling parameters. The best value of (*qe*, *abs*, *cx*) is (0.90, 1.25, 0.80), and the value of χ^2 at the best fit point is 13.47. The *abs* scaling is larger than nominal and the *cx* scaling is smaller than nominal, because the data point from past experiment is larger than prediction for ABS and smaller for CX in Fig. 6.5 and 6.6.

In order to determine the parameter sets for (*qe*, *abs*, *cx*) which correspond to 1σ deviation, we calculate χ^2 difference from the best fit point.

$$\Delta\chi^2 = \chi^2 - \chi^2_{best}. \tag{6.7}$$

The $\Delta\chi^2$ value which corresponds to 1σ deviation is 3.53, in case the number of fit parameters is 3. Therefore, we define the parameter sets that represent 1σ deviation from $\Delta\chi^2 = 3.53$ surface in the (*qe*, *abs*, *cx*) parameter space. We choose eight points such that they lie at the corner of each octant of the 3-parameter space. This ensures all extreme correlations are taken into account. Figure 6.8 shows the 3D distribution of the eight parameter sets derived in the old and new tuning. The deviation of the values of the parameter sets for the new parameter set is only $\sim$1/4 of the old parameter set. This is mainly because the tuning method is improved so that the correlations between data points from different experiments do not exist. Figure 6.9 and 6.10 show the predicted cross section for all of the interaction channels, for eight parameter sets (blue lines) and for the best fit value (red lines). The predicted cross section is consistent with the data points from past experiments.

These parameter sets can be used for estimating the systematic uncertainties in ND280 and SK measurements. As we describe later in Chapter 9 and 10, the observables at ND280 and SK

are the momentum and angular distribution of the charged leptons from the neutrino interaction. For a given analysis (ND280 or SK), we built a covariance matrix V which represents the errors in each bins of the observables and the correlations between the bins:

$$V_{ij} = \frac{1}{N_{par}} \sum_{k}^{N_{par}} (x_i^k - x_i^0)(x_j^k - x_j^0), \tag{6.8}$$

where V_{ij} is the (i, j) bin of the covariance matrix, N_{par} is the number of parameter sets, x_i^k and x_i^0 are observables at i^{th} bin for k^{th} parameter set and for nominal parameter set. The covariance matrix is evaluated separately for ND280 and SK, and the correlation between ND280 and SK is not taken into account for this analysis.

The effect of the FSI and SI uncertainty to the number of ν_e candidate events at SK can be estimated by using the covariance matrix. In the previous analysis, the systematic uncertainty from FSI and SI for the predicted number of ν_e candidate events at SK was estimated to be 2.3 % (assuming $\sin^2 2\theta_{13} = 0.1$). With the improved model, the size of the 1σ deviation of the scaling parameter reduced to 1/4, so the uncertainty in the predicted number of ν_e candidate events is expected to become 2.3 / 4 $\sim$ 0.6 %, which is negligibly small compared to the total uncertainty, 9.9 %. This improvement is, however, not yet included in the ν_e appearance analysis which we describe in the following chapter. As we will see in Chapter 11, the total systematic uncertainty for number of ν_e candidate events is 8.8 %, which is much larger than the error from FSI in 2012. Therefore, the effect of the improvement in the FSI error is expected to be not significant for this analysis which we report in this thesis. However, the other important systematic errors, such as the ones which come from neutrino beam flux and cross section uncertainty are being reduced and expected to become as small as the FSI error, so the improvement in FSI error will be definitely important in the near future.

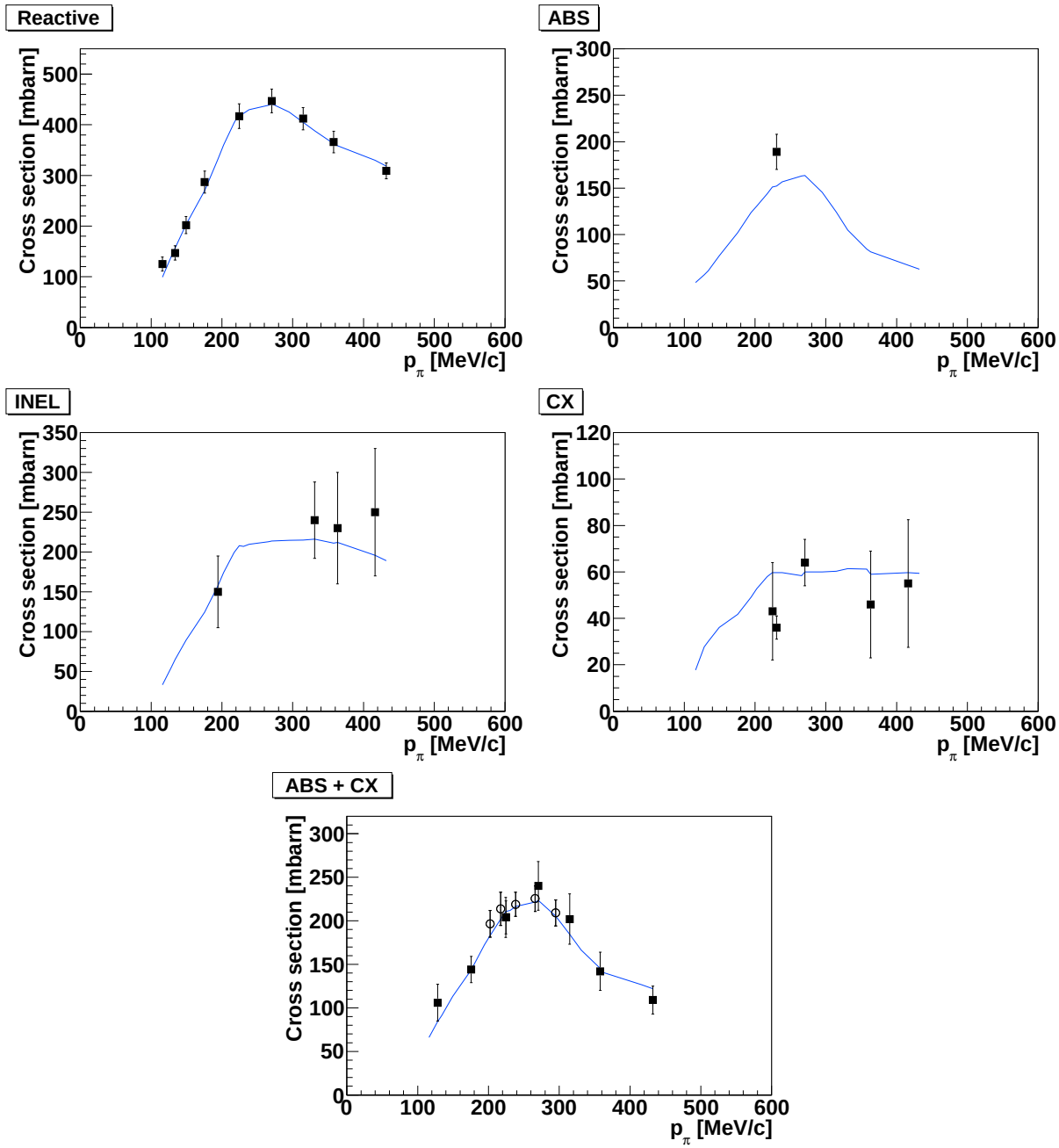

Figure 6.5: π^+-^{12}C cross section for five different interaction channels, compared between NEUT nominal prediction (blue curves) and data points from past experiments. The white circle points in ABS + CX sample are the data points from our measurements.

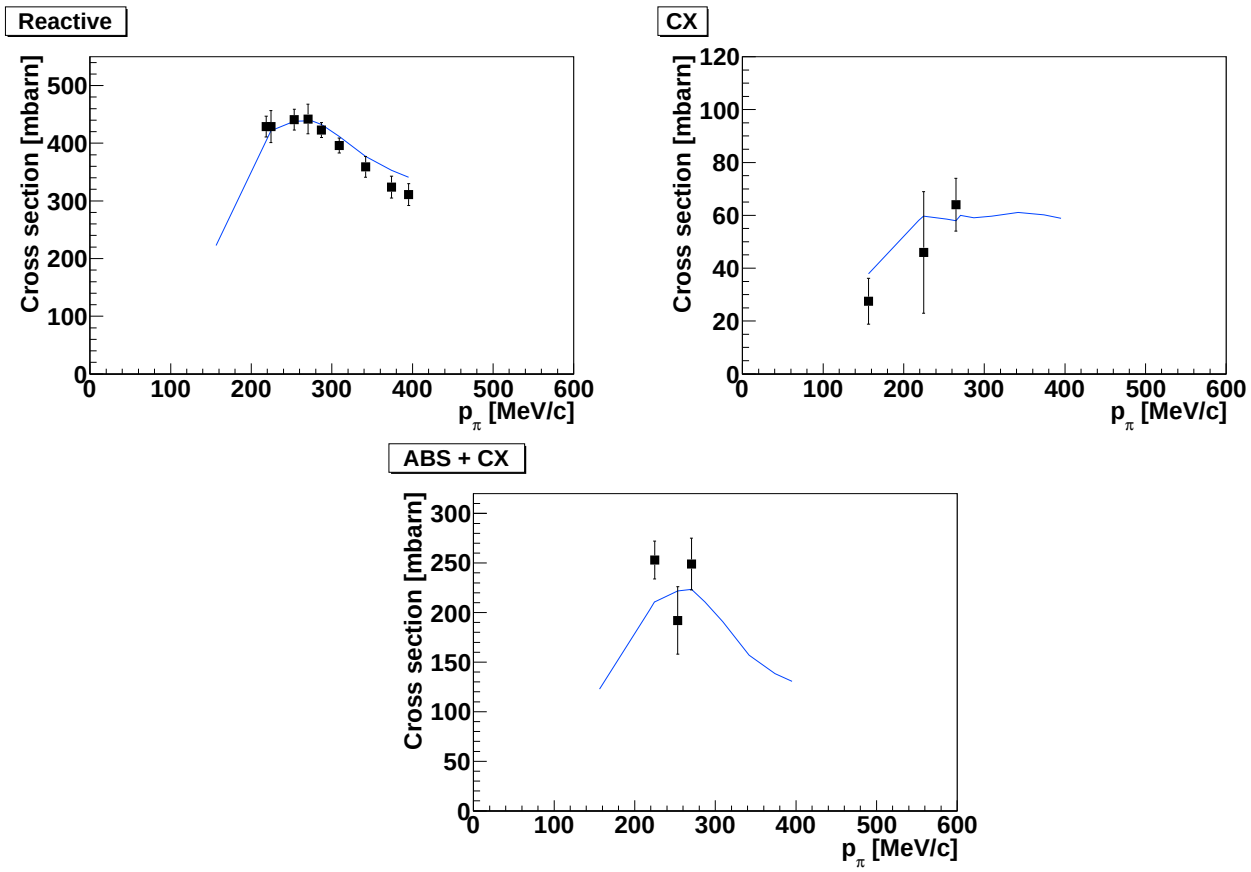

Figure 6.6: π^--^{12}C cross section for five different interaction channels, compared between NEUT nominal prediction (blue curves) and data points from past experiments.

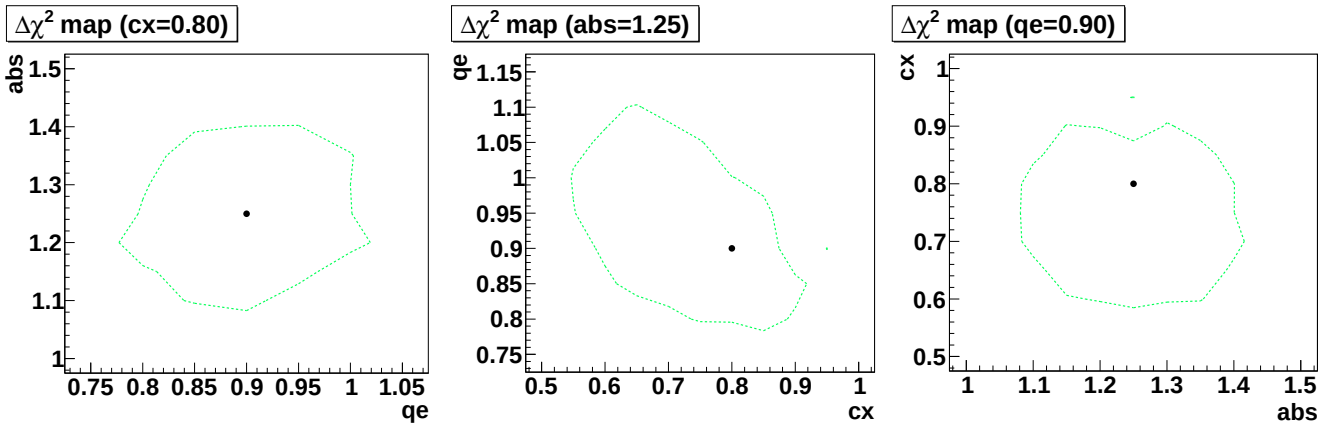

Figure 6.7: Best fit (black point) and 1 sigma allowed region (green line) of the NEUT scaling parameters.

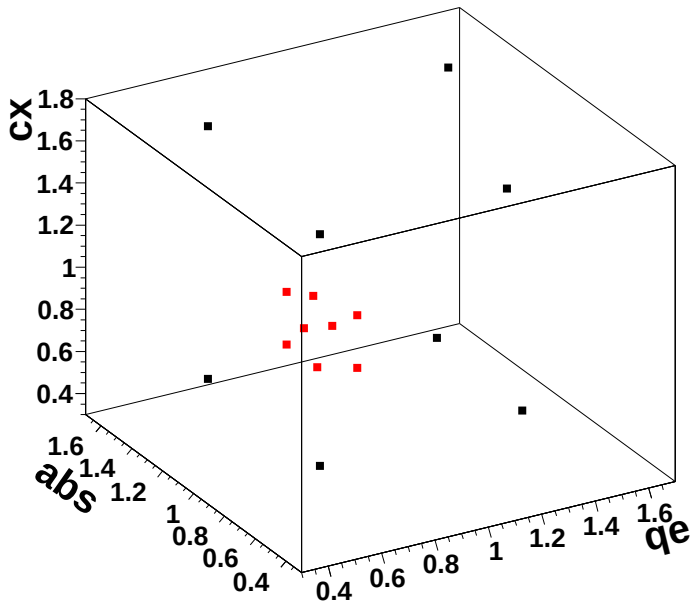

Figure 6.8: The 3D distribution of the eight parameter sets which represent 1σ deviation. The red (black) points shows the parameter sets derived in the new (old) tuning.

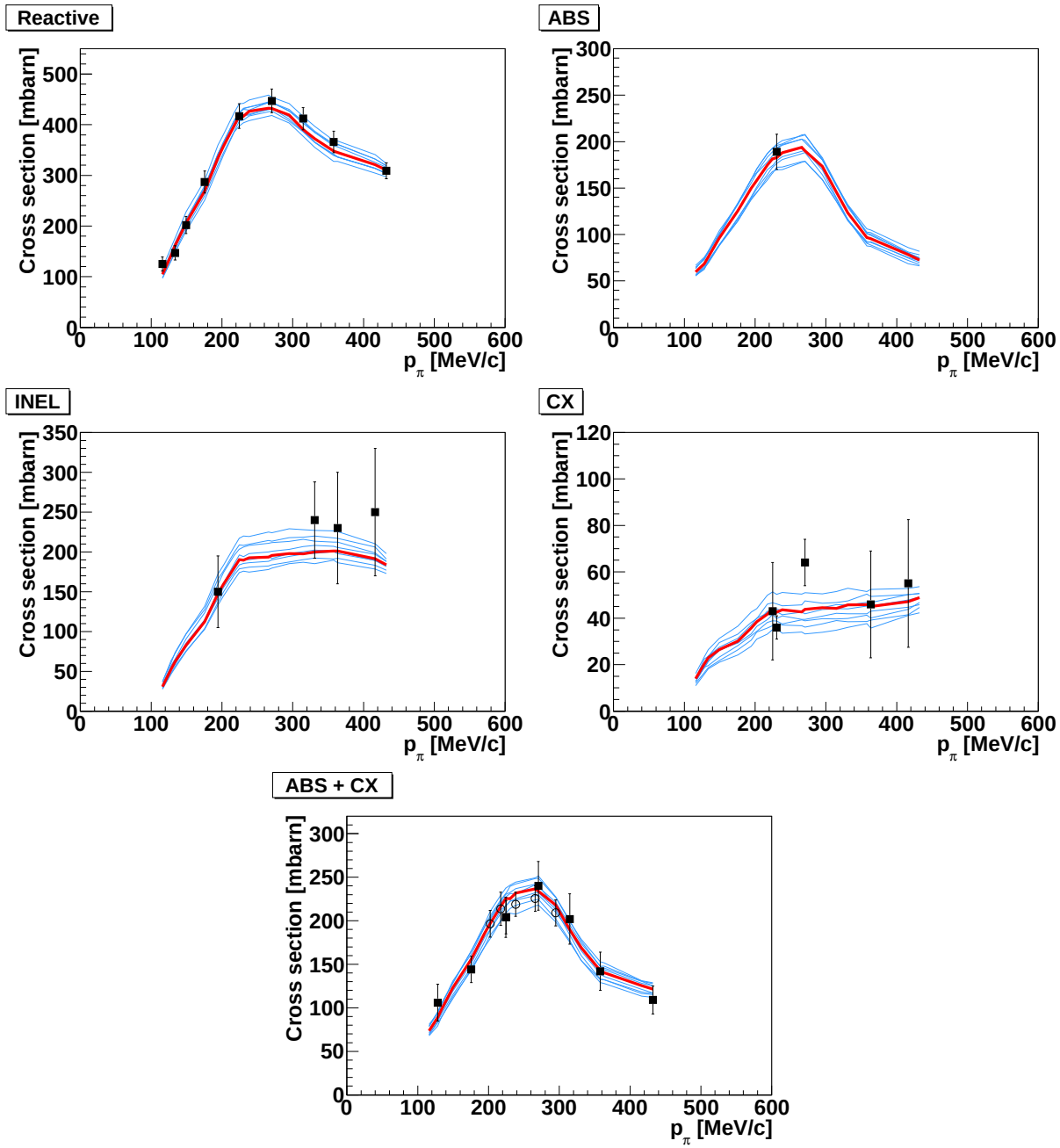

Figure 6.9: π^+-^{12}C cross section for five different interaction channels, compared between NEUT nominal prediction and data points from past experiments. The red lines represent the NEUT prediction with best fit parameters, and the blue lines represent the 1 sigma deviation. The white circle points in ABS + CX sample are the data points from our measurements.

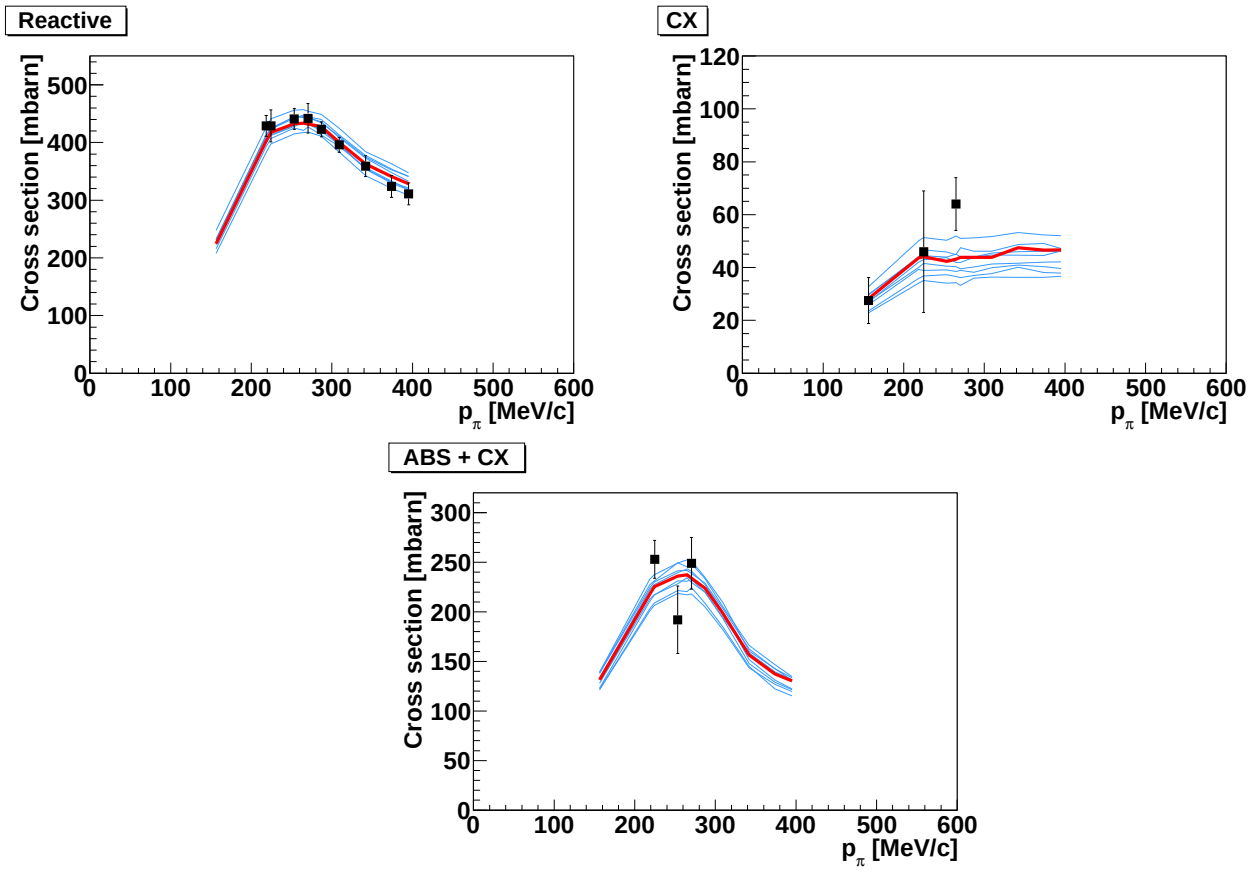

Figure 6.10: π^--^{12}C cross section for five different interaction channels, compared between NEUT nominal prediction and data points from past experiments. The red lines represent the NEUT prediction with best fit parameters, and the blue lines represent the 1 sigma deviation.

Part IV

Analysis of $\nu_\mu \to \nu_e$ oscillation

Chapter 7

Overview of the oscillation analysis

In this chapter, we describe the overview of the ν_e appearance analysis. Figure 7.1 illustrates the overview of the oscillation analysis. In the oscillation analysis, our goal is to measure the oscillation parameters by comparing the SK ν_e candidate events between data and MC prediction. Before the comparison, we apply constraints to the neutrino cross section uncertainties using external data sets. We apply further constraint to the flux and cross section using the ND280 data. Then we select ν_e candidate events at SK. Finally, we perform a fit to measure the oscillation parameters, by comparing the SK ν_e candidate events between data and MC prediction.

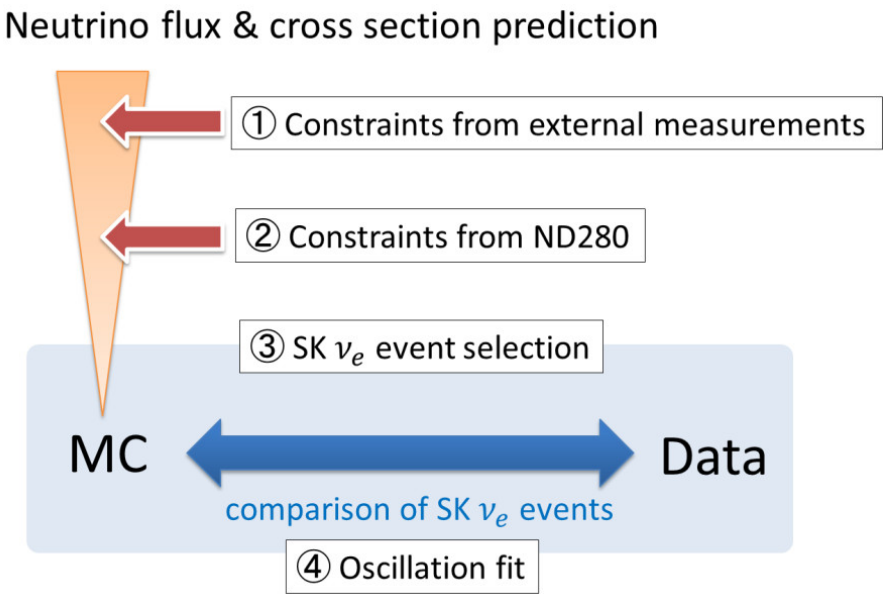

Figure 7.1: Illustration of the overview of the oscillation analysis.

The signal of the oscillation analysis is the CC interaction of ν_e which is oscillated from ν_μ. We select the events with one electron-like Cherenkov ring. The most significant background sources are 1) the CC interaction of the intrinsic ν_e contamination, and 2) the NCπ^0 interaction of the ν_μ beam. The intrinsic ν_e is the contamination of ν_e in the ν_μ beam. The fraction of ν_e in the ν_μ beam is less than 1%. The NCπ^0 events are the NC interaction with π^0 in the final state. The NCπ^0 event is misidentified as one electron event, when one of the two γ-rays from the π^0 decay is not reconstructed.

In the oscillation parameter fit, the number of ν_e candidate events and the reconstructed

momentum and angular distribution of the electron candidates (p_e, θ_e distribution) is compared between data and MC prediction. By changing the oscillation parameters in the MC, we search for the oscillation parameters which best reproduces the data. In this procedure, the systematic uncertainties of the neutrino beam flux, cross section, SK event selection efficiency and final state interaction (FSI) are implemented as the systematic parameters.

The uncertainty of the neutrino beam flux mainly comes from the uncertainty of pion and kaon production in the proton beam interaction with the hadron production target. They are constrained by the external hadron production data such as those from the NA61/SHINE experiment [106, 107]. The neutrino-nucleus interaction is simulated by NEUT, in which the model parameters and the uncertainties of the cross section parameters are derived primarily from the MiniBooNE experiment [108–111]. The neutrino beam flux parameters and neutrino-nucleon cross section parameters are further constrained by the measurements in the ND280 detector, as we explain in Chapter 9. Because the number of neutrino interaction events depends on the product of neutrino beam flux and cross section, the uncertainty of *flux* $\times$ *cross section* is largely reduced by the constraint from ND280.

The uncertainties related to the event selection efficiency at SK is constrained by using atmospheric neutrino data and cosmic ray data. This is described in Chapter 10. The FSI parameters are constrained by the external pion-nucleus cross section measurements, as mentioned in the previous chapter.

One of the main difference compared to the previous T2K ν_e appearance is the amount of data. In the previous analysis, we used the beam data collected until 2012 [29], which corresponded to 3.01×10^{20} POT. In the analysis described in this thesis, we use the data collected until May 2013, which corresponds to 6.57×10^{20} POT. There are also significant improvements in the neutrino-nucleus cross section uncertainty and SK event selection, which are described in Chapter 9 and 10.

Chapter 8

Monte Carlo simulation

The uncertainties in the prediction of neutrino beam flux and cross section are the main source of systematic errors in the neutrino oscillation measurement, as they directly affect the prediction of ν_e candidate events at SK. In this chapter, we describe the simulation of flux and neutrino interaction in Section 8.1 and 8.2, respectively.

8.1 Flux prediction with systematic uncertainties

The neutrino flux at ND280 and SK are predicted by simulations starting from the primary proton beam and its interaction on production target. Figure 8.1 shows an overview of the flux simulation. Each component of the simulation is described as follows.

Primary proton beam
The simulation starts from injecting the proton beam from the upstream of the graphite target. The beam parameters such as beam position and width are measured by the beam position and profile monitors (ESM, SSEM and OTR) which sits at the upstream of the beamline. Those parameters are used in the simulation to reproduce the actual beam.

Hadronic interactions in the target
The interaction of hadrons in the target is the most important part of the simulation, because the uncertainty in the hadron production process is the main source of the flux uncertainty. This part is simulated by using FLUKA 2008 [112], and the hadron interaction

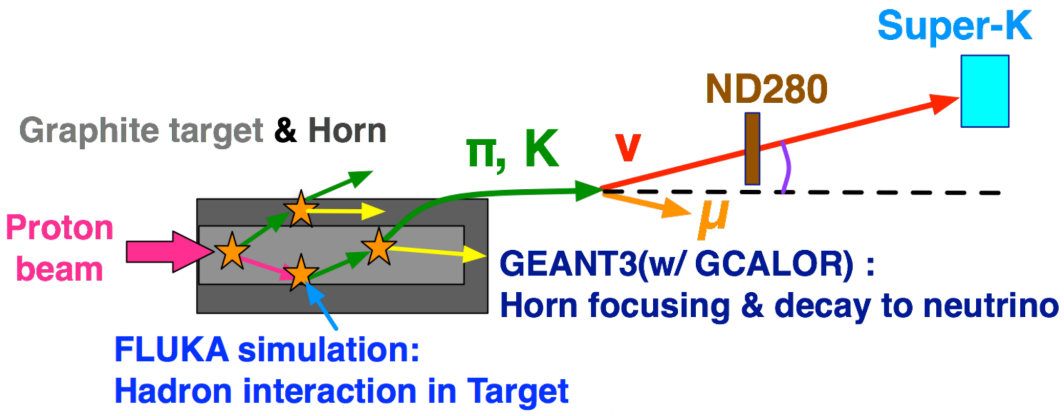

Figure 8.1: Overview of the neutrino beam flux simulation.

cross sections are tuned using the data from external cross section measurements. For the external data, we use the data sets from NA61/SHINE experiment [106, 107], Eichten et al. [113], Allaby et al. [114] and others.

Interactions outside the target

Information of the particles that exit the target is transferred to JNUBEAM, which is a simulation code based on GEANT3 [115]. The hadronic interactions in GEANT3 are simulated by GCALOR [116]. The propagation of pions and kaons in the magnetic field of horn, interaction with horn material and decay to neutrino in the decay volume are simulated in JNUBEAM.

Figure 8.2 shows the energy spectrum of the predicted neutrino flux at ND280 and SK. The energy spectrum is similar in ND280 and SK. About 93% of the flux is the ν_μ flux, and it is peaked around 0.6 GeV. The uncertainties of the ν_μ flux at ND280 and SK is shown in Figure 8.3. The total error is ∼15% near the peak of the flux energy spectrum, and it is dominated by the uncertainties on the NA61/SHINE data and the modeling of hadronic interactions. The detail of the flux prediction and the errors are described in Appendix B.1.

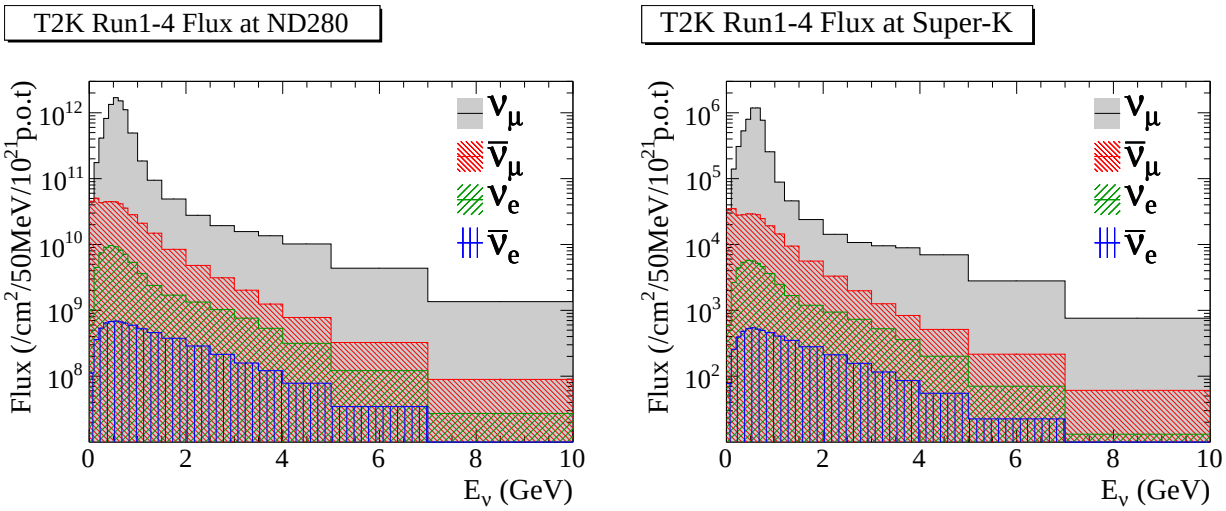

Figure 8.2: Predicted neutrino flux at ND280 (left) and SK (right).

There is a strong correlation between the predicted flux at ND280 and SK. Figure 8.4 shows the ND280/SK flux correlation matrix, which is produced by using the predicted flux and errors. This correlation matrix is used to constrain the SK flux by the measurement at ND280.

8.2 Neutrino interaction model and constraints

We use a simulation code called NEUT [69] to simulate the neutrino interaction with nucleus, as well as the interaction of secondary hadrons inside the nucleus which are generated in the neutrino interaction. The information of the particles generated in the neutrino interaction is then passed to the Geant4 simulation. The Geant4 simulation code is used for simulating the interaction of the particles inside the ND280 detectors, and the detector response. For the simulation in SK, the Geant3 simulation code is used instead of Geant4, together with NEUT.

In this section, we describe the neutrino interaction model used in NEUT and the parameters used in the model, and the constraint of the parameters from external measurements.

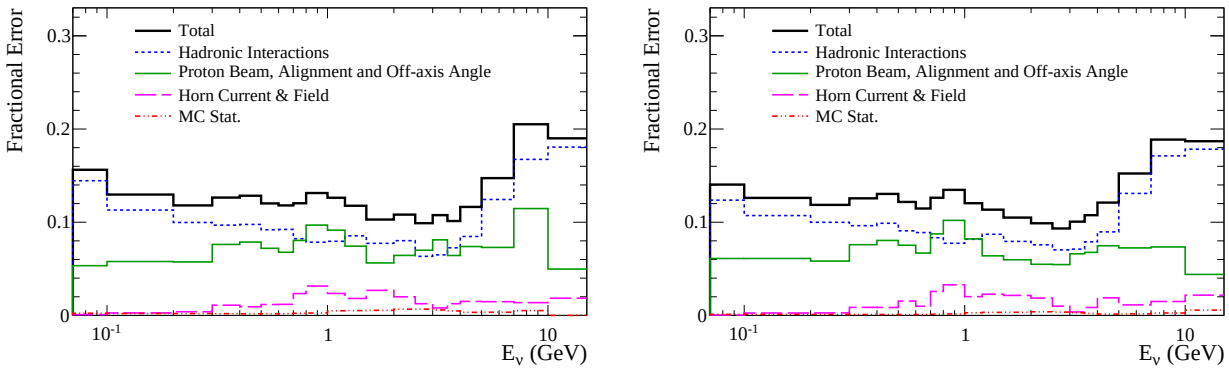

(a) ND280 flux error

(b) SK flux error

Figure 8.3: Fractional uncertainties of the ν_μ flux at ND280 (left) and SK (right).

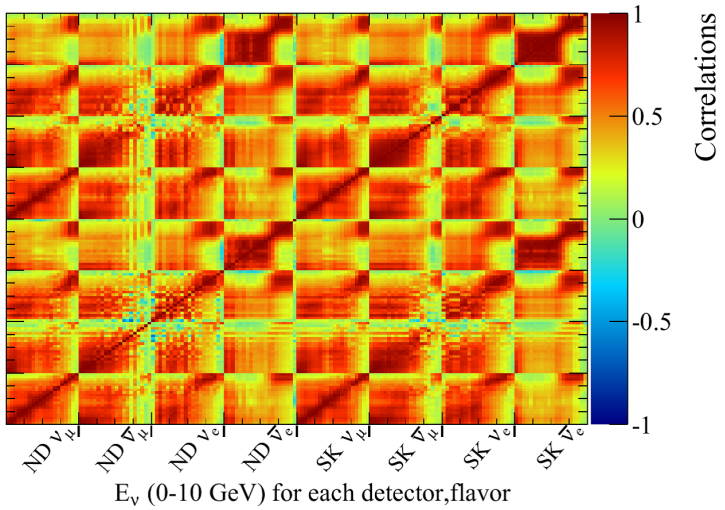

Figure 8.4: ND280/SK flux correlation matrix.

8.2.1 Neutrino interaction model

The NEUT simulation calculates the neutrino-nucleus cross section for different interaction modes. Figure 8.5 shows the neutrino-nucleus cross section per nucleon, as a function of neutrino energy.

Among all of the interaction modes, CCQE interaction ($\nu + N \rightarrow l + N'$, Fig. 8.6) is the most important one because ~40% of the neutrino interactions at ND280 and SK are the CCQE interaction, and we use this interaction mode as a signal. After applying the SK ν_e event selection, the fraction of CCQE events is 80% (assuming $\sin^2 2\theta_{13} = 0.1$).

The fraction of CC1π interaction ($\nu + N \rightarrow l + N' + \pi$, Fig. 8.7) is 16% after ν_e event selection. The CC1π interaction consists of resonant pion production and coherent pion production, and the cross section for coherent pion production is much smaller than that of resonant pion production.

NC (Neutral Current) interaction is not explicitly shown in Fig. 8.5, but it is also important. About 30% of the neutrino interactions at ND280 and SK are the NC interactions. The fraction of NC events is 4.5%, after ν_e event selection at SK. For example, for NC1π^0 events, gamma ray from the decay of π^0 may be identified as electron from ν_e CCQE interaction. The NC

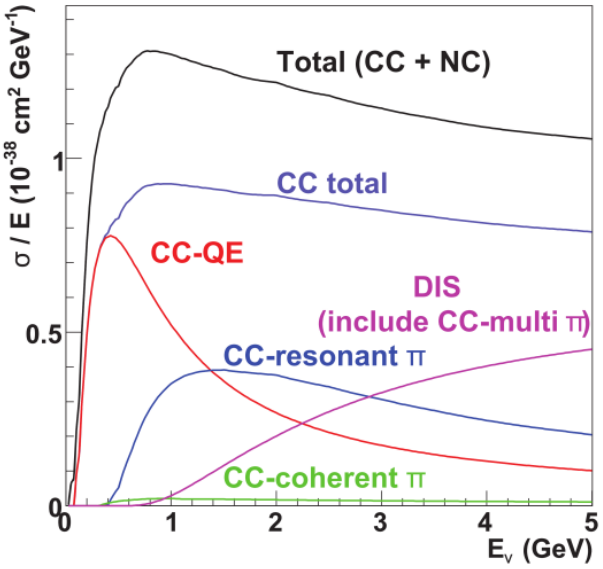

Figure 8.5: Neutrino-nucleus cross section per nucleon as a function of neutrino energy calculated by using NEUT.

background events can be generated from the muon neutrinos, so they are one of the main background in the ν_e appearance analysis.

In the following text, we describe the models for each interaction.

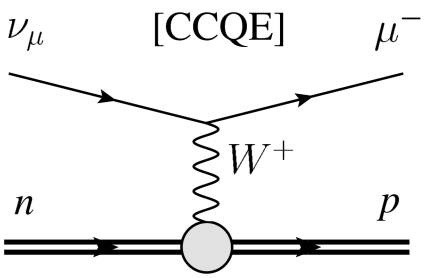

Figure 8.6: Feynman diagram for CCQE interaction.

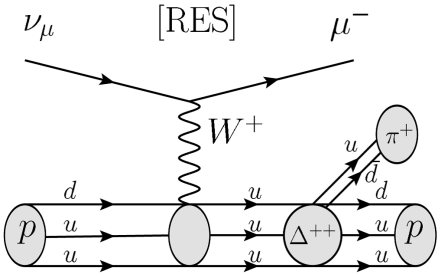

Figure 8.7: Feynman diagram for CC1π interaction via baryon resonance.

CCQE interaction

The CCQE cross section is calculated by using the model of Llewellyn-Smith [117]. The amplitude of this cross section is described by the product of lepton and hadron weak currents:

$$T = \frac{G_F}{\sqrt{2}} \overline{u}_l(k_2)\gamma^\mu(1-\gamma_5)u_\nu(k_1)\langle N'(p_2)|J_\mu^{\text{hadron}}|N(p_1)\rangle, \tag{8.1}$$

where G_F is the Fermi coupling constant, $p_1(p_2)$ is a initial (final) nucleon 4-momentum, and $k_1(k_2)$ is a initial (final) lepton 4-momentum, respectively. The hadronic weak current is expressed as follows:

$$\langle N'(p_2)|J_\mu^{\text{hadron}}|N(p_1)\rangle = \cos\theta_c \overline{u}_{N'}(p_2)\left[\gamma_\mu F_V^1(q^2) + \frac{i\sigma_{\mu\nu}q^\nu \xi F_V^2(q^2)}{M} + \gamma_\mu\gamma_5 F_A(q^2)\right] u_N(p_1), \tag{8.2}$$

where $q = k_1 - k_2$ is a 4-momentum transfer, M is a target nucleon mass, θ_c is Cabibbo angle, $\xi = \mu_p - \mu_n = 3.71$ is the difference of anomalous dipole moments between a proton and a neutron. F_V^1 and F_V^2 are the vector form factors, written in terms of electric and magnetic vector form factors G_E and G_M.

$$G_E(q^2) = \frac{1}{(1 + \frac{q^2}{M_V^2})^2}, \quad G_M(q^2) = \frac{1+\xi}{(1 + \frac{q^2}{M_V^2})^2}, \tag{8.3}$$

where $M_V = 0.84$ GeV/c^2 is a vector mass, experimentally determined from the electron scattering experiments. F_A is the axial vector form factor.

$$F_A(q^2) = \frac{g_A}{1 + \frac{q^2}{M_A}}, \tag{8.4}$$

where $g_A = -1.267$ is determined from neutron beta decay measurements. The M_A is an axial vector mass, which is set to 1.21 GeV/c^2 for the default MC setting. Both vector and axial-vector form factors are assumed to be dipole. The vector form factors are precisely measured by charged lepton scattering experiments, but the axial form factors are still uncertain because neutrino experiments that measure it do not agree themselves.

When the target is a free proton, the q^2 dependence of the cross section is directly calculated from Eq. 8.1. For other nuclei such as ^{16}O (for SK) and ^{12}C (for FGD in ND280 detector), Fermi motion of the nucleon and Pauli blocking effect is taken into account in the model. We assume relativistic Fermi gas model (RFG) with the Fermi surface $p_F = 225$ MeV/c for ^{16}O and 217 MeV/c for ^{12}C. The outgoing nucleon is required to have momentum above p_F, due to Pauli blocking effect. The nuclear potential (binding energy) is set to 27 MeV for ^{16}O and 25 MeV for ^{12}C.

CC1π and NC1π interaction (via baryon resonance)

A single meson production model in NEUT is based on Rein and Sehgal's theory [118]. This theory assumes an intermediate baryon resonance, N^*:

$$\nu + N \rightarrow l(\nu') + N^*, \tag{8.5}$$
$$N^* \rightarrow N'\pi, \tag{8.6}$$

where N^* is a baryon resonance, N and N' are nucleons, and l or ν' is outgoing charged lepton or neutrino. In the T2K neutrino energy range, resonance production is dominated by the $\Delta(1232)$ resonance. The amplitude of the resonant production for CC and NC interaction are given by:

$$T_{CC} = \frac{G_F \cos\theta_C}{\sqrt{2}} \left[\bar{l}\gamma^\mu(1-\gamma_5)\nu\right] \langle N^*|J_\mu|N\rangle, \tag{8.7}$$
$$T_{NC} = \frac{G_F}{\sqrt{2}} \left[\bar{\nu}\gamma^\mu(1-\gamma_5)\nu\right] \langle N^*|J_\mu|N\rangle, \tag{8.8}$$

where $\langle N^*|J_\mu|N\rangle$ is the weak current for this process. This factor is calculated by using FKR (Feynman-Kislinger-Ravndal) baryon model [119], which includes vector and dipole form factors with vector mass M_V and axial vector mass M_A.

Other interactions

The other interactions which is not described yet are CC1π and NC1π coherent pion productions, multi-pion production and DIS (Deep Inelastic Scattering: $\nu + N \rightarrow l(\nu) + N' + hadrons$). The

cross section of the coherent pion production is small, and multi-pion production and DIS cross sections are also small for the neutrino energy below 1 GeV.

In coherent pion production, a neutrino interacts with entire nucleus and produces a pion coherently without changing a nucleus. This interaction is simulated by using Rein and Sehgal's model [120,121], which is based on the Adler's PCAC formula (Partially Conserved Axial-Vector Current) [122].

The differential cross section for the multi-pion production and DIS are calculated as follows [123]:

$$\begin{aligned}
\frac{d^2\sigma}{dxdy} &= \frac{G_F^2 M E_\nu}{\pi}\left\{(1-y+\frac{y^2}{2}+C_1)F_2'(x,q^2) \pm (1-\frac{y}{2}+C_2)(xF_3'(x,q^2))\right\}, \qquad (8.9)\\
C_1 &= \frac{ym^2}{4ME_\nu x} - \frac{xyM}{2E_\nu} - \frac{m^2}{4E_\nu^2} - \frac{m^2}{2ME_\nu x},\\
C_2 &= -\frac{m^2}{4ME_\nu x},
\end{aligned}$$

where x, y are the Bjorken parameters, M and m are the target nucleon mass and the outgoing lepton mass, respectively. F_2 and xF_3 are the nuclear structure functions are taken from the GRV98 (Glueck-Rey-Vogt-1998) parton distribution functions [124], with corrections proposed by Bodek and Yang [125]. The multi-hadron final states are simulated with two different models, depending on the invariant mass of hadronic system, W. In the range of $1.3 < W < 2.0$ GeV/c^2, a custom made program [126] is employed. In the region of $W > 2$ GeV/c^2, PYTHIA/JETSET program [127] is used.

8.2.2 Cross section parameters

Table 8.1 summarizes the parameters used in the NEUT cross section model. Parameters such as M_A^{QE}, M_A^{RES} and Fermi momentum are directly related to the neutrino interaction model which have been discussed so far. Most of other parameters such as normalization parameters (norm) are the empirical parameters introduced to account for the uncertainty in current knowledge of the cross section which cannot be covered by the uncertainty in the physics parameters.

The uncertainties of these parameters affects the prediction of neutrino interaction at ND280 and SK. In Table 8.1, the parameters with check marks in "ND" and "SK" columns are relevant for ND280 or SK measurement. Some of the parameters are only relevant to ND280 or SK due to the difference in neutrino interaction target (CH for ND280 and H_2O for SK) and the difference in the event selection. The parameters with check marks in "ND/SK" column are strongly correlated between ND280 and SK, so they are constrained by the ND280 measurement. The others are not constrained by ND280, because the correlation is assumed to be weak.

The cross section parameters are defined as follows.

$\mathbf{M_A^{QE}}$, $\mathbf{M_A^{RES}}$
M_A^{QE} (M_A^{RES}) is the axial mass for axial vector form factors for CCQE interaction (CC1π and NC1π interaction via baryon resonance).

Normalization parameters
Normalization parameters changes the overall scaling of the cross section. The CCQE norm and CC1π norm parameters are defined separately for different energy regions, but the normalization in high energy regions are not relevant to SK because we require $E_\nu < 1.25$ GeV in the ν_e event selection (see Chapter 10). CC coh. norm and NC coh. norm are the normalization parameters for CC1π and NC1π coherent interactions. The normalization for CC other interaction defines the normalization of the combination of CC multiple

Table 8.1: Summary of the parameters used in the NEUT cross section model. The central values and errors are the values before ND280 fit which we describe in Chapter 9. Check marks are written in the "ND" and "SK" columns for the parameters used in ND280 fit and the SK ν_e oscillation analysis fit. Check marks are also written for the "ND/SK" column for the parameters correlated between ND280 and SK, that are constrained by ND280 measurement.

Parameter	Value	Error	ND	SK	ND/SK
CCQE interaction					
M_A^{QE}	1.21 GeV/c^2	0.45 GeV/c^2	✓	✓	✓
CCQE norm1 ($E_\nu < 1.5$ GeV)	1.0	0.11	✓	✓	✓
CCQE norm2 ($1.5< E_\nu < 3.5$ GeV)	1.0	0.30	✓		✓
CCQE norm3 ($E_\nu > 3.5$ GeV)	1.0	0.30	✓		✓
Fermi momentum p_F (^{12}C)	217 MeV/c	30 MeV/c	✓		
Fermi momentum p_F (^{16}O)	225 MeV/c	30 MeV/c		✓	
Spectral function	0 (off)	1 (on)	✓	✓	
CC1π, NC1π resonance interaction					
M_A^{RES}	1.41 GeV/c^2	0.22 GeV/c^2	✓	✓	✓
CC1π norm1 ($E_\nu < 2.5$ GeV)	1.15	0.32	✓	✓	✓
CC1π norm2 ($E_\nu > 2.5$ GeV)	1.0	0.40	✓		✓
NC1π^0 norm	0.96	0.33	✓	✓	✓
W-shape	87.7 MeV/c^2	45.3 MeV/c^2		✓	
π-less Δ decay	0.2	0.2	✓	✓	
Others					
CC coh. norm	1.0	1.0	✓	✓	
NC coh. norm	1.0	0.3	✓	✓	
CC other norm	0.0 GeV	0.4 GeV	✓	✓	
NC other norm	1.0	0.3	✓	✓	
$\sigma_{\nu_e}/\sigma_{\nu_\mu}$	1.0	0.03		✓	

pion production and DIS cross sections, while the NC other normalization includes NC resonant $\pi^\pm$ production, NC elastic and NC multi-pion/DIS. The normalization of CC other is defined as energy dependent parameter, as we describe in Appendix B.2.

Fermi momentum p_F, Spectral function (SF)

These parameters are related to the nuclear model. As described in the previous section, we use the RFG model with the Fermi momentum p_F to simulate the nuclear model. The value of p_F is determined from electron scattering data [128]. Spectral function (SF) is a more sophisticated model which is known as better representation of the nuclear model. The SF defines the probability distribution of nuclear momenta and energies required to remove a nucleon. SF is not implemented in NEUT yet, and the effect of using SF instead of RFG is estimated by using another neutrino interaction simulator called NuWro [129]. The error is assigned from the difference between RFG and SF.

W-shape

The W-shape is a parameter introduced to modify the shape of the pion momentum distribution in the NC1π^0 interaction, which shows poor agreement with the MiniBooNE data. This parameter represents the decay width of the resonant pion production, which is correlated with the pion momentum. The re-weighting function $r(W, \Gamma)$ is defined as

follows.

$$r(W,\Gamma) = \alpha \cdot \frac{\Gamma}{(W - M_{N^*})^2 + \Gamma^2/4} \cdot P(W; m_\pi, m_N), \tag{8.10}$$

where α is a normalization factor to make the total cross section unchanged as Γ varied, $P(W; m_\pi, m_N)$ is the phase space for two body decay of a particle with mass W into particles with masses m_π and m_N. The default value of Γ and M_{N^*} are determined from the W distribution for $n + \pi^+$ and $p + \pi^0$ in NEUT. The error for this parameter is defined from the difference between the nominal value and the best fit values to the MiniBooNE NC1π^0 data [111].

π-less Δ decay

In the resonant pion production process, the baryon resonance, mainly Δ, can interact with other nucleons and disappear without pion emissions, resulting in a CCQE-like event.

$$N^* + N \to N' + N'',$$

where N^* is baryon resonance, N, N', N'' are nucleons. Probability of this interaction is estimated to be 20% from a theoretical calculation [130]. This process is currently implemented in NEUT independently of energy and target, and an absolute error of 20% is assigned.

$\sigma_{\nu_e}/\sigma_{\nu_\mu}$

This parameter represents the uncertainty in the difference in the cross section of charged current neutrino-nucleon interaction for ν_e and ν_μ. An overall 3% uncertainty is assigned based on calculations [131] over T2K's energy range.

The central values and the errors for M_A^{QE}, M_A^{RES}, W-shape and the normalization parameters are determined using the external data sets, primary from MiniBooNE experiment [108–111]. This is described in Appendix B.2 in more detail.

Chapter 9

Near detector measurement

This chapter describes the measurements at the ND280 detector. The flux and cross section uncertainties described in the previous chapter are further constrained by the measurements at the ND280 detector. The parameters constrained by the measurements are used for predicting SK ν_e candidate events.

9.1 Event reconstruction

Before explaining the event selection, we describe the event reconstruction procedure which is relevant to the event selection. The neutrino interaction types such as CCQE and CC1π are identified from the existence of pions. In the ND280 event selection, we use the following objects to find the pions: TPC tracks, FGD tracks and FGD delayed hits.

TPC tracks

Charged particles crossing TPCs ionize the gas. The charge deposit of the ionized electrons are read out by the pads of the Micromegas detectors. The charge waveforms which are consecutive in space and overlapped in time are grouped together into vertical or horizontal clusters. The TPC tracks are formed from the clusters, using a pattern recognition based on the cellular automaton algorithm (which is the algorithm used for K2K SciBar detector and T2K INGRID detector).

The time that track is created, T_0 is determined from the adjacent scintillator detectors such as FGD, ECAL and P0D, or from the tracks crossing the central cathode. Then the track x position (x is a direction of electric field) is determined from the drifting time with T_0.

Once the track is reconstructed, the transverse momentum p_t (a momentum in the direction perpendicular to the magnetic field) of the particle is calculated from the curvature (sagitta) of the track: $p_t = 0.3BR$, where B is the magnetic field in Tesla, R is the radius of the curvature in meter. Then the total momentum p is calculated as $p = p_t / \sin\phi$, where ϕ is the angle between the track and the direction of the magnetic field. The sign of the charge of the particle is also determined from the curvature.

Particle identification in TPC uses the energy loss measured from the charge deposit and the momentum. Figure 9.1 shows the energy loss vs. momentum of the particle tracks in TPC. The "probability of the particle type" is calculated from the pull criteria. The pull for particle type α is defined as follows.

$$pull(\alpha) = \frac{\left(\frac{dE}{dx}\right)_{\rm meas} - \left(\frac{dE}{dx}\right)_{\rm MC}(\alpha)}{\sigma(\alpha)} \tag{9.1}$$

where $(dE/dx)_{\text{meas}}$ is the measured energy loss, $(dE/dx)_{\text{MC}}$ is the expected energy loss as a function of momentum for given particle α, σ is the total width including the variance and the uncertainty in the measurement. Then the "probability of the particle type" $\mathcal{L}_\alpha$ is defined as follows:

$$\mathcal{L}_\alpha = \frac{e^{-pull(\alpha)^2}}{\sum_i e^{-pull(i)^2}}, \tag{9.2}$$

where i corresponds to electrons, pions, muons and protons. As we explain in the next section, we use the pion, electron and positron tracks to distinguish the event categories. Figure 9.2 shows the momentum distribution of the reconstructed tracks in TPC using the pion, electron and positron probability criteria, in the CC sample.

The TPC tracks are extrapolated to the hits in FGD, as we described in Chapter 3. For the TPC tracks that we use in the event selection, we require that the track starting position to be inside FGD1 fiducial volume (FV) described in the next section.

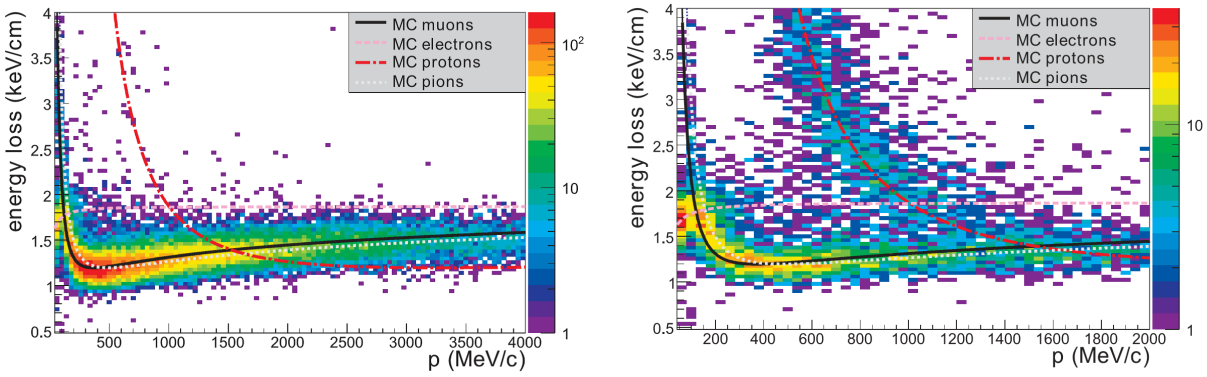

Figure 9.1: Energy loss vs. momentum for the particle tracks in TPC, for negatively charged particles (left) and positively charged particles (right). The lines represents the prediction by MC [57].

FGD tracks

The tracks in FGD are reconstructed from the pattern of the hits on scintillator bars, as already explained in Chapter 3. Particle identification in FGD is performed by using a pull defined as in the same way as the pull of TPC tracks, but the expected dE/dx is defined as a function of particle range (track length), not momentum.

For this analysis, we use the FGD track PID only when there is one fully contained track in FGD and no FGD delayed hits is found. This is done in order to eliminate the possibility of having broken tracks that can be reconstructed as two pions when there is only one. Also, the cosine of the track angle must be $|\cos\theta| > 0.3$, to be consistent with systematic error studies. Figure 9.3 left plot shows the pion pull distribution of the tracks that are fully contained in FGD. For selecting pions, we require $-2 < pull < 2.5$.

FGD delayed hits

The pions are also identified by using the delayed hits in FGD, which corresponds to the electron signal in $\pi \to \mu \to e$ decay chain (Michel electrons). For the delayed signal, we require that the timing of the hits are at least 100 nsec after the initial neutrino interaction, not within the beam bunch. The total charge deposit of the delayed hits must be greater than 200 p.e. (Fig. 9.4).

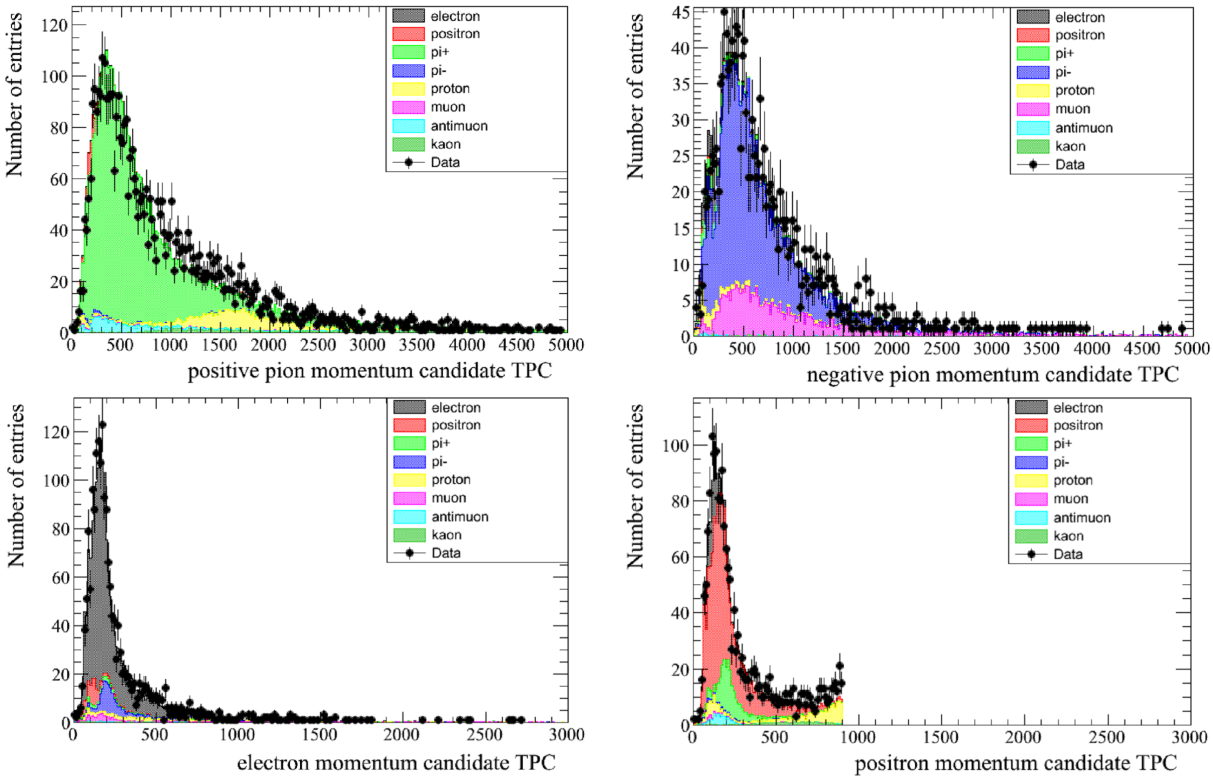

Figure 9.2: Distribution of the momentum of positive pions (left top), negative pions (right top), electrons (left bottom) and positrons (right bottom) reconstructed in TPC using the TPC probability criteria, in the CC sample. The color of the histograms represents the types of particles.

9.2 Event selection

In this section, we describe the cuts to select CC events. The event selection starts from selecting inclusive CC sample, and then we divide the samples in three sub-samples. The CC-inclusive selection cuts are defined as follows.

1. Data quality flag
   We require that the whole ND280 off-axis detector is working properly.

2. Time bunching
   The tracks are grouped together according to their times. Tracks are associated within a bunch if their timing from the mean bunch time is less than 60 nsec.

3. Negatively charged track from FGD1
   At least one negatively charged FGD1-TPC track must exist, which start in FGD1 FV. The FGD1 FV is defined as the inner part of FGD, which excludes five scintillator bars at the end of each layers in X, Y direction, and the most upstream scintillator plane (X+Y) in Z direction. The TPC track must contain at least 18 clusters to ensure the reliability of momentum reconstruction and particle identification (this is called "TPC quality cut").
   If there is more than one negatively charged track, we select the highest momentum track as the muon candidate.

4. Upstream veto
   In order to remove the events with tracks which is generated in the upstream of FGD1 and

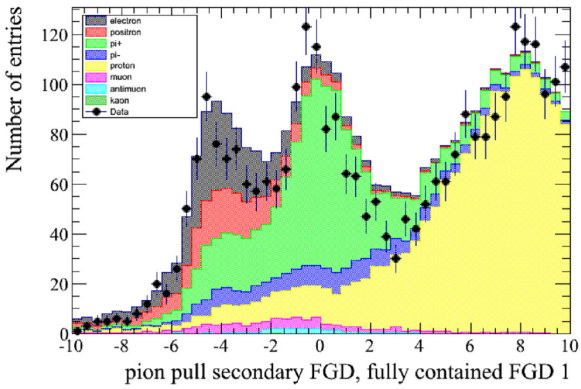

Figure 9.3: Pion pull distribution for the FGD fully contained tracks, before applying the PID cut. The color of the histograms represents the types of particles.

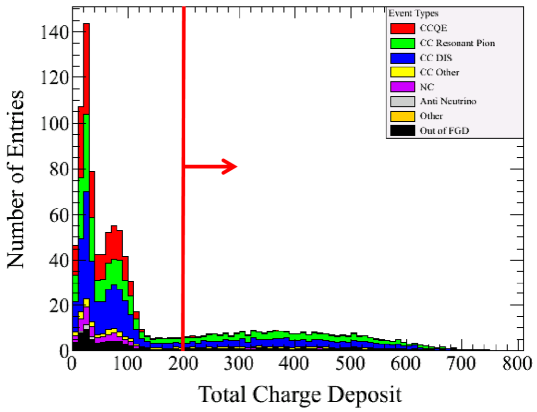

Figure 9.4: Distribution of the total charge in a delayed time hits. The color of the histograms represents the neutrino interaction modes.

entering to FGD1, we reject the events if there is a track other than the muon candidate track which starts from more than 150 mm upstream of the muon candidate starting position.

5. TPC track PID
   For the muon candidate track, we require two cuts depending on the momentum p
   $$(\mathcal{L}_\mu + \mathcal{L}_\pi)/(1 - \mathcal{L}_p) < 0.8 \qquad (p < 500 \text{ MeV/c}),$$
   $$\mathcal{L}_\mu > 0.05 \qquad (p > 500 \text{ MeV/c})$$
   The first cut is optimized to reject electrons, and the second cut removes protons and pions.

The CC sample is divided to three sub-samples, depending on the existence of pions in the final state. We use the TPC tracks, FGD tracks and FGD delayed hits to distinguish the event categories.

- CC0π sample (Fig. 9.5 (a))
  For this sample, we require no π in the final state. We require no pion tracks in TPC or FGD, and no delayed hits in FGD. Electrons and positrons are generated in CC1π^0 or NC1π^0 interaction from γ-rays from π^0 decay, so we also reject events with electron tracks in TPC. Majority of the events in this category are CCQE events, but the events also includes CC1π events with pion absorbed in the final state interaction.

- CC1π^+ sample (Fig. 9.5 (b))
  This is a CC interaction with one π^+ in the final state. (Note that pions in the neutrino CC1π interaction are always π^+ or π^0, not π^-). For this sample, we require one π^+ track other than the muon candidate track. When there are FGD delayed hits, we require no π^+ track in TPC. Otherwise, we require one π track in FGD or one π^+ track in TPC. In order to reject π^0 and π^-, we require no e^-, e^+ or π^- track in TPC.

- CCother sample (Fig. 9.5 (c))
  Rest of the CC interactions which was not included in the previous two samples.

Figure 9.6 shows the momentum distribution of the muon candidate tracks for CC-inclusive samples and three sub-samples. In the MC histograms, "BKG" denotes background events, which consists of neutral current interactions and anti-neutrino interactions. The "External"

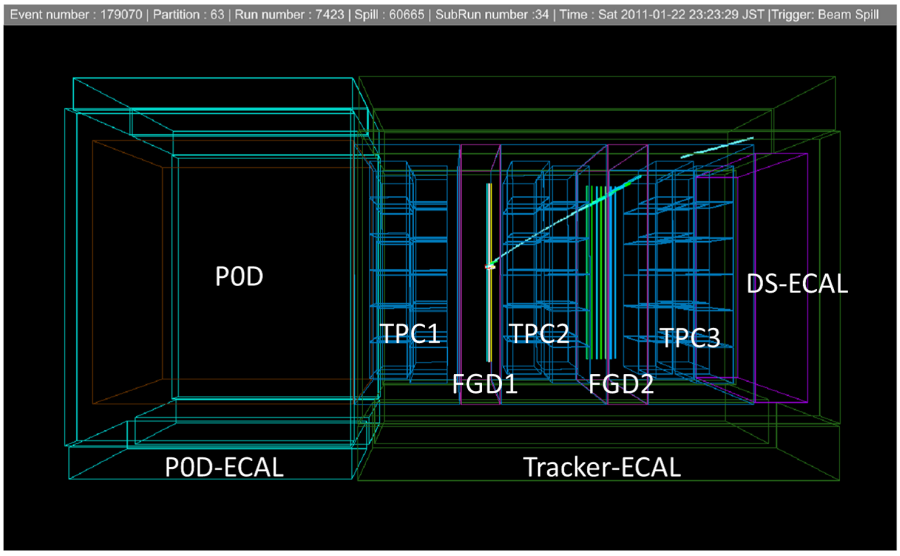

(a) CC0π.

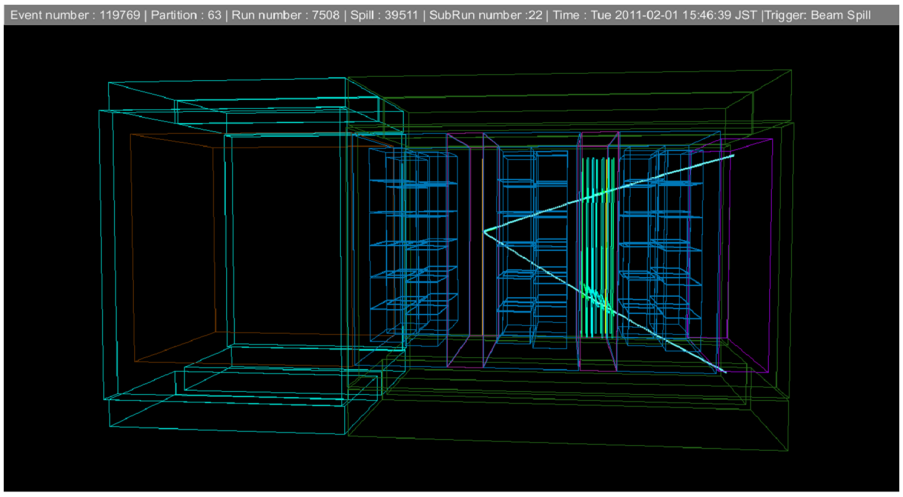

(b) CC1π^+.

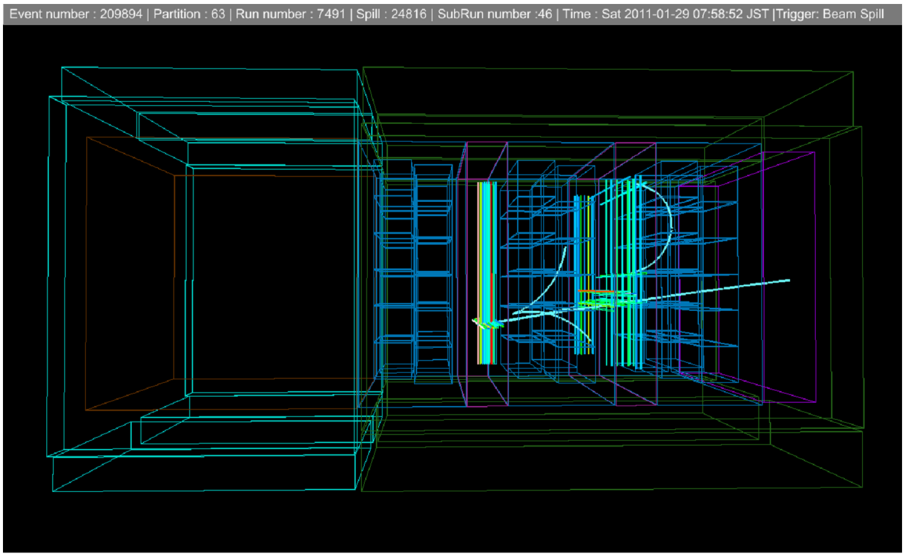

(c) CC other.

Figure 9.5: Example of selected events in three event topologies.

denotes the interaction which happened outside of FGD1, or inside of FGD1 but outside of the FV. Table 9.1 and 9.2 summarizes the composition of the events and the efficiency in three sub-samples, respectively. The efficiency is defined as the number of events in the given sample, where the true category matches the selected category, over the number of events generated in the FGD1 FV with true category corresponding to the category of the selected sample.

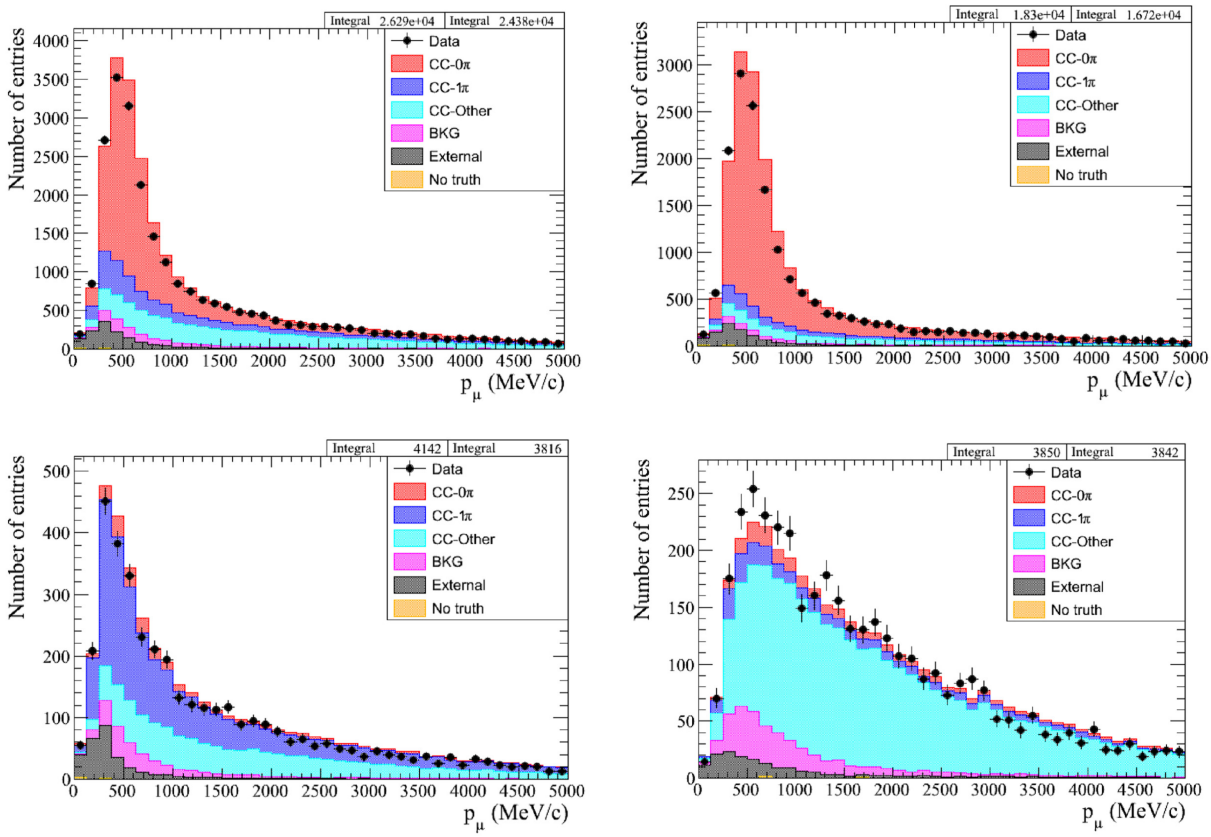

Figure 9.6: Momentum distribution of the muon candidate tracks in CC-inclusive sample (left top), CC0π sample (right top), CC1π sample (left bottom) and CC other sample (right bottom).

Table 9.1: Composition of the three sub-samples.

	CC0π sample	CC1π sample	CC other sample
CC0π	72.4%	6.4%	5.8%
CC1π	8.6%	49.2%	7.8%
CC other	11.5%	31.0%	73.6%
BKG	2.3%	6.8%	8.7%
External	5.2%	6.6%	4.1%

While we use three sub-samples in this analysis, there were only two sub-samples in the 2012 ν_e appearance analysis: "CCQE" and "CC-nonQE". The latter one included all of the CC interactions which were not CCQE. It is found that, with this categorization, it is not possible to further improve the flux and cross section constraints, even if we collect more data. Therefore, in this analysis, we changed the event categorization to have three sub-samples. By having an separate CC1π^+ sample, it is possible to improve the determination of M_A^{RES} parameter.

Table 9.2: Efficiency per each sample.

Sample	Efficiency
CC0π	47.81%
CC1π	28.37%
CC other	29.71%

9.3 Systematic uncertainties

There are many sources of the detector systematic errors that affects this measurement. Figure 9.7 shows momentum distributions for three sub-samples together with the total systematic errors represented as red bands. Table 9.3 shows the list of the systematic error sources and the largest relative error in all momentum bins in all categories. The dominant contributions to overall systematic errors are explained as follows:

- Backgrounds from outside of FV
  This is a systematic error due to neutrino interaction happened outside of the FGD1 FV but miss-reconstructed as the event generated inside the FGD1 FV. This background is caused by several different physics processes. For example, i) high energy neutrons generates π^- in FGD, which is misidentified as muon, ii) backward-going π^+ which come from ECAL in the downstream and misidentified as forward-going μ^-, iii) through going muons passing completely through FGD, but the reconstructed track is broken up in such a way that it looks like the track started in FGD. For each type of physics process, the systematic errors are assigned separately.
  In the estimation of the systematic errors, we assign 20% uncertainty for the cross section of the interaction happened outside FGD and TPC, which comes from the data/MC comparison in the neutrino interaction event rates measured in P0D, ECAL and SMRD. The uncertainty of the track reconstruction failure is estimated by comparing the data with MC in the cosmic-ray muon data, and in the control sample which selects muons from the neutrino interaction at the upstream of FGD. The error in p and cosθ bins are <10% in p bins and <22% in cosθ bins.

- Pion secondary interaction
  As described in Chapter 4 to 6, the uncertainty in pion interactions, such as absorption, charge exchange and inelastic scattering affects the neutrino interaction measurement. The uncertainty of the final state interaction (FSI, interaction of hadrons before it escape the nucleus) is taken into account in the fit to constrain the flux and cross section parameters that we describe in the next Section 9.4. The uncertainty we consider here is the uncertainty of the secondary interaction (SI, the interactions which happen after escaping the nucleus). For the near detector, the initial neutrino interaction and FSI is simulated by NEUT, while the interactions of the secondary particles inside the detector is simulated by Geant4. We adjusted the default Geant4 pion-nucleus cross section to agree with the data sets from the past experiments (the results of our measurements are not used yet), and the systematic uncertainty is set to the error on the data. The largest error is 8% in both p bins and cosθ bins.

- TPC momentum resolution
  The TPC momentum resolution is measured in data and MC, by comparing the reconstructed momentum between different TPCs for the muon tracks which pass through multiple TPCs. The momentum resolution in data is found to be worse than MC, due to

imperfect modeling of the detector alignment. We have smeared the reconstructed momentum of the MC tracks in TPC by 34% to match the data resolution, and the uncertainty of the correction (10%) is used to set the systematic uncertainty. The largest error is 5% in both p bins and cosθ bins.

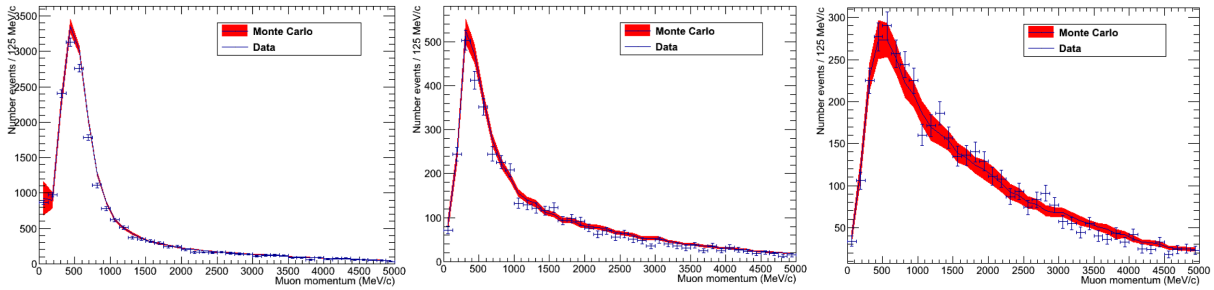

Figure 9.7: Muon momentum distribution for CC0π sample (left), CC1π^+ sample (middle) and CC other sample (right), with error band (red) representing the systematic errors.

Table 9.3: Summary of the systematic errors. The errors in this table are the largest relative error in all bins in all categories.

Systematic error source	Error on p bins (%)	Error on cosθ bins (%)
Magnetic field distortion	0.3	0.3
TPC tracking efficiency	0.6	0.2
TPC-FGD track matching efficiency	1	1.8
TPC charge miss-identification	2.2	5.0
TPC momentum scale	2	2
TPC momentum resolution	5	5
TPC quality cut	0.7	0.7
FGD delayed hits efficiency	0.7	0.7
FGD mass	0.65	0.65
Out of FV background	10	22
Event pile-up	0.07	0.07
Muons from ν_μ int. in the upstream of ND280	0.02	0.02
TPC PID	3.5	9.0
FGD PID	0.3	0.3
FGD tracking efficiency	1.4	1.4
Pion secondary interaction	8	8

9.4 Constraining the neutrino flux and cross section

Because the CC interaction rates at ND280 depends on the neutrino beam flux and cross sections, the uncertainty of the flux $\times$ cross section can be constrained by the ND280 measurement. We fit the muon momentum and angular distribution measured in three categories to derive the constraint on the beam flux and cross section parameters. The detail of the fit method is described in Appendix C. Figure 9.8 shows the muon momentum and cosθ distribution for data, compared with both original predictions and the predictions based on the fit result. All the samples shows better agreement between data and MC after the fit.

The p-value of the fit is checked by fitting many toy MC experiments and comparing the $\Delta\chi^2$ of the fit between data and many toy MCs. The $\Delta\chi^2$ for data was 564.9. Comparing this value with the $\Delta\chi^2$ distribution for toy MC experiments, the p-value is evaluated to be 0.66.

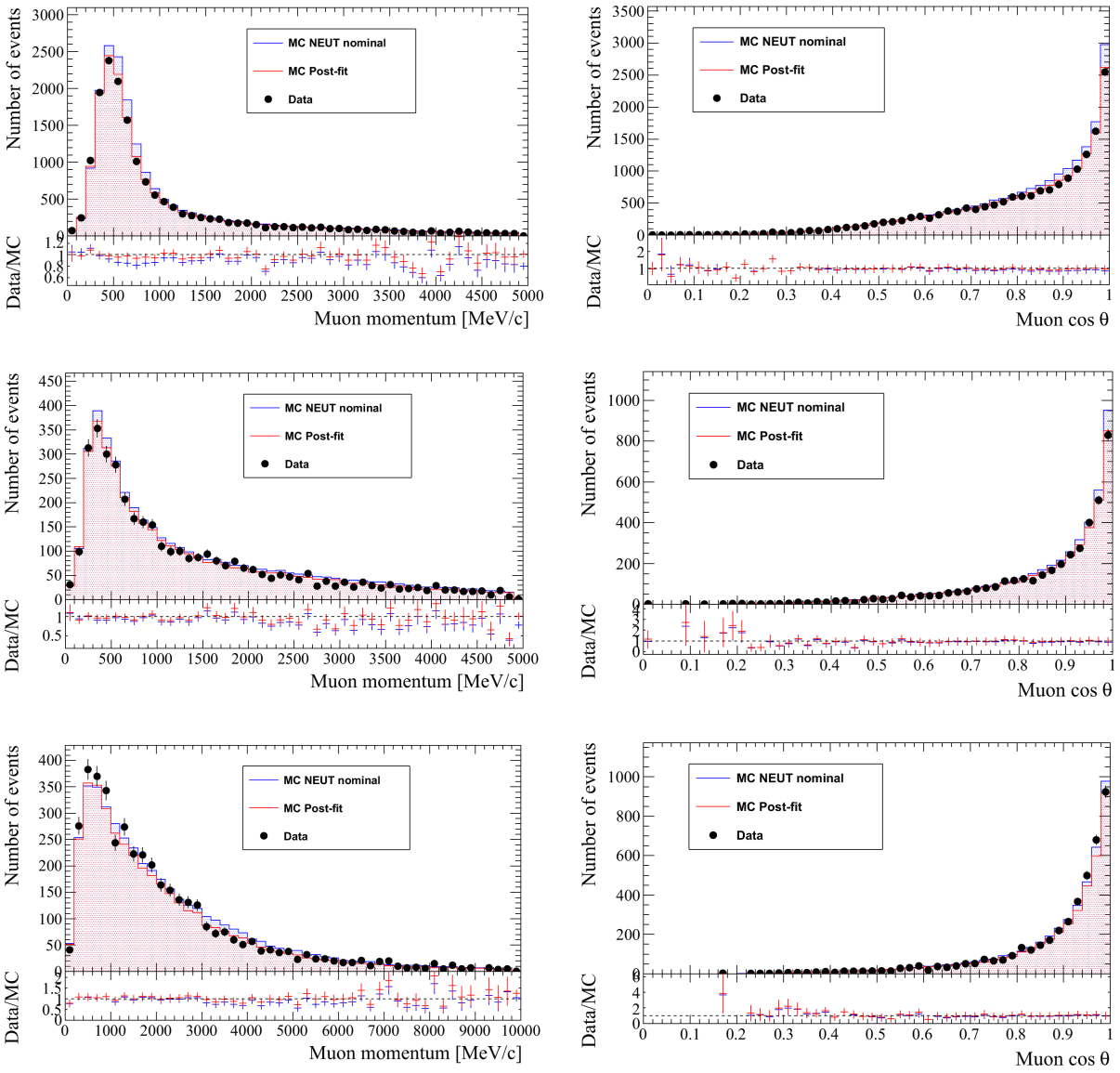

Figure 9.8: Muon momentum and $\cos\theta$ distribution for data compared with MC, for CC0π sample (top), CC1π sample (middle) and CC-Other sample (bottom). The blue and red histograms shows the MC distributions before and after data constraint, respectively.

Table 9.4 summarizes the cross section parameters before and after the fit. The uncertainties of the parameters are significantly reduced after the fit. The NC events are not selected in the event selection, but the NC1π^0 norm parameter is also constrained by the ND280 fit due to the correlation between the cross section parameters related to CC1π and NC1π interactions. Figure 9.9 shows the ν_μ and ν_e flux parameters before and after the fit. The uncertainty of the parameters, represented by red and blue bands, are much smaller after the fit.

Figure 9.10 shows the correlations between flux and cross section parameters, before and after ND280 fit. After the fit, there is an anti-correlations between the flux parameters and the cross section parameters. Therefore, the flux times cross section uncertainty is much reduced

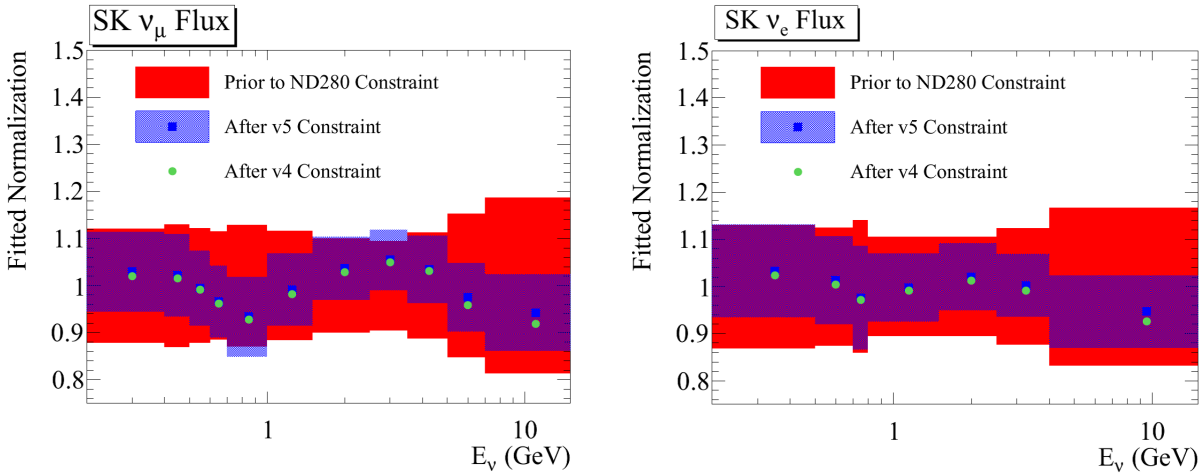

Figure 9.9: SK ν_μ (left) and ν_e (right) flux parameters, before and after the fit. The red and blue bands represents the uncertainty of the parameters before and after the fit.

Table 9.4: Summary of the cross section parameter values before and after the fit.

	before ND280 fit		after ND280 fit	
Source	value	error	value	error
M_A^{QE}	1.21 GeV/c^2	0.45 GeV/c^2	1.24 GeV/c^2	0.072 GeV/c^2
M_A^{RES}	1.41 GeV/c^2	0.22 GeV/c^2	0.96 GeV/c^2	0.068 GeV/c^2
CCQE norm. ($E_\nu < 1.5$ GeV)	1	0.11	0.97	0.076
CC1π norm. ($E_\nu < 2.5$ GeV)	1.15	0.32	1.26	0.16
NC1π^0 norm.	0.96	0.33	1.14	0.25

after the fit, as we see in Chapter 11. The improvement compared to the 2012 ν_e oscillation analysis is also described in Chapter 11.

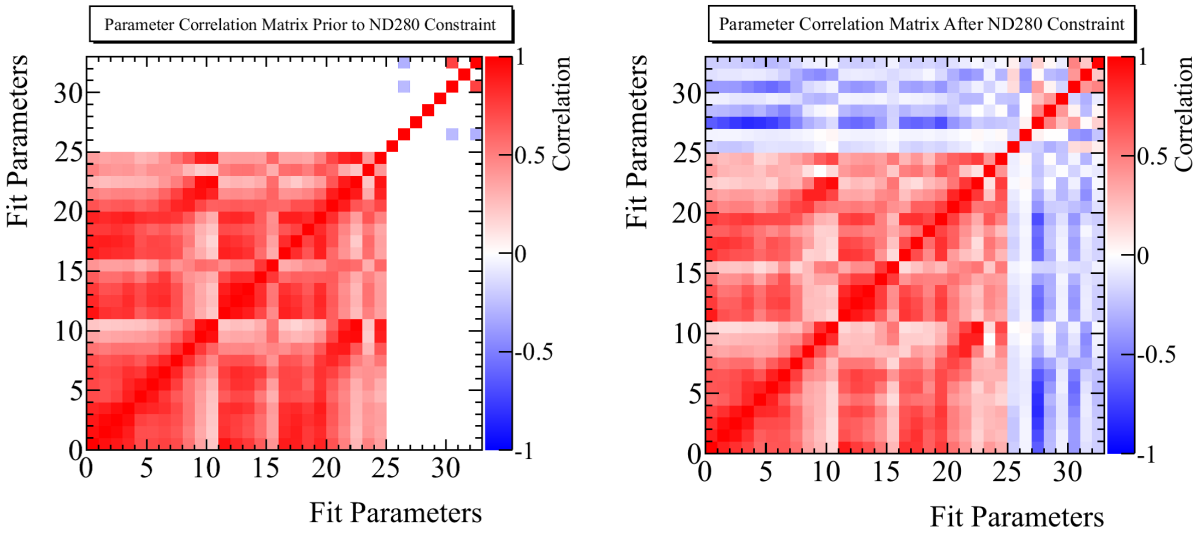

Figure 9.10: The parameter correlations prior to (left) and after (right) ND280 fit. The parameters are 0-24 SK flux parameters, 25 M_A^{QE}, 26 M_A^{RES}, 27-29 CCQE normalization, 30-31 CC1π normalization, 32 NC1π^0 normalization.

Chapter 10

Far detector measurement

In this chapter, we describe the ν_e event selection at SK and the systematic uncertainties in the event selection.

10.1 ν_e event selection

To detect the oscillated ν_e, we select SK events with a single electron-like Cherenkov ring which provides the CCQE ν_e enriched sample. The main backgrounds are the ν_μ NC interactions and intrinsic ν_e contamination in the beam. Figure 10.1 shows the example of the event displays for the SK simulation of ν_e CCQE, ν_μ CCQE and ν_μ NC1π^0 interactions. The electron ring can be distinguished from the muon ring with the diffuse pattern of ring shape due to the multiple scatterings and electromagnetic showers. The γ-rays from the π^0 decay in the NC1π^0 events can be misidentified as a single electron ring, when one of the two rings is not reconstructed properly.

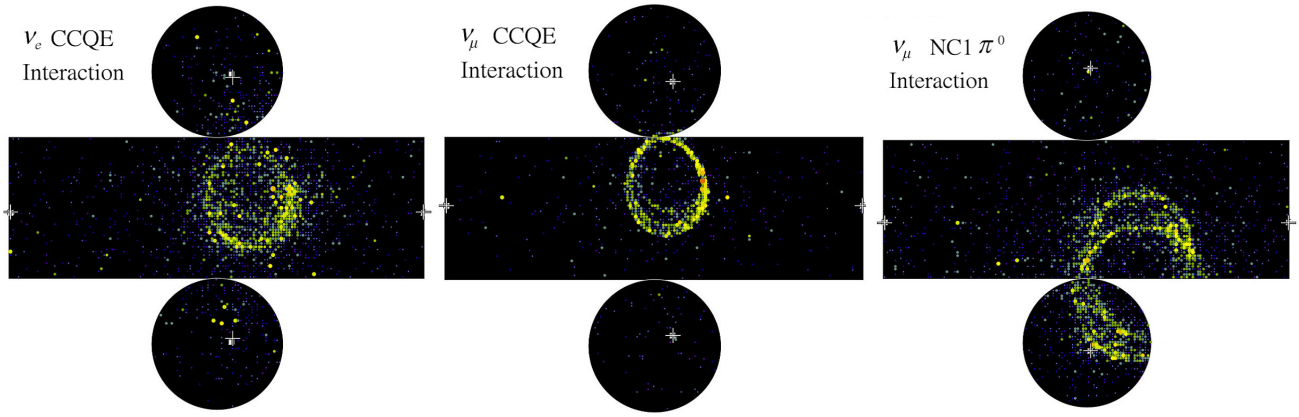

Figure 10.1: Event displays for the SK simulation of ν_e CCQE event (left), ν_μ, ν_μ CC event (middle) and NC1π^0 event (right).

Compared to the ν_e appearance analysis in 2012, the reconstruction program to identify the π^0 background is improved. The cuts that we apply to select ν_e candidate events are listed below.

1. Fully contained events in fiducial volume (FCFV)
   We select fully contained events in which all of the charged particles deposit their energy inside the SK inner detector (ID), so that the energy of the charged particles can be reconstructed. We require no cluster of PMT hits (PMT which register sufficient charge) in

the outer detector (OD) with 16 or more PMTs. The interaction vertex is reconstructed from the timing of the hits in PMTs. The fiducial cut requires the reconstructed vertex to be at least 2 m from the ID wall.
The timing of the detection of event is required to be between -2 μsec to 10 μsec from the expected arrival timing of the first beam bunch. This cut reduces the contamination from other neutrino sources such as atmospheric neutrino to 0.0085 events for full sample. We also apply cuts based on charge and timing of the PMT hits to reject low energy backgrounds and PMT "flasher" events (lights produced from discharge around the dynode).

2. Single electron-like ring
The number of reconstructed Cherenkov rings is one, and it is identified as an electron ring. This cut identifies the ν_e CCQE events, and rejects ν_μ CC interactions. Each of the ring is identified as e-like or μ-like, based on the shape and the opening angle of the Cherenkov ring [132]. The PID parameter distribution that we use for this cut is shown in Fig. 10.2 for data and MC. The MC prediction is made assuming $\sin^2 2\theta_{13} = 0.1$. In the figure, "Osc ν_e CC" represents the $\nu_\mu \to \nu_e$ signal CC events, "$\nu_\mu + \overline{\nu}_\mu$ CC" and "$\nu_e + \overline{\nu}_e$ CC" represent the background events from $\nu_\mu(\overline{\nu}_\mu)$ and $\nu_e(\overline{\nu}_e)$ CC interactions, and "NC" represents the NC background events.

3. Visible energy ($E_{\rm vis}$) greater than 100 MeV
This cut rejects low energy events, such as NC backgrounds and Michel electrons produced by invisible muons. $E_{\rm vis}$ is calculated from total amount of Cherenkov light assuming the rings to be electron-like. Figure 10.3 shows the visible energy distribution. The events below 100 MeV are rejected by this cut.

4. Number of decay electrons is zero
This cut rejects the events with time-delayed hits, which indicates a presence of invisible muons or pions which do not exist in ν_e CCQE events.

5. $E_{rec} < 1250$ MeV cut
We reconstruct the neutrino energy ($E_\nu^{\rm rec}$) from the electron momentum and angle, and reject high energy neutrino events. Nearly all of the oscillated ν_e signal events are below this value, while most of the events above 1250 MeV comes from intrinsic ν_e contamination in the beam, as shown in Fig. 10.4. The neutrino energy is reconstructed assuming CCQE kinematics:
$$E_\nu^{\rm rec} = \frac{m_p^2 - (m_n - E_b)^2 - m_e^2 + 2(m_n - E_b)E_e}{2(m_n - E_b - E_e + p_e \cos\theta_e)}, \tag{10.1}$$
where m_p, m_n and m_e are the mass of proton, neutron and electron. E_b is the neutron binding energy in oxygen. p_e, E_e and θ_e are the momentum, energy and angle (with respect to beam axis) of the electron.

6. π^0 rejection cut
This is a cut to reject π^0 backgrounds from NC interactions. This cut is improved from the one used in 2012 ν_e appearance analysis. The original cut is based on the algorithm called "POLfit" [133]. In the POLfit, a second photon ring is searched assuming the 2-ring π^0 event, while the first ring is already reconstructed. The timing information of the PMTs are not used in the second ring search. We require the reconstructed invariant mass of the event is to be less than 105 MeV/c^2 to reject π^0 events.
The new cut is based on the event reconstruction algorithm called "fiTQun", which is an extension of the model described in Reference [134]. In the fiTQun, we define a likelihood as a function of the track parameters: the vertex position, the timing, the direction and the momentum. For a given set of the parameters, the time (T) and charge (Q) are predicted

for every PMT. The likelihood is maximized when the predicted change and time of the PMTs best agree with the data. All of the track parameters are fit simultaneously by maximizing the likelihood.
The fiTQun provides a likelihood for particle type such as $\mathcal{L}_{\pi^0}$ and $\mathcal{L}_e$ which allows to distinguish π^0 and electron. Figure 10.5 shows the two-dimensional distribution of likelihood ratio ($\mathcal{L}_{\pi^0}/\mathcal{L}_e$) vs. invariant mass. We reject the events above the red line to separate π^0 events from ν_e CC events. By using the fiTQun instead of POLfit, the π^0 background events was reduced by ∼70%, with only a 2% loss in the signal efficiency.

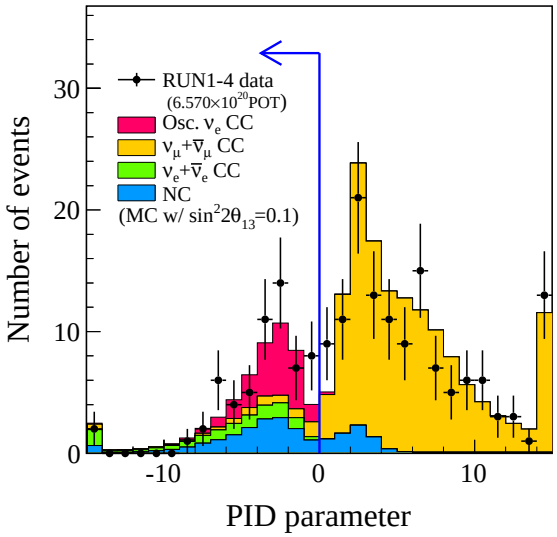

Figure 10.2: PID parameter distribution for the FCFV single-ring events.

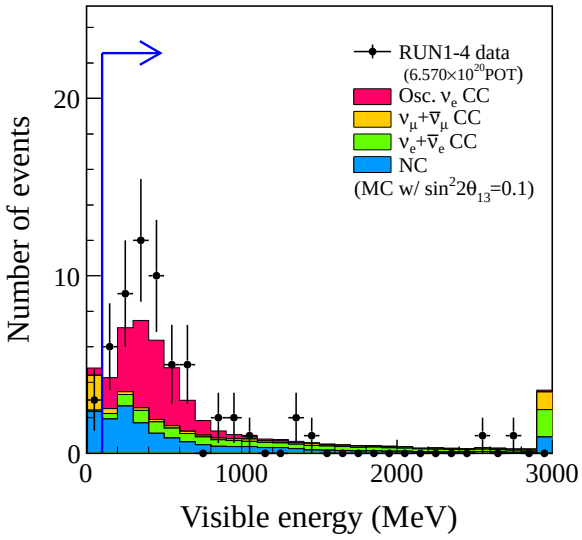

Figure 10.3: Visible energy distribution for the FCFV single-ring electron like events.

Table 10.1: Summary of the number of events at each stage of the cuts. The numbers for MC is estimated assuming $\sin^2 2\theta_{13} = 0.1$.

		MC				
	Data	Total	$\nu_\mu \to \nu_e$ CC signal	$\nu_\mu + \overline{\nu}_\mu$ CC BG	$\nu_e + \overline{\nu}_e$ CC BG	NC BG
(0) Interaction in FV	-	656.8	27.1	325.7	16.0	288.1
(1) FCFV	377	198.4	22.7	142.4	9.8	23.5
(2) Single e-like ring	60	49.4	22.4	5.6	9.7	16.3
(3) $E_{vis} > 100$ MeV	57	49.4	22.0	3.7	9.7	14.0
(4) No decay electron	44	40.0	19.6	0.7	7.9	11.8
(5) $E_\nu^{rec} < 1250$ MeV	39	31.7	18.8	0.2	3.7	9.0
(6) π^0 rejection	28	21.6	17.3	0.1	3.2	1.0

Table 10.1 summarizes the number of events after each stage of the cuts. There is 28 events found in data after applying all the cuts.

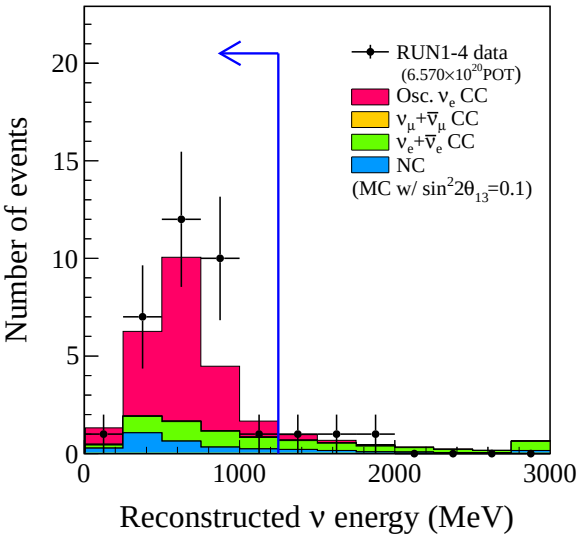

Figure 10.4: Reconstructed neutrino energy distribution.

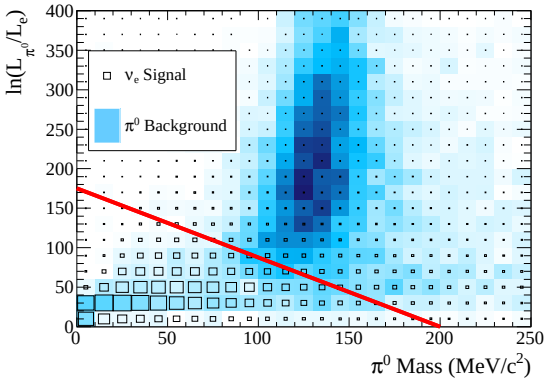

Figure 10.5: $\mathcal{L}_\pi/\mathcal{L}_e$ vs. invariant mass distribution for π^0 rejection cut. The red line indicates the threshold to distinguish π^0 and e. Events at the upper right side of the line is rejected [32].

10.2 Systematic uncertainties

The errors of the cuts are estimated by comparing the data and MC in various control samples. Table 10.2 summarizes the efficiency error of each cut. The dominant error comes from the "topological cuts", which represents the single ring cut, e-like cut and π^0 rejection cut. For the ν_e CC interactions, the errors of the topological cut are estimated by using the atmospheric neutrino control sample. For the interactions with π^0 in the final state, the errors are estimated by using "hybrid-π^0 control sample. The hybrid-π^0 control sample is constructed by combining the electron data and a MC-generated gamma ray assuming π^0 kinematics. The electron data is derived from atmospheric data sample or from the decay-electrons of cosmic ray muon data sample. The effect of the momentum (energy) scale uncertainty (2.4%) is not included in the covariance matrix, but the effect is evaluated in the oscillation analysis. The detail of the systematic error estimation is described in Appendix D.

Table 10.2: Summary of the SK efficiency error.

Cut	$\nu_\mu \to \nu_e$ CC signal	$\nu_\mu + \overline{\nu}_\mu$ CC BG	$\nu_e + \overline{\nu}_e$ CC BG	NC BG
Fully contained	1.0%			
Fiducial volume	1.0%			
No decay electron	0.2%	0.4%	0.2%	0.4%
Topological cuts	Interaction mode and (p_e, θ_e) bin dependent errors Total signal error: 1.6%, Total BG error: 7.3%			

The SK systematic errors are propagated to the oscillation analysis as a covariance matrix. The covariance matrix represents the efficiency error in each of the electron momentum and angle (p_e, θ_e) bin and the correlation of the errors between bins. The covariance matrix contains the (p_e, θ_e) bins for four event categories: ν_e signal, $\nu_\mu + \overline{\nu}_\mu$ background, $\nu_e + \overline{\nu}_e$ background and NC background. The (p_e, θ_e) bins for the covariance matrix is shown in Table 10.3.

In order to generate the covariance matrix, we vary the efficiency of the cuts with the uncertainty in MC and calculate the fluctuation of number of events at each (p_e, θ_e) bin. The size of the fluctuation corresponds to the size of the efficiency error for that bin.

Table 10.3: Binning of SK detector efficiency uncertainty.

momentum bin	angle bin	# of bins
$100 < p_e \leq 300$ MeV/c	`0-40, 40-60, 60-80, 80-100, 100-120, 120-140, 140-180 (degrees)`	7
$300 < p_e \leq 700$ MeV/c	`0-40, 40-60, 60-80, 80-180 (degrees)`	4
$p_e > 700$ MeV/c	`0-40, 40-180 (degrees)`	2

Figure 10.6 left plot shows the square root of the diagonal elements in the covariance matrix, and the right plot shows the correlation matrix. The uncertainty of ν_μ CC backgrounds (bin 13-25) is large, but the fraction of those event in the ν_e candidate events is very small, as shown in Table 10.1. There is a strong correlation between ν_e signal (bin 0-12) and ν_e background (bin 39-53), because both of those errors are estimated from atmospheric neutrino control sample.

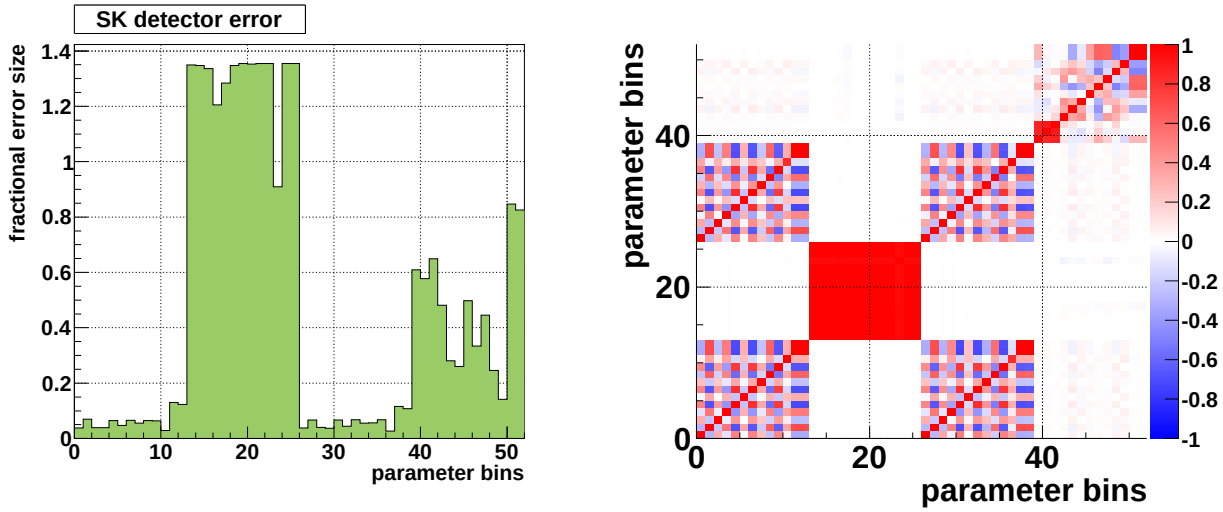

Figure 10.6: Square root of the diagonal elements in the covariance matrix (left), and the correlation matrix (right). The definition of the bins are: 0-12 for signal ν_e, 13-25 for ν_μ CC background, 26-38 for ν_e CC background and 39-53 for NC background.

As shown in Table 10.2, the total signal error for the efficiency of the topological cuts is 1.6%, and the total background error is 7.3%. In the ν_e appearance analysis in 2012, the total signal and background errors were 2.2% and 8.8%, respectively. The errors are reduced because the statistics in the control samples increased roughly by a factor of 2, and also because the simulation is improved. In the simulation, the model for the emission of γ-rays by the de-excitation of nucleus is updated, and the absorption of photons by the nucleus (photo-nuclear effect) is introduced.

Chapter 11

Oscillation analysis and results

11.1 Overview

In this chapter, we fit the SK ν_e candidate data to measure the $\sin^2 2\theta_{13}$ and δ_{CP}. The analysis presented in this thesis (hereafter called "2013 analysis") is the updated version of the analysis presented in 2012 [29] ("2012 analysis"). The fit procedure is basically unchanged from 2012, but there are two additional things:

- The value of $\sin^2 2\theta_{23}$ and Δm^2_{32} were fixed in the 2012 analysis, but in the 2013 analysis we also do the fit with the uncertainties of these parameters taken into account. Because $P(\nu_\mu \to \nu_e)$ depends on these parameters (Eq. 1.17), the uncertainties of these parameters are important in the precision measurement of $\sin^2 2\theta_{13}$ and δ_{CP}.
- Additionally, we apply the constraint on $\sin^2 2\theta_{13}$ from the reactor experiments to measure δ_{CP}.

Our fit uses information of the number of ν_e candidate events and the momentum and angular distribution (p_e-θ_e distribution) of the electron. The number of ν_e signal events changes roughly in proportion to the value of $\sin^2 2\theta_{13}$, while it also depends on the number of background events. Table 11.1 summarizes the predicted number of signal and background events, in case of $\sin^2 2\theta_{13} = 0.1$ and 0.0, with the neutrino flux and cross section parameters derived from the fit to ND280 data. For this calculation, the values of the oscillation parameters are set as shown in Table 11.2. The number of ν_e signal event is not 0 at $\sin^2 2\theta_{13} = 0$, due to the solar term in Eq. 1.17.

Table 11.1: The predicted number of events for each event category in the SK MC simulation. The oscillation parameters are set as shown in Table 11.2.

	# of pre-calculated events	
Event category	$\sin^2 2\theta_{13} = 0.0$	$\sin^2 2\theta_{13} = 0.1$
Total	4.92	21.56
ν_e signal	0.40	17.30
ν_e background	3.37	3.12
ν_μ background	0.94	0.94
$\overline{\nu}_\mu$ background	0.05	0.05
$\overline{\nu}_e$ background	0.16	0.15

The p_e-θ_e distribution helps to distinguish the signal and the background contributions. Figure 11.1 shows the p_e-θ_e distribution for the signal and background events predicted by the

Table 11.2: Default values of the neutrino oscillation parameters and earth matter density used for the calculation of oscillation probabilities. The values of $\sin^2 2\theta_{23}$ and Δm^2_{32} are derived from T2K ν_μ disappearance measurement [22], and the values of $\sin^2 2\theta_{12}$ and Δm^2_{12} are derived from [135]. The earth matter density is obtained from [136].

Parameter	Value
Δm^2_{12}	7.6×10^{-5} eV^2
Δm^2_{32}	2.4×10^{-3} eV^2
$\sin^2 2\theta_{23}$	1.0
$\sin^2 2\theta_{12}$	0.8495
$\sin^2 2\theta_{13}$	0.1
δ_{CP}	0 degree
Earth matter density	2.6 g/cm^3
Mass hierarchy	normal
Base-line length	295 km

MC simulation. The signal events are dominated by the CCQE events, in which the p_e and θ_e satisfies the relation of Eq. 10.1. Therefore, we see a kinematically correlated p_e-θ_e distribution for the signal events. On the other hand, ν_μ and $\overline{\nu}_\mu$ background events are originated from the NC interactions, such as NC1π^0. For the NC1π^0 events, the p_e-θ_e distribution depends on the π^0 production kinematics. As for the intrinsic ν_e and $\overline{\nu}_e$ background, their energy distribution have high energy components, which produce more forward going or higher momentum electron events.

In the following text, we first describe the detail of the fit procedure in Section 11.2. The prediction that we use in the likelihood calculation is summarized in Section 11.3. The systematic uncertainties in the prediction is explained in Section 11.4. In Section 11.5, we discuss the fit result for MC data sets in order to evaluate the sensitivity to $\sin^2 2\theta_{13}$. The results of the fit to the observed data is shown in Section 11.6. Finally in Section 11.7, we take into account the uncertainty of $\sin^2 2\theta_{23}$ and Δm^2_{32} and apply the constraint on $\sin^2 2\theta_{13}$ from the reactor experiments to measure the δ_{CP}.

11.2 Fit procedure

11.2.1 Definition of the likelihood

This analysis is based on the extended maximum likelihood method. We scan over the oscillation parameters and compare the expectation at each oscillation parameter set and the observed events, to find the best values of the parameters which maximizes the likelihood. We define the likelihood as follows:

$$\mathcal{L}(N_{obs.}, \boldsymbol{x}; \boldsymbol{o}, \boldsymbol{f}) = \mathcal{L}_{norm}(N_{obs.}; \boldsymbol{o}, \boldsymbol{f}) \times \mathcal{L}_{shape}(\boldsymbol{x}; \boldsymbol{o}, \boldsymbol{f}) \times \mathcal{L}_{syst.}(\boldsymbol{f}),$$

where the variables have the following meanings:

- $N_{obs.}$ is the number of ν_e candidate events observed in SK
- $\boldsymbol{x}$ represents measurement variables (momentum and angle (p_e, θ_e))
- $\boldsymbol{o}$ represents the oscillation parameters we measure (θ_{13} and δ_{CP})
- $\boldsymbol{f}$ corresponds to the nuisance parameters describing the systematic uncertainties

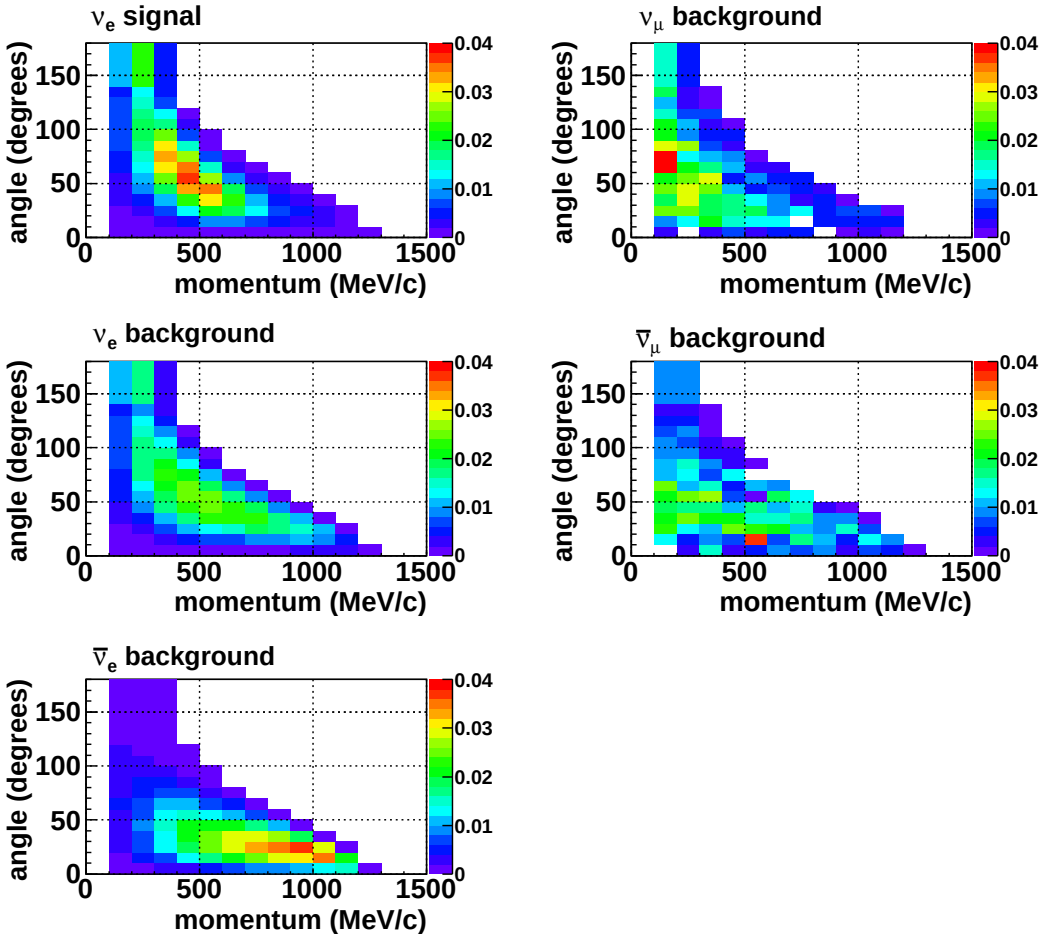

Figure 11.1: Distribution of (p_e, θ_e) for signal ν_e events and the different categories of background events. All distributions are normalized to one.

The normalization term, $\mathcal{L}_{norm}$, is defined by the Poisson probability to observe the number of ν_e candidate events $N_{obs.}$, when the expected number of events is $N_{pred.}$:

$$\mathcal{L}_{norm}(N_{obs.}; \boldsymbol{o}, \boldsymbol{f}) = \frac{e^{-N_{pred.}(\boldsymbol{o},\boldsymbol{f})}[N_{pred.}(\boldsymbol{o}, \boldsymbol{f})]^{N_{obs}}}{N_{obs}!}. \tag{11.1}$$

The shape term $\mathcal{L}_{shape}$ uses the information coming from the p_e-θ_e distribution. This term is the product of the probabilities obtained for each of the observed events.

$$\mathcal{L}_{shape}(\boldsymbol{x}; \boldsymbol{o}, \boldsymbol{f}) = \prod_{i=1}^{N_{obs}} \phi(p_{ei}, \theta_{ei}, \boldsymbol{o}, \boldsymbol{f}), \tag{11.2}$$

where ϕ represents the probability density function (PDF). The PDF is the predicted p_e-θ_e distribution normalized to 1, with the binnings defined as follows.

- Momentum: 100 MeV/c per bin from 0 to 1500 MeV/c
- Angle: 10 degrees per bin from 0 to 140 degrees and an integrated bin over 140 degrees.

The $\mathcal{L}_{syst.}$ term is the prior probability density function for the systematic parameters. We assume it to be a multivariate normal distribution,

$$\mathcal{L}_{syst.}(\boldsymbol{f}) = \frac{1}{(\sqrt{2\pi})^k \sqrt{|\Sigma|}} \exp(-\frac{1}{2}\Delta\boldsymbol{f}^T\Sigma^{-1}\Delta\boldsymbol{f}), \tag{11.3}$$

where k is the number of systematic parameters, Σ is the covariance matrix of the systematic uncertainties and $\Delta\boldsymbol{f}$ is the deviation from nominal for $\boldsymbol{f}$. There are in total 89 systematic parameters, which will be described in Section 11.4.

11.2.2 Likelihood marginalization

The best fit value of the oscillation parameter is found by scanning over the oscillation parameter space to find the value which maximizes the likelihood. However, the likelihood also depends on the systematic parameters. Therefore, we calculate the "marginal" likelihood by integrating over $\boldsymbol{f}$:

$$\mathcal{L}'(N_{obs.}, \boldsymbol{x}; \boldsymbol{o}) = \int \mathcal{L}_{norm}(N_{obs.}; \boldsymbol{o}, \boldsymbol{f}) \times \mathcal{L}_{shape}(\boldsymbol{x}; \boldsymbol{o}, \boldsymbol{f}) \times \mathcal{L}_{syst.}(\boldsymbol{f})\, d\boldsymbol{f}. \tag{11.4}$$

This marginal likelihood $\mathcal{L}'(N_{obs.}, \boldsymbol{x}; \boldsymbol{o})$ only depends on the value of the oscillation parameters $\boldsymbol{o}$, and so we can look for the value of $\boldsymbol{o}$ that maximizes it. However, in the actual calculation, it is computationally difficult to integrate over 89 systematic parameters. Therefore, instead, we define the marginal likelihood as follows:

$$\mathcal{L}'(N_{obs.}, \boldsymbol{x}; \boldsymbol{o}) = \frac{1}{M}\sum_{i=1}^{M} \mathcal{L}_{norm}(N_{obs.}; \boldsymbol{o}, \boldsymbol{f}_i) \times \mathcal{L}_{shape}(\boldsymbol{x}; \boldsymbol{o}, \boldsymbol{f}_i). \tag{11.5}$$

The $\mathcal{L}_{syst.}$ term is removed in this formula, but instead we throw the systematic parameter $\boldsymbol{f}_i$ according to the probability density function $\mathcal{L}_{syst.}$ and the average of $M = 10^4$ throws is calculated*.

11.3 Prediction of SK observables

The likelihood calculation requires prediction of the number of events and the p_e-θ_e distribution, as a function of the oscillation parameters and the systematic parameters. In order to obtain those predictions, we first generate a nominal prediction assuming no oscillation, and then multiply it by the oscillation probability and the re-weighting factors that account for the systematic parameters.

The nominal predicted number of events for each p_e-θ_e bin is calculated by using the neutrino flux prediction and cross-section models.

$$T(\mathcal{F}_i, \mathcal{E}_j, \mathcal{I}_k, p_e, \theta_e) = \Phi^{\mathrm{SK}}(\mathcal{E}_j) \cdot \sigma(\mathcal{F}_i, \mathcal{E}_j, \mathcal{I}_k, p_e, \theta_e) \cdot \epsilon^{\mathrm{SK}}(\mathcal{F}_i, \mathcal{I}_k, p_e, \theta_e), \tag{11.6}$$

where Φ^{SK} is the neutrino beam flux, σ is the cross section and ϵ^{SK} is the detection efficiency. $\mathcal{F}_i$ represents the neutrino flavour type, $\mathcal{E}_j$ represents the neutrino energy bin and $\mathcal{I}_k$ represents the neutrino interaction mode. They are defined as follows:

- Flavour: ν_e signal ($\nu_\mu \to \nu_e$ appearance signal), ν_μ background ($\nu_\mu \to \nu_\mu$), ν_e background ($\nu_e \to \nu_e$), $\overline{\nu}_\mu$ background ($\overline{\nu}_\mu \to \overline{\nu}_\mu$) and $\overline{\nu}_e$ background ($\overline{\nu}_e \to \overline{\nu}_e$)

*We studied the different possible values of M, and found that the likelihood $\mathcal{L}'$ is almost the same even if we increase the M.

- Energy: 200 energy bins from 0 to 10 GeV, and one additional bin going from 10 to 30 GeV
- Interaction mode: CCQE, CC1π, CC coherent, CC others, NC1π^0, NC coherent and NC other

We multiply the nominal number of events by the oscillation probability and the re-weighting factors that account for the systematic parameters.

$$N_{pred.}(p_e, \theta_e, \boldsymbol{o}, \boldsymbol{f}) = \sum_{i=1}^{N_{flv}} \sum_{j=1}^{N_{ene}} \sum_{k=1}^{N_{int}} P(\mathcal{F}_i, \mathcal{E}_j) f(\mathcal{F}_i, \mathcal{E}_j, \mathcal{I}_k, p_e, \theta_e) T(\mathcal{F}_i, \mathcal{E}_j, \mathcal{I}_k, p_e, \theta_e), \tag{11.7}$$

where P is the oscillation probability, f is the product of the re-weighting factors for the systematic parameters, N_{flv}, N_{ene} and N_{int} are the number of flavour types, energy bins and the interaction modes. The oscillation probability is calculated by using the Prob3++ library [137], which is based on three flavour oscillation framework with matter effect taken into account. The detail of the systematic errors are described in the next section. The example of the predicted p_e-θ_e distribution for $\sin^2 2\theta_{13} = 0.0, 0.1$ are shown in Figure 11.2. In this figure, the other oscillation parameters are fixed to the values in Table 11.2, and the systematic parameters are fixed to the central values.

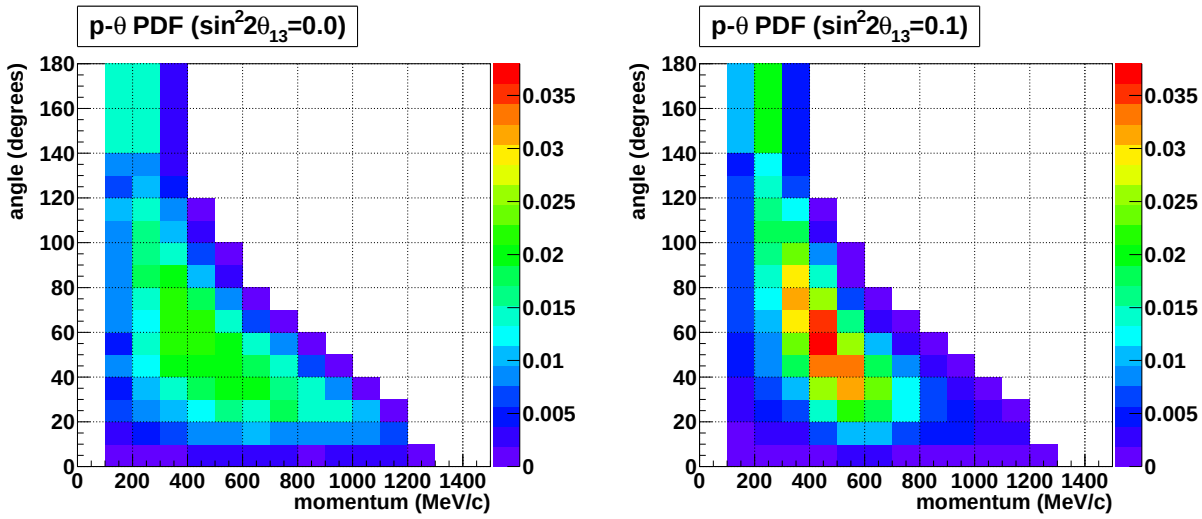

Figure 11.2: The predicted (p_e, θ_e) PDF for $\sin^2 2\theta_{13} = 0.0$ (left) and 0.1 (right).

11.4 Systematic uncertainties

As we described in Section 11.3, the systematic parameters affects the MC prediction. There are 89 systematic parameters which are summarized in Table 11.3. Figure 11.3 shows the fractional error sizes of 89 parameters and the correlation matrix.

11.4.1 Description and implementation of the systematic errors

The effect of these systematic parameters are implemented in the likelihood calculation as re-weighting factors $f^{p-scale}$, f^{Beam}, f^{xsec} and $f^{SK+FSI+PN}$. The beam flux parameters and the

Table 11.3: Summary of systematic parameters used in the oscillation analysis. No.0∼21 systematic parameters are categorized into the beam flux systematics parameters. No.22∼36 systematic parameters are categorized into the neutrino interaction cross-section systematics parameters. Other systematic parameters are categorized into SK detection efficiency and FSI-SI systematics parameters. The SK detection efficiency, FSI-SI and PN parameters are combined into the common parameters having a size of quadratic sum of uncertainties. E_ν represents the true (reconstructed) energy in GeV unit.

No.	Parameter	Value	Error(1σ)
0∼21	Beam flux norm	0.93∼1.06	∼0.09
22	M_A^{QE}	1.24 GeV/c^2	0.072 GeV/c^2
23	M_A^{RES}	0.96 GeV/c^2	0.068 GeV/c^2
24	CCQE norm (E_ν <1.5 GeV)	0.97	0.076
25	CC1π norm (E_ν <2.5 GeV)	1.26	0.16
26	NC1π^0 norm	1.14	0.25
27	CC other norm	0	0.4
28	Spectral function	0(Off)	1(On)
29	p_F	225 MeV	30 MeV
30	CC coherent norm	1	1
31	NC coherent norm	1	0.3
32	NC other norm	1	0.3
33	$\sigma_{\nu_e}/\sigma_{\nu_\mu}$	1	0.03
34	W-shape	87.7 MeV/c^2	45.3 MeV/c^2
35	π-less Δ decay	0.2	0.2
36∼48	SK eff.+ FSI + SI + PN for ν_e signal	1	0.03∼0.13
49∼61	SK eff.+ FSI + SI + PN for ν_μ CC	1	0.14∼1.35
62∼74	SK eff.+ FSI + SI + PN for ν_e CC	1	0.03∼0.12
75∼87	SK eff.+ FSI + SI + PN for NC	1	0.25∼0.85
88	SK momentum scale	1	0.024

part of the cross section parameters are constrained by the ND280 measurements. Description of each type of systematic parameters are explained in the following text.

As one can see in Figure 11.3, some parameters are anti-correlated, which leads to reduction of the uncertainties on the predicted number of events and the p_e-θ_e PDF. Those anti-correlations appear in the parameters constrained by the ND280 measurement (parameter bins:0-26) where the beam flux parameters and cross sections parameters are correlated after the ND280 fit (they were uncorrelated before the fit).

Beam flux parameters

The beam flux errors are implemented as a normalization parameters in bins of neutrino energy and flavor. The binning of f^{beam} is shown in Table 11.4.

Neutrino interaction uncertainties

In Table 11.3, the number 22 to 35 correspond to the neutrino interaction parameters. These parameters are categorized into two types. CCQE norm, CC1π norm, NC1π^0 norm, CC coherent norm, NC coherent norm, NC other norm and $\sigma_{\nu_e}/\sigma_{\nu_\mu}$ are the parameters that simply changes

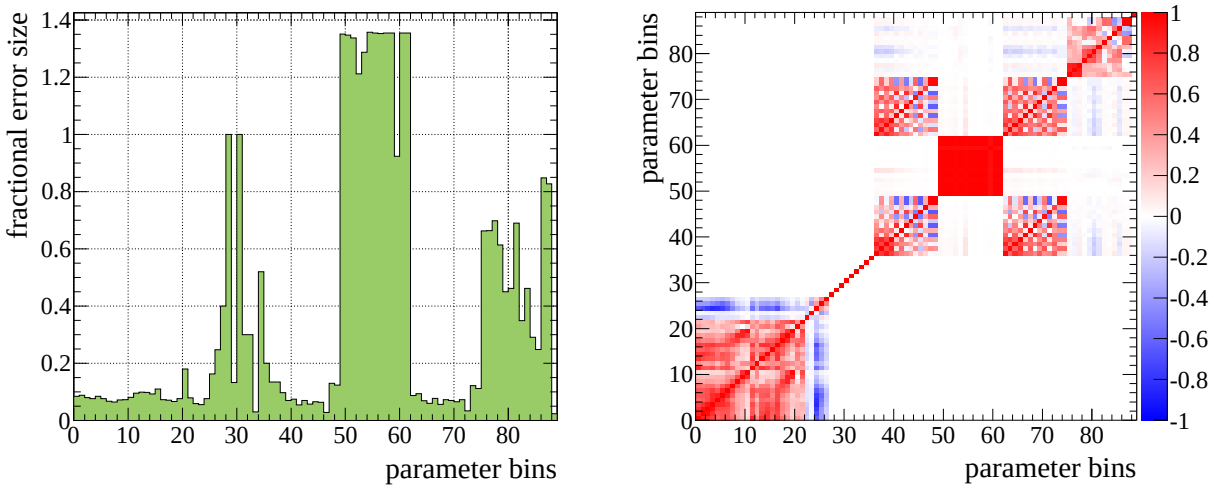

Figure 11.3: Size (left) and correlation matrix (right) of all the systematic uncertainties. The definition of the binning is shown in Table 11.3: 0-21=Beam parameters, 22-35=Cross section parameters, 36-87=SK efficiency+FSI+PN, 88=SK p-scape error. The definition of the beam parameter bins are same as the bins defined in Table 11.4, and the definition of the SK efficiency + FSI + PN parameters bins are same as in Fig. 10.6.

Table 11.4: Binning of f^{Beam}

event category	ν flavor	energy binning	# of bins

ν_e signal
ν_μ background
	ν_μ flavor	`0-0.4, 0.4-0.5, 0.5-0.6, 0.6-0.7,`
		`0.7-1.0, 1.0-1.5, 1.5-2.5, 2.5-3.5,`
		`3.5-5.0, 5.0-7.0, 7.0-30.0 (GeV)`
			11

$\overline{\nu}_\mu$ background	$\overline{\nu}_\mu$ flavor	`0-1.5, 1.5-30.0 (GeV)`	2
ν_e background	ν_e flavor	`0-0.5, 0.5-0.7, 0.7-0.8, 0.8-1.5,` `1.5-2.5, 2.5-4.0, 4.0-30.0 (GeV)`	7
$\overline{\nu}_e$ background	$\overline{\nu}_e$ flavor	`0-2.5, 2.5-30.0 (GeV)`	2

the overall normalization, so they are treated in the same way as the beam flux parameters. On the other hand, M_A^{QE}, M_A^{RES}, spectral function, p_F, W-shape and π-less Δ decay parameters also changes the p_e-θ_e distribution. The effect of the uncertainty of the cross section parameters are implemented as re-weighting factors for the p_e-θ_e bins. The re-weighting factors for each p_e-θ_e bin for each neutrino energy bin E_ν are derived by using MC in the following way.

1. Generate p_e-θ_e distribution with cross section parameters changed by -3σ, -2σ, -1σ, $+1\sigma$, $+2\sigma$ and $+3\sigma$. We derive these distributions by re-weighting the nominal MC for event by event, according to the change in the cross section.

2. The nominal and re-weighted p_e-θ_e distribution are prepared for all of the neutrino energy bins[†] for all of the flavours. From the ratio of those nominal and re-weighted p_e-θ_e distributions, we derive the response function which represents the fractional change in each p_e-θ_e bin as a function of the cross section parameter, for each E_ν bin and neutrino flavours.

[†]The true energy bin for the response function is practically defined to be the same for all event categories with 9 bins: 0-0.4, 0.4-0.5, 0.5-0.6, 0.6-0.8, 0.8-1.2, 1.2-2.0, 2.0-3.0, 3.0-5.0, 5.0-30 (GeV).

Figure 11.4 shows an example of the response function. The values of the response function are linearly interpolated between the calculated points. For the region below -3σ and above $+3\sigma$, we linearly extrapolate the $\pm 2\sigma$ and $\pm 3\sigma$ points.

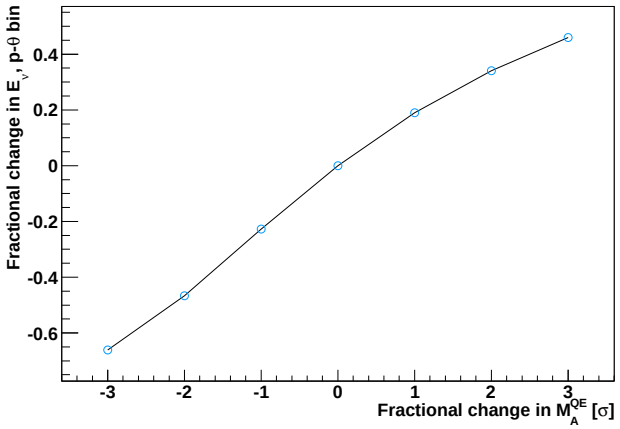

Figure 11.4: An example of a response function for p = 400-500 MeV/c^2, θ = 60-70 degrees, E_ν = 0.8-1.2 GeV.

SK efficiency uncertainties

The SK efficiency errors are described in Chapter 10. Except for the momentum scale error, all of the errors are derived as the uncertainty in each p_e-θ_e bin, for four different event categories: ν_e signal, ν_μ CC BG, ν_e CC BG and NC BG. The errors are implemented as the 52×52 covariance matrix. The FSI+SI error and PN error are also implemented as the 52×52 covariance matrices, and added to the SK covariance matrix.

The SK momentum scale error is evaluated to be 2.4%. The effect of this uncertainty is implemented by shifting the predicted p_e-θ_e distribution in the momentum direction. After applying all the other systematic parameters to obtain the distribution, we look at how many events would move from one bin to another if all the momentum were multiplied by the p-scale systematic parameter as illustrated on Figure 11.5. We assume that events are uniformly distributed in each bin: we consider that if α% of the surface of bin i moves into bin i+1 when rescaling the momentum by $f^{p-scale}$, α% of the events of bin i move into bin i+1. The final predicted (p_e, θ_e) distribution is the one obtained by applying those events migrations.

The number of ν_e candidate events is also affected by the p-scale because of the visible energy cut and the reconstructed energy cut in the ν_e event selection. This effect is taken into account, by an additional normalization error. The size of the normalization error is estimated by varying the momentum scale in the SK MC files. According to this estimation, the normalization error is 0.6% (1.5%) at $\sin^2 2\theta_{13}$=0.1 (0.0).

Final State Interaction and secondary interaction uncertainty

The hadronic final state interaction (FSI) and secondary interaction (SI) uncertainties are also implemented as covariance matrices over the (p_e, θ_e) distributions and different event categories, using the same binning and categories as the SK detector efficiency error. The method to build the covariance matrix is explained in Chapter 6. The effect of FSI and SI uncertainties are first evaluated separately, then added to produce a 52×52 FSI+SI covariance matrix. Figure

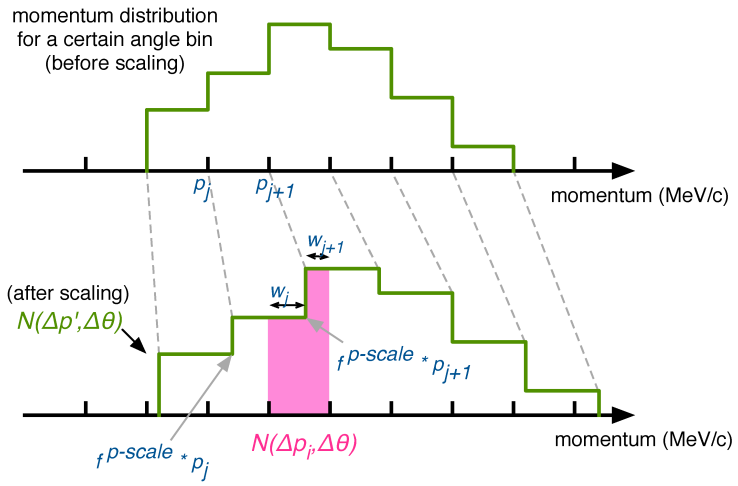

Figure 11.5: An illustration of the implementation of the SK momentum scale error.

11.6 shows the size of the the FSI+SI uncertainties (square root of the diagonal terms in the covariance matrix).

Photo nuclear effect

Photo-Nuclear (PN) effect is the interactions of the photon with a nucleus. It leads to the absorption of a photon in the detector before it convert to a e^+e^- pair in which case the photon would go undetected. This affects the detection of the events with π^0 in the final state, which is supposed to have at least two photons in the final state. For example, when one of the two photons in the NC1π^0 event is absorbed, the event is misidentified as ν_e CCQE event. Figure 11.7 shows the size of the PN uncertainty.

11.4.2 Effect of systematic uncertainties

In this section, we show the effect of the systematic errors on the predicted number of events and the (p_e, θ_e) PDF. We vary the systematic parameters according to a covariance matrix which describe their variance and correlations. We generate a large number (20000) of sets of values of the systematic parameters and compute the predicted number of events and the (p_e, θ_e) PDF for each set.

Effect on the predicted number of events

To see the change and the reduction of systematic uncertainties by the measurements at ND280, we compute the predicted number of events and the (p_e, θ_e) PDF with the covariance matrix obtained with ("after ND280 fit") and without ("before ND280 fit") the ND280 fit.

Table 11.5 shows the number of expected events before and after ND280 fit. Because the central values of the flux and cross section parameters are different between these three cases, the expected number of events are different. The total number of events with $\sin^2 2\theta_{13} = 0.1$ is reduced from 23.21 to 21.56 after the ND280 fit. This is because the value of M_A^{RES} parameter significantly reduced after the fit (Table 9.4). The numbers in the last row shows the number of events derived by replacing the fiTQun π^0 cut to the POLfit π^0 cut. The expected number of ν_μ background events is larger in the POLfit case. By using fiTQun, the signal to background ratio is improved from 2.91 to 4.06 at $\sin^2 2\theta_{13} = 0.1$.

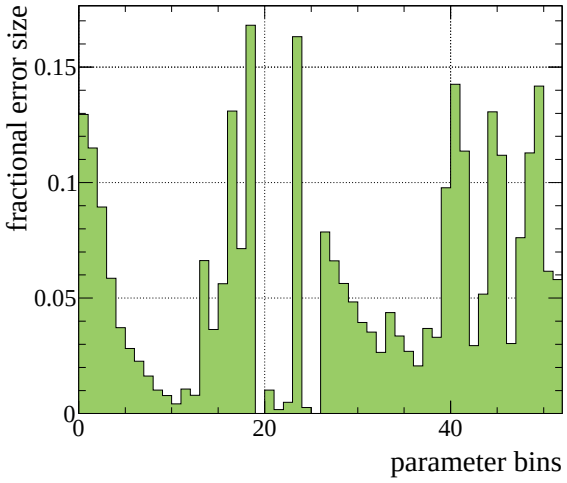

Figure 11.6: Size of the FSI+SI systematic error. The definition of the bins are: 0-12 for signal ν_e, 13-25 for ν_μ CC background, 26-38 for ν_e CC background and 39-53 for NC background.

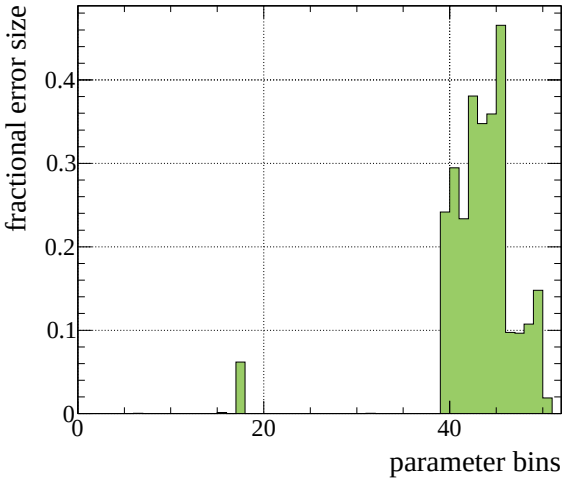

Figure 11.7: Size of the PN systematic error. The definition of the bins are: 0-12 for signal ν_e, 13-25 for ν_μ CC background, 26-38 for ν_e CC background and 39-53 for NC background.

The pink histograms in Figure 11.8 shows the variation of number of expected events by systematic error sources. The top and bottom plots shows the variation with and without ND280 fit, respectively. These histograms are obtained by randomly throwing the systematic parameters according to the covariance matrix. The blue histograms shows the statistical variation of the number of events. The variation due to the systematic errors becomes much smaller than the statistical fluctuation thanks to the ND280 measurement.

We also study the effect of each systematic parameter on the predicted number of events with a similar method. The contributions of each individual parameter are summarized in Table 11.6, and Table 11.7 gives a summary by group of systematic uncertainties. The correlation between the beam flux and cross section error is not taken into account in Table 11.6, while it is taken into account in Table 11.7. The beam flux and cross section errors become much smaller after the correlation is taken into account. The largest contribution to the systematic error comes from the cross section systematic parameters which are not constrained by the ND280 fit. Especially, the spectral function error is large, but this error will be reduced in the near future when the spectral function is implemented in NEUT.

In Table 11.7, we also show the total error on the predicted number of events as of the 2012 analysis. The total error without ND280 fit increased from 21.0% to 24.2% (24.2% to 27.7%) at $\sin^2 2\theta_{13}$=0.0 ($\sin^2 2\theta_{13}$=0.1). This is because the M_A^{QE} error is the dominant error and the fraction of CCQE events is increased in the 2013 analysis by using the fiTQun π^0 cut. On the other hand, the total error with ND280 fit is reduced in the 2013 analysis. This is due to significant improvement in cross section parameter errors and SK detector efficiency errors. For example, comparing the 2012 analysis with the 2013 analysis, the error for the number of expected events due to M_A^{RES} decreased from 3.9% to 2.2% at $\sin^2 2\theta_{13}$=0.0, and the SK detector efficiency error is reduced from 6.8% to 5.6%. The total error for the flux and interaction parameters constrained by ND280 is 2.9% (4.8%) at $\sin^2 2\theta_{13}$=0.1 (0.0) for the 2013 analysis, while it was 5.0% (8.5%) in the 2012 analysis. The size of the FSI+SI error is comparable to the flux and interaction error, but it will become negligible in the future once we use the improved model.

Table 11.5: The predicted number of events with $\sin^2 2\theta_{13} = 0.1$ (top) and 0.0 (bottom).

(a) $\sin^2 2\theta_{13} = 0.1$

Configuration	Total	ν_e signal	ν_e BG	ν_μ BG	$\overline{\nu}_\mu$ BG	$\overline{\nu}_e$ BG
Before ND280 fit	23.21	18.44	3.34	1.20	0.07	0.17
After ND280 fit	21.56	17.30	3.12	0.94	0.05	0.15
After ND280 fit (POLfit π^0 cut)	23.75	17.67	3.30	2.46	0.14	0.17

(b) $\sin^2 2\theta_{13} = 0.0$

Configuration	Total	ν_e signal	ν_e BG	ν_μ BG	$\overline{\nu}_\mu$ BG	$\overline{\nu}_e$ BG
Before ND280 fit	5.46	0.41	3.60	1.20	0.07	0.18
After ND280 fit	4.92	0.40	3.37	0.94	0.05	0.16
After ND280 fit (POLfit π^0 cut)	6.75	0.40	3.56	2.46	0.14	0.18

Table 11.6: Summary of the contributions of the systematic errors on the predicted number of events. Each error is evaluated as the RMS/mean of the distribution of the predicted number of events and given in the unit of percent. Note that the sum in quadrature of those effects is not equal to the total effect because some of the systematic parameters are correlated.

	$\sin^2 2\theta_{13} = 0$		$\sin^2 2\theta_{13} = 0.1$	
Error source	w/o ND280 fit	w/ ND280 fit	w/o ND280 fit	w/ ND280 fit
Flux & Interaction (constrained by the ND280 fit)				
Beam only	10.6	7.2	11.4	7.4
M_A^{QE}	15.2	2.3	20.7	3.1
M_A^{RES}	7.1	2.2	3.2	1.0
CCQE norm. ($E_\nu < 1.5$ GeV)	6.9	4.7	9.0	6.2
CC1π norm. ($E_\nu < 2.5$ GeV)	4.6	2.4	4.0	2.0
NC1π^0 norm.	2.5	1.9	0.6	0.4
Neutrino interaction (not constrained by ND280)				
CC other norm	0.3	0.3	0.1	0.1
Spectral Function	4.7	4.7	5.9	5.9
p_F	0.1	0.1	0.1	0.1
CC coh. norm.	0.3	0.3	0.2	0.2
NC coh. norm.	1.1	1.1	0.2	0.2
NC other norm.	2.2	2.2	0.5	0.5
$\sigma_{\nu_e}/\sigma_{\nu_\mu}$	2.4	2.4	2.8	2.8
W shape	1.0	1.0	0.2	0.2
pion-less Δ decay	3.2	3.2	3.6	3.6
SK, FSI and PN				
SK detector eff.	5.6	5.6	2.4	2.4
FSI+SI	3.0	3.0	2.3	2.3
PN	3.4	3.4	0.8	0.8
SK momentum scale	1.5	1.5	0.6	0.6
Total	24.0	11.1	27.2	8.8

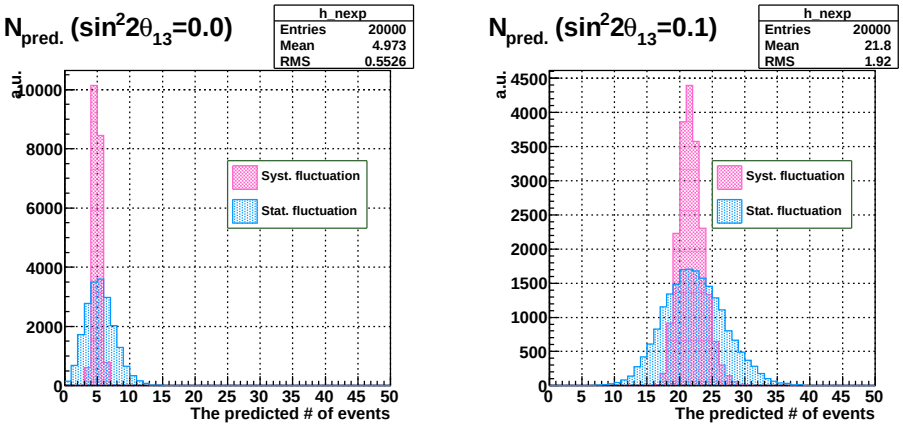

(a) After ND280 fit

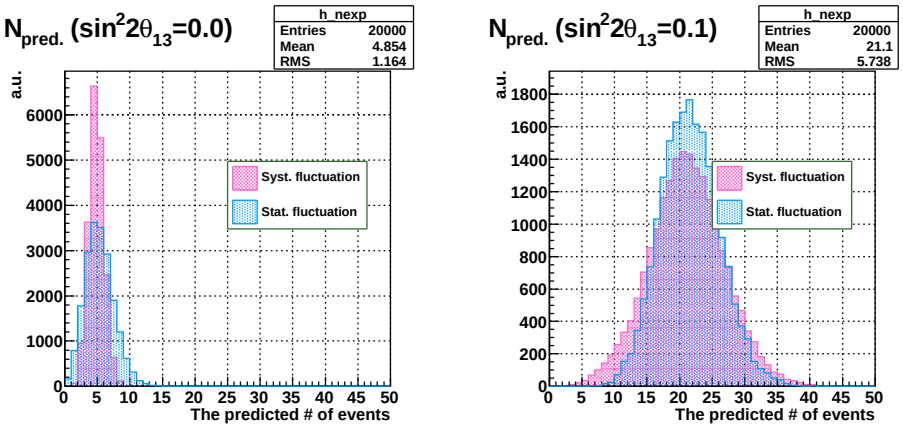

(b) Before ND280 fit

Figure 11.8: The distribution of the predicted number of events for $\sin^2 2\theta_{13} = 0$ (left) and 0.1 (right), obtained by throwing the systematic parameters with (top) and without (bottom) the ND280 fit results. Blue histograms shows the statistical fluctuation without systematic fluctuation.

Table 11.7: Summary of the contributions of systematic errors on the predicted number of events. Each error is given in the unit of percent. The total size of error in the 2012 analysis is shown for comparison.

	$\sin^2 2\theta_{13} = 0$		$\sin^2 2\theta_{13} = 0.1$	
Error source	w/o ND280 fit	w/ ND280 fit	w/o ND280 fit	w/ ND280 fit
Flux & Interaction	21.7	4.8	25.9	2.9
ν int. (not constrained by ND280)	6.8	6.8	7.5	7.5
SK+FSI+PN	7.3	7.3	3.5	3.5
Total	24.0	11.1	27.2	8.8
2012 analysis	21.0	13.0	24.2	9.9

Effect on the (p_e, θ_e) PDF

We look at the effect of the systematic uncertainties on the (p_e, θ_e) PDF that is used to compute the shape term of the likelihood. For this, we evaluate the one-sigma deviation of each (p_e, θ_e) bin of the total PDF (including both signal and background event categories) using 20000 throws of the nuisance parameters as before. One dimensional representations of the results are shown for some of the bins on Figure 11.9 in the case $\sin^2 2\theta_{13} = 0.1$ and on Figure 11.10 for the case $\sin^2 2\theta_{13} = 0.0$.

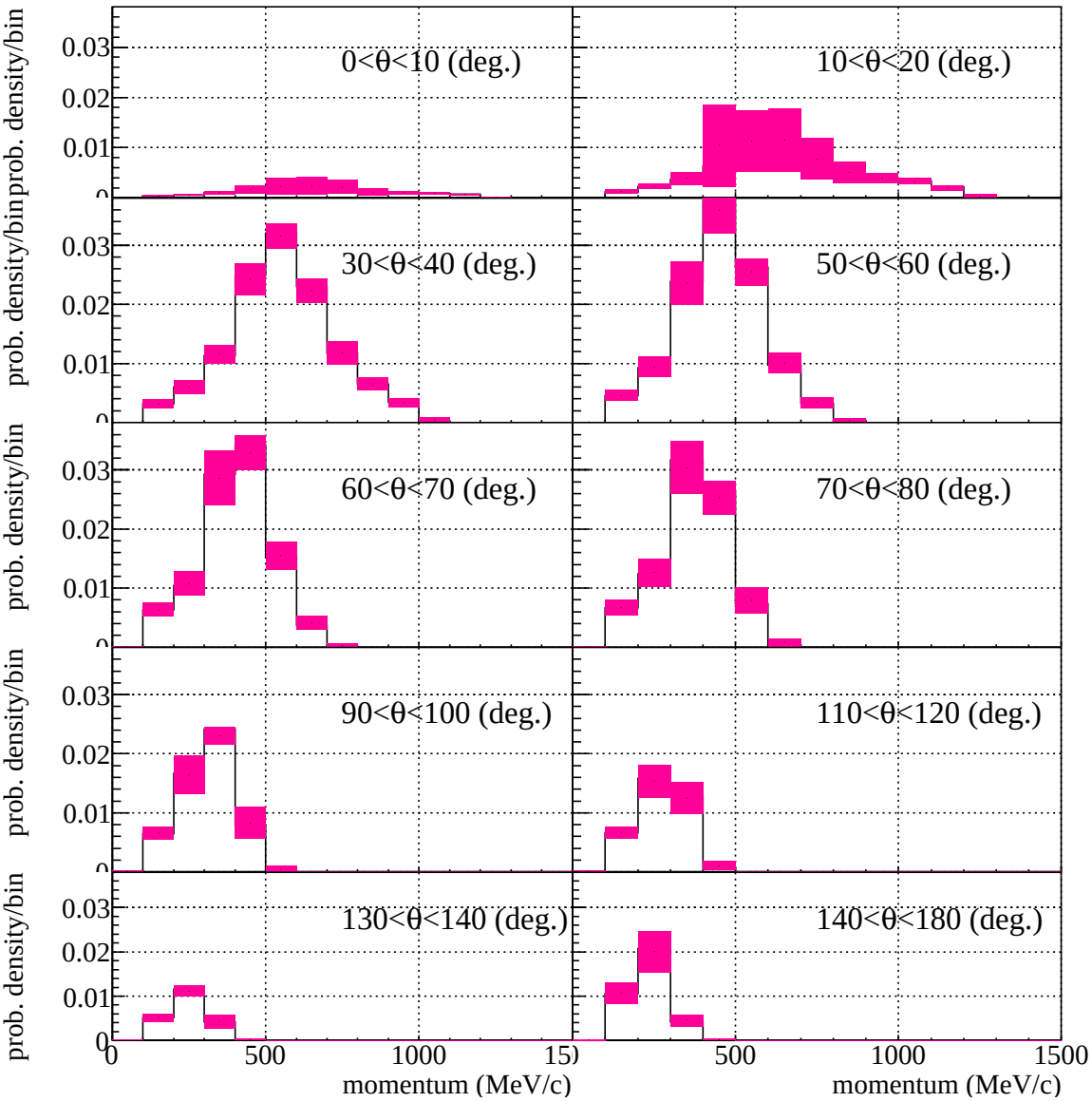

Figure 11.9: The (p_e, θ_e) PDF distribution as a function of momentum for different angle bins (10 out of 15 bins are shown here for example) in the $\sin^2 2\theta_{13} = 0.1$ case. Red areas represent one sigma deviations evaluated using 20000 throws of the systematic parameters following the multivariate normal distribution using their central values and covariance matrix.

To quantify the effect, from those distributions, we compute a total variation ΔPDF, as a

weighted average of the one sigma variation on each bin:

$$\Delta PDF \equiv \frac{\sum_{i=1}^{225} p_i \cdot (e_i/p_i)}{\sum_{i=1}^{225} p_i} = \sum_{i=1}^{225} e_i \tag{11.8}$$

where:

- p_i is the default value of the PDF for the i-th p_e-θ_e bin
- e_i is the one sigma deviation of that bin
- 225 is the total number of p_e-θ_e bins.

The values of ΔPDF for each individual systematic parameter are listed in Table 11.8, and are summarized by group of uncertainties in Table 11.9.

Again, as we see in Table 11.7, the error without ND280 fit is larger in 2013 because the M_A^{QE} is the dominant error source and the fraction of CCQE events is increased by using fiTQun. The error with ND280 fit is slightly smaller in the 2013 analysis compared to the 2012 analysis at $\sin^2 2\theta_{13}$=0.0. This is because the SK efficiency error, which is the dominant error in that column, become small. At $\sin^2 2\theta_{13}$=0.1, however, the error with ND280 fit is not improved in 2013 because the spectral function error increased while the cross section errors constrained by ND280 are decreased. The spectral function error is larger in 2013, because the fraction of CCQE events is increased with the fiTQun π^0 cut.

11.5 Sensitivity

Before applying the fit to the real data, we applied the fit to toy MC data sets to estimate the sensitivity. We compare the likelihood curve as a function of $\sin^2 2\theta_{13}$ in several different conditions.

For this study, we calculate the averaged likelihood by averaging the negative log likelihood from randomly generated 4000 toy MC experiments.

$$\langle \ln \mathcal{L}'(\theta_{13}) \rangle = \frac{1}{4000} \sum_{i=1}^{4000} \ln \mathcal{L}'(\boldsymbol{x}_i; \theta_{13}) \tag{11.9}$$

The toy MC experiments are generated in the following way.

1. Randomly generate a set of systematic parameters following the multivariate normal distribution using their central values and the total covariance matrix.
2. Calculate the predicted number of events and p_e-θ_e PDF with the generated systematic parameters and oscillation parameters according to Equation 11.7. We use the default values of oscillation parameters shown in Table 11.2. The value of $\sin^2 2\theta_{13}$ is set to 0.1.
3. Determine the observed number of events, N_{obs}, by generating a Poisson random value with the mean of the predicted number of events.
4. Randomly generate a ν_e candidate event which has (p_e, θ_e) following the p_e-θ_e PDFThis step is repeated until the number of events becomes N_{obs}.

We define the $\Delta\chi^2$ from the likelihood as follows.

$$\Delta\chi^2(\theta_{13}) = -2\Delta \ln \mathcal{L}'(\theta_{13}), \tag{11.10}$$

Table 11.8: Summary of the contributions to the error on the p_e-θ_e PDF from each systematic source. The definition of the errors are shown in Equation 11.8. Each error is given in the unit of percent.

	$\sin^2 2\theta_{13} = 0$		$\sin^2 2\theta_{13} = 0.1$	
Error source	w/o ND280 fit	w/ ND280 fit	w/o ND280 fit	w/ ND280 fit
Flux & Interaction (constrained by the ND280 fit)				
Beam only	1.9	1.7	1.8	1.4
M_A^{QE}	10.0	1.5	13.8	1.7
M_A^{RES}	2.1	0.6	2.1	0.7
CCQE norm. ($E_\nu < 1.5$ GeV)	1.8	1.2	2.0	1.3
CC1π norm. ($E_\nu < 2.5$ GeV)	1.3	0.7	3.3	1.7
NC1π^0 norm.	1.2	0.9	0.4	0.3
Neutrino interaction (not constrained by ND280)				
CC other norm	0.1	0.1	0.1	0.1
Spectral Function	7.2	7.2	11.7	11.7
p_F	2.2	2.2	2.9	2.9
CC coh. norm.	0.4	0.4	0.4	0.4
NC coh. norm.	1.4	1.4	0.3	0.3
NC other norm.	1.6	1.6	0.5	0.5
$\sigma_{\nu_e}/\sigma_{\nu_\mu}$	0.4	0.4	0.1	0.1
W shape	2.9	2.9	0.7	0.7
pion-less Δ decay	1.9	1.9	3.0	3.0
SK, FSI and PN				
SK detector eff.	10.9	10.9	6.2	6.2
FSI	1.7	1.7	1.5	1.5
PN	3.2	3.2	0.8	0.8
SK momentum scale	5.3	5.3	6.7	6.7
Total	21.8	17.9	24.5	18.3

Table 11.9: Summary of the contributions to the error on the p_e-θ_e PDF from each group of systematic sources. The definition of the errors are shown in Equation 11.8. Each error is given in the unit of percent.

	$\sin^2 2\theta_{13} = 0$		$\sin^2 2\theta_{13} = 0.1$	
Error source	w/o ND280 fit	w/ ND280 fit	w/o ND280 fit	w/ ND280 fit
Flux & Interaction	11.3	2.8	15.0	2.9
ν int. (not constrained by ND280)	9.9	9.9	13.8	13.8
SK+FSI+PN	13.6	13.4	9.9	9.9
Total	22.0	17.9	24.5	18.3
2012 analysis	21.4	19.5	22.3	18.2

where

$$\Delta \ln \mathcal{L}'(\theta_{13}) = \langle \ln \mathcal{L}'(\theta_{13}) \rangle - \langle \ln \mathcal{L}'(\theta_{13}^{best}) \rangle. \tag{11.11}$$

The θ_{13}^{best} represents the best fit value of θ_{13}.

Figure 11.11 solid curve shows $-2\Delta \ln \mathcal{L}'$ vs. $\sin^2 2\theta_{13}$ for Run1-4 POT (6.57×10^{20} POT) case. The minimum point in the likelihood curve corresponds to the best fit value of $\sin^2 2\theta_{13}$,

which is consistent with 0.1, as we set the true value of $\sin^2 2\theta_{13}$ to 0.1. The expected significance of excluding $\theta_{13} = 0$ is calculated as $\sqrt{\Delta\chi^2} = \sqrt{-2\Delta \ln \mathcal{L}'}$ at $\theta_{13} = 0$, assuming a two-sided Gaussian probability distribution. For the Run1-4 data, the significance is calculated to be 5.6σ. The dotted curve in the same figure corresponds to Run1-3 case (3.01×10^{20} POT). In this case, the significance is 3.9σ.

Figure 11.12 shows the likelihood curve comparing between 2012 and 2013 systematic parameters. The expected number of events with 2012 and 2013 systematic parameters are 22.4 and 21.6, respectively. This makes the expected significance smaller in the 2013 analysis. On the other hand, the uncertainties of the systematic parameters reduced in the 2013 analysis, which makes the significance larger. With these two effects combined, the expected significance do not change largely with new ND280 fit. The significance is 5.5σ and 5.6σ for old and new ND280 fit, respectively.

Figure 11.13 shows the averaged log likelihood curve comparing the POLfit π^0 cut with the fiTQun π^0 cut. The significance is improved from 5.3σ to 5.6σ by using the fiTQun π^0 cut. This improvement with fiTQun π^0 cut is not huge with the current POT, but it shows apparently better sensitivity compared to the POLfit π^0 cut.

11.6 Fit results for Run1-4 data

In this section, we discuss the results of the fit.

11.6.1 Fit to Run1-4 data

Figure 11.14 (11.15) shows the results of the fit assuming the normal (inverted) mass hierarchy and $\delta_{\mathrm{CP}} = 0$. The p_e-θ_e distribution, the angular distribution and the momentum distribution are shown. The black points represent the data, while the histograms represent the best fit distributions obtained with the best fit value of $\sin^2 2\theta_{13}$ and the central values of the systematic parameters. In the bottom right of those figures, the negative log likelihood as a function of $\sin^2 2\theta_{13}$ is shown.

The best fit value of $\sin^2 2\theta_{13}$ is 0.140 (0.170) for the normal (inverted) hierarchy. We define the confidence level (C.L.) regions by using the fixed threshold for the $\Delta\chi^2$ values. The 68 % C.L. (90 % C.L.) is defined as the region of $\sin^2 2\theta_{13}$ where $\Delta\chi^2 < 1$ ($\Delta\chi^2 < 2.71$). Then, the 68% (90%) C.L. allowed region is $0.108 < \sin^2 2\theta_{13} < 0.178$ ($0.090 < \sin^2 2\theta_{13} < 0.205$) for the normal hierarchy case and $0.133 < \sin^2 2\theta_{13} < 0.214$ ($0.111 < \sin^2 2\theta_{13} < 0.246$) for the inverted hierarchy case. We calculate the significance to exclude $\theta_{13} = 0$ from $\Delta\chi^2$ at $\theta_{13} = 0$, which is 7.3σ for both normal and inverted hierarchy cases. The results of Run1-4 data fit is summarized in Table 11.10 together with the results in 2012. The consistency between different run periods is discussed in detail in the Appendix E.

Figure 11.16 shows the allowed region of 68 % (green) and 90 % C.L. (blue) for $\sin^2 2\theta_{13}$ for each value of δ_{CP}. The black solid line is the best fit value for each value of δ_{CP}. Again, the allowed regions are produced by using fixed $\Delta\chi^2$ thresholds.

The significance of 7.3σ is equivalent to the p-value of 1.2×10^{-13}. We also calculated the p-value in a frequentist approach. In this case, we generate large number of toy MC experiments with $\theta_{13} = 0$ and calculate the p-value which is defined in two ways: 1) Fraction of toy MC experiments with $\Delta\chi^2$ greater than the value of $\Delta\chi^2$ in data (= 53.64), 2) Fraction of toy MC experiments with number of ν_e candidate events larger than the observed number in data (= 28).

In order to generate the large number of toy MC experiments, we used the time saving method. In the usual way, we throw systematic parameters for each of the toy experiments and define the number of observed events randomly from Poisson statistics for that toy experiment. However, this time, for each systematic parameter throw, we perform 6×10^6 Poisson throws to

generate 6×10^6 toy experiments. In total, we throw systematics for 1.6×10^8 times and throw Poisson for 6×10^6, so the number of generated toy experiments is equivalent to 9.6×10^{14}.

When calculating the p-value in method 1, it is not necessary to calculate the $\Delta\chi^2$ for the toy MC experiments with small number of ν_e events, because the probability to get $\Delta\chi^2$ value greater than 53.64 is negligibly small for those toy experiments. Therefore, we calculate the $\Delta\chi^2$ only when the number of observed events is greater than 24. Figure 11.17 shows the number of observed events vs. $\Delta\chi^2$ distribution. There is no toy experiments above $\Delta\chi^2$=53.64 when the number of observed events is 25. Figure 11.18 shows the distribution of $\Delta\chi^2$ for the toy experiments whose number of observed events were greater than 24. We observed 100 toy experiments above $\Delta\chi^2$ =53.64 out of 9.6×10^{14} toy experiments (all of them were generated from different systematic throws). The p-value is therefore 1.0×10^{-13}, which is equivalent to an exclusion significance of 7.3σ (assuming one sided Gaussian).

We also calculate the p-value with the method 2. There is 14373 toy experiments found with the number of observed events greater than or equal to 28. Therefore the p-value is 1.5×10^{-11}, equivalent to an exclusion significance of 6.6σ. The significance is lower than the value obtained in the method 1, because the p_e-θ_e shape information is not used in the method 2.

11.6.2 Fit with different $\sin^2\theta_{23}$ values

The uncertainty of $\sin^2\theta_{23}$ affects our measurement of $\sin^2 2\theta_{13}$ and δ_{CP}, because the leading term of $P(\nu_\mu \to \nu_e)$ is proportional to $\sin^2\theta_{23}$ (Eq. 1.17). For the results shown in the previous sections, the value of $\sin^2\theta_{23}$ is fixed to 0.5 in the fit, while the 1σ uncertainty is 0.432 $\sim$0.596 in the T2K Run1-3 ν_μ disappearance measurement [22]. Figure 11.19 shows the comparison of δ_{CP} vs. $\sin^2 2\theta_{13}$ contours for Run1-4 data, for $\sin^2\theta_{23}$ = 0.4, 0.5 and 0.6. The value of $\sin^2\theta_{23}$ significantly affects our measurement. In Section 11.7, we discuss how to incorporate the uncertainty of $\sin^2\theta_{23}$.

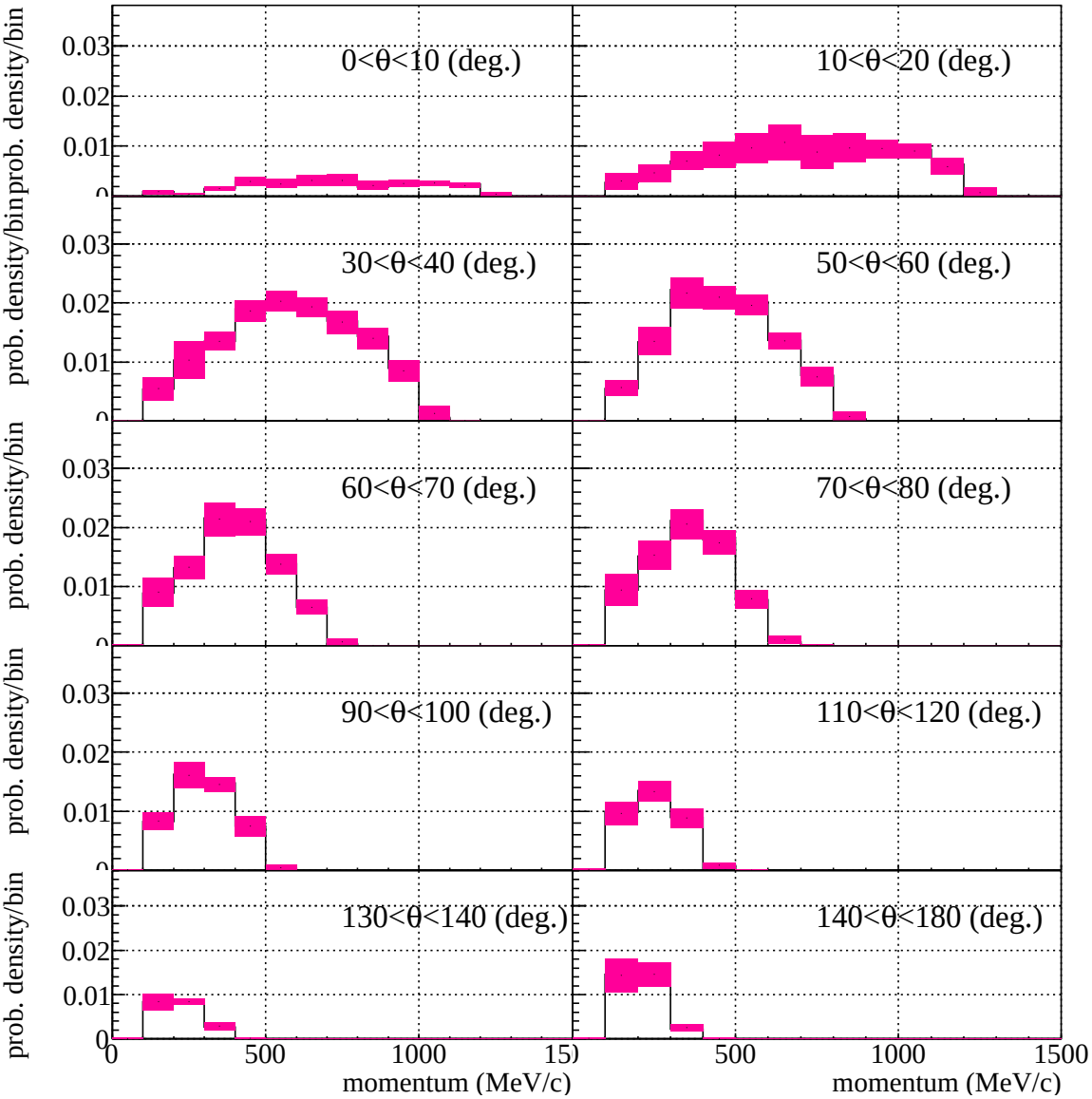

Figure 11.10: Same as Fig. 11.9, for $\sin^2 2\theta_{13} = 0.0$ case.

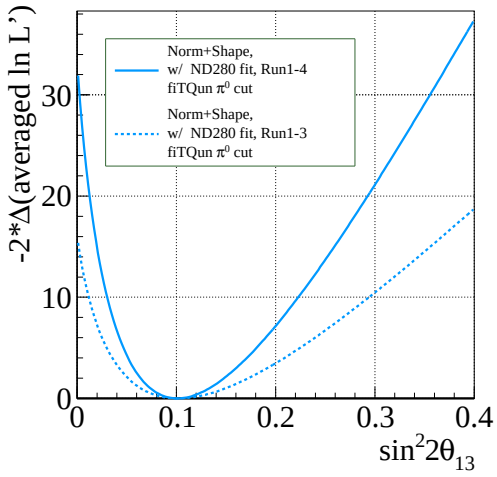

Figure 11.11: Negative averaged log likelihood as a function of $\sin^2 2\theta_{13}$ for Run1-3 POT case (dotted) and Run1-4 POT case (solid). Both of them are analyzed in the same way except for the difference in POT.

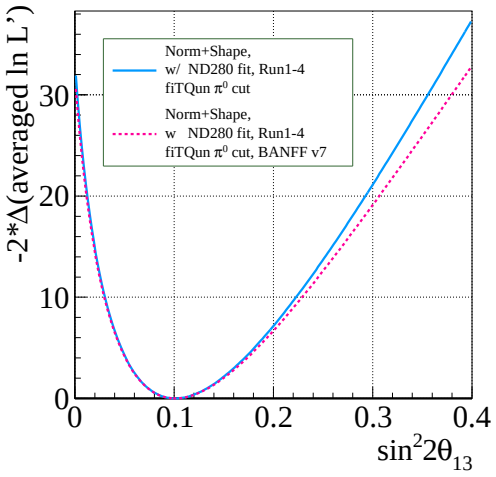

Figure 11.12: Negative averaged log likelihood as a function of $\sin^2 2\theta_{13}$ with old 2012 systematic errors (pink) and with new 2013 systematic errors (blue), for Run1-4 POT case.

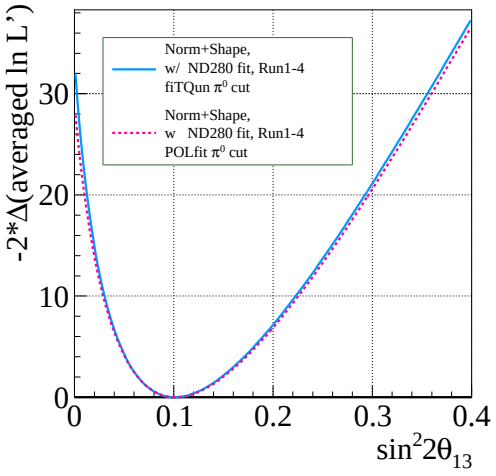

Figure 11.13: Negative averaged log likelihood as a function of $\sin^2 2\theta_{13}$ with POLfit π^0 cut (pink) and with fiTQun π^0 cut (blue), for Run1-4 POT case.

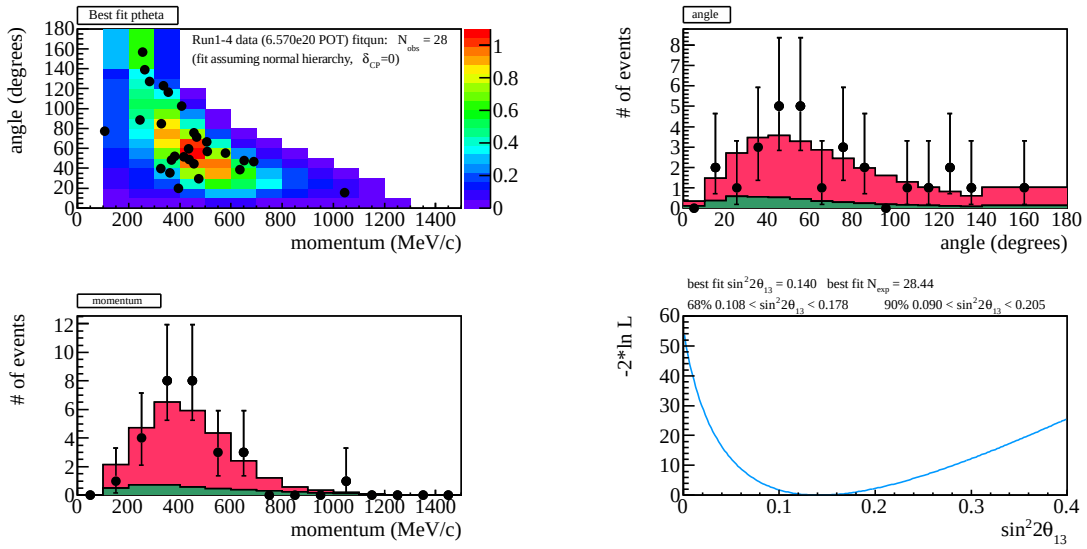

Figure 11.14: Fit results of the Run1-4 data until May 8^{th} 2013 assuming $\delta_{\mathrm{CP}} = 0$ and normal hierarchy. Top left : the p_e-θ_e distribution with the best fit value of θ_{13} and the central values of systematic parameters plotted with the data (black dots). Top right : the angular distribution of the best fit point with the data. Bottom left : the momentum distribution of the best fit point with the data. The error bars show the statistical errors in Poisson distribution. The pink (green) histograms represent the expected signal (background) component. Bottom right : the negative log likelihood distribution as a function of $\sin^2 2\theta_{13}$.

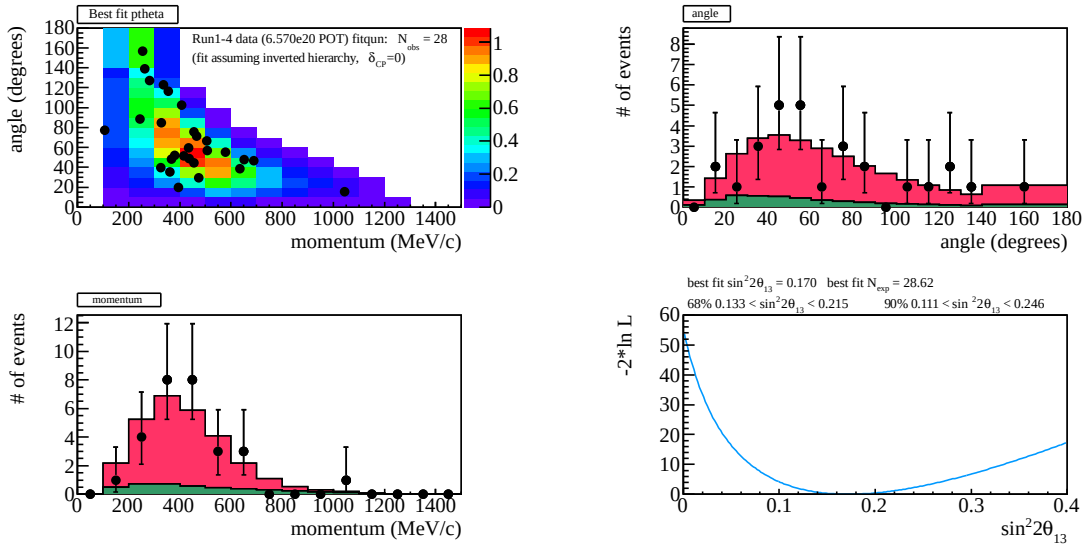

Figure 11.15: Same as in Fig. 11.14 for inverted hierarchy case.

Table 11.10: Summary of the results and comparison with the 2012 results, with $\sin^2 2\theta_{23} = 1.0$, $|\Delta m^2_{32}| = 2.4 \times 10^{-3}$ eV^2 and $\delta_{\rm CP} = 0$.

Result	This analysis	2012 analysis
POT	6.570×10^{20}	3.010×10^{20}
The observed number of events	28	11
Normal hierarchy		
Best fit value of $\sin^2 2\theta_{13}$	0.140	0.088
90 % C.L. allowed region	$0.090 < \sin^2 2\theta_{13} < 0.205$	$0.030 < \sin^2 2\theta_{13} < 0.175$
68 % C.L. allowed region	$0.108 < \sin^2 2\theta_{13} < 0.178$	$0.049 < \sin^2 2\theta_{13} < 0.137$
Inverted hierarchy		
Best fit value of $\sin^2 2\theta_{13}$	0.170	0.108
90 % C.L. allowed region	$0.111 < \sin^2 2\theta_{13} < 0.246$	$0.038 < \sin^2 2\theta_{13} < 0.212$
68 % C.L. allowed region	$0.133 < \sin^2 2\theta_{13} < 0.214$	$0.062 < \sin^2 2\theta_{13} < 0.167$

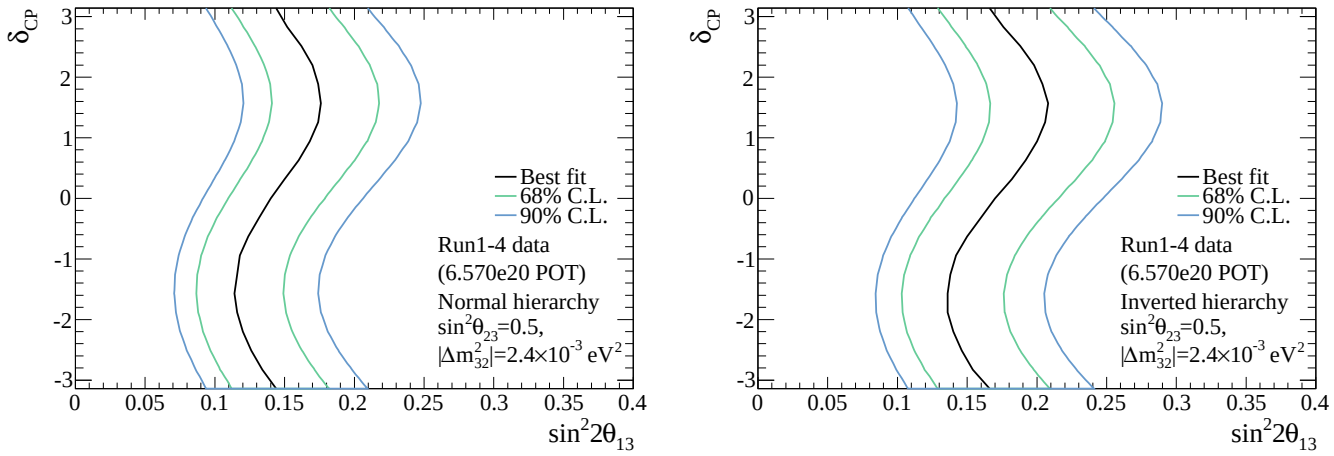

Figure 11.16: Allowed region of 68 % (green) and 90 % C.L. (blue) for $\sin^2 2\theta_{13}$ for each value of $\delta_{\rm CP}$, for normal (left) and inverted (right) hierarchy. The black solid line is the best fit value for each value of $\delta_{\rm CP}$. Left (right) plot: normal (inverted) hierarchy is assumed.

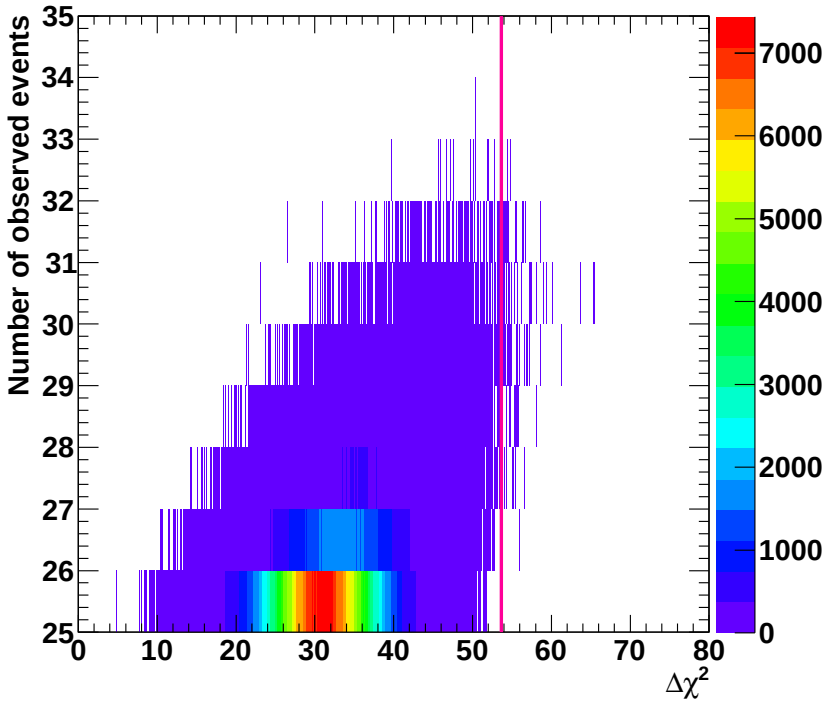

Figure 11.17: Distribution of $\Delta\chi^2$ for different number of observed events, in the case of $\sin^2 2\theta_{13} = 0$ over 9.6×10^{14} toy MC experiments for 6.570×10^{20} POT, $N_{obs} > 24$. The systematic errors are incorporated. The $\Delta\chi^2$ value for Run1-4 data was 53.64, which is shown as a pink line in the plot.

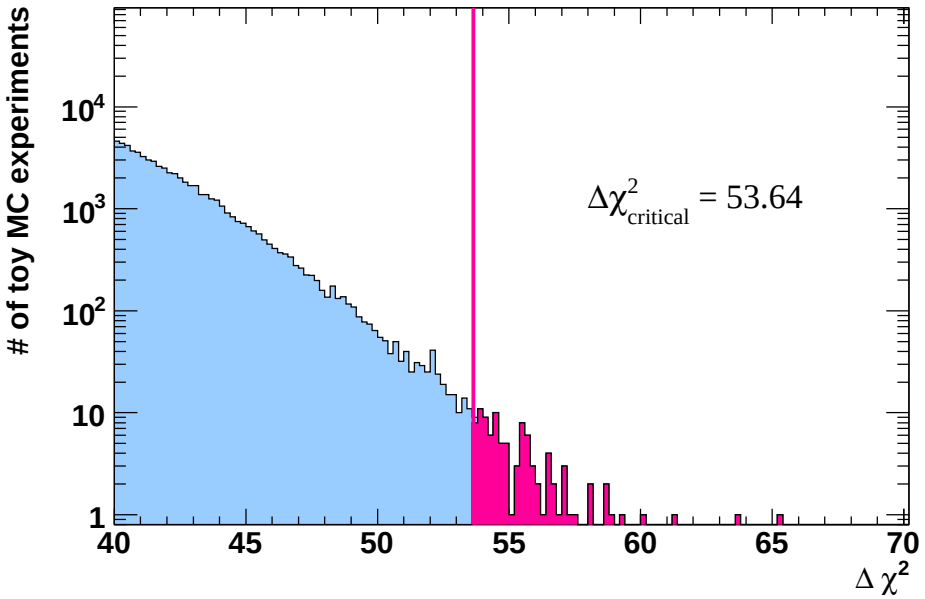

Figure 11.18: Distribution of $\Delta\chi^2$ in the case of $\sin^2 2\theta_{13} = 0$ over 9.6×10^{14} toy MC experiments for 6.570×10^{20} POT, $N_{obs} > 24$. The systematic errors are incorporated. The $\Delta\chi^2$ value for Run1-4 data was 53.64, which is shown as a pink line in the plot. The integrated fraction of toy MC experiments for which the $\Delta\chi^2 > 53.64$ is 1.0×10^{-13}.

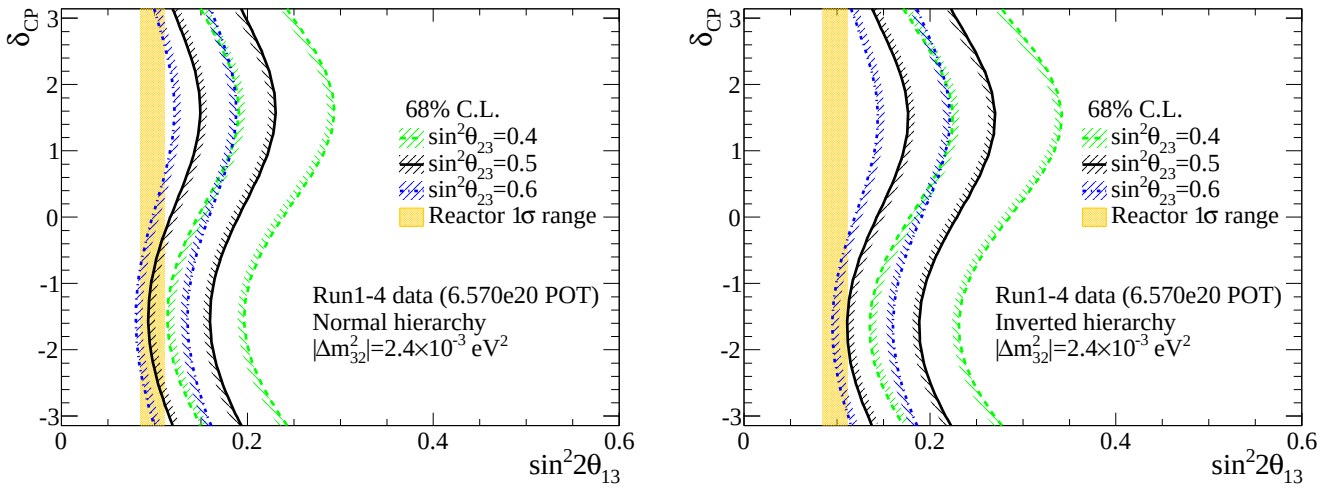

Figure 11.19: Allowed region of 68 % C.L. for $\sin^2 2\theta_{13}$ for each value of $\sin^2\theta_{23}$, for Run1-4 data. The green, black and blue contours corresponds to $\sin^2\theta_{23} = 0.4, 0.5$ and 0.6. The $|\Delta m^2_{32}|$ is fixed to 2.4×10^{-3} eV^2. The yellow shaded region shows the reactor 1σ range (0.098 ± 0.013) from PDG2012. Left (right) plot: normal (inverted) hierarchy is assumed.

11.7 Results using the reactor measurements

In this section, we incorporate the uncertainties of $\sin^2\theta_{23}$ and Δm^2_{32} in the fit by allowing them to vary. We apply constraints to these parameters by using the result of T2K ν_μ disappearance measurement. We also add a constraint on $\sin^2 2\theta_{13}$ from the reactor experiments to measure the δ_{CP}. In this section, we discuss the method to add a constraint from the other measurements.

11.7.1 Constraint term and marginalization

The constraint from other measurements can be added by introducing a constraint term $\mathcal{L}_{const.}$ in the likelihood.

$$\mathcal{L}(N_{obs.}, \boldsymbol{x}; \boldsymbol{o}, \boldsymbol{f}) = \mathcal{L}_{norm}(N_{obs.}; \boldsymbol{o}, \boldsymbol{f}) \times \mathcal{L}_{shape}(\boldsymbol{x}; \boldsymbol{o}, \boldsymbol{f}) \times \mathcal{L}_{syst.}(\boldsymbol{f}) \times \mathcal{L}_{const.}(\boldsymbol{o}). \tag{11.12}$$

The constraint term represents the prior probability density function of the oscillation parameters. We define the constraint term for θ_{23} and Δm^2_{32} as follows:

$$\mathcal{L}_{const.}(\boldsymbol{o}) = \exp\left(-\frac{\chi^2(\sin^2\theta_{23}, \Delta m^2_{32})}{2}\right), \tag{11.13}$$

where the χ^2 is calculated by using the $\Delta\chi^2$ map obtained from T2K Run1-3 ν_μ disappearance measurement [22] (Fig. 11.20). The best fit values of $\sin^2\theta_{23}$ and Δm^2_{32} are: $\sin^2\theta_{23}$ =0.514±0.082 and Δm^2_{32} =$2.44^{+0.17}_{-0.15} \times 10^{-3}$ eV^2. The correlation of the systematic errors between ν_e appearance and ν_μ disappearance measurement is ignored in this analysis, because the effect of the systematic error correlation is negligibly small compared to the statistical error.

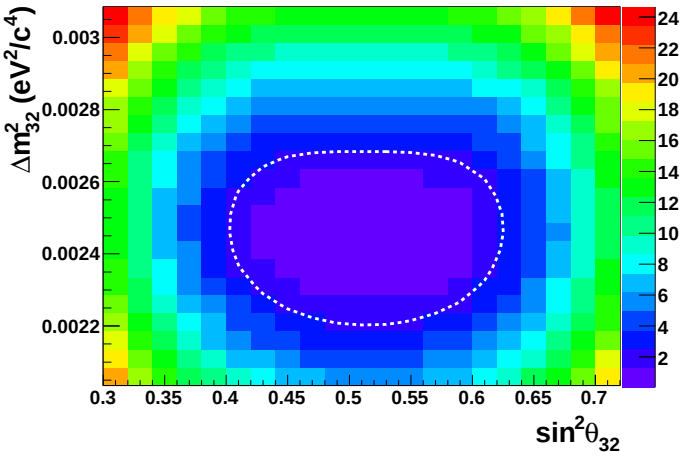

Figure 11.20: $\Delta\chi^2$ map for $\sin^2\theta_{23}$ and Δm^2_{32}, obtained from T2K Run1-3 ν_μ disappearance measurement. The white dotted line represents the 68% C.L. contour region.

When we further add the constraint on $\sin^2 2\theta_{13}$ from the reactor experiments, we use the following constraint term:

$$\mathcal{L}_{const.}(\boldsymbol{o}) = \exp\left(-\frac{\chi^2(\sin^2\theta_{23}, \Delta m^2_{32})}{2}\right) \times \exp\left(-\frac{(\sin^2 2\theta_{13} - 0.098)^2}{2 \times 0.013^2}\right), \tag{11.14}$$

where $\sin^2 2\theta_{13} = 0.098 \pm 0.013$ is the value from the PDG2012 [51], which was obtained by averaging the results of reactor measurements.

In the fit procedure, the constraint term is taken into account by calculating the marginal likelihood. The method to marginalize over the oscillation parameters is same as the method we used to marginalize over the systematic parameters, which is explained in Section 11.2.2. When we marginalize over the systematic parameters, we throw the systematic parameters according to $\mathcal{L}_{syst.}$ (Eq. 11.5). When we marginalize over some of the oscillation parameters, we throw the systematic parameters and the oscillation parameters at the same time.

11.7.2 Fit results with θ_{23} and Δm^2_{32} varied

In this section, we use the constraint term defined in Eq. 11.13, to take into account the uncertainty on $\sin^2\theta_{23}$ and Δm^2_{32}. Before performing the fit to data, we checked the sensitivity by fitting toy MC data sets. Figure 11.21 shows the negative log likelihood curves, averaged over 4000 toy MC experiments. The true values for the oscillation parameters in MC are fixed to the default values in Table 11.2. The likelihood is marginalized over θ_{23} and Δm^2_{32} for the pink curve, while they are fixed in the black curve. The pink curve is lower than the black curve due to the additional uncertainty of θ_{23} and Δm^2_{32}. The expected significance to exclude $\theta_{13} = 0$ is 5.65σ (assuming normal hierarchy).

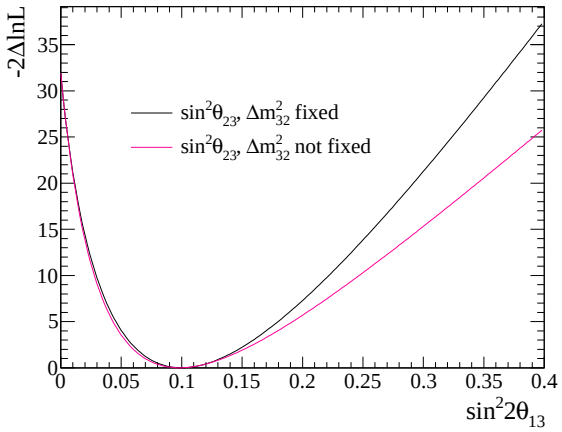

Figure 11.21: Negative delta log likelihood as a function of $\sin^2 2\theta_{13}$, averaged over 4000 toy MC experiments. The sensitivity is obtained from these curves. In the fit, the values of $\sin^2\theta_{23}$ and Δm^2_{32} are fixed to 0.5 and 2.4×10^{-3} for the black curve, while for the pink curve we marginalize over $\sin^2\theta_{23}$ and Δm^2_{32} with constraint from the T2K Run1-3 ν_μ disappearance measurement. The true value of the oscillation parameters to generate toy data sets are fixed to the nominal values. Toy MC experiments are generated in normal hierarchy and fitted assuming normal hierarchy.

The results of the fit to Run1-4 data is shown in Figure 11.22. The best fit values and the C.L. regions are summarized in Table 11.11. The best fit values and the significance to exclude $\theta_{13} = 0$ slightly decreased by marginalizing over $\sin^2\theta_{23}$ and Δm^2_{32}, and the C.L. regions became wider. Figure 11.23 shows the allowed region for $\sin^2 2\theta_{13}$ for each value of $\delta_{\rm CP}$. The C.L. regions are wider than the contours in Fig. 11.16, in which the values of $\sin^2\theta_{23}$ and Δm^2_{32} are fixed.

11.7.3 Fit results with reactor measurements

We extract the constraint on $\delta_{\rm CP}$ by combining our measurements with the reactor measurements, by using the constraint term defined in Eq. 11.14.

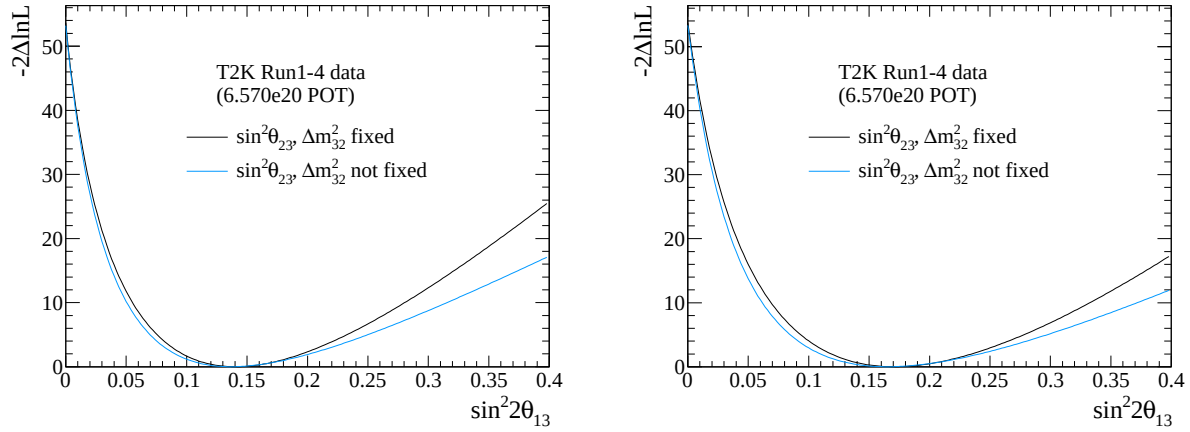

Figure 11.22: Comparison of the negative log likelihood as a function of $\sin^2 2\theta_{13}$, with (blue) and without (black) marginalizing over θ_{23} and Δm^2_{32}, for the T2K Run1-4 data. Left (right) plot shows the result assuming normal (inverted) hierarchy.

Table 11.11: Summary of the fit results for Run1-4 data (6.570×10^{20}), with and without marginalizing over θ_{23} and Δm^2_{32}, with $\delta_{\rm CP} = 0$.

Fit configuration		Normal hierarchy	Inverted hierarchy
$\sin^2\theta_{23} = 0.5$, $\Delta m^2_{32} = 2.4\times10^{-3}$ eV^2	best-fit	0.140	0.170
	68 % C.L.	0.108 - 0.178	0.133 - 0.215
	90 % C.L.	0.090 - 0.205	0.111 - 0.246
	Significance	7.32σ	7.33σ
Marginalized over $\sin^2\theta_{23}$ and Δm^2_{32}	best-fit	0.136	0.166
	68 % C.L.	0.103 - 0.180	0.124 - 0.217
	90 % C.L.	0.084 - 0.214	0.102 - 0.256
	Significance	7.29σ	7.30σ

Figure 11.24 shows the negative delta log likelihood curve for Run1-4 data. In this plot, the χ^2_{min} is defined from the minimum between two hierarchies.

The best fit value of $\delta_{\rm CP}$ is -1.65 (-1.57) for normal (inverted) hierarchy case, which is close to $-\pi/2$. The fitter finds the best fit value around $-\pi/2$ when the number of observed events is larger than expected. Assuming $\sin^2 2\theta_{13} = 0.1$, $\sin^2\theta_{23} = 0.5$, $\Delta m^2_{32} = 2.4\times10^{-3}$ eV^2 and normal hierarchy, the expected number of ν_e events is 25.4, while we observed 28 events. The expected number of ν_e events become largest at $\delta_{\rm CP} = -\pi/2$, because the CPV term in $P(\nu_\mu \to \nu_e)$ (Eq. 1.17) is proportional to $-\sin\delta_{\rm CP}$. Therefore our data prefers $\delta_{\rm CP} \sim -\pi/2$, but the best fit value is not exactly $-\pi/2$ for normal hierarchy case, due to the shape term. The normal hierarchy is preferred by our data, because the number of expected events is larger in the normal hierarchy case than in the inverted hierarchy case.

We derive the excluded region of $\delta_{\rm CP}$ by using the Feldman-Cousins method [138]. Using the Feldman-Cousins method, the critical $\Delta\chi^2$ value ($\Delta\chi^2_{crit}$) which correspond to the $\Delta\chi^2$ limits for 68% and 90% are derived. The critical $\Delta\chi^2$ value depends on the value of $\delta_{\rm CP}$ and hierarchy. For example, the value of $\Delta\chi^2_{crit}$ at $\delta_{\rm CP} = x$, in the normal hierarchy case is derived in the following way.

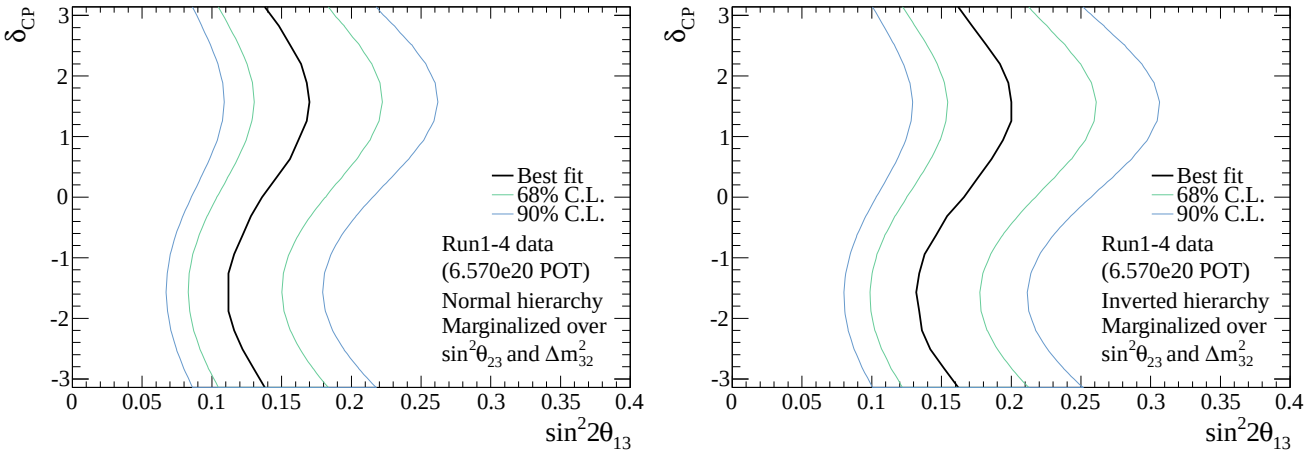

Figure 11.23: Allowed region of 68 % (green) and 90 % C.L. (blue) for $\sin^2 2\theta_{13}$ for each value of δ_{CP}, for Run1-4 data (6.570×10^{20} POT) [32]. The likelihood is marginalized over $\sin^2\theta_{23}$ and Δm^2_{32}. The black solid line is the best fit value for each value of δ_{CP}. Left (right) plot: normal (inverted) hierarchy is assumed.

1. Generate 4000 toy MC experiments assuming $\delta_{\mathrm{CP}} = x$ and normal hierarchy. The systematic parameters, $\sin^2\theta_{23}$, Δm^2_{32} and $\sin^2 2\theta_{13}$ are thrown according to $\mathcal{L}_{syst}$ and $\mathcal{L}_{const}$.

2. Fit each toy MC experiment assuming both normal and inverted hierarchy, and calculate the $\Delta\chi^2$ which is defined as follows.

$$\Delta\chi^2 = \chi^2_{true} - \chi^2_{min} \tag{11.15}$$

   where χ^2_{true} is the value of $-2\ln\mathcal{L}'$ at $\delta_{\mathrm{CP}} = x$ and normal hierarchy, and χ^2_{min} is the global minimum value of $-2\ln\mathcal{L}'$ from normal and inverted hierarchy.

3. Calculate the critical point of χ^2, such that 90% (68%) of toy MC experiments have $\Delta\chi^2 < \Delta\chi^2_{crit}$.

Figure 11.25 shows the critical χ^2 limits drawn on top of the negative delta log likelihood curve for δ_{CP} for Run1-4 data. The green (blue) lines correspond to 90% (68%) C.L. critical $\Delta\chi^2$, and the solid (broken) lines correspond to normal (inverted) hierarchy. The 90% C.L. excluded region of δ_{CP} is defined as the region where the likelihood curve is higher than the critical $\Delta\chi^2$ limits. In order to extract the 90% C.L. excluded regions, we further perform the Feldman-Cousins method with finer binning in δ_{CP}, only around the region where the likelihood curves cross the 90% C.L. limit. The bin size is $2\pi/20$ in Fig. 11.25, while we change it to $2\pi/80$ for the finer binning. The 90% C.L. excluded regions are summarized in Table 11.12.

Table 11.12: The 90% C.L. excluded region in δ_{CP} for Run1-4 data, extracted by using the Feldman-Cousins method.

	90% C.L. excluded region
Normal hierarchy	$0.604 \sim 2.509$
Inverted hierarchy	$-3.142 \sim -3.043$, $-0.132 \sim 3.142$

As shown in Fig. 11.24, the maximum value of $-2\Delta\ln\mathcal{L}'$ is 3.38 (5.76) for the normal (inverted) hierarchy, at $\delta_{\mathrm{CP}} = \pi/2$. In order to verify that this is not too large compared to the

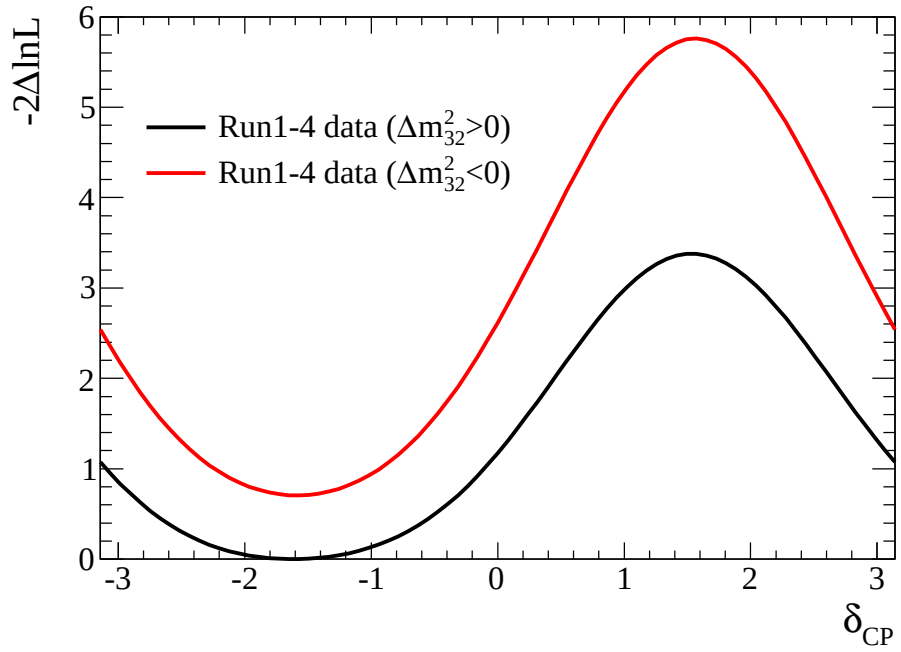

Figure 11.24: Negative delta log likelihood as a function of δ_{CP}, for T2K Run1-4 data. Black (red) curve shows normal (inverted) hierarchy case [32]. Likelihoods are marginalized over $\sin^2\theta_{23}$, Δm^2_{32} and $\sin^2 2\theta_{13}$.

expectation, we compare this value with large number of toy MC experiments. Fig. 11.26 shows the distribution of $-2\Delta \ln \mathcal{L}'$ at $\delta_{\mathrm{CP}} = \pi/2$, for 4000 toy MC experiments. Normal (inverted) hierarchy is assumed in the fit for the left (right) plot. In the toy MC experiments, the true value of δ_{CP} is set to $-\pi/2$, and the other oscillation parameters are set to the nominal values. The fraction of toy MC experiments above 3.38 (5.76) is 34.1% (33.4%) for normal (inverted) hierarchy. Therefore, the data is consistent with MC.

We fit the toy MC experiments to check the sensitivity of the fit. Figure 11.27 shows the negative log likelihood curve as a function of δ_{CP}, averaged over 4000 toy MC experiments. Again, the true value of δ_{CP} for the toy MC experiments is set to $-\pi/2$, and the other oscillation parameters are fixed to the nominal values in Table 11.2. The black and red curves correspond the fits assuming normal and inverted hierarchy, but in both cases, toy MC experiments are generated with normal hierarchy. We extract the expected 90% C.L. exclusion region from these averaged negative log likelihood curves using the Feldman-Cousins method. The expected exclusion regions are summarized in Table 11.13. The size of the exclusion regions in MC are comparable with those in data. The exclusion regions are wider in data, because we observed 28 ν_e candidate events, while the the expected number of events is 25.4 with $\sin^2\theta_{23} = 0.5, \Delta m^2_{32} = 2.4 \times 10^{-3}$ eV^2, $\sin^2 2\theta_{13} = 0.098$ and $\delta_{\mathrm{CP}} = -\pi/2$.

Figure 11.28 and 11.29 shows the momentum and angular distributions for the T2K Run1-4 data compared with MC with $\delta_{\mathrm{CP}} = -\pi/2$, 6.570×10^{20} POT. In these plots, the MC true values for $\sin^2 2\theta_{13}$, $\sin^2\theta_{23}$ and Δm^2_{32} are taken from the reactor average value and the best fit value in T2K Run1-3 ν_μ disappearance measurement ($\sin^2 2\theta_{13} = 0.098, \sin^2\theta_{23} = 0.514, \Delta m^2_{32} = 2.44 \times 10^{-3}$ eV^2). The distributions in data looks consistent with MC.

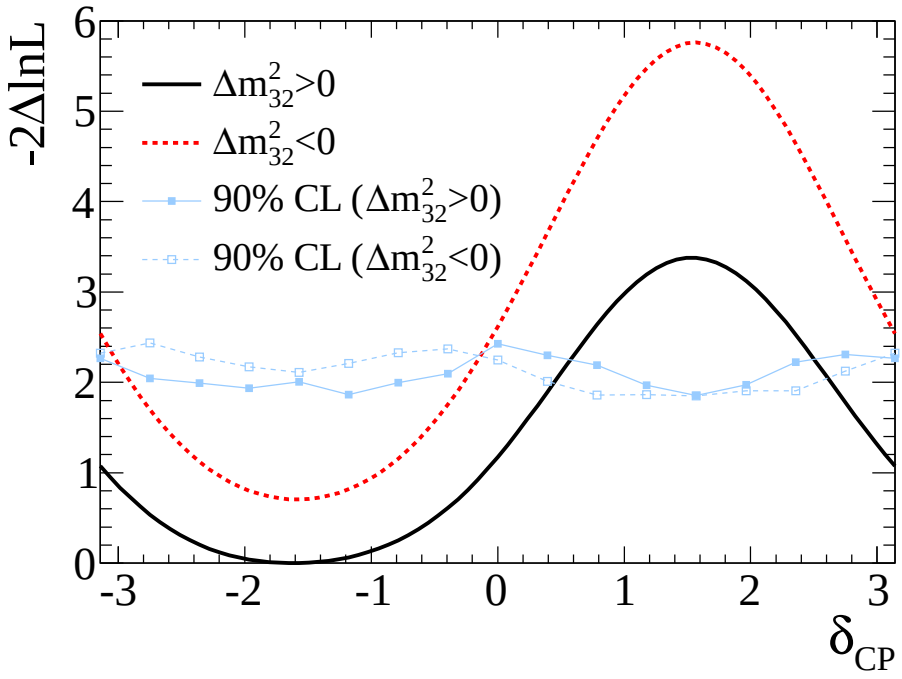

Figure 11.25: Critical χ^2 90% C.L. limit drawn on top of Fig. 11.24. The blue line corresponds to the critical $\Delta\chi^2$ for 90% C.L., extracted by using the Feldman-Cousins method. The solid (broken) lines correspond to normal (inverted) hierarchy [32].

Table 11.13: The 90% C.L. excluded region in δ_{CP} for averaged toy MC likelihood curves, extracted by using the Feldman-Cousins method. The toy MC experiments are generated assuming normal hierarchy and $\delta_{CP} = -\pi/2$.

	90% C.L. excluded region
Normal hierarchy	$1.122 \sim 1.971$
Inverted hierarchy	$0.280 \sim 2.850$

11.8 Summary

The updated result of the T2K $\nu_\mu \rightarrow \nu_e$ oscillation measurement is presented in this thesis. Compared to the previous result presented in 2012, there are many improvements in the 2013 analysis. The number of protons on target was increased from 3.01×10^{20} POT to 6.57×10^{20} POT. The uncertainties of the neutrino flux and cross section was significantly reduced from 5.0% to 2.9% (at $\sin^2 2\theta_{13} = 0.1$), because the uncertainty of single pion production cross section was reduced by measuring CC1π^+ events at ND280, using the FGD and TPC tracks (Chapter 9). The number of NCπ^0 background events was reduced by ∼70%, using the new π^0 rejection cut in the SK ν_e event selection (Chapter 10). The FSI+SI error (2.3% at $\sin^2 2\theta_{13} = 0.1$) is one of the dominant systematic errors, but it will become negligible in the future by using the improved pion interaction model (Chapter 6).

With the fixed parameters $\Delta m^2_{32} = 2.4 \times 10^{-3}$ eV^2, $\sin^2 2\theta_{23} = 1.0$ and $\delta_{CP} = 0$, we obtained the best fit value as $\sin^2 2\theta_{13} = 0.140^{+0.038}_{-0.032}$ ($\sin^2 2\theta_{13} = 0.170^{+0.045}_{-0.037}$) for normal (inverted) hierarchy case. The significance to exclude $\theta_{13} = 0$ is 7.3σ for both hierarchy cases. This is the first

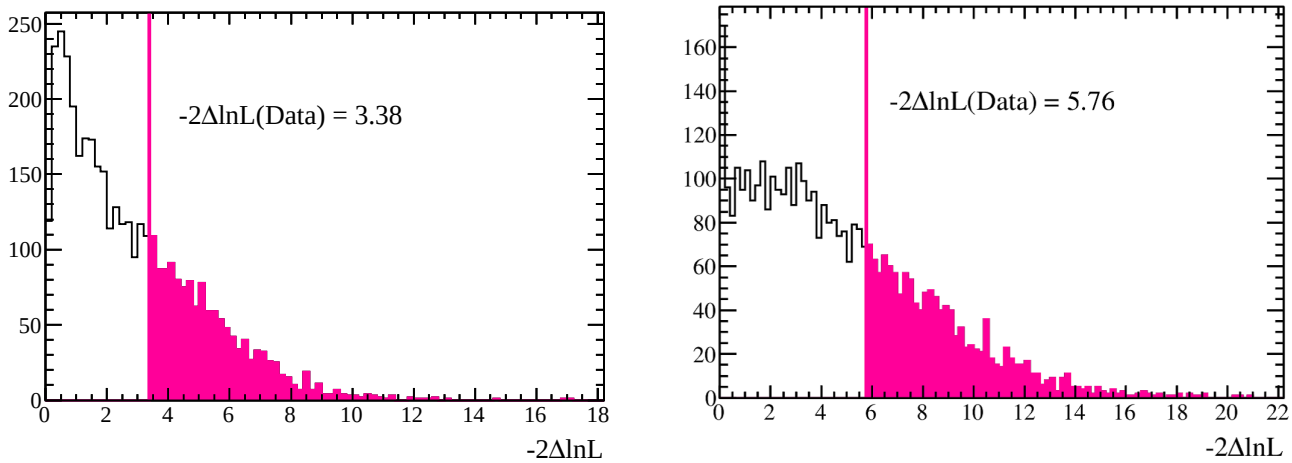

Figure 11.26: Distribution of $-2\Delta \ln \mathcal{L}'$ at $\delta_{\mathrm{CP}} = \pi/2$, for 4000 toy MC experiments. The left (right) plot shows the distribution for the fit assuming normal (inverted) hierarchy. The pink line corresponds to the -2$\Delta \ln \mathcal{L}'$ value obtained for data. The true values in MC is set to $\sin^2 2\theta_{13}$= 0.1, $\sin^2 \theta_{23} = 0.5, \Delta m^2_{32} = 2.4 \times 10^{-3}$ eV^2 and $\delta_{\mathrm{CP}} = -\pi/2$.

time to observe the appearance of a different neutrino flavor from neutrinos of another flavor with more than 5σ significance.

The constraint on δ_{CP} was derived by combining the T2K result with the $\sin^2 2\theta_{13}$ measurements from the reactor experiments. The uncertainties of $\sin^2 \theta_{23}$ and Δm^2_{32} were taken into account by using the constraint from T2K Run1-3 ν_μ disappearance analysis. The 90% excluded region of δ_{CP} is obtained as $0.604 \sim 2.509$ ($-3.142 \sim -3.043$, $-0.132 \sim 3.142$) for normal (inverted) hierarchy case. There are several other experiments which give constraint in δ_{CP} [139, 140], but our constraints gives the strongest constraint among these experiments. The constraint from our measurement is still weak to claim an evidence of non-zero δ_{CP}, but this is a great achievement.

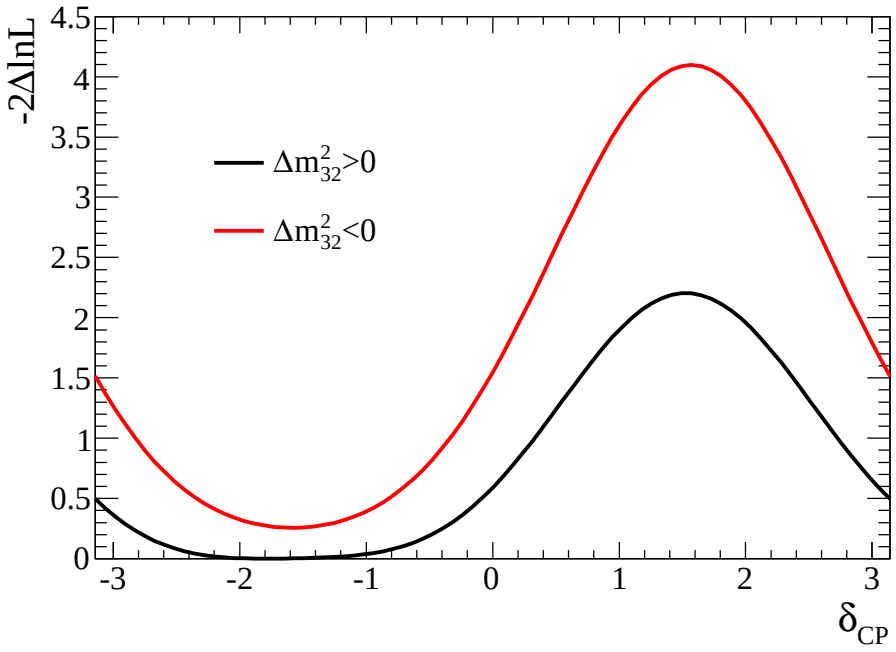

Figure 11.27: Negative log delta likelihood as a function of δ_{CP}, averaged over 4000 toy MC experiments, for 6.570×10^{20} POT case. Black (red) curve shows normal (inverted) hierarchy case. Likelihoods are marginalized over $\sin^2\theta_{23}, \Delta m^2_{32}$ and $\sin^2 2\theta_{13}$.

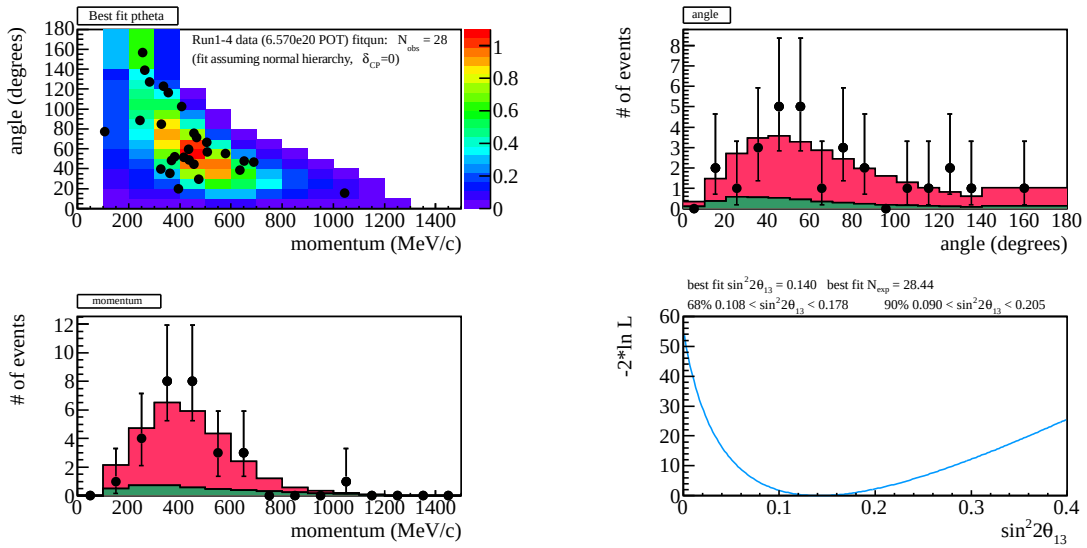

Figure 11.28: Run1-4 full data compared to MC with $\delta_{\mathrm{CP}} = -\pi/2$, $\sin^2 2\theta_{13} = 0.098$, $\sin^2\theta_{23} = 0.514$, $\Delta m^2_{32} = 2.44\times10^{-3}$ eV^2 and normal hierarchy.

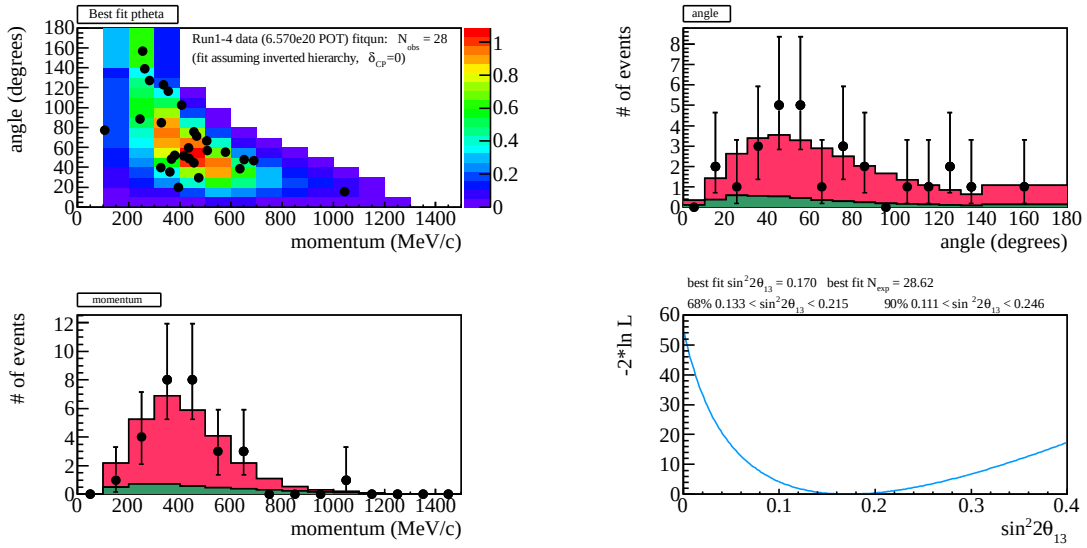

Figure 11.29: Same as Fig. 11.28, for inverted hierarchy case.

Part V

Conclusion

Chapter 12

Conclusion

The study of neutrino oscillations provides a unique window to physics beyond SM. There have been a lot of progress in the neutrino oscillation physics in the recent years. The mixing angle θ_{13} is finally measured in 2012. To date, we know the value of all of the three mixing angles $(\theta_{12}, \theta_{23}, \theta_{13})$ and the mass splittings $(\Delta m^2_{12}, |\Delta m^2_{32}|)$. However, the value of CP phase $\delta_{\rm CP}$ is still not known yet.

In this thesis, we reported the measurement of $\nu_\mu \to \nu_e$ oscillation. This oscillation mode is particularly important because it is sensitive to the value of $\delta_{\rm CP}$ and θ_{13}. There are two fundamental questions related to the measurement of neutrino oscillation.

- Is there a CP violation in the lepton sector?
- What is the physics behind the mixing pattern?

Precise measurement of $\nu_\mu \to \nu_e$ is essential to address these questions.

In the T2K neutrino oscillation analysis, the dominant systematic error is originated from the uncertainty in the measurement of neutrino-nucleus interactions. When we measure the neutrino beam at ND280 and SK, we select the CCQE interaction ($\nu + N \to l + N$) as a signal, while the main background for CCQE is CC1π interaction ($\nu + N \to l + N + \pi$). Distinguishing these two interaction modes is very important in the measurement of neutrino oscillation.

The FGD is the key detector in the ND280 detector complex for distinguishing the neutrino interaction modes. The CCQE and CC1π^+ interaction modes can be distinguished by detecting the pion track in the final state. Because the FGD is made of fine-grained scintillator bars and acts as active target, it is capable of detecting the short-ranged pion tracks around the interaction vertex. The light from scintillator bars are read out by the MPPCs, which are suitable to be used in ND280 thanks to its compactness and insensitivity to magnetic fields. We developed a new track reconstruction algorithm based on the Radon transform method. Using this algorithm, the reconstruction efficiency for multiple tracks is increased by $\sim$15%.

In the CC1π^+ interaction, pions are often absorbed inside a nuclei before being observed in the detector. Also, π^+ may convert to π^0 via the charge exchange interaction ($\pi^+ + N \to \pi^0 + N$). When the pion absorption (ABS) or charge exchange (CX) happens, there are no π^+ in the final state, so the CC1π event is misidentified as the CCQE event. About half of the π^+ in the final state of CC1π interactions disappear before escaping the nuclei due to ABS and CX. Although these interactions are important, we apply a large uncertainty in the pion-nucleus interaction model, because the uncertainties in the past pion-nucleus cross section measurements used for tuning the model parameters is large. The uncertainties of $\pi-$C cross section in the past experiments is typically $\sim$25% for ABS and $\sim$50% for CX. The uncertainty in ABS and CX results in the uncertainty of the number of ν_e signal candidate events at SK.

In order to reduce the uncertainties in those pion interactions, we performed a pion-nucleus cross section measurement at the pion secondary beam line at TRIUMF. A scintillating fiber

tracking detector was newly developed for this measurement. As it is super-fine-grained and fully active, we were able to select the ABS and CX interaction with high efficiency (∼80%) and high purity (∼75%). We measured the sum of ABS and CX cross section with total uncertainty of ∼6.5%. Compared to the uncertainties of the past experiments, the uncertainty is improved by a factor of 2.

By using this results together with the $\pi-$C cross section data sets from past experiments, we tuned the parameters in the pion-nucleus interaction model used in T2K. By improving the tuning method and using our own new data sets, we reduced the uncertainty of the model parameters to ∼1/4. In the current T2K neutrino oscillation analysis, the improved model is not used yet. Without this improvement, the uncertainty of the model results in 2.3% error for the number of ν_e events at SK (assuming $\sin^2 2\theta_{13} = 0.1$). This is one of the dominant systematic error sources in 2013 ν_e appearance analysis. This error will become negligible once we use the improved model.

Compared to the T2K ν_e appearance analysis in 2012, the measurements at both ND280 and SK were improved. In ND280, we changed the event categorization that we use in the ν_μ beam measurement. There were only two categories (CCQE-like, non-CCQE-like) in 2012, while in this analysis we divided the sample to three categories (CC0π, CC1π^+ and CC other), using the reconstructed tracks at TPC and FGD. With this new categorization, the systematic errors for the single pion production cross section was reduced, and the uncertainty of the predicted number of ν_e events related to the ND280 measurement was reduced to 2.9% (assuming $\sin^2 2\theta_{13} = 0.1$), while it was 5.0% in 2012.

In the SK ν_e event selection, the cut to reject the background from NC1π^0 interaction ($\nu_\mu + N \to \nu_\mu + N + \pi^0$) was improved by using a new event reconstruction algorithm. The new algorithm defines the particle type, vertex position and momentum at the same time by using a maximum likelihood method, while in the old algorithm those parameters were defined one by one. Using the new algorithm, the NC1π^0 background was reduced to less than half.

Using the improved measurement from ND280 and SK, we fitted the SK ν_e candidate events to extract the oscillation parameters. The data sets we used for this analysis was ∼2.2 times larger than the data sets used in 2012 analysis. The result of the fit assuming $\sin^2\theta_{23} = 0.5, \Delta m^2_{32} = 2.4 \times 10^{-3}$ eV^2, $\delta_{\rm CP} = 0$ and normal (inverted) hierarchy is:

Best fit: $\sin^2 2\theta_{13} = 0.140$ (0.170)
68% C.L.: $0.108 < \sin^2 2\theta_{13} < 0.178$ ($0.133 < \sin^2 2\theta_{13} < 0.214$)
90% C.L.: $0.090 < \sin^2 2\theta_{13} < 0.205$ ($0.111 < \sin^2 2\theta_{13} < 0.246$)

The significance to exclude $\theta_{13} = 0$ was 7.3σ for both hierarchy cases. We also performed a fit with the uncertainty of $\sin^2\theta_{23}$ and Δm^2_{32} taken into account. The constraints on $\sin^2\theta_{23}$ and Δm^2_{23} are applied by using the results from T2K Run 1-3 ν_μ disappearance measurement.

Best fit: $\sin^2 2\theta_{13} = 0.136$ (0.166)
68% C.L.: $0.103 < \sin^2 2\theta_{13} < 0.180$ ($0.124 < \sin^2 2\theta_{13} < 0.217$)
90% C.L.: $0.084 < \sin^2 2\theta_{13} < 0.214$ ($0.102 < \sin^2 2\theta_{13} < 0.256$)

Finally, by adding the constraint on $\sin^2 2\theta_{13}$ from the average of reactor measurement ($\sin^2 2\theta_{13} = 0.098 \pm 0.013$), we obtained 90% excluded regions for $\delta_{\rm CP}$.

Normal hierarchy: $0.604 \sim 2.509$
Inverted hierarchy: $-3.142 \sim -3.043$, $-0.132 \sim 3.142$

Our data prefers $\delta_{\rm CP} = -\pi/2$. The constraint on $\delta_{\rm CP}$ is still weak to claim an evidence of non-zero CP violation, but this is an important milestone in the neutrino oscillation physics. T2K or the next generation experiments such as T2HK [141] may reveal the value of $\delta_{\rm CP}$ in the near future.

Appendix A

Simulation and the systematic errors in the pion interaction measurement

The detail of the detector simulation which we use in the pion interaction measurement is described in section A.1 and A.2. The systematic errors in the measurement is explained in detail in section A.3.

A.1 Detector

The detector geometry, material and response are included in the simulation.

Fiber core, clad and coating structure is implemented in the simulation. The fractional size of the coating part of the fiber affects the efficiency to detect a hit above 2.5 p.e. threshold for through going pions. The efficiency is measured to be ∼94% in MC, while it was measured to be 93% in the real data.

The mis-alignment of the fiber layer position is measured from the difference between measured hit position and the expected hit position in through going pion data. The distance from the nominal position is measured to be 0±80 μm, and implemented in the simulation by setting the layer position to the measured position for that layer.

The light yield of the fibers in simulation are tuned so that it agree with pion through going data. The energy deposit for each fiber in simulation is converted to p.e. in the following procedure.

1. Conversion from an energy deposit to the number of photons
   The expected number of photons generated in the fiber is calculated by multiplying the value of energy deposit by a conversion factor C_{conv} (∼57 p.e. / MeV), which is defined for channel by channel from the light yield distribution observed in through going pion data.
   $$\text{The expected number of photons} = C_{conv} \times \text{(energy deposit)},$$
   The saturation of scintillation light is taken into account by using Birk's formula, in the same way as we do in the simulation of FGD. The Birk's constant that we use for the fiber is same as the value that we use in FGD, because the material of the scintillator is same for both FGD and PIAνO fiber (Polystyrene).

2. Adding an effect of statistical fluctuation
   The number of photo-electrons is randomly defined from the Poisson distribution with the mean of the expected number of photons. The statistical fluctuation in the multiplication of electrons in PMT is taken into account by randomly fluctuating the observed number of photo-electrons assuming Gaussian fluctuation.
   $$\text{Observed number of photons} = N + \sqrt{N} \times C_{fluc} \times \text{Gauss}(1),$$

where N is the number of photons before fluctuation, Gauss(1) is a random value which follows Gaussian distribution with mean = 0 and sigma = 1. The size of the fluctuation C_{fluc} is ~60%, and it is defined for channel by channel. They are defined from the charge distribution of 1 p.e. light, which was measured in a bench test by using LED.

3. Adding an effect of the response of electronics
   The number of photo-electrons is converted to ADC count by multiplying the conversion factor $C_{conv2} \sim 60$ ADC / p.e. which is defined by measuring 1 p.e. light from LED in a bench test. Then we apply an empirical non-linearity correction as follows:
   $$\text{Corrected ADC} = \text{Raw ADC} \;/\; (1 + C_{nonlin} \times \text{Raw ADC}),$$
   where C_{nonlin} is 0.000135 / ADC. In case the ADC count is greater than 4095, it is set to 4095 to account for an overflow of the electronics.

The conversion factor C_{conv} and non-linearity correction factor C_{nonlin} are defined by fitting charge distribution of through going pions with $p_\pi = 150$ and 300 MeV/c. In the fit, we scanned over the parameter space and searched for the value which minimizes $\chi^2 = \sum(N_i^{data} - N_i^{MC})^2/\sigma_i^2$, where N_i^{data} and N_i^{MC} are the number of entries in i-th bin of charge distribution, σ_i is the statistical error for that bin. Figure A.1 shows the charge distribution for data, compared with MC after fit. The charge distribution in MC reproduces the distribution in data very well.

The crosstalk hits are also implemented in the simulation. For each of the "real" hit which is associated with particle trajectory, crosstalk hits are generated in adjacent channels in MAPMT. The expected number of photons for those crosstalk hits are calculated by multiplying the "real" hit by crosstalk probability. Crosstalk probability in MC is tuned so that the charge distribution of crosstalk hits in the through going pion data agree with data. In this tuning, crosstalk hits are selected from the hits which were not on the pion track. The crosstalk probability for adjacent channel in MAPMT is determined to be ~2%, and the crosstalk between adjacent fiber due to light which leak through the reflective coating is determined to be ~0.8%.

The simulation and calibration procedure for the Harpsichord detector is same as those in the FGD. Figure A.2 shows an charge distribution for through going muons in $p_\pi = 250$ MeV/c setting, for data and MC (in this thesis, we usually select the 250 MeV/c data set as an example). The agreement between data and MC is good except for the low p.e. region. The disagreement in the low p.e. region is due to MPPC noise hits, which is not implemented in simulation.

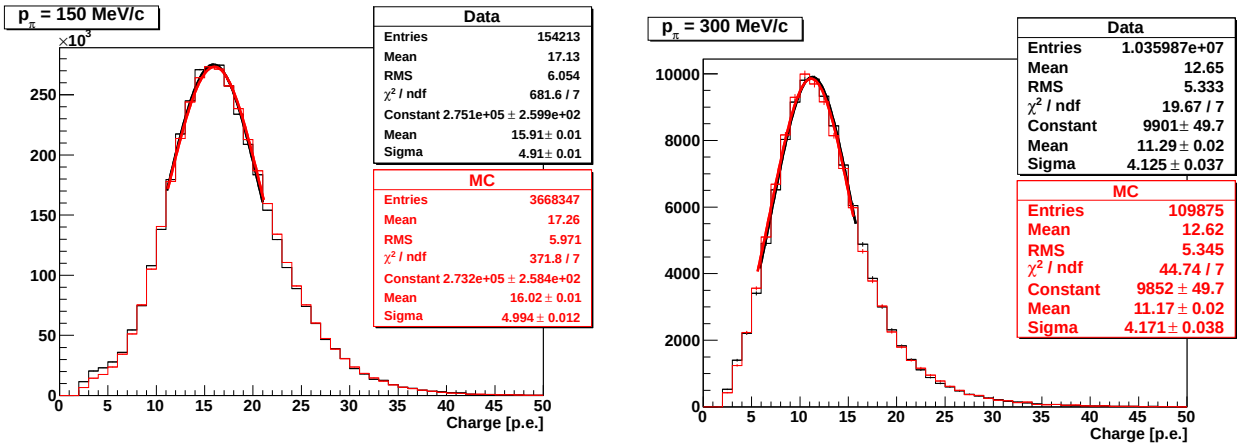

Figure A.1: Charge distribution of through going pions for data and MC, for $p_\pi = 150$ and 300 MeV/c data set.

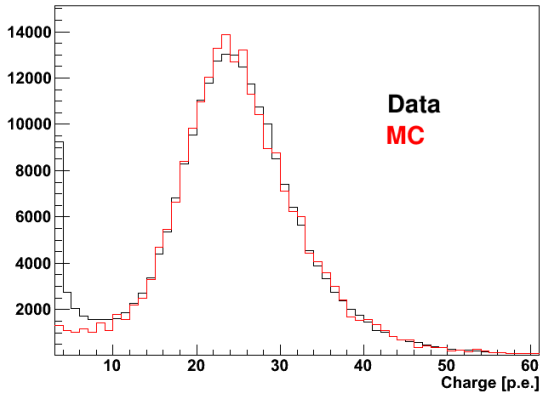

Figure A.2: Charge distribution of through going muons in $p_\pi = 250$ MeV/c setting.

A.2 Beam

The beam position distribution and momentum are measured in the data and reproduced in the simulation.

In the simulation, pions are generated 1 cm upstream from the S0 trigger. The X, Y position of the generation point, angular distribution of the beam are tuned so that the measured beam position distribution and the angular distribution of the through going tracks in fiber tracker agree between data and MC. Gaussian distribution is assumed for the initial position distribution and the angular distribution, and the mean and sigma of the distributions are tuned for X and Y. Figure A.3 and A.4 shows example of beam position distribution and angular distribution for data with 250 MeV/c setting, compared to distribution for MC after tuning.

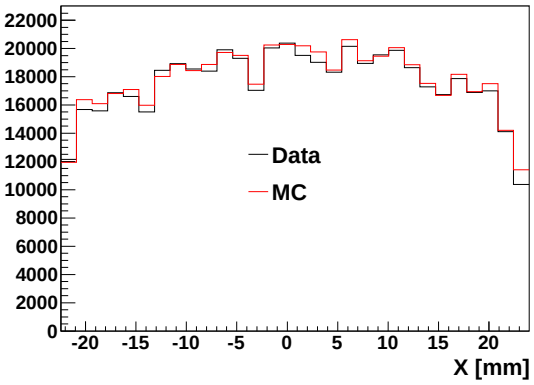

Figure A.3: Beam position distribution in X, for the data set with $p_\pi = 250$ MeV/c setting. The black (red) histogram shows the distribution for data (MC).

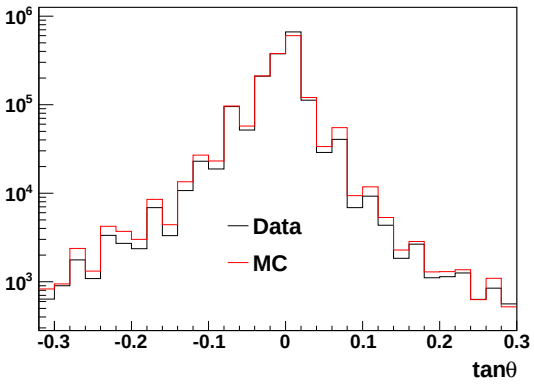

Figure A.4: Beam angular distribution in X projection, for the data set with $p_\pi = 250$ MeV/c setting. The variable θ is the angle from horizontal line (X=0). The black (red) histogram shows the distribution for data (MC).

The momentum of the beam is extracted from the pion stopping range in Harpsichord. It is also extracted from TOF measurement, and from the measurement in the past, and they all agree within the uncertainty of the measurements. Figure A.5 shows the stopping layer

distribution in Harpsichord for data with $p_\pi = 250$ MeV/c setting, compared with MC with in several different momentum. The actual momentum for 250 MeV/c setting is found to be 258.5 MeV/c, and the uncertainty is 0.8 MeV/c. The stopping range could not be measured for the data set with $p_\pi = 275$ and 300 MeV/c settings, because the pions penetrate the detector. For those data sets, the pion momentum is measured by fitting the charge distribution of the hits in Harpsichord. Figure A.6 shows the charge distribution for last three XY layers in Harpsichord, for through going tracks in data with $p_\pi = 300$ MeV/c setting and in MC with several different momentum settings. For this fit, as we did in tuning of the detector response parameters C_{conv} and C_{nonlin}, we defined a χ^2 from the difference between data and MC. Then the best value of the momentum is defined from the value which minimizes the χ^2. The incident pion momentum for this setting is measured to be 314 ± 1 MeV/c. The actual momentum of the pions at the fiber tracker is smaller than the incident momentum, because the pions lose their energy when passing through the Cherenkov counter and beam trigger counters. The measured incident pion momentum values and the estimated momentum at the fiber tracker is summarized in Table A.1, for five momentum data sets.

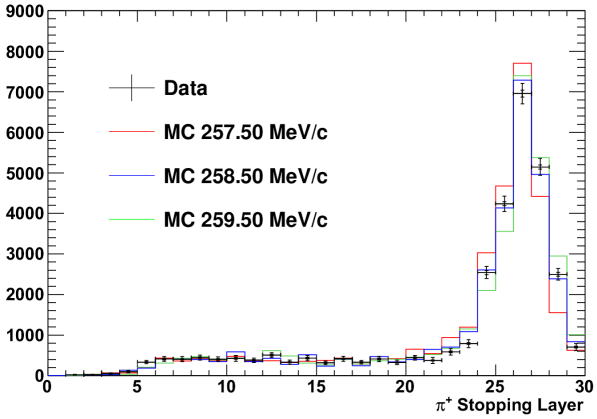

Figure A.5: Stopping layer distribution in Harpsichord, for data with 250 MeV/c settings and MC with several different momentum settings.

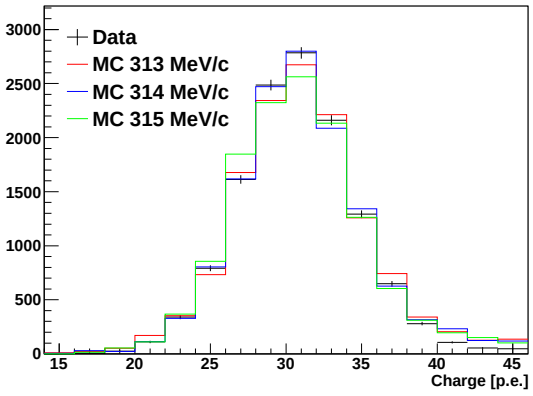

Figure A.6: Charge distribution of through going particles at the downstream three XY layers in Harpsichord, for data with $p_\pi = 300$ MeV/c setting and MC with several different momentum settings.

Momentum setting [MeV/c]	200	225	250	275	300
Incident momentum [MeV/c]	213.8	238.8	258.5	285.5	314.0
Momentum uncertainty [MeV/c]	0.5	0.8	0.6	0.5	1.0
Momentum at fiber tracker [MeV/c]	201.6	216.6	237.2	265.5	295.1
Fraction of muon [%]	0.16	0.71	0.43	0.54	0.34

Table A.1: The measured momentum and contamination of muons for five different data sets.

After the beam PID cut, more than 99% of the beam particles are pions, but the small fraction of muons remains. For 200, 225 and 250 MeV/c data sets, the fraction of muons in the beam is estimated from Cherenkov light vs. TOF distribution. In Figure A.7, the distance from the threshold line for the data points in Fig. 4.6 is plotted. In this plot, negative distance correspond to the region rejected by the beam PID cut. Fraction of muons in the beam is estimated by fitting

the peak which correspond to a muon by Gaussian distribution, and integrating the Gaussian distribution above 0.

For 275 and 300 MeV/c data sets, the fraction of muons can not be estimated in this way. Figure A.8 shows the distribution of the distance from the threshold for 300 MeV/c data set. Because the distribution of muons and pions overlap, the peak which correspond to the muon is not identified. The fraction of muons for these data sets are measured again by using the charge distribution of through going particles in Harpsichord. Figure A.9 shows the charge distribution of through going particles, measured in the last three XY layers of Harpsichord, for 300 MeV/c data set. The left and right plot corresponds to the distribution before and after applying the beam PID cut. The normalizations of histograms in the right plot for muon and pion in MC are tuned so that it agree with data. From this measurement, the contamination of muons after applying the beam PID cut is estimated to be 0.34 ± 0.34 % for 300 MeV/c data set. The fraction of muons in the beam is summarized in Table A.1.

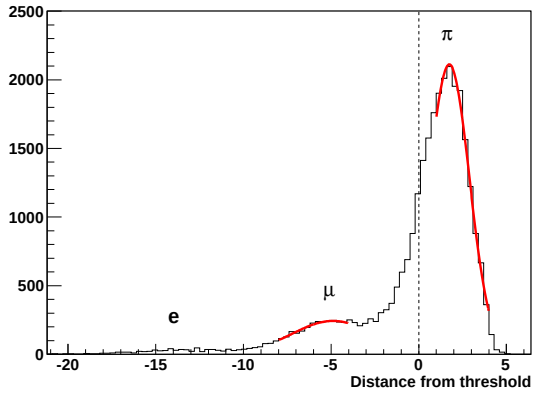

Figure A.7: Distribution of distance from the threshold line in Fig. 4.6.

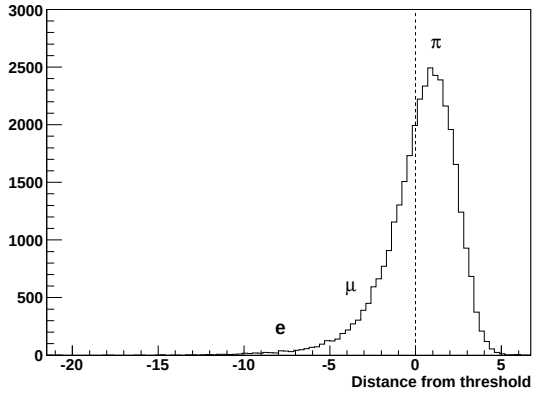

Figure A.8: Same as Fig. A.7, but for 300 MeV/c data set.

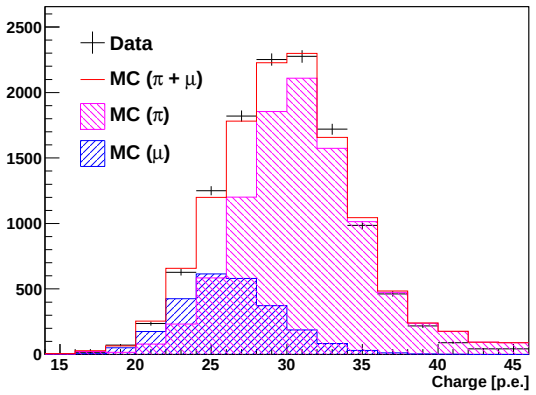

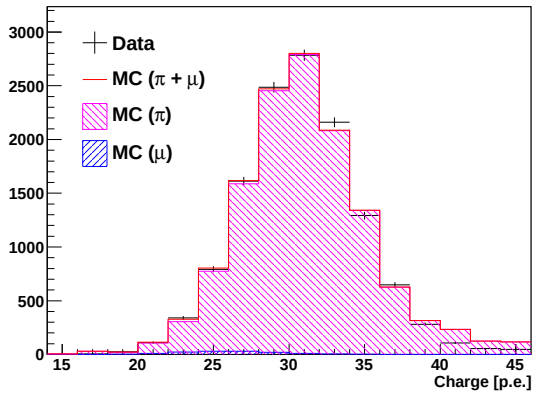

Figure A.9: Charge distribution of through going particles, measured in the last three XY layers of Harpsichord, for 300 MeV/c data set. The left (right) shows the distribution before (after) applying the beam PID cut. The normalization of muons and pion component in MC is tuned so that it agree with data.

A.3 Estimation of the systematic errors

In this section, we describe the detail of the estimation of the systematic errors in the pion interaction measurement. The summary of the systematic errors is shown in Table 5.6.

- Beam profile and momentum
  The position distribution of the beam is measured in through going pion data, and its mean and sigma is measured with $\sim$ 1 mm accuracy or less. The uncertainty of the beam momentum is less than 1 MeV/c. The effect of those uncertainties to the cross section calculation is estimated in MC, by changing those properties of the beam withing their uncertainty. The systematic error is defined from the difference in the cross section derived using nominal and changed MC data sets. The statistical error in MC data set should be taken into account. Number of events in MC is $\sim$ 3 times larger than data. The statistical error in MC is $\sim$0.6 %, and it is added to the error. The other systematic errors that we describe in the following text also includes the statistical error in MC, when they are derived by comparing nominal and changed MC.

- Fiducial volume
  Because of finite resolution in interaction vertex position reconstruction, an interaction which occurred inside the fiducial volume is sometimes reconstructed outside the fiducial volume, or vice versa. This event migration happens when the interaction occurred near the edge of the fiducial volume, and the size of this effect become more significant by changing the size of volume become smaller. The systematic error of this effect to the cross section is evaluated by calculating the cross section with two different definitions of the fiducial volume, FV1 and FV2. FV1 is smaller than the nominal fiducial volume by 4 fibers in XY direction and 2 layers in Z direction. FV2 is smaller than the nominal fiducial volume by 8 fibers in XY direction and 4 layers in Z direction.

- Charge distribution and crosstalk probability
  The parameters which defines the charge distribution in MC are C_{conv}, C_{fluc} and C_{nonlin}. The effect of the uncertainties of these parameters are evaluated by changing these parameters within their uncertainty in MC, as we did for the beam profile and momentum systematic errors. As for C_{conv} and C_{nonlin}, the best fit values are $(C_{conv}, C_{nonlin}) = (1.36, 0.000135)$, which are extracted by fitting the charge distribution in the data sets with 150 and 300 MeV/c settings. Two sets of values after 1 σ shift are defined to be (1.35, 0.000126) and (1.38, 0.000150), which are also evaluated from the fit. The value of C_{fluc} is defined from charge distribution of 1 p.e. light, and its measured uncertainty was $\sim$6 %. The uncertainty of the crosstalk probability is $\sim$10 %, and its effect to the cross section is also estimated by changing it in the MC.

- Layer alignment
  The shift in the position of fiber layers from the nominal position are measured in pion through going data. The effect of the uncertainty in the layer position to the cross section measurement is estimated by changing the layer position in MC to nominal and checking the difference in the measured cross section. As shown in Table 5.6, the error for the data sets with 225 MeV/c setting is larger than 2 %, while it is less than 1 % for the other data sets. This is assumed to be due to statistical uncertainty in the MC data sets. The statistical uncertainty in MC data sets can be reduced by increasing the amount of MC data sets, but the effect of the statistical uncertainty to the total systematic error is only $\sim$ 0.5 %, so we decided not to increase.

- Hit efficiency
  The efficiency to find a hit above 2.5 p.e. threshold for the charged particles passing through

the layer is measured in through going pion data. The efficiency for data was $\sim$ 93 %, while it was $\sim$ 94 % for MC, so the uncertainty is assumed to be $\sim$ 1 %. The effect to the cross section is estimated by randomly deleting the hits in MC with $\sim$ 1 % probability and checking the difference in the resulting cross section.

- Muon contamination
  The uncertainty in muon contamination directly affects the normalization of the measured cross section. For the data sets with 275 and 300 MeV/c settings, the fraction of muons in the beam is measured by using Harpsichord, and the absolute error is 0.3 and 0.2 %. For the other data sets, the fraction of muons is measured using TOF and Cherenkov light data. However, a small fraction of pions decay just before reaching the fiber tracker, and muons from the pion decay may pass the good incident pion cut. A fraction of those muons in the beam is estimated to be 0.8$\sim$0.9 %. Therefore, 0.8$\sim$0.9 % error is assigned for the cross section for these data sets.

- Target material
  The number of carbon nuclei in the fiducial volume is calculated from the materials which constitute the fiber. The number of carbon nuclei and its uncertainty is estimated to be $1.518\pm0.007\times10^{24}$, and this directly affects the normalization of the ABS + CX cross section. There is also an uncertainty in the number of ABS + CX events on O and Ti nuclei. The ABS + CX cross section for these nuclei and its uncertainty is estimated by interpolating the measurements from past experiment [70]. The uncertainty of ABS + CX cross section for those nuclei are estimated to be 11$\sim$14 %. Uncertainty for the number for O and Ti nuclei and the ABS + CX cross section uncertainty for those nuclei affects $R_{\mathrm{TiO}}^{\mathrm{data}}$ in Eq. 5.4.

- Physics model (selection efficiency)
  The efficiency to select ABS and CX events is expected to be different between data and MC, because the physics model in MC do not perfectly reproduce the real data. The N_{sig}^{pred} in Eq. 5.4 is affected by the uncertainty in the physics model. The ABS or CX events are misidentified as pion scattering event in following four cases, and the uncertainties for those events are evaluated for each of them. The systematic errors are summarized in Table A.2.

  Event reconstruction failure due to forward / backward going protons
  In the final state of ABS or CX events, when the angle of the proton tracks with respect to the beam direction is $\sim$ 180 degree (backward going), the proton track may overlap with the incident pion track, and the incident pion track is not reconstructed properly. Also, when the proton track angle is $\sim$ 0 degree, the interaction vertex position may be miss-reconstructed at the downstream of the true vertex position, outside the fiducial volume. Figure A.10 left plot shows angular distributions for backward going proton-like tracks for data and MC with p_π = 250 MeV/c setting. The ABS + CX event selection is applied for this plot. The background component (pion scattering) is subtracted according to the prediction in MC, and the histograms are normalized by number of events after subtraction. The data is 1.4 times larger in the region above $\theta > 160$ degrees. A same check is done for forward going proton-like track and the data is found to be 1.3 times larger in the region below $\theta < 20$ degree. In order to estimate the effect of this difference to the cross section measurement, we generated a re-weighted MC sample, in which the fraction of events with forward and backward angle proton track is increased to reproduce the data. Fig. A.10 right plot is the same distribution as in the left plot, but for nominal and re-weighted MC. For the re-weighted MC, number of backward angle proton tracks is 1.4 times larger than

the nominal MC, and number of forward angle proton tracks is 1.3 times larger than the nominal MC, which is same as data. The efficiency to reconstruct a interaction vertex inside the fiducial volume is compared between the nominal and re-weighted MC, and the difference is assigned for the systematic error for cross section. The systematic error varies from 0.4 % to 3.2 % depending on the data sets, because the agreement between data and MC was different for different data sets.

Protons misidentified as pions due to finite dQ/dx resolution

When a proton track is misidentified as pions in the dQ/dx cut due to finite dQ/dx resolution, those events are rejected by no π^+ cut. Probability to misidentify a proton track as a pion track is estimated from the dQ/dx difference in X and Y projections. As mentioned in Section 5.2, the dQ/dx is calculated from X or Y projection and not from both projections, to minimize the effect of saturation of the electronics. Figure A.11 shows examples of the dQ/dx distribution for the projection which was not used for the dQ/dx cut, but the dQ/dx is required to be above threshold in the other projection. The probability to pass the dQ/dx cut in one projection but not in the other projection is compared between data and MC. For example, for the left plot in Fig. A.11, the fraction of events below the threshold is 5 % for data, while it is 4 % for MC. Therefore, 25 % error is applied for the number of ABS and CX events with proton-like track reconstructed in this angular region, for this data set. Although this error is not small, the effect to the total cross section is not very large because the efficiency of the dQ/dx cut is large ($\sim$ 90 %) and the number of ABS or CX events which do not pass this cut is small.

High momentum protons misidentified as pions

A small fraction of ABS events have very high momentum protons ($>$ 600 MeV/c) in the final state, which can not be distinguished from pions. Figure A.12 shows an example of predicted momentum distribution of protons in the final state of ABS event for Geant4 and NEUT, for p_π =295.1 MeV/c case. A large difference is observed between two different models, and the difference in the fraction of events above 600 MeV/c is assigned as the error for the number of high momentum proton events. Because the number of high momentum proton events itself is small, the error for those events do not significantly affect the error in the cross section.

Electrons (positrons) from γ conversion in CX event misidentified as pions

When the γ-rays from π^0 decay in CX event is converted to electrons and positrons, those electron tracks may misidentified as pion tracks. Those CX events are rejected by no π^+ cut. The uncertainty for the number of those events are estimated from uncertainty in the fraction of CX events and the uncertainty in γ conversion probability. The uncertainty in fraction of CX events is $\sim$ 50 % [70], and uncertainty of γ conversion probability is $\sim$ 5 % [142]. The systematic errors for the cross section is small because the fraction of those events is only $\sim$ 2 % of the total number of ABS and CX events. [142].

- Physics model (background prediction)

In the pion scattering events, scattered pion tracks are not always reconstructed properly, especially when the scattered pion angle is near 90 degree and the particle track passed between fiber layers. Also, due to finite dQ/dx resolution, pion tracks are sometimes misidentified as protons. Those background events pass the event selection. Although the cross section of pion elastic scattering in MC is tuned, a linear interpolation of the data points from the past measurements do not perfectly reproduces the actual cross section. Therefore, we estimated the uncertainty for the number of predicted background events as follows.

Difference in pion scattering data sample

The number of pion scattering event in data is compared with MC by making pion scattering data sample. For this data sample, π-like track is required in the event selection instead of applying no π^+ cut. Figure A.13 shows example of angular distribution for π-like tracks, compared between data and MC. The angular distribution is divided in following six different regions: 0-30, 30-60, 60-100, 80-100, 100-130 and 130-160 degree. The definition of these are different from the angular regions that we use in dQ/dx cut, because the region around 90 degree is important and it should not be divided into two regions. For each region, the difference between data and MC is assigned for the error for number of predicted background events in that region.

Back-scattered pions

For the angular region above 160 degree, a special data sample is prepared to compare the difference between data and MC. When the scattering angle is near 180 degree, the scattered pion track overlaps with the incident pion track and not reconstructed properly. The total charge deposit for the incident pion track become larger than the usual incident tracks. Even though the scattering angle is 180 degree in one projection, it is smaller than 180 degree in other projection for most of the case. Therefore, this kind of back-scattered pion scattering events can be selected by requiring an incident track with large dQ/dx ($>$ 14 p.e./mm) and π-like (dQ/dx $<$ 15 p.e. / mm) 2D track which was only reconstructed in one projection. Figure A.14 shows an example of dQ/dx distribution for incident track for the data sets with $p_\pi = 250$ MeV/c setting, after requiring π-like 2D track. The difference between data and MC is assigned for the error for the predicted number of back-scattered pion background events.

Multiple interaction

Scattered pion track may not be reconstructed properly when they interact again in the fiber tracker. For example, if a pion is absorbed right after being scattered, the scattered pion track will be too short to be reconstructed. Among all of the pion scattering events which are misidentified as ABS or CX, $\sim$ 30 % of those are due to a multiple interaction like this. The uncertainty of the number of events for this type of background events is estimated from the uncertainty in the cross section from past experiment, which we used in MC tuning [70]. For example, for the events in which pions are absorbed right after elastic scattering, the uncertainty of elastic scattering cross section (10 %) and the uncertainty of ABS cross section ($\sim$ 20 %) is applied.

Low momentum pions

When the momentum of the pions after scattering is small ($<$ 130 MeV/c), those pions are always identified as protons because the dQ/dx is large. Figure A.15 shows an example of predicted pion momentum distribution after inelastic (quasi-elastic) scattering for Geant4 and NEUT, for $p_\pi = 201.6$ MeV/c. The uncertainty for the number of low momentum pion background events are taken from the difference between two models below 130 MeV/c.

	p_π at the fiber tracker [MeV/c]				
Error source	201.6	216.6	237.2	265.5	295.1
Forward / Backward protons	0.4	3.2	1.4	3.2	1.8
dQ/dx resolution	2.7	3.6	2.2	3.4	1.7
High momentum protons	0.5	0.9	1.2	0.9	2.5
γ conversion	0.3	0.6	0.8	0.4	0.6
Subtotal	2.8	4.9	2.9	4.8	3.7

Table A.2: Summary of the physics model systematic errors related to event selection efficiency (in percentage).

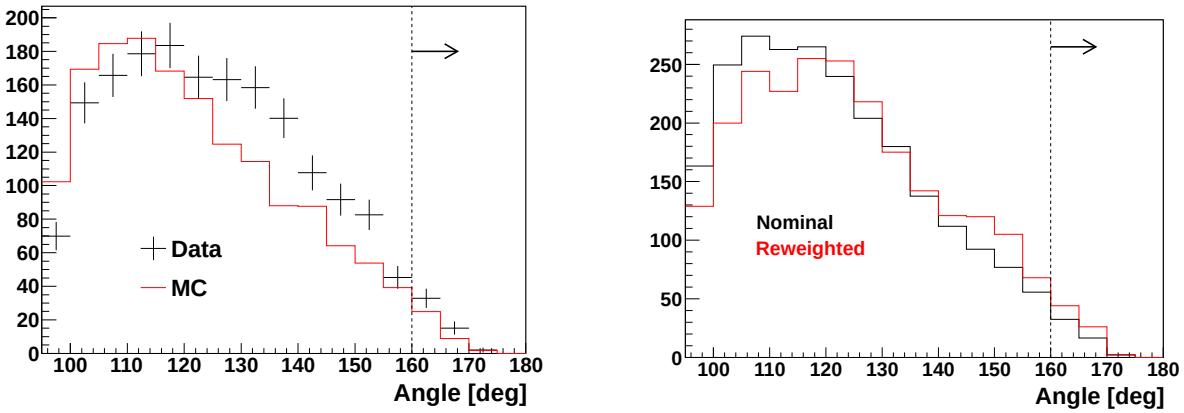

Figure A.10: Angular distribution of the backward going proton-like track, for ABS and CX events, for $p_\pi = 250$ MeV/c setting. For each event, a proton-track with largest angle is selected and filled in the histogram. The left plot shows the distribution for data and MC, and the right plot shows the distribution for nominal and reweighted MC.

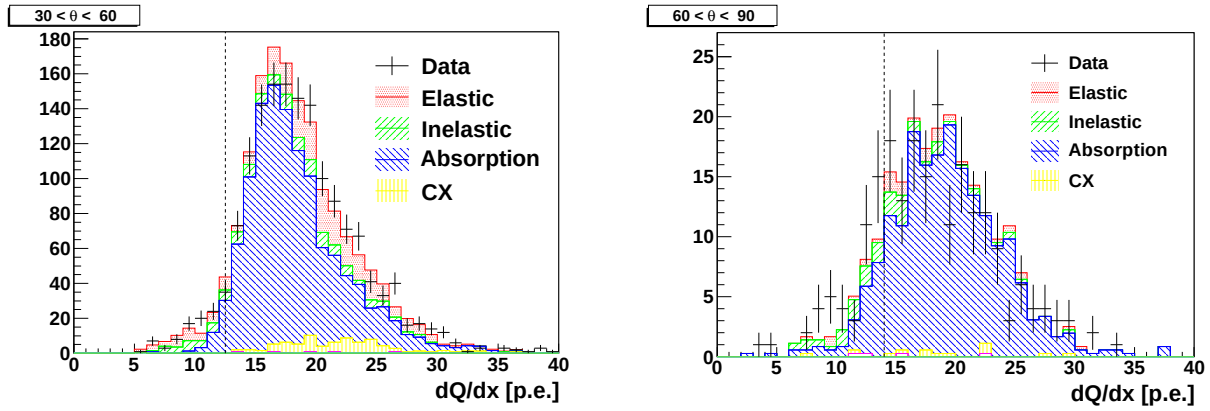

Figure A.11: Example of dQ/dx distribution after event selection, for the projection which was not used for calculating dQ/dx in no π^+ cut, for the data set with p_π =250MeV/c setting. The left plot is an example for $30 < \theta < 60$ degree, and the right plot is for $60 < \theta < 90$ degree. The broken line shows the threshold to distinguish pion-like tracks and proton-like tracks.

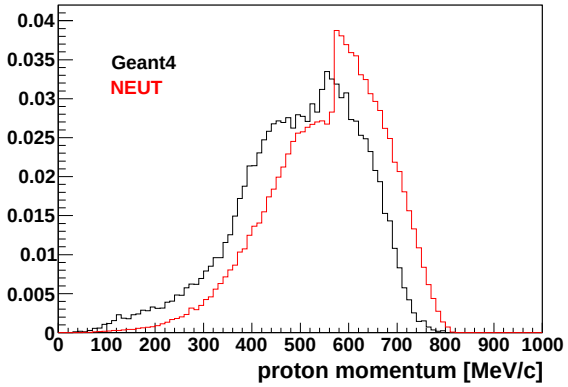

Figure A.12: The predicted momentum distribution of protons from the ABS events, for Geant4 (black) and NEUT (red), for p_π = 295.1 MeV/c. The histograms are normalized by number of ABS events.

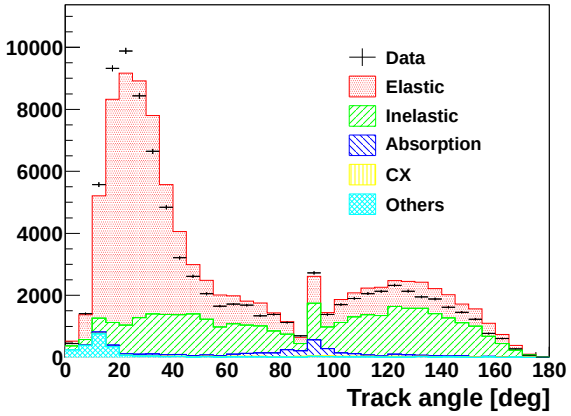

Figure A.13: Angular distribution of π-like tracks for data and MC with $p_\pi = 250$ MeV/c setting. The histograms are normalized by number of incident pions in data.

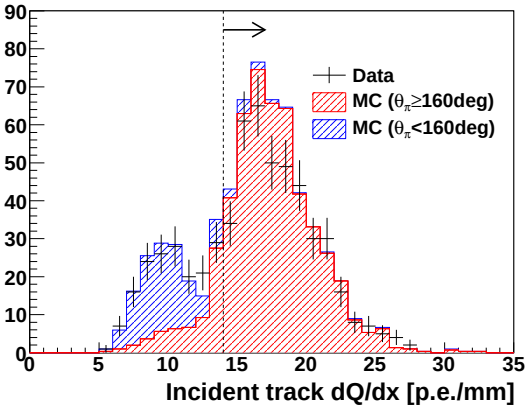

Figure A.14: Example of dQ/dx distribution for incident track for the data set with p_π = 250 MeV/c setting, after requiring π-like 2D track which was only reconstructed in one projection. The histograms are normalized by number of incident pions.

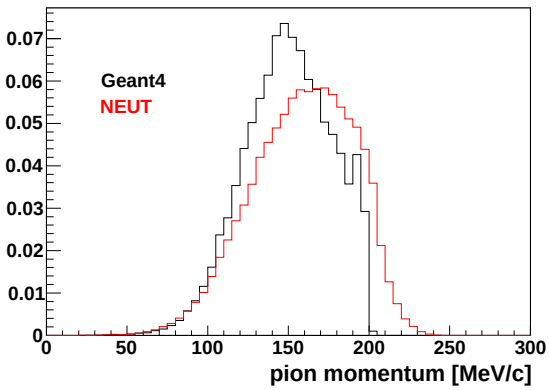

Figure A.15: Predicted momentum distribution of pions from inelastic scattering event, for Geant4 (black) and NEUT (red), for p_π = 201.6 MeV/c. The histograms are normalized by area.

Appendix B

Neutrino flux and cross section uncertainties

In this chapter, we describe the detail of the prediction and the errors of the neutrino flux and cross section. The complete description of the neutrino flux prediction is explained in [143].

B.1 Flux tuning and errors

Figure B.1 and B.2 shows the fractional error in the flux prediction at ND280 and SK, respectively. Other than the MC statistical error, there are three different types of errors in the flux prediction:

1. Hadronic interactions
   Uncertainty in the hadron production process. This is a main component of the error.

2. Proton beam, alignment and off-axis angle
   This is the uncertainty of incident proton beam parameters, alignment of the beamline components (monitors, horns and target) and off-axis angle. The off-axis angle is measured by INGRID.

3. Horn current & field
   Uncertainty in horn current and the magnetic field of the horn.

We describe the estimation of these errors in the following sections.

B.1.1 Hadronic interactions

There are uncertainties in the hadronic process of producing pions and kaons. The hadronic production process depends on the following parameters.

- Production cross section σ_{prod}
  This is an inclusive cross section to produce hadrons, defined as $\sigma_{\mathrm{prod}} = \sigma_{\mathrm{total}} - \sigma_{\mathrm{el}} - \sigma_{\mathrm{qe}}$, where σ_{total} is the total interaction cross section, σ_{el} is the elastic scattering cross section and σ_{qe} is the quasi-elastic scattering cross section.

- Multiplicity $dn/(dpd\theta)$
  This is a differential production cross section normalized by σ_{prod}.

$$\frac{d^2n}{dpd\theta} = \frac{1}{\sigma_{\mathrm{prod}}} \frac{d^2\sigma}{dpd\theta} \tag{B.1}$$

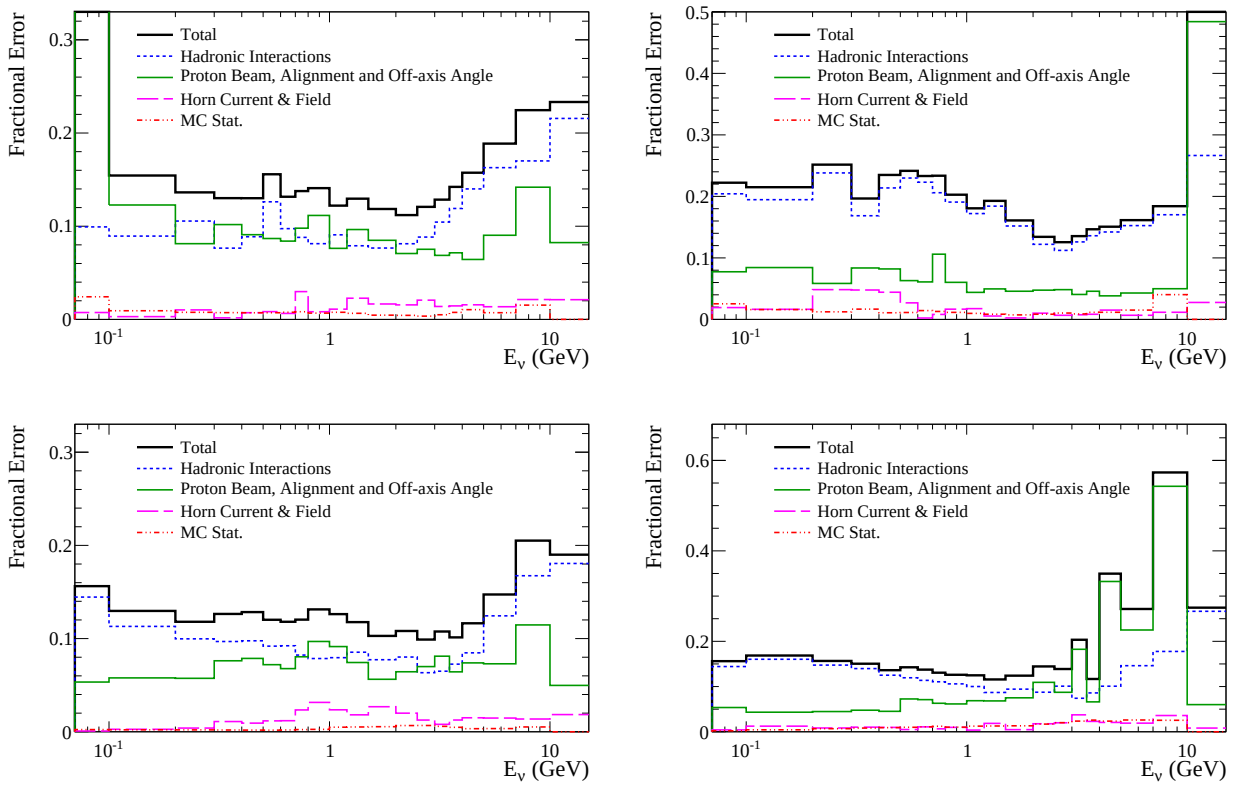

Figure B.1: Fractional uncertainties of the neutrino beam flux at ND280 detector, for ν_e flux (left top), $\overline{\nu}_e$ flux (right top), ν_μ flux (left bottom) and $\overline{\nu}_\mu$ flux (right bottom).

We tune these parameters not only for the 30 GeV primary protons, but also for the secondary particles which have lower momentum than the primary protons. The secondary interactions happens either in the graphite target or in the other materials such as the horn aluminum conductor. For the interaction of primary protons, we use the data sets from the NA61/SHINE experiment [106, 107]. NA61/SHINE measured the interaction of 30 GeV protons on 2 cm thin carbon target. We also use the data sets from other experiments or interpolate/extrapolate the data sets to obtain the cross section not measured by NA61/SHINE.

Production cross section ($\sigma_{\rm prod}$) tuning and errors

The inclusive production cross section $\sigma_{\rm prod}$ is measured by the NA61/SHINE experiment [106] for the 30 GeV protons on carbon. The cross section for proton at lower momentum and the cross sections for other particles on carbon and other targets are derived from other measurements [106, 144–154]. The FLUKA prediction agree well with the data, so the production cross section in FLUKA is not tuned. On the other hand, the GCALOA prediction has significant disagreements with the external data for low momentum incident particles, so we weight the production cross section in GCALOA to reproduce the data. The weight W is calculated with an exponential factor that account for attenuation in the target.

$$W = \frac{\sigma'_{\rm prod}}{\sigma_{\rm prod}} e^{-x(\sigma'_{\rm prod}-\sigma_{\rm prod})\rho}, \tag{B.2}$$

where ρ is the number density of the nuclear targets in the material, $\sigma'_{\rm prod}$ and $\sigma_{\rm prod}$ are the production cross section in data and in the original simulation, x is the distance traveled by the

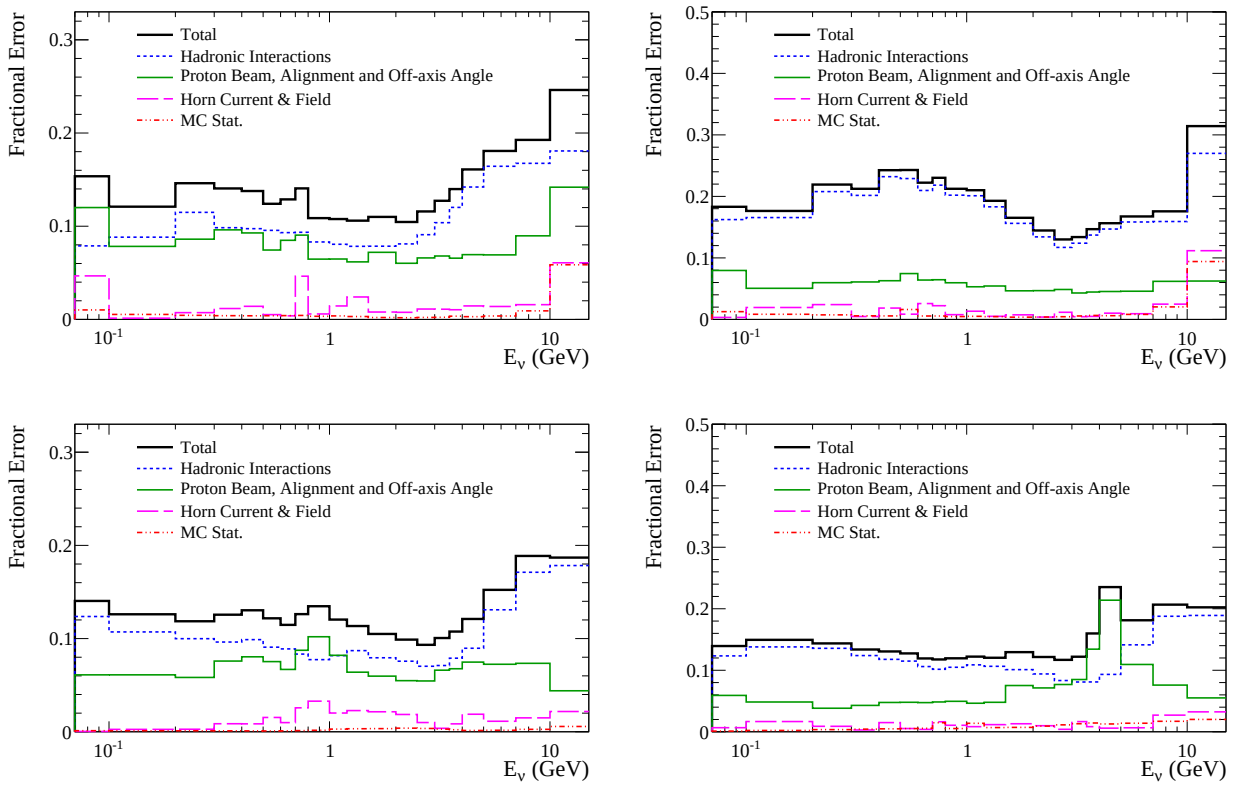

Figure B.2: Fractional uncertainties of the neutrino beam flux at SK detector, for ν_e flux (left top), $\overline{\nu}_e$ flux (right top), ν_μ flux (left bottom) and $\overline{\nu}_\mu$ flux (right bottom).

particle through the material.

The uncertainty is estimated from the discrepancy seen between different measurements at similar incident energies. The magnitude of the discrepancies are similar in size of the quasi-elastic scattering cross section, which might be due to the ambiguity in the actual quantity being measured. The amount of quasi-elastic cross section is assigned for the uncertainty of inclusive production cross section, which corresponds to less than 8% uncertainty for the flux for all energies.

Multiplicity ($dn/(dpd\theta)$) tuning and errors

For the primary protons, the $dn/(dpd\theta)$ is tuned by using NA61/SHINE data. The NA61/SHINE data set for pions covers more than 90% of the phase space in (p, θ), relevant for the T2K flux. The data set for K^+ also covers 60% of the phase space. The $K^\pm$ data sets from Eichten et al. [113] and Allaby et al. [114] cover the forward production of high energy kaons, which has not been measured by NA61/SHINE experiment yet. The weights for dn/dp are calculated as follows.

$$W(p,\theta) = \frac{\left[\frac{dn}{dp}(p,\theta)\right]_{\text{data}}}{\left[\frac{dn}{dp}(p,\theta)\right]_{\text{MC}}}, \tag{B.3}$$

where p and θ are the momentum and angle of pions or kaons. No tuning is applied for the region which is not covered by data.

The uncertainty of $dn/(dpd\theta)$ is derived from the systematic error in the data points from

NA61, which is typically ∼7% for $\pi^{\pm}$, corresponding to maximum uncertainty of 6% on the flux. the uncertainty for the phase space not covered by data is estimated to be less than 2%. The uncertainty for kaons mainly comes from the statistical uncertainty of NA61 data points.

For the secondary nucleons, the weights for $dn/(dpd\theta)$ is estimated by scaling the weights calculated from NA61 data, assuming Feynman scaling. The weights from NA61 data is calculated in $x_F - p_T$ space, where $x_F = p_L/p_{max}$ is called Feynman variable, p_T is the transverse momentum of the produced particle, p_L and p_{max} are the longitudinal momentum of the produced particle and the maximum momentum the produced particle can have. The weight for the nucleons with other momentum is then calculated assuming the weights at same $x_F - p_T$ is independent of the collision center of mass energy.

The uncertainty of the scaling is estimated from the difference between the prediction by FLUKA and the measurements by Eichten et al. and Allaby et al. The uncertainty propagated to the flux is estimated to be less than 10% for all energies.

B.1.2 Proton beam, alignment and off-axis angle

Table B.1 summarizes the proton beam parameters measured by the beam monitors. The uncertainty in beam flux due to the uncertainty of the beam parameters is estimated by varying these parameters within the errors in the simulation. The variations corresponds to shifts in off-axis angle of ∼0.35 mrad, or shifts in neutrino energy spectrum peak of ∼10 MeV.

Table B.1: Summary of the measured proton beam parameters and their uncertainties for a typical run period: mean position (X, Y) and angle (X', Y'), width σ, emittance ϵ and twiss parameter α.

	X profile		Y profile	
Parameter	Center value	Error	Center value	Error
X, Y [mm]	0.00	0.35	-0.37	0.38
X', Y' [mm]	0.03	0.07	0.07	0.28
σ [mm]	4.03	0.14	4.22	0.12
ϵ [π mm mrad]	4.94	0.54	6.02	3.42
α	0.33	0.08	0.34	0.41

The uncertainty in flux due to the uncertainty in horn and target alignment is estimated by changing the alignment of the horns in the simulation within their uncertainty. The uncertainty of the alignment of the horns and target is summarized in Table B.2. The total alignment uncertainty on the flux is less than 3% around the peak of the energy spectrum.

Table B.2: Uncertainty in the alignment of the target and horn. There are uncertainties in x, y, z position, horizontal and vertical rotation angle θ_H and θ_V.

	Target	Horn1	Horn2	Horn3
δx [mm]	-	0.3	0.3	0.3
δy [mm]	-	1.0	1.0	1.0
δz [mm]	-	1.0	1.0	1.0
$\delta\theta_H$ [mrad]	1.3	0.2	0.2	0.2
$\delta\theta_V$ [mrad]	0.1	0.2	0.2	0.2

The off-axis angle of the beam is measured by INGRID with the precision of ∼0.38 mrad,

and the effect of its uncertainty to the flux is estimated by changing the off-axis angle in the simulation by this uncertainty. The uncertainty of the flux due to the off-axis angle is estimated to be 2∼4% around the peak of the energy spectrum.

B.1.3 Horn current & field

The uncertainty in the magnetic field affects the neutrino flux. The uncertainty in horn current measurement is 1.3%. The magnetic field varies as $1/r$, where r is the distance from the horn axis. The magnetic field was measured using a Hall probe, and found to be consistent with the expected field strength within 2%. Therefore, 2% uncertainty is assigned for the absolute field strength, which results in 2% uncertainty at most in the flux.

Inside the first horn, there was an anomalous magnetic field observed in a direction perpendicular to the horn axis, with a maximum strength of 0.065 T. The effect of this anomalous magnetic field is taken into account as a systematic error, which results in less than 3% error for the flux below 7 GeV.

B.2 Constraints on the cross section parameters

The prior values and the errors for M_A^{QE}, M_A^{RES}, W-shape and normalization parameters are defined with comparisons of NEUT to external data as follows.

B.2.1 CCQE model uncertainty

The constraints on M_A^{QE} and CCQE normalization parameters are applied from a comparison between NEUT and external CCQE cross section measurements. These parameters are also directly constrained by the ND280 data.

The error for M_A^{QE} is derived from the fit to the MiniBooNE CCQE double differential cross sections [108] in bins of $(T_\mu, \cos\theta_\mu)$, where T_μ and θ_μ are the kinetic energy and the angle of the muon in the final state of CCQE interaction. The difference between the nominal and best fit value of M_A^{QE} is assigned to the error of M_A^{QE}.

The CCQE normalization parameters accounts for the uncertainties in the cross section measured by the external experiments. Below 1.5 GeV, 11% error is assigned from the MiniBooNE CCQE cross section measurement [108]. To allow a discrepancy in the CCQE cross section measured around $\mathcal{O}(10)$ GeV by NOMAD [155] and around $\mathcal{O}(1)$ GeV by MiniBooNE, 30 % uncertainty is applied for the CCQE normalization above 1.5 GeV.

B.2.2 CC1π, NC1π^0 resonance interaction model uncertainty

The prior constraints for CC1π, NC1π^0 resonance interactions are derived from the fit to the external data. We perform a joint fit to MiniBooNE CC1π^+, CC1π^0 and NC1π^0 differential cross section data [109–111], as shown in Fig. B.3. The constraints on M_A^{RES}, CC1π norm, NC1π^0 norm and W-shape parameters are derived from this fit. The CC coh. norm, NC coh. norm, CC other norm, NC other norm, NC1$\pi^\pm$ norm are also varied in the fit. However, since the contributions of these interactions in the MiniBooNE data sample is small, it has little power to constrain these parameters. We can not constrain all of the parameters separately by using MiniBooNE data, but we can apply a constraint to the parameter space. The fit results are also compared with the K2K NC measurement on 1 kton water Cherenkov detector. For CC1π normalization parameter above 2.5 GeV, we assign 40% error conservatively, motivated by the NOMAD data [155].

B.2.3 Other interaction channels

The uncertainty on CC coh. normalization is assigned based on the measurements by K2K [156] and SciBooNE [157]. Since no clear CC coherent signal has been observed at $\mathcal{O}(1)$ GeV, we apply 100% error for this parameter.

The uncertainty on NC coh. is derived from the measurement by SciBooNE [158]. We apply conservative 30% error for this parameter, motivated from 15% discrepancy between NEUT prediction and SciBooNE measurement with a 20% systematic error.

CC other cross section is constrained by CC-inclusive cross section measurement [159]. At energies above 4 GeV, this interaction mode dominates the cross section, and well constrained with 10 % uncertainties. At lower energies the constraint from inclusive cross section measurement is weaker because the other interaction modes are significant. Therefore, we apply an uncertainty as a function of energy, which is 10% at high energies and increases at low energy. Not like the other normalization parameters, the weight w for this interaction is as energy dependent:

$$w = 1 + \frac{x_{CCoth}}{E_\nu(\mathrm{GeV})} \tag{B.4}$$

The parameter x_{CCoth} is allowed to vary around a nominal value of 0 with an uncertainty of 0.4 GeV. The error do not become infinite at $E_\nu \to 0$ GeV because the threshold of this interaction is $\sim$0.6 GeV.

NC other interaction channels are assigned a 30% uncertainty, following the studies done for the first published T2K oscillation analysis [24].

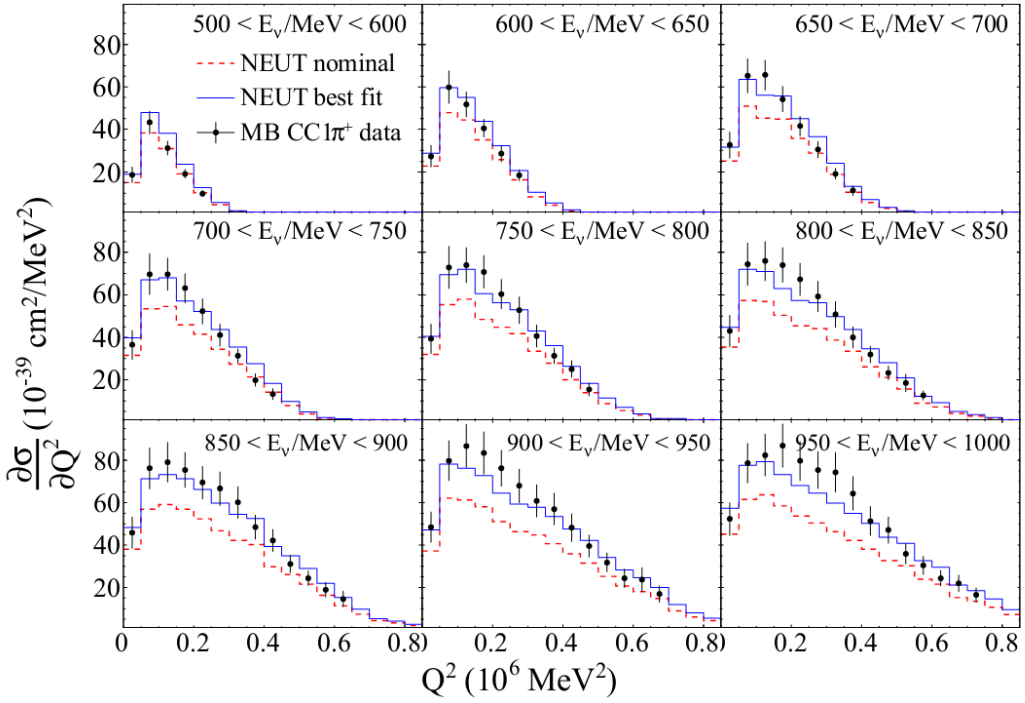

(a) CC1$\pi^+ d\sigma/dQ^2$ in bins of energy.

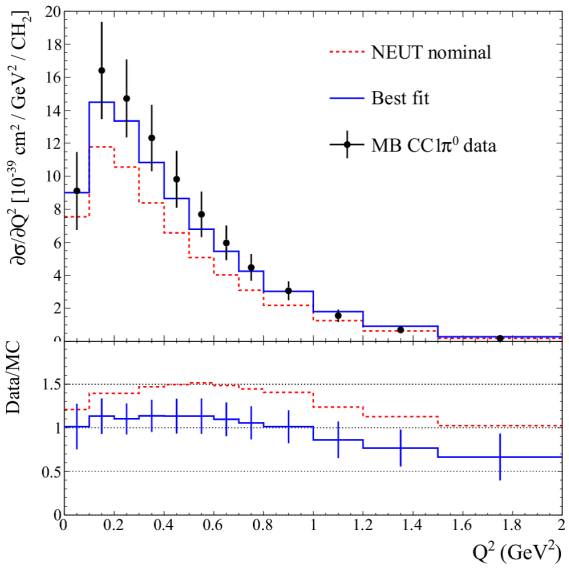

(b) CC1π^0 $d\sigma/dQ^2$.

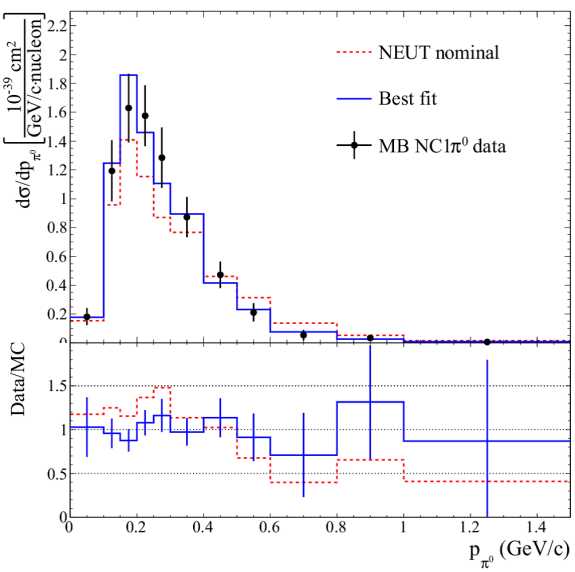

(c) NC1π^0 $d\sigma/dp_{\pi^0}$.

Figure B.3: Fits to MiniBooNE single pion production cross section data.

Appendix C

ND280 data fit

Figure C.1 shows the $(p, \cos\theta)$ distribution of three sub-samples, where p and θ are the momentum of the muon and its angle with respect to the beam axis. We fit these distributions to constrain the beam flux and neutrino interaction parameters. The binnings for $(p, \cos\theta)$ distribution is defined as follows:

- p (CC0π, CC other): 0, 300, 400, 500, 600, 700, 800, 900, 1000, 1250, 1500, 2000, 3000, 5000, 30000
- p (CC1π): 0, 300, 400, 500, 600, 700, 800, 900, 1000, 1250, 1500, 2000, 5000, 30000
- $\cos\theta$ (CC0π, CC1π, CC other): -1.0, 0.6, 0.7, 0.8, 0.85, 0.9, 0.92, 0.94, 0.96, 0.98, 0.99, 1

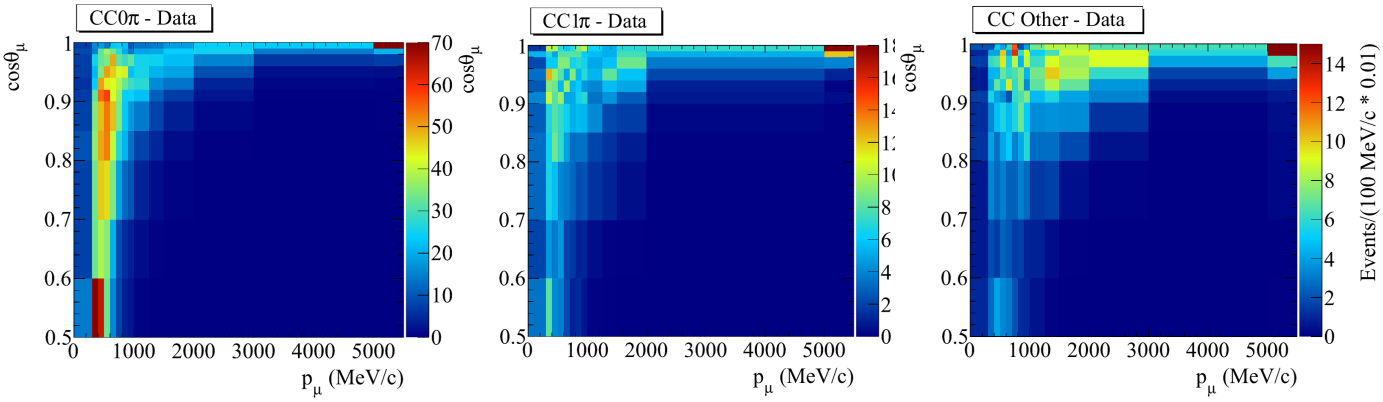

Figure C.1: The $(p, \cos\theta)$ distribution of muons for CC0π (left), CC1π (middle) and CC other sample (right).

C.1 Parameters for the fit

The fit includes neutrino beam flux parameters, interaction parameters and detector systematic parameters. The flux parameters defines the normalization of the neutrino beam flux at ND280 and SK for each energy bins. The energy bins for ND280 and SK neutrino beam flux is defined as follows:

- ν_μ: 0.0, 0.4, 0.5, 0.6, 0.7, 1.0, 1.5, 2.5, 3.5, 5.0, 7.0, 30.0 (GeV)
- $\overline{\nu}_\mu$: 0.0, 0.7, 1.0, 1.5, 2.5, 30.0 (GeV)

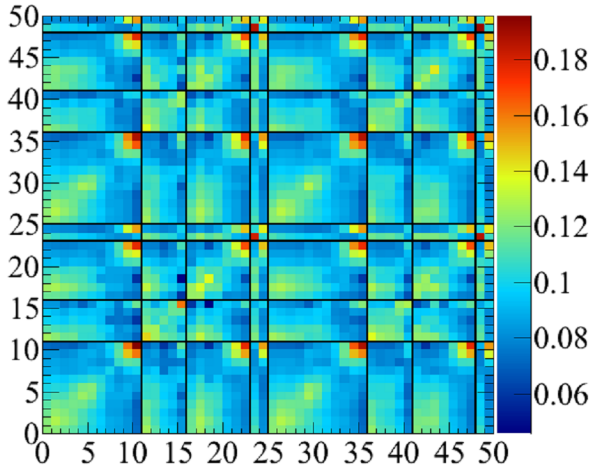

Figure C.2: Covariance matrix for flux parameters. The bin indices are defined as follows: ND280 ν_μ (0-10), ND280 $\overline{\nu}_\mu$ (11-15), ND280 ν_e (16-22), ND280 $\overline{\nu}_e$ (23-24), SK ν_μ (25-35), SK $\overline{\nu}_\mu$ (36-40), SK ν_e (41-47), and SK $\overline{\nu}_e$ (48-49), with the energy divisions for the neutrino types given in the text.

- ν_e: 0.0, 0.5, 0.7, 0.8, 1.5, 2.5, 4.0, 30.0 (GeV)
- $\overline{\nu}_e$: 0.0, 2.5, 30.0 (GeV)

Their prior values are set to 1 (nominal value). Figure C.2 shows the covariance matrix for the flux parameters. There is a strong correlation between ND280 and SK flux parameters, so the flux at SK can be constrained by constraining the flux parameters at ND280. There is also a correlation between ν_μ flux and ν_e flux, because their parent hadrons (π, K) are common.

The cross section parameters are shown in Table 8.1. For this fit, the NC coh. and NC other parameter are combined into a single normalization parameter with a prior uncertainty of 0.3. The FSI parameters are also included in the fit. These parameters directly affects the probability of the interactions to happen.

The detector systematic parameters are defined for each of the systematic sources listed in Table 9.3. Their prior values are 1, and their effect to the $(p, \cos\theta)$ are different for different type of the systematic errors.

C.2 Definition of the likelihood

The fit maximizes the likelihood that includes the binned likelihood of the ND280 data and the prior constraints on the flux model, interaction model and detector response model:

$$\mathcal{L}_{ND}(\vec{f}, \vec{x}, \vec{d}|N_i^d) = \pi_{\text{flux}}(\vec{f})\pi_{\text{xsec}}(\vec{x})\pi_{\text{det}}(\vec{d}) \prod_{i=1}^{N_{\text{bins}}} \frac{[N_i^p(\vec{f}, \vec{x}, \vec{d})]^{N_i^d} e^{-N_i^p(\vec{f},\vec{x},\vec{d})}}{N_i^d!}, \tag{C.1}$$

where $\pi_{\text{flux}}(\vec{f})$, $\pi_{\text{xsec}}(\vec{x})$ and $\pi_{\text{det}}(\vec{d})$ are multivariate normal distribution that are functions of the flux $(\vec{f})$, neutrino cross section $(\vec{x})$ and detector response $(\vec{d})$ nuisance parameters. For each bin the predicted number of events, N_i^p is evaluated based on the values of $\vec{f}, \vec{x}$ and $\vec{d}$, and compared to the measurement, N_i^d. The predicted $(p, \cos\theta)$ distribution for certain values of $\vec{f}, \vec{x}$ and $\vec{d}$ is calculated by re-weighting the MC events.

$$N_i^p = \sum_j^{\text{events}} w_j^f(\vec{f}) w_j^x(\vec{x}) w_j^d(\vec{d}) \delta_j^d(p(\vec{d}), \theta(\vec{d}), s(\vec{d})), \tag{C.2}$$

where $w_j^f(\vec{f})$, $w_j^x(\vec{x})$ and $w_j^d(\vec{d})$ are the weights for that event which is determined from the true neutrino energy, interaction type and interaction position of that event. The δ_j^d is just the algorithm that matches the event to the correct $(p, \cos\theta)$ bin and sample s after any changes in the detector response.

To obtain fit results that more closely follow a χ^2 distribution, we define a $\Delta\chi^2$ from likelihood ratio:

$$\Delta\chi^2 = -2\ln\frac{\mathcal{L}(\vec{f},\vec{x},\vec{d}|N_i^d)}{\mathcal{L}(\vec{f},\vec{x},\vec{d},N_i^p = N_i^d|N_i^d)} \tag{C.3}$$

Here the denominator is the likelihood evaluated with N_i^p set to equal to N_i^d, and the nuisance parameters set to their nominal values. We minimize the $\Delta\chi^2$ in the fit to obtain a best fit values of the flux and cross section parameters.

The M_A^{QE}, M_A^{RES}, CCQE norm, CC1π norm and NC1π^0 norm parameters are constrained by this fit. The other parameters are not constrained by the ND280 fit because the correlation between ND280 and SK is weak. They are marginalized by integrating their dependence in $\mathcal{L}$.

The result of the fit is described in Section 9.4.

Appendix D

SK efficiency error

The systematic error for the SK ν_e event selection cuts are summarized in Table 10.2. Followings are the descriptions of the estimation of the uncertainty of each cut.

- Fully contained cut (FC) uncertainty
  The uncertainty of FC cut is estimated to be 1%. It is dominated by the uncertainty in flasher event rejection, which is evaluated from the difference in the cut efficiency between data and MC in the atmospheric neutrino sample.

- Fiducial volume cut (FV) uncertainty
  We estimate the uncertainty of this cut to be 1%, by comparing the reconstructed vertex distributions of observed and simulated cosmic-ray muons which stopped inside the ID.

- No decay electron cut uncertainty
  This error is evaluated to be 0.2% for ν_e signal sample and $\nu_e + \overline{\nu}_e$ background sample, and 0.4% for $\nu_\mu + \overline{\nu}_\mu$ and NC background sample. We estimated the errors from the comparison of the efficiency to find delayed signals in data and MC for the cosmic-ray muons which stopped in SK.

- Single ring cut, e-like cut and π^0 rejection cut uncertainties
  The errors of these topological cuts are estimated for each (p_e, θ_e) bin in each interaction mode. The total error for the ν_e CC signal event is 1.6%, while the total error for sum of the background events is 7.3%. The error for each interaction mode is estimated as follows.

  - The ν_e signal CC interactions and ν_e background (ν_e contamination in the beam) CC interactions are the signal and the dominant background in the ν_e candidate events. The efficiency errors for these events are estimated by using the atmospheric neutrino data. The atmospheric data is useful because it covers the same energy range of the T2K neutrino beam and the same detector response is expected.

    We categorize the atmospheric data to "ν_e CC single-e", "ν_e CC other", "ν_μ background" and "NC background" sample. The first two samples are subdivided to one "core" sample which passes all of the topological cuts, and three "tail" samples which fails one of the three topological cuts. The number of events in each samples are counted for each of the (p_e, θ_e) bins defined in Table 10.3.

    We fit the atmospheric data to derive the efficiencies of the topological cuts and their errors. In the fit, we define the efficiency parameters ε for three topological cuts and the nuisance parameters α which represents atmospheric neutrino flux and cross section uncertainties. The ε parameters are defined for each of the (p_e, θ_e) bins in "ν_e CC single-e" sample. For "ν_e CC other" sample, we define the efficiency parameter for sum of all (p_e, θ_e) bins.

From the fit, we derive the fractional uncertainties of the number of events n_{SK} in each (p_e, θ_e) bin. The fractional uncertainties are calculated from the difference between the nominal value and the best fit value ("shift"), and the uncertainties in the fit which is dominated by the statistical uncertainty ("stat"). The nominal value is defined by fitting the data with ε parameters fixed to nominal. Figure D.1 shows the results. The points represent the "shift" errors, and the error bars represent the "stat" errors. The green band represents the quadratic sum of the two.

– The NCπ^0 interaction is also important because it is one of the main background. The topological cut efficiency errors for "NC1π^0", "NCπ^0 other" and "CCπ^0" samples are derived by difference in the event selection efficiency between "hybrid-π^0 data" and "hybrid-π^0 MC" control sample.

  The "hybrid-π^0" control samples are constructed by combining the simulated γ-ray with real electron data (hybrid π^0 data) or with simulated electron data (hybrid π^0 MC) to mimic the π^0 events. The electron data is derived from atmospheric ν_e data and from the decay electrons of the cosmic-ray muon data. They are combined in such a way that the two rings follows the decay kinematics of π^0. For "NCπ^0 other" and "CCπ^0" samples, the other particles such as π, μ and p are also added by simulation.

  We define two samples called "primary" and "secondary". The "primary" sample uses electron rings from atmospheric samples, with the electron having energy higher than the simulated γ energy. In the "secondary" sample the electron energy is lower than simulated γ energy, and the electrons from atmospheric or cosmic-ray muon decay are used.

  The efficiency error is defined from the difference in the number of selected events between data and MC, after applying the ν_e event selection cuts. The statistical errors are also included in the error. The errors in "primary" sample and "secondary" sample are added in quadrature to derive the total error. Figure D.2 shows an example of data/MC relative difference for p <300 MeV/c.

– The efficiency error for ν_μ CC interaction is estimated to be 126%. This is a combined error for decay in flight muons (DIF) and non-DIF muon events. This is a conservative error, but the effect to the ν_e oscillation analysis is small because fraction of ν_μ CC events is very small after the ν_e selection cuts.

– The NC interaction producing single photon via the radiative decay of Δ resonances is called NC1γ. The NC1γ events looks very similar ν_e CC single electron events, but the fraction of NC1γ events is very small. The selection efficiency between NC1γ events and ν_e CC single-e events is compared in MC, and the difference in the relative efficiencies is no larger than 1%. Therefore, for NC1γ events, we assign additional 1% error, added in quadrature with the ν_e CC single-e efficiency error.

– The remaining interaction modes are NC1$\pi^\pm$ and NC other. A conservative 100% error is assigned for the efficiency of the three topological cuts for these events.

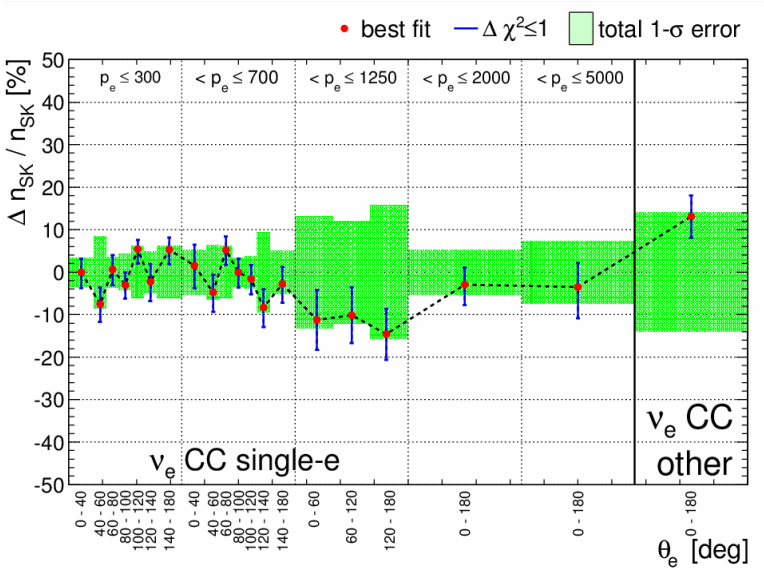

Figure D.1: Efficiency errors of the topological cuts in (p_e, θ_e) bins for "ν_e CC single-e" and "ν_e CC other" samples, derived from atmospheric control sample.

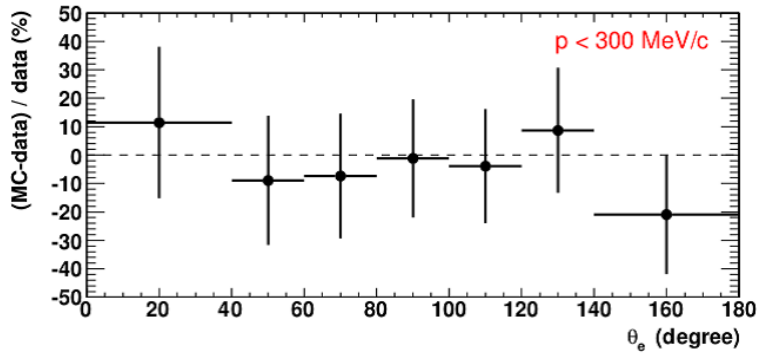

Figure D.2: Example of the data/MC relative difference in NC1π^0 hybrid-π^0 control sample for the θ_e bins, at p_e <300 MeV/c.

Appendix E

Comparison with 2012 ν_e appearance analysis

In order to check the consistency among the individual data sets, we perform separately the fit of the Run1+2+3 data, Run4 data and Run1-4 data. In this check, we do the analysis with 2013 method, so the updated systematic errors and fiTQun π^0 cut are used. Table E.1 summarizes the number of POT and the observed number of ν_e candidate events for each run period. The number of POT for Run4 is similar to that of Run1+2+3, but the observed number of events is much higher in Run4. Figure E.1 (E.2) shows the fit results for the Run1+2+3 data assuming $\delta_{\rm CP} = 0$ and the normal (inverted) hierarchy. Similarly, Fig. E.3 (E.4) shows the fit results for the Run4 data. We compare the results obtained from each individual data set in Fig. E.5.

Table E.1: Summary of the number of POT for analysis and the observed number of events in each run period.

	Run1+2+3	Run4	Run1-4
POT	3.010×10^{20}	3.560×10^{20}	6.570×10^{20}
The observed number of events	11	17	28

The best fit value of $\sin^2 2\theta_{13}$, 68 % C.L. and 90 % C.L. allowed regions are summarized in Table E.2, and visually shown in Fig.E.6. Since we observe more events in Run4 compared to Run1+2+3, the best fit value of $\sin^2 2\theta_{13}$ is higher in Run4 and Run1-4, but they are consistent with each other. Figure E.7 (E.8) shows the $\delta_{\rm CP}$ vs. $\sin^2 2\theta_{13}$ contours for Run1+2+3 (Run4 only). Figure E.9 and (E.10) shows the comparison of $\delta_{\rm CP}$ vs. $\sin^2 2\theta_{13}$ contours between Run1-4 and Run1+2+3 (Run4 only).

The best fit value of Run1+2+3 with 2013 analysis in Table E.2 is different from the 2012 analysis value in Table 11.10. Figure E.11 shows the comparison of likelihood curves. The best fit values are higher in 2013 analysis. This is mainly due to fiTQun π^0 cut and the updated ND280 fit. By using fiTQun, the expected number of background events decreased, while the observed number of events in Run1-3 did not change. Therefore background-subtracted observed number of events is larger in case of fiTQun, resulting in higher best fit value of $\sin^2 2\theta_{13}$. Also, by using the new ND280 fit, the expected background and signal events reduced, which also makes the best fit value larger.

The difference between 2012 and 2013 can be roughly estimated from the change in the number of expected signal and background events. The number of expected background events in 2012 is reduced from 3.3 to 2.4 by using fiTQun (with old ND280 fit), while the signal events is reduced from 8.3 to 8.1 for $\sin^2 2\theta_{13}$=0.1. With new ND280 fit, the expected background

events is further reduced from 2.4 to 2.3, and the expected signal events reduced from 8.1 to 7.9. Therefore, in total, the difference of the best fit value between 2012 and 2013 is estimated to be ((11-2.3)/7.9) / ((11-3.3)/8.3) $\sim$ 1.19 ($\sim$19% increase). The actual difference is 0.108/0.088 $\sim$ 1.23, which is roughly consistent but slightly higher due to the effect of the shape term.

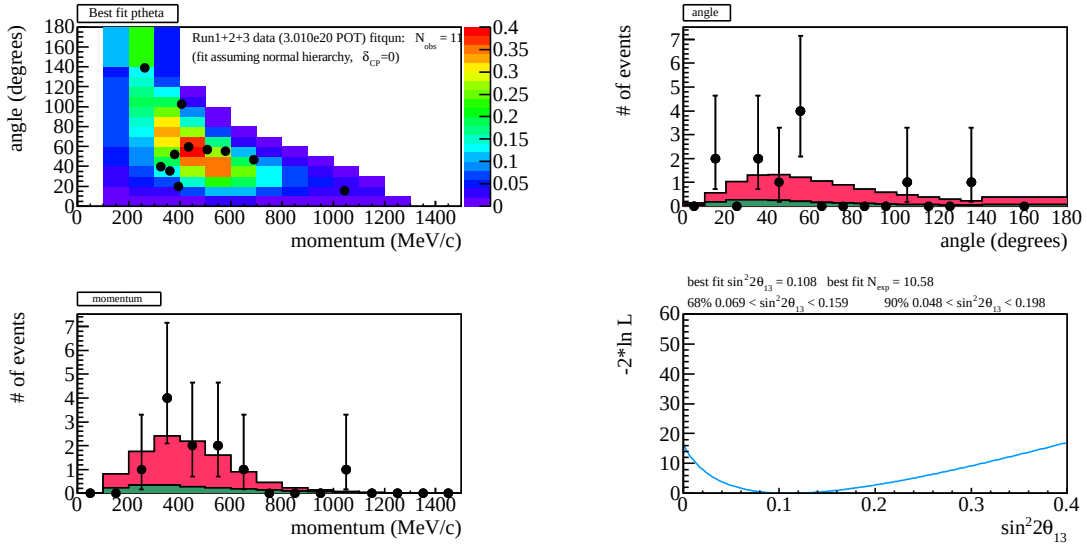

Figure E.1: Fit results for the Run1+2+3 data assuming $\delta_{\mathrm{CP}} = 0$ and normal hierarchy.

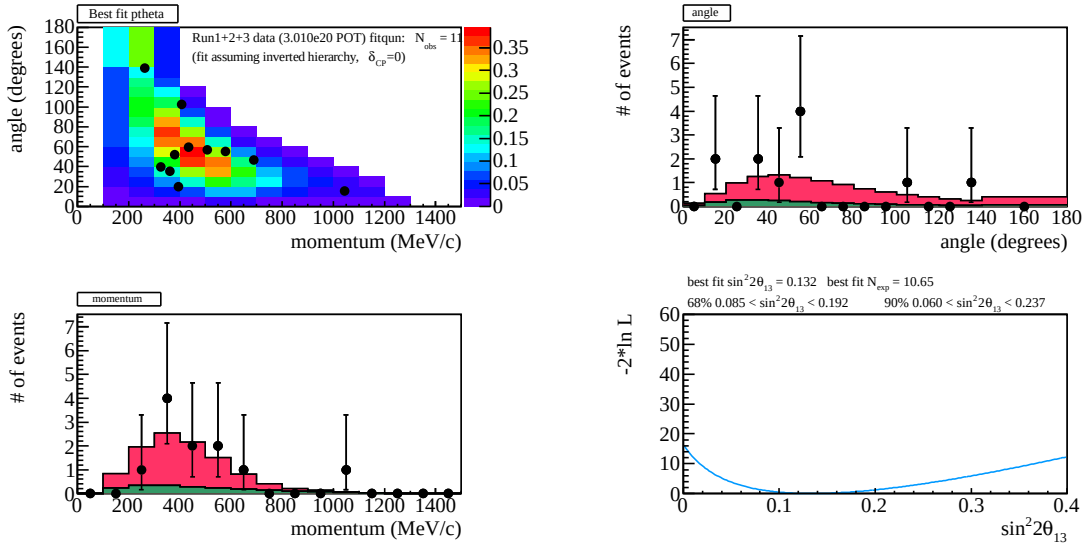

Figure E.2: Fit results for the Run1+2+3 data assuming $\delta_{\mathrm{CP}} = 0$ and inverted hierarchy.

Table E.2: Summary of the fit results for data of individual run periods.

Data period		Normal hierarchy	Inverted hierarchy
Run1+2+3	best-fit	0.108	0.132
	68 % C.L.	0.069 - 0.159	0.085 - 0.192
	90 % C.L.	0.048 - 0.198	0.060 - 0.237
Run4	best-fit	0.164	0.198
	68 % C.L.	0.120 - 0.217	0.146 - 0.260
	90 % C.L.	0.096 - 0.257	0.118 - 0.306
Run1-4	best-fit	0.140	0.170
	68 % C.L.	0.108 - 0.178	0.133 - 0.215
	90 % C.L.	0.090 - 0.205	0.111 - 0.247

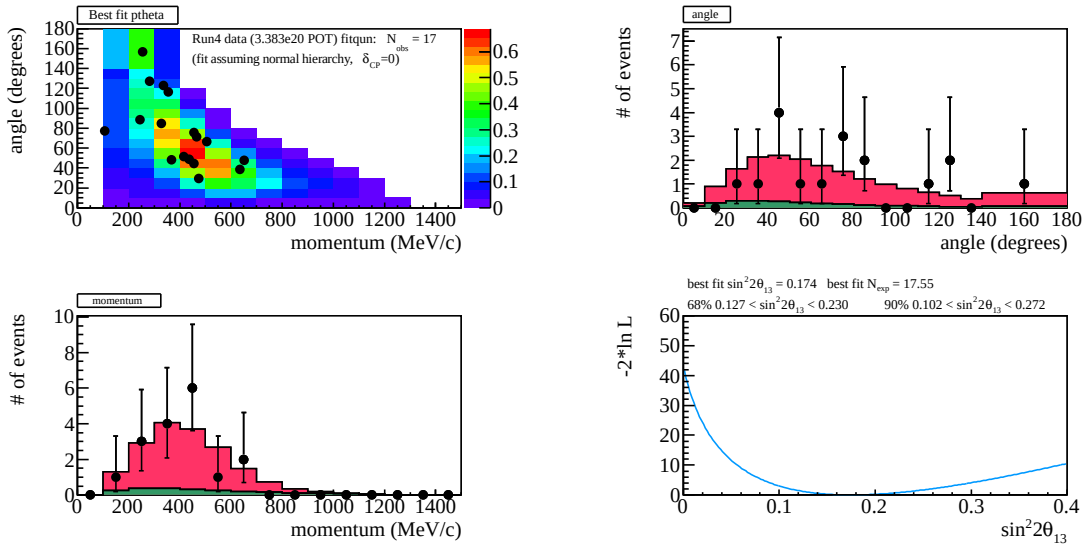

Figure E.3: Fit results for the Run4 data until May 8^{th} 2013 assuming $\delta_{\mathrm{CP}} = 0$ and normal hierarchy.

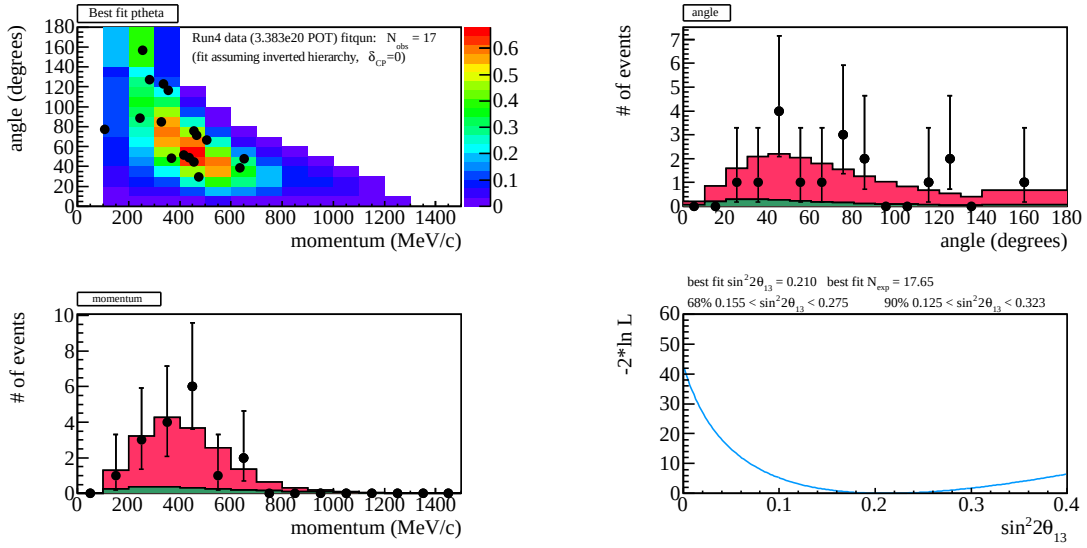

Figure E.4: Fit results for the Run4 data until May 8^{th} 2013 assuming $\delta_{\mathrm{CP}} = 0$ and inverted hierarchy.

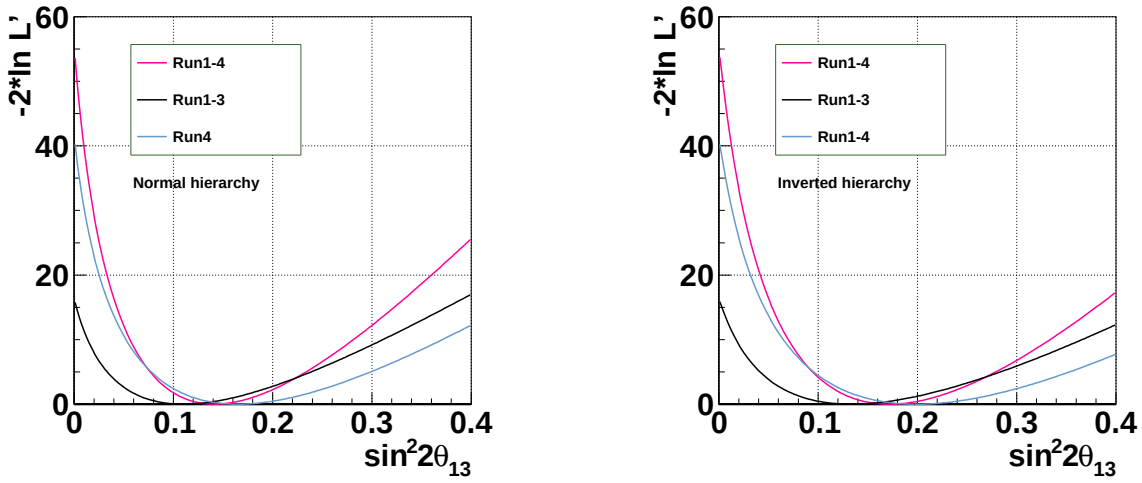

Figure E.5: Comparison of the negative log likelihood as a function of $\sin^2 2\theta_{13}$ among the Run1+2+3 data, Run4 data and Run1-4 data. Left (right) plot shows the result assuming normal (inverted) hierarchy.

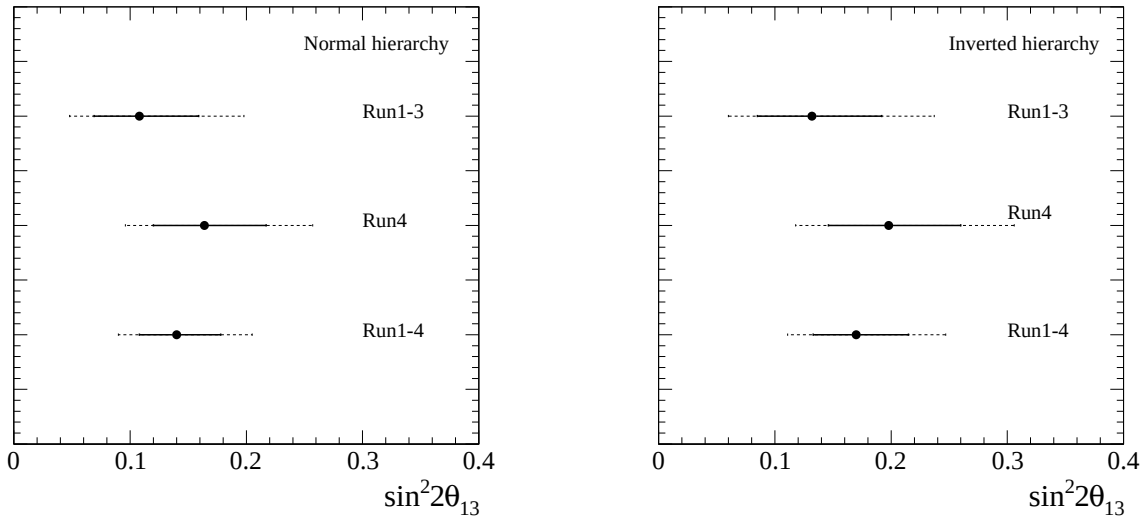

Figure E.6: Comparison of the best fit value of $\sin^2 2\theta_{13}$ and its 68 % C.L. and 90 % allowed region among the Run1+2+3 data, Run4 data and Run1-4 data. The solid (broken) lines correspond to 68 % (90 %) C.L. regions. Left (right) plot shows the result assuming normal (inverted) hierarchy.

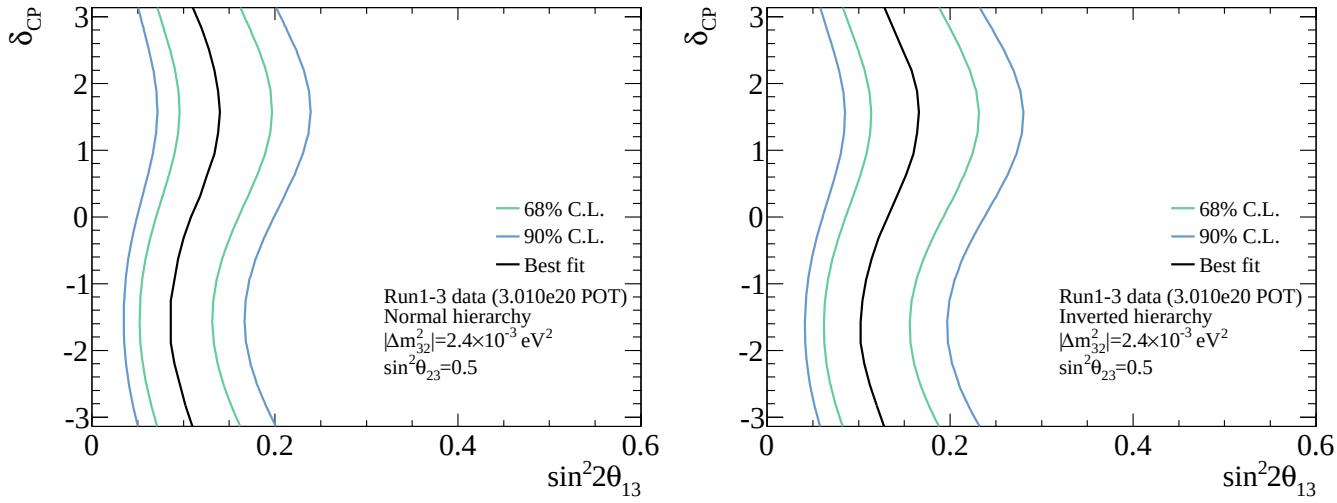

Figure E.7: Allowed region of 68 % (green) and 90 % C.L. (blue) for $\sin^2 2\theta_{13}$ for each value of δ_{CP}, for Run1+2+3 data. The black solid line is the best fit value for each value of δ_{CP}. Top (bottom) plot: normal (inverted) hierarchy is assumed.

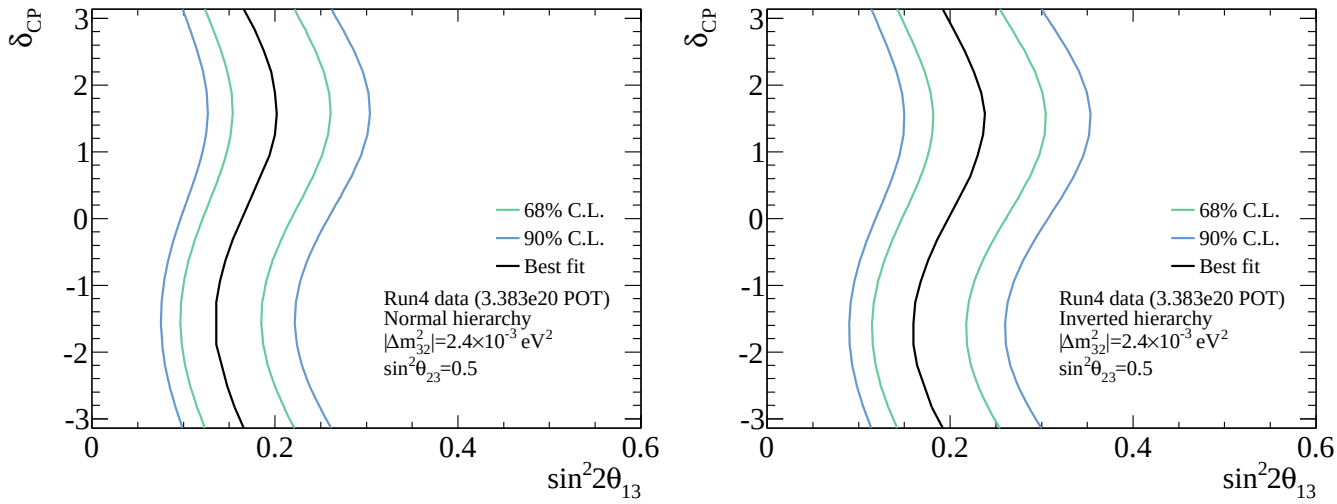

Figure E.8: Allowed region of 68 % (green) and 90 % C.L. (blue) for $\sin^2 2\theta_{13}$ for each value of δ_{CP}, for Run4 data only. The black solid line is the best fit value for each value of δ_{CP}. Top (bottom) plot: normal (inverted) hierarchy is assumed.

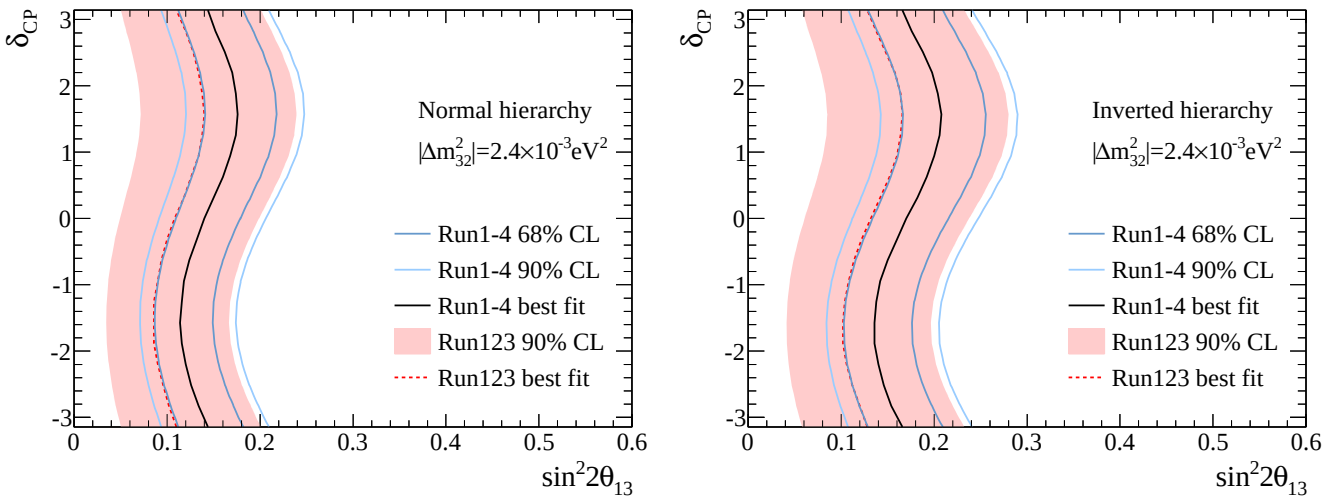

Figure E.9: Run1-4 δ_{CP} vs. $\sin^2 2\theta_{13}$ contours compared with Run1-3. Dark (light) blue lines correspond to 68 % (90 %) C.L. regions. The black solid line is the best fit value for each value of $\sin^2\theta_{23}$. Pink area shows the 90 % C.L. region of Run1-3 data fit (using 2013 analysis method). Red dotted line shows the best fit of Run1-3. Top (bottom) plot: normal (inverted) hierarchy is assumed.

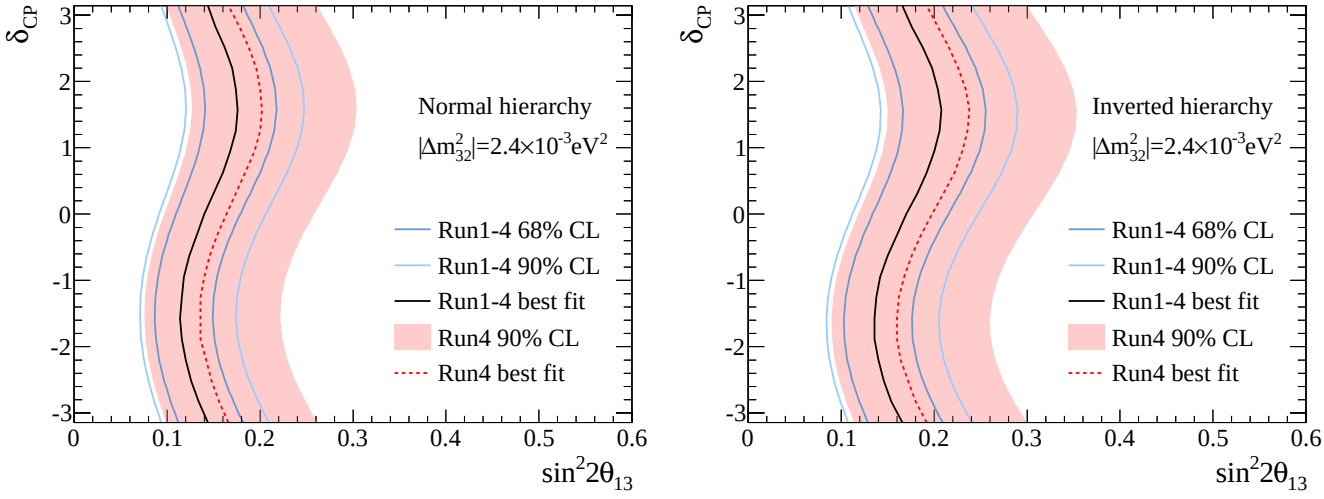

Figure E.10: Run1-4 δ_{CP} vs. $\sin^2 2\theta_{13}$ contours compared with Run4 only. Dark (light) blue lines correspond to 68 % (90 %) C.L. regions. The black solid line is the best fit value for each value of $\sin^2\theta_{23}$. Pink area shows the 90 % C.L. region of 4 only data fit (using 2013 analysis method). Red dotted line shows the best fit of Run4 only. Top (bottom) plot: normal (inverted) hierarchy is assumed.

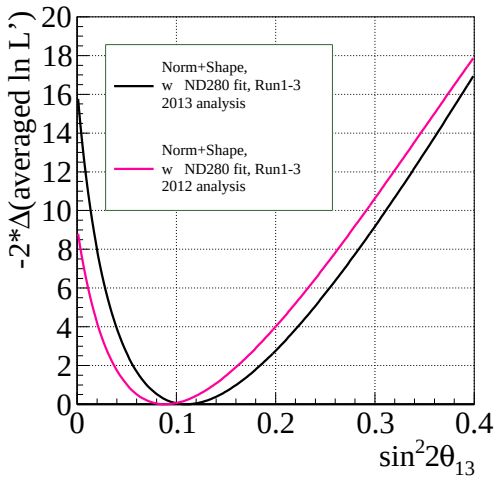

Figure E.11: Run1-3 data fit result with 2013 analysis (Black) compared with 2012 analysis (Pink), for normal hierarchy.

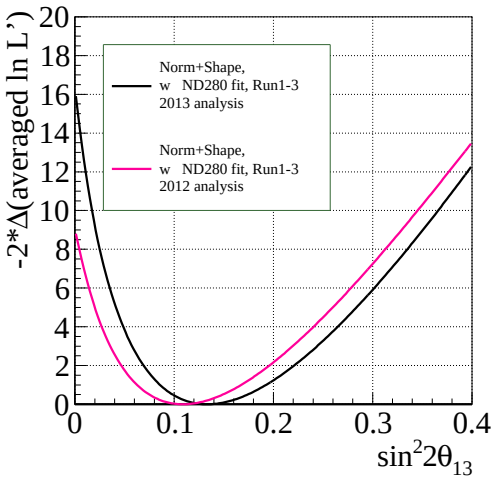

Figure E.12: Run1-3 data fit result with 2013 analysis (Black) compared with 2012 analysis (Pink), for inverted hierarchy.

List of Tables

1.1 Best fit values of the oscillation parameters from PDG 2012. 8
1.2 Upper limits for neutrino mass. 10

2.1 Summary table of beam parameters 18
2.2 Summary of data taking periods 26

3.1 Specifications for the FGDs 31

4.1 Specifications of the fiber tracker 46

5.1 The number of events after each stage of the cut. The numbers for MC are normalized by the numbers of good incident pion events in data. 54
5.2 List of data sets used for cross section tuning in simulation. 57
5.3 The measured momentum for five different data sets. 57
5.4 The number of nuclei in the fiducial volume of the fiber tracker. 58
5.5 Summary of the measurements. In this table, p_π is the momentum of pions at the fiber tracker. 58
5.6 Summary of the statistical and systematic errors in percentage. 61

6.1 List of external data sets used for tuning the scaling parameters. 66

8.1 Summary of the parameters used in the NEUT cross section model. The central values and errors are the values before ND280 fit which we describe in Chapter 9. Check marks are written in the "ND" and "SK" columns for the parameters used in ND280 fit and the SK ν_e oscillation analysis fit. Check marks are also written for the "ND/SK" column for the parameters correlated between ND280 and SK, that are constrained by ND280 measurement. 82

9.1 Composition of the three sub-samples. 89
9.2 Efficiency per each sample. 90
9.3 Summary of the systematic errors. The errors in this table are the largest relative error in all bins in all categories. 91
9.4 Summary of the cross section parameter values before and after the fit. 93

10.1 Summary of the number of events at each stage of the cuts. The numbers for MC is estimated assuming $\sin^2 2\theta_{13} = 0.1$. 97
10.2 Summary of the SK efficiency error. 98
10.3 Binning of SK detector efficiency uncertainty. 99

11.1 The predicted number of events for each event category in the SK MC simulation. The oscillation parameters are set as shown in Table 11.2. 100

11.2 Default values of the neutrino oscillation parameters and earth matter density used for the calculation of oscillation probabilities. The values of $\sin^2 2\theta_{23}$ and Δm^2_{32} are derived from T2K ν_μ disappearance measurement [22], and the values of $\sin^2 2\theta_{12}$ and Δm^2_{12} are derived from [135]. The earth matter density is obtained from [136]. 101
11.3 Summary of systematic parameters used in the oscillation analysis 105
11.4 Binning of f^{Beam} 106
11.5 The predicted number of events with $\sin^2 2\theta_{13} = 0.1$ (top) and 0.0 (bottom). . . 110
11.6 Summary of the contributions of the systematic errors on the predicted number of events. Each error is evaluated as the RMS/mean of the distribution of the predicted number of events and given in the unit of percent. Note that the sum in quadrature of those effects is not equal to the total effect because some of the systematic parameters are correlated. 110
11.7 Summary of the contributions of systematic errors on the predicted number of events. Each error is given in the unit of percent. The total size of error in the 2012 analysis is shown for comparison. 111
11.8 Summary of the contributions to the error on the p_e-θ_e PDF from each systematic source. The definition of the errors are shown in Equation 11.8. Each error is given in the unit of percent. 114
11.9 Summary of the contributions to the error on the p_e-θ_e PDF from each group of systematic sources. The definition of the errors are shown in Equation 11.8. Each error is given in the unit of percent. 114
11.10 Summary of the results and comparison with the 2012 results, with $\sin^2 2\theta_{23} = 1.0$, $|\Delta m^2_{32}| = 2.4 \times 10^{-3}$ eV^2 and $\delta_{\rm CP} = 0$. 120
11.11 Summary of the fit results for Run1-4 data (6.570×10^{20}), with and without marginalizing over θ_{23} and Δm^2_{32}, with $\delta_{\rm CP} = 0$. 125
11.12 The 90% C.L. excluded region in $\delta_{\rm CP}$ for Run1-4 data, extracted by using the Feldman-Cousins method. 126
11.13 The 90% C.L. excluded region in $\delta_{\rm CP}$ for averaged toy MC likelihood curves, extracted by using the Feldman-Cousins method. The toy MC experiments are generated assuming normal hierarchy and $\delta_{\rm CP} = -\pi/2$. 128

A.1 The measured momentum and contamination of muons for five different data sets. 138
A.2 Summary of the physics model systematic errors related to event selection efficiency (in percentage). 144

B.1 Summary of the measured proton beam parameters and their uncertainties for a typical run period: mean position (X, Y) and angle (X', Y'), width σ, emittance ϵ and twiss parameter α. 149
B.2 Uncertainty in the alignment of the target and horn. There are uncertainties in x, y, z position, horizontal and vertical rotation angle θ_H and θ_V. 149

E.1 Summary of the number of POT for analysis and the observed number of events in each run period. 159
E.2 Summary of the fit results for data of individual run periods. 161

List of Figures

1.1 Coherent forward scattering in matter. . . . 5
1.2 The $\nu_\mu \to \nu_e$ and $\overline{\nu}_\mu \to \overline{\nu}_e$ oscillation probability as a function of neutrino energy, with $\sin^2 2\theta_{13} = 0.098$, $\delta_{\rm CP} = \pi/2$, $\sin^2 2\theta_{23} = 0.97$, $|\Delta m^2_{32}| = 2.35 \times 10^{-3}{\rm eV}^2$, normal hierarchy and baseline of 295 km. . . . 7
1.3 Neutrino mass hierarchy. . . . 10
1.4 Feynman diagram of double beta decay. . . . 12

2.1 The overview the of T2K experiment [50]. . . . 15
2.2 Bird's eye view of J-PARC. . . . 16
2.3 Neutrino beam line and the near detectors. . . . 17
2.4 Illustration of the first horn. The graphite target sits inside the first horn. The positively charged particles produced by the proton beam are focused in the forward direction due to the magnetic field. . . . 17
2.5 Locations of the beam monitors [50]. . . . 18
2.6 Illustrations of the beam monitors. . . . 19
2.7 Neutrino energy in the function of the momentum of parent pion, for different off-axis angles. . . . 20
2.8 The neutrino energy spectrum for different off-axis angles (top) and the oscillation probability in the function of neutrino energy (bottom). . . . 20
2.9 Schematic view of MUMON. Neutrino beam comes from the left side of the figure. 21
2.10 The near detectors located at 280 m downstream from the neutrino production target. . . . 22
2.11 The INGRID detector. . . . 23
2.12 Schematic view of ND280 detectors. In this figure, the magnet yoke and the inner detectors are drawn separately, but they are combined in the actual detector, as shown in Fig. 2.10. . . . 24
2.13 The TPC detector [57]. . . . 25
2.14 TPC micromegas readout. . . . 25
2.15 Super Kamiokande detector. . . . 26
2.16 Delivered POT to neutrino facility. . . . 27
2.17 Stability of neutrino event rate normalized by POT in INGRID (top), and the stability of neutrino beam direction measured by INGRID and MUMON (middle, bottom). . . . 27

3.1 Example event display of ND280 tracker. CCQE interaction is simulated. . . . 29
3.2 FGD architecture. . . . 29
3.3 Cross-sectional view of the water panel [56]. . . . 30
3.4 Cross-sectional view of the scintillator bar [56]. . . . 30
3.5 Hit finding efficiency as a function of the distance from the center axis of the bar [56]. . . . 30

3.6 The overview of read out system for the FGDs. 31
3.7 Example of pulse height distribution for MPPC dark noise. The peak around 40 ADC corresponds to the 1 p.e. signal [56]. 34
3.8 The 1 p.e. pulse height vs. Bias voltage before (left) and after (right) the temperature correction for typical MPPC. The different colors corresponds to the different temperature [56]. 34
3.9 The number of photo-electrons normalized by the path length, as a function of the hit position. The data points are derived from cosmic-ray measurement. The line represents the empirical attenuation formula [56]. 35
3.10 Charge distribution after correction, compared with simulation [56]. 35
3.11 Deposited energy vs. stopping range for FGD1. The scatter-plot shows stopping particles in neutrino beam data, while the curves show the MC expectations for protons, muons, and pions [56]. 36
3.12 Example of the hit bars for a given particle, following the true trajectory in red. 37
3.13 Example of the tracks (blue lines), reconstructed by Hough transform method. . 37
3.14 Illustration of Radon transform in FGD reconstruction. 37
3.15 Example of the neutrino event after track reconstruction (MC). 39
3.16 Reconstruction efficiency vs. Number of tracks 39

4.1 Pion interactions on nuclei. 41
4.2 π^+-C absorption and charge exchange cross sections from past experiments [70–76] The lines represent the prediction from the NEUT cascade model. 42
4.3 Overview of the M11 beam line. 43
4.4 Overview of the detector setup (side view). The pion beam comes from the left side of this figure. 44
4.5 Illustration of light propagation in Cherenkov detector for pion (left) and muon (right). 44
4.6 Cherenkov light vs. TOF for the beam particle at $p_\pi = 250$ MeV/c setting. The red line correspond to the threshold to distinguish pions from muons and electrons. 45
4.7 Front view of the fiber tracker detector. 45
4.8 Schematic drawing of MAPMT readout electronics. 47
4.9 Experimental setup in configuration B. 48

5.1 Example of ABS candidate event in data (p_π =250MeV/c). The red circles correspond to the large hits (> 20 p.e.), and the crosses correspond to the hits identified as crosstalk hits. 51
5.2 Example of pion scattering candidate event in data (p_π =250MeV/c). The blue track is identified as the incident pion track, and the green track is identified as a scattered pion track. 52
5.3 Example of CX candidate event in data (p_π =250MeV/c). The blue track is assumed to be the incident pion track, and the green track is assumed to be a proton track from CX interaction. 52
5.4 Illustration of *good incident pion* cut requirement. The black broken line represents the definition of the fiducial volume. 54
5.5 The X-Y view of incident beam position distribution. The white broken line represents the definition of the fiducial volume. 54
5.6 dQ/dx distribution in six different angular regions, for $p_\pi = 250$ MeV/c data and MC. The dotted vertical lines represent the threshold to distinguish pions and protons. For multiple tracks events, only the smallest value of dQ/dx among the tracks is filled in the histogram. The events in the "Others" category are mainly pion decay in flight events and Coulomb scattering events. 55

5.7 Comparison of elastic inclusive cross section between the past experiments (summarized in Table 5.2) and Geant4 default. The cross sections are plotted as a function of pion kinetic energy. 56
5.8 Comparison of inelastic inclusive cross sections between the past experiment [70] and Geant4 default. The cross sections are plotted as a function of pion momentum. 56
5.9 The number of tracks and angular distribution of reconstructed tracks for MC before and after tuning, and for data, for p_π =250 MeV/c data set. The *No* π^+ cut is not applied. 58
5.10 Angular distribution of the reconstructed tracks in the final state, for 200 (left), 250 (center) and 300 (right) MeV/c data sets, before (top) and after (bottom) applying *No* π^+ cut. When the true track angle is close to 90 degrees, the track reconstruction algorithm tends to reconstruct the track exactly at 90 degrees, so the number of events in the bin corresponding to 90 degrees is larger than the neighbor bins. 59
5.11 Distribution of number of reconstructed tracks in the final state, for 200 (left), 250 (center) and 300 (right) MeV/c data sets, before (top) and after (bottom) applying *No* π^+ cut. 60
5.12 Charge distribution of through going pions in $p_\pi = 250$ MeV/c setting. 60
5.13 Result of ABS + CX cross section vs. Pion momentum, compared with the results from past experiments. 61

6.1 Illustration of the NEUT cascade model. The large circle represents the nuclei. . 62
6.2 Example of normalized nuclear density distributions. 63
6.3 Interaction probability per step for π^+ with $p_\pi = 275$ MeV/c in ^{16}O. 64
6.4 The predicted π^+-C cross section compared to measurements in the past, for four different interaction channels. 65
6.5 π^+-^{12}C cross section for five different interaction channels, compared between NEUT nominal prediction (blue curves) and data points from past experiments. The white circle points in ABS + CX sample are the data points from our measurements. 68
6.6 π^--^{12}C cross section for five different interaction channels, compared between NEUT nominal prediction (blue curves) and data points from past experiments. 69
6.7 Best fit (black point) and 1 sigma allowed region (green line) of the NEUT scaling parameters. 69
6.8 The 3D distribution of the eight parameter sets which represent 1σ deviation. The red (black) points shows the parameter sets derived in the new (old) tuning. 70
6.9 π^+-^{12}C cross section for five different interaction channels, compared between NEUT nominal prediction and data points from past experiments. The red lines represent the NEUT prediction with best fit parameters, and the blue lines represent the 1 sigma deviation. The white circle points in ABS + CX sample are the data points from our measurements. 71
6.10 π^--^{12}C cross section for five different interaction channels, compared between NEUT nominal prediction and data points from past experiments. The red lines represent the NEUT prediction with best fit parameters, and the blue lines represent the 1 sigma deviation. 72

7.1 Illustration of the overview of the oscillation analysis. 74

8.1 Overview of the neutrino beam flux simulation. 76
8.2 Predicted neutrino flux at ND280 (left) and SK (right). 77

8.3 Fractional uncertainties of the ν_μ flux at ND280 (left) and SK (right). 78
8.4 ND280/SK flux correlation matrix. 78
8.5 Neutrino-nucleus cross section per nucleon as a function of neutrino energy calculated by using NEUT. 79
8.6 Feynman diagram for CCQE interaction. 79
8.7 Feynman diagram for CC1π interaction via baryon resonance. 79

9.1 Energy loss vs. momentum for the particle tracks in TPC, for negatively charged particles (left) and positively charged particles (right). The lines represents the prediction by MC [57]. 85
9.2 Distribution of the momentum of positive pions (left top), negative pions (right top), electrons (left bottom) and positrons (right bottom) reconstructed in TPC using the TPC probability criteria, in the CC sample. The color of the histograms represents the types of particles. 86
9.3 Pion pull distribution for the FGD fully contained tracks, before applying the PID cut. The color of the histograms represents the types of particles. 87
9.4 Distribution of the total charge in a delayed time hits. The color of the histograms represents the neutrino interaction modes. 87
9.5 Example of selected events in three event topologies. 88
9.6 Momentum distribution of the muon candidate tracks in CC-inclusive sample (left top), CC0π sample (right top), CC1π sample (left bottom) and CC other sample (right bottom). 89
9.7 Muon momentum distribution for CC0π sample (left), CC1π^+ sample (middle) and CC other sample (right), with error band (red) representing the systematic errors. 91
9.8 Muon momentum and $\cos\theta$ distribution for data compared with MC, for CC0π sample (top), CC1π sample (middle) and CC-Other sample (bottom). The blue and red histograms shows the MC distributions before and after data constraint, respectively. 92
9.9 SK ν_μ (left) and ν_e (right) flux parameters, before and after the fit. The red and blue bands represents the uncertainty of the parameters before and after the fit. 93
9.10 The parameter correlations prior to (left) and after (right) ND280 fit. The parameters are 0-24 SK flux parameters, 25 M_A^{QE}, 26 M_A^{RES}, 27-29 CCQE normalization, 30-31 CC1π normalization, 32 NC1π^0 normalization. 94

10.1 Event displays for the SK simulation of ν_e CCQE event (left), ν_μ, ν_μ CC event (middle) and NC1π^0 event (right). 95
10.2 PID parameter distribution for the FCFV single-ring events. 97
10.3 Visible energy distribution for the FCFV single-ring electron like events. 97
10.4 Reconstructed neutrino energy distribution. 98
10.5 $\mathcal{L}_\pi/\mathcal{L}_e$ vs. invariant mass distribution for π^0 rejection cut. The red line indicates the threshold to distinguish π^0 and e. Events at the upper right side of the line is rejected [32]. 98
10.6 Square root of the diagonal elements in the covariance matrix (left), and the correlation matrix (right). The definition of the bins are: 0-12 for signal ν_e, 13-25 for ν_μ CC background, 26-38 for ν_e CC background and 39-53 for NC background. 99

11.1 Distribution of (p_e, θ_e) for signal ν_e events and the different categories of background events. All distributions are normalized to one. 102
11.2 The predicted (p_e, θ_e) PDF for $\sin^2 2\theta_{13} = 0.0$ (left) and 0.1 (right). 104

11.3 Size (left) and correlation matrix (right) of all the systematic uncertainties. The definition of the binning is shown in Table 11.3: 0-21=Beam parameters, 22-35=Cross section parameters, 36-87=SK efficiency+FSI+PN, 88=SK p-scape error. The definition of the beam parameter bins are same as the bins defined in Table 11.4, and the definition of the SK efficiency + FSI + PN parameters bins are same as in Fig. 10.6. 106
11.4 An example of a response function for p = 400-500 MeV/c^2, θ = 60-70 degrees, E_ν = 0.8-1.2 GeV. 107
11.5 An illustration of the implementation of the SK momentum scale error. 108
11.6 Size of the FSI+SI systematic error. The definition of the bins are: 0-12 for signal ν_e, 13-25 for ν_μ CC background, 26-38 for ν_e CC background and 39-53 for NC background. 109
11.7 Size of the PN systematic error. The definition of the bins are: 0-12 for signal ν_e, 13-25 for ν_μ CC background, 26-38 for ν_e CC background and 39-53 for NC background. 109
11.8 The distribution of the predicted number of events for $\sin^2 2\theta_{13} = 0$ (left) and 0.1 (right), obtained by throwing the systematic parameters with (top) and without (bottom) the ND280 fit results. Blue histograms shows the statistical fluctuation without systematic fluctuation. 111
11.9 The (p_e, θ_e) PDF distribution as a function of momentum for different angle bins (10 out of 15 bins are shown here for example) in the $\sin^2 2\theta_{13} = 0.1$ case. Red areas represent one sigma deviations evaluated using 20000 throws of the systematic parameters following the multivariate normal distribution using their central values and covariance matrix. 112
11.10 Same as Fig. 11.9, for $\sin^2 2\theta_{13} = 0.0$ case. 117
11.11 Negative averaged log likelihood as a function of $\sin^2 2\theta_{13}$ for Run1-3 POT case (dotted) and Run1-4 POT case (solid). Both of them are analyzed in the same way except for the difference in POT. 118
11.12 Negative averaged log likelihood as a function of $\sin^2 2\theta_{13}$ with old 2012 systematic errors (pink) and with new 2013 systematic errors (blue), for Run1-4 POT case. 118
11.13 Negative averaged log likelihood as a function of $\sin^2 2\theta_{13}$ with POLfit π^0 cut (pink) and with fiTQun π^0 cut (blue), for Run1-4 POT case. 118
11.14 Fit results of the Run1-4 data until May 8^{th} 2013 assuming $\delta_{\rm CP} = 0$ and normal hierarchy. Top left : the p_e-θ_e distribution with the best fit value of θ_{13} and the central values of systematic parameters plotted with the data (black dots). Top right : the angular distribution of the best fit point with the data. Bottom left : the momentum distribution of the best fit point with the data. The error bars show the statistical errors in Poisson distribution. The pink (green) histograms represent the expected signal (background) component. Bottom right : the negative log likelihood distribution as a function of $\sin^2 2\theta_{13}$. 119
11.15 Same as in Fig. 11.14 for inverted hierarchy case. 119
11.16 Allowed region of 68 % (green) and 90 % C.L. (blue) for $\sin^2 2\theta_{13}$ for each value of $\delta_{\rm CP}$, for normal (left) and inverted (right) hierarchy. The black solid line is the best fit value for each value of $\delta_{\rm CP}$. Left (right) plot: normal (inverted) hierarchy is assumed. 120
11.17 Distribution of $\Delta\chi^2$ for different number of observed events, in the case of $\sin^2 2\theta_{13} = 0$ over 9.6×10^{14} toy MC experiments for 6.570×10^{20} POT, $N_{obs} > 24$. The systematic errors are incorporated. The $\Delta\chi^2$ value for Run1-4 data was 53.64, which is shown as a pink line in the plot. 121

11.18Distribution of $\Delta\chi^2$ in the case of $\sin^2 2\theta_{13} = 0$ over 9.6×10^{14} toy MC experiments for 6.570×10^{20} POT, $N_{obs} > 24$. The systematic errors are incorporated. The $\Delta\chi^2$ value for Run1-4 data was 53.64, which is shown as a pink line in the plot. The integrated fraction of toy MC experiments for which the $\Delta\chi^2 > 53.64$ is 1.0×10^{-13}. 122
11.19Allowed region of 68 % C.L. for $\sin^2 2\theta_{13}$ for each value of $\sin^2\theta_{23}$, for Run1-4 data. The green, black and blue contours corresponds to $\sin^2\theta_{23} = 0.4, 0.5$ and 0.6. The $|\Delta m^2_{32}|$ is fixed to 2.4×10^{-3} eV^2. The yellow shaded region shows the reactor 1σ range (0.098 ± 0.013) from PDG2012. Left (right) plot: normal (inverted) hierarchy is assumed. 122
11.20$\Delta\chi^2$ map for $\sin^2\theta_{23}$ and Δm^2_{32}, obtained from T2K Run1-3 ν_μ disappearance measurement. The white dotted line represents the 68% C.L. contour region. . . 123
11.21Negative delta log likelihood as a function of $\sin^2 2\theta_{13}$, averaged over 4000 toy MC experiments. The sensitivity is obtained from these curves. In the fit, the values of $\sin^2\theta_{23}$ and Δm^2_{32} are fixed to 0.5 and 2.4×10^{-3} for the black curve, while for the pink curve we marginalize over $\sin^2\theta_{23}$ and Δm^2_{32} with constraint from the T2K Run1-3 ν_μ disappearance measurement. The true value of the oscillation parameters to generate toy data sets are fixed to the nominal values. Toy MC experiments are generated in normal hierarchy and fitted assuming normal hierarchy. 124
11.22Comparison of the negative log likelihood as a function of $\sin^2 2\theta_{13}$, with (blue) and without (black) marginalizing over θ_{23} and Δm^2_{32}, for the T2K Run1-4 data. Left (right) plot shows the result assuming normal (inverted) hierarchy. 125
11.23Allowed region of 68 % (green) and 90 % C.L. (blue) for $\sin^2 2\theta_{13}$ for each value of $\delta_{\rm CP}$, for Run1-4 data (6.570×10^{20} POT) [32]. The likelihood is marginalized over $\sin^2\theta_{23}$ and Δm^2_{32}. The black solid line is the best fit value for each value of $\delta_{\rm CP}$. Left (right) plot: normal (inverted) hierarchy is assumed. 126
11.24Negative delta log likelihood as a function of $\delta_{\rm CP}$, for T2K Run1-4 data. Black (red) curve shows normal (inverted) hierarchy case [32]. Likelihoods are marginalized over $\sin^2\theta_{23}$, Δm^2_{32} and $\sin^2 2\theta_{13}$. 127
11.25Critical χ^2 90% C.L. limit drawn on top of Fig. 11.24. The blue line corresponds to the critical $\Delta\chi^2$ for 90% C.L., extracted by using the Feldman-Cousins method. The solid (broken) lines correspond to normal (inverted) hierarchy [32]. 128
11.26Distribution of $-2\Delta\ln\mathcal{L}'$ at $\delta_{\rm CP} = \pi/2$, for 4000 toy MC experiments. The left (right) plot shows the distribution for the fit assuming normal (inverted) hierarchy. The pink line corresponds to the -2$\Delta\ln\mathcal{L}'$ value obtained for data. The true values in MC is set to $\sin^2 2\theta_{13}$= 0.1, $\sin^2\theta_{23} = 0.5, \Delta m^2_{32} = 2.4 \times 10^{-3}$ eV^2 and $\delta_{\rm CP} = -\pi/2$. 129
11.27Negative log delta likelihood as a function of $\delta_{\rm CP}$, averaged over 4000 toy MC experiments, for 6.570×10^{20} POT case. Black (red) curve shows normal (inverted) hierarchy case. Likelihoods are marginalized over $\sin^2\theta_{23}, \Delta m^2_{32}$ and $\sin^2 2\theta_{13}$. . 130
11.28Run1-4 full data compared to MC with $\delta_{\rm CP} = -\pi/2$, $\sin^2 2\theta_{13} = 0.098$, $\sin^2\theta_{23} = 0.514$, $\Delta m^2_{32} = 2.44 \times 10^{-3}$ eV^2 and normal hierarchy. 130
11.29Same as Fig. 11.28, for inverted hierarchy case. 131

A.1 Charge distribution of through going pions for data and MC, for $p_\pi = 150$ and 300 MeV/c data set. 136
A.2 Charge distribution of through going muons in $p_\pi = 250$ MeV/c setting. 137
A.3 Beam position distribution in X, for the data set with $p_\pi = 250$ MeV/c setting. The black (red) histogram shows the distribution for data (MC). 137

A.4 Beam angular distribution in X projection, for the data set with $p_\pi = 250$ MeV/c setting. The variable θ is the angle from horizontal line (X=0). The black (red) histogram shows the distribution for data (MC). 137
A.5 Stopping layer distribution in Harpsichord, for data with 250 MeV/c settings and MC with several different momentum settings. 138
A.6 Charge distribution of through going particles at the downstream three XY layers in Harpsichord, for data with $p_\pi = 300$ MeV/c setting and MC with several different momentum settings. 138
A.7 Distribution of distance from the threshold line in Fig. 4.6. 139
A.8 Same as Fig. A.7, but for 300 MeV/c data set. 139
A.9 Charge distribution of through going particles, measured in the last three XY layers of Harpsichord, for 300 MeV/c data set. The left (right) shows the distribution before (after) applying the beam PID cut. The normalization of muons and pion component in MC is tuned so that it agree with data. 139
A.10 Angular distribution of the backward going proton-like track, for ABS and CX events, for $p_\pi = 250$ MeV/c setting. For each event, a proton-track with largest angle is selected and filled in the histogram. The left plot shows the distribution for data and MC, and the right plot shows the distribution for nominal and reweighted MC. 144
A.11 Example of dQ/dx distribution after event selection, for the projection which was not used for calculating dQ/dx in no π^+ cut, for the data set with p_π =250MeV/c setting. The left plot is an example for $30 < \theta < 60$ degree, and the right plot is for $60 < \theta < 90$ degree. The broken line shows the threshold to distinguish pion-like tracks and proton-like tracks. 144
A.12 The predicted momentum distribution of protons from the ABS events, for Geant4 (black) and NEUT (red), for $p_\pi = 295.1$ MeV/c. The histograms are normalized by number of ABS events. 145
A.13 Angular distribution of π-like tracks for data and MC with $p_\pi = 250$ MeV/c setting. The histograms are normalized by number of incident pions in data. . . 145
A.14 Example of dQ/dx distribution for incident track for the data set with $p_\pi = 250$ MeV/c setting, after requiring π-like 2D track which was only reconstructed in one projection. The histograms are normalized by number of incident pions. . . 145
A.15 Predicted momentum distribution of pions from inelastic scattering event, for Geant4 (black) and NEUT (red), for $p_\pi = 201.6$ MeV/c. The histograms are normalized by area. 145

B.1 Fractional uncertainties of the neutrino beam flux at ND280 detector, for ν_e flux (left top), $\overline{\nu}_e$ flux (right top), ν_μ flux (left bottom) and $\overline{\nu}_\mu$ flux (right bottom). . 147
B.2 Fractional uncertainties of the neutrino beam flux at SK detector, for ν_e flux (left top), $\overline{\nu}_e$ flux (right top), ν_μ flux (left bottom) and $\overline{\nu}_\mu$ flux (right bottom). . . . 148
B.3 Fits to MiniBooNE single pion production cross section data. 152

C.1 The $(p, \cos\theta)$ distribution of muons for CC0π (left), CC1π (middle) and CC other sample (right). 153
C.2 Covariance matrix for flux parameters. The bin indices are defined as follows: ND280 ν_μ (0-10), ND280 $\overline{\nu}_\mu$ (11-15), ND280 ν_e (16-22), ND280 $\overline{\nu}_e$ (23-24), SK ν_μ (25-35), SK $\overline{\nu}_\mu$ (36-40), SK ν_e (41-47), and SK $\overline{\nu}_e$ (48-49), with the energy divisions for the neutrino types given in the text. 154

D.1 Efficiency errors of the topological cuts in (p_e, θ_e) bins for "ν_e CC single-e" and "ν_e CC other" samples, derived from atmospheric control sample. 158

D.2 Example of the data/MC relative difference in NC1π^0 hybrid-π^0 control sample for the θ_e bins, at p_e <300 MeV/c. 158

E.1 Fit results for the Run1+2+3 data assuming $\delta_{\mathrm{CP}} = 0$ and normal hierarchy. . . 160
E.2 Fit results for the Run1+2+3 data assuming $\delta_{\mathrm{CP}} = 0$ and inverted hierarchy. . . 160
E.3 Fit results for the Run4 data until May 8^{th} 2013 assuming $\delta_{\mathrm{CP}} = 0$ and normal hierarchy. 162
E.4 Fit results for the Run4 data until May 8^{th} 2013 assuming $\delta_{\mathrm{CP}} = 0$ and inverted hierarchy. 162
E.5 Comparison of the negative log likelihood as a function of $\sin^2 2\theta_{13}$ among the Run1+2+3 data, Run4 data and Run1-4 data. Left (right) plot shows the result assuming normal (inverted) hierarchy. 163
E.6 Comparison of the best fit value of $\sin^2 2\theta_{13}$ and its 68 % C.L. and 90 % allowed region among the Run1+2+3 data, Run4 data and Run1-4 data. The solid (broken) lines correspond to 68 % (90 %) C.L. regions. Left (right) plot shows the result assuming normal (inverted) hierarchy. 163
E.7 Allowed region of 68 % (green) and 90 % C.L. (blue) for $\sin^2 2\theta_{13}$ for each value of δ_{CP}, for Run1+2+3 data. The black solid line is the best fit value for each value of δ_{CP}. Top (bottom) plot: normal (inverted) hierarchy is assumed. 164
E.8 Allowed region of 68 % (green) and 90 % C.L. (blue) for $\sin^2 2\theta_{13}$ for each value of δ_{CP}, for Run4 data only. The black solid line is the best fit value for each value of δ_{CP}. Top (bottom) plot: normal (inverted) hierarchy is assumed. 164
E.9 Run1-4 δ_{CP} vs. $\sin^2 2\theta_{13}$ contours compared with Run1-3. Dark (light) blue lines correspond to 68 % (90 %) C.L. regions. The black solid line is the best fit value for each value of $\sin^2\theta_{23}$. Pink area shows the 90 % C.L. region of Run1-3 data fit (using 2013 analysis method). Red dotted line shows the best fit of Run1-3. Top (bottom) plot: normal (inverted) hierarchy is assumed. 165
E.10 Run1-4 δ_{CP} vs. $\sin^2 2\theta_{13}$ contours compared with Run4 only. Dark (light) blue lines correspond to 68 % (90 %) C.L. regions. The black solid line is the best fit value for each value of $\sin^2\theta_{23}$. Pink area shows the 90 % C.L. region of 4 only data fit (using 2013 analysis method). Red dotted line shows the best fit of Run4 only. Top (bottom) plot: normal (inverted) hierarchy is assumed. 165
E.11 Run1-3 data fit result with 2013 analysis (Black) compared with 2012 analysis (Pink), for normal hierarchy. 166
E.12 Run1-3 data fit result with 2013 analysis (Black) compared with 2012 analysis (Pink), for inverted hierarchy. 166

Bibliography

[1] Y. Fukuda, et al. Evidence for oscillation of atmospheric neutrinos. *Phys.Rev.Lett.*, Vol. 81, pp. 1562–1567, 1998.

[2] M. Fukugita and T. Yanagida. Baryogenesis without grand unification. *Phys. Rev.*, Vol. B174, p. 45, 1986.

[3] C. L. Cowan, et al. Detection of the free neutrino: A confirmation. *Science*, Vol. 124, p. 103, 1956.

[4] G. Danby, et al. Observation of high-energy neutrino reactions and the existence of two kinds of neutrinos. *Phys. Rev. Lett.*, Vol. 9, p. 36, 1962.

[5] The ALEPH, DELPHI, L3 and OPAL Collaborations and others. Precision electroweak measurements on the Z resonance. *Phys. Reports.*, Vol. 427, pp. 257–454, 2006.

[6] Jr. Davis, Raymond, Don S. Harmer, and Kenneth C. Hoffman. Search for neutrinos from the sun. *Phys.Rev.Lett.*, Vol. 20, pp. 1205–1209, 1968.

[7] K. S. Hirata et al. Results from one thousand days of real-time, directional solar-neutrino data. *Phys. Rev. Lett.*, Vol. 65, p. 1297, 1990.

[8] P. et al. Anselmann. Solar neutrinos observed by gallex at gran sasso. *Phys. Lett.*, Vol. B285, pp. 376–389, 1992.

[9] W. et al. Hampel. Gallex solar neutrino observations: Results for gallex iv. *Phys. Lett.*, Vol. B447, pp. 127–133, 1999.

[10] M. Altmann et al. Complete results for five years of gno solar neutrino observations. *Phys. Lett.*, Vol. B616, p. 174, 2005.

[11] J. N. et al. Abdurashitov. Measurement of the solar neutrino capture rate with gallium metal, part iii. *Phys. Rev.*, Vol. C80, p. 015807, 2009.

[12] B. Pontecorvo. Inverse beta processes and nonconservation of lepton charge. *Sov. Phys. JETP*, Vol. 7, p. 172, 1958.

[13] M. Nakagawa Z. Maki and S. Sakata. Remarks on the unified model of ele-mentary particles. *Prog. Theor. Phys.*, Vol. 28, p. 870, 1962.

[14] S. Tanaka Y. Katayama, K. Matumoto and E. Yamada. Possible unified models of elementary particles with two neutrinos. *Prog. Theor. Phys.*, Vol. 28, p. 675, 1962.

[15] Q.R. Ahmad, et al. Measurement of the rate of $\nu_e + d \rightarrow p + p + e^-$ interactions produced by b-8 solar neutrinos at the sudbury neutrino observatory. *Phys. Rev. Lett.*, Vol. 87, p. 071301, 2001.

[16] S. Fukuda, et al. Solar ^{8}B and hep Neutrino Measurements from 1258 Days of Super-Kamiokande Data. *Phys.Rev.Lett.*, Vol. 86, pp. 5651–5655, 2001.

[17] L. Wolfenstein. Neutrino oscillations in matter. *Phys.Rev.*, Vol. D17, pp. 2369–2374, 1978.

[18] Burton Richter. Conventional beams or neutrino factories: The Next generation of accelerator based neutrino experiments. *Arxiv preprint hep-ph*, 2000.

[19] J. Beringer et al. (Particle Data Group). Review of particle physics. *Phys. Rev. D*, Vol. 86, p. 010001, 2012.

[20] A. Gando, et al. Constraints on θ_{13} from a three-flavor oscillation analysis of reactor antineutrinos at kamLAND. *Phys. Rev.*, Vol. D83, p. 052002, 2011.

[21] K. Abe, et al. Search for Differences in Oscillation Parameters for Atmospheric Neutrinos and Antineutrinos at Super-Kamiokande. *Phys.Rev.Lett.*, Vol. 107, p. 241801, 2011.

[22] K. Abe, et al. Measurement of Neutrino Oscillation Parameters from Muon Neutrino Disappearance with an Off-Axis Beam. *Phys. Rev. Lett.*, Vol. 111, p. 211803, 2013.

[23] P. Adamson, et al. Measurement of the neutrino mass splitting and flavor mixing by MINOS. *Phys. Rev. Lett.*, Vol. 106, p. 181801, 2011.

[24] K. Abe, et al. Indication of Electron Neutrino Appearance from an Accelerator-produced Off-axis Muon Neutrino Beam. *Phys. Rev. Lett.*, Vol. 107, p. 041801, 2011.

[25] M. Apollonio, et al. Search for neutrino oscillations on a long baseline at the CHOOZ nuclear power station. *Eur.Phys.J.*, Vol. C27, pp. 331–374, 2003.

[26] F.P. An, et al. Observation of electron-antineutrino disappearance at Daya Bay. *Phys.Rev.Lett.*, Vol. 108, p. 171803, 2012.

[27] J.K. Ahn, et al. Observation of Reactor Electron Antineutrino Disappearance in the RENO Experiment. *Phys.Rev.Lett.*, Vol. 108, p. 191802, 2012.

[28] Y. Abe, et al. Indication for the disappearance of reactor electron antineutrinos in the Double Chooz experiment. *Phys.Rev.Lett.*, Vol. 108, p. 131801, 2012.

[29] K. Abe, et al. Evidence of electron neutrino appearance in a muon neutrino beam. *Phys. Rev.*, Vol. D88, p. 032002, 2013.

[30] T. Nakaya. New Results from T2K. In *New Results from T2K*, `http://www.sciencedirect.com/science/article/pii/S0920563213001199`, 2012.

[31] K. Sakashita. Results from T2K. In *Results from T2K*, `http://pos.sissa.it/archive/conferences/174/380/ICHEP2012_380.pdf`, 2012.

[32] K. Abe, et al. Observation of electron neutrino appearance in a muon neutrino beam. *Phys. Rev. Lett.*, Vol. TBA, , 2013.

[33] D. H. Perkins P.F. Harrison and W. G. Scott. Tri-bimaximal mixing and the neutrino oscillation data. *Phys. Rev.*, Vol. B530, p. 167, 2002.

[34] S. Antusch and S.F. King. Charged lepton corrections to neutrino mixing angles and CP phases revisited. *Phys. Rev.*, Vol. B631, p. 42, 2005.

[35] H. Murayama L. Hall and N. Weiner. Neutrino mass anarchy. *Phys. Rev. Lett.*, Vol. 84, p. 2572, 2000.

[36] A. Aguilar, et al. Evidence for neutrino oscillations from the observation of $\overline{\nu}_e$ appearance in a $\overline{\nu}_\mu$ beam. *Phys. Rev.*, Vol. D64, p. 112007, 2001.

[37] A. Aguilar, et al. Improved search for $\overline{\nu}_\mu \to \overline{\nu}_e$ oscillations in the MiniBooNE experiment. *Phys. Rev. Lett.*, Vol. 110, p. 161801, 2013.

[38] G. Mention, et al. Reactor antineutrino anomaly. *Phys. Rev.*, Vol. D83, p. 073006, 2011.

[39] Carlo Giunti and Marco Laveder. Statistical significance of the gallium anomaly. *Phys. Rev.*, Vol. C83, p. 065504, 2011.

[40] B. Armbruster, et al. Upper limits for neutrino oscillations $\overline{\nu}_\mu \to \overline{\nu}_e$ from muon decay at rest. *Phys. Rev.*, Vol. D65, p. 112001, 2002.

[41] K. B. M. Mahn, et al. Dual baseline search for muon neutrino disappearance at $0.5\text{eV}^2 < \delta m^2 < 40$ eV^2. *Phys. Rev.*, Vol. D85, p. 032007, 2012.

[42] P. Adamson, et al. Active to sterile neutrino mixing limits from neutral-current interactions in MINOS. *Phys. Rev. Lett.*, Vol. 107, p. 011802, 2011.

[43] F. R. Klinkhamer and N. S. Manton. A saddle-point solution in the weinberg-salam theory. *Phys. Rev.*, Vol. D30, p. 2212, 1984.

[44] L. Wolfenstein. Results on Neutrinoless Double-β Decay of ^{76}Ge from Phase I of the GERDA Experiment. *Phys. Rev. Lett.*, Vol. 111, p. 122503, 2013.

[45] E. Andreotti, et al. Search for double-$\overline{\beta}$ decay of ^{130}Te to the first 0^+ excited state of ^{130}Xe with the CUORICINO experiment bolometer array. *Phys. Rev.*, Vol. C85, p. 045503, 2012.

[46] M. Auger, et al. Search for neutrinoless double-beta decay in ^{136}Xe with EXO-200. *Phys. Rev. Lett.*, Vol. 109, p. 032505, 2012.

[47] A. Gando, et al. Measurement of the double-β decay half-life of ^{136}xe with the KamLAND-Zen experiment. *Phys. Rev.*, Vol. C85, p. 045504, 2012.

[48] C. S. Wu, et al. Experimental test of parity conservation in beta decay. *Phys. Rev. Lett.*, Vol. 105, p. 1413, 1957.

[49] V. L. Fitch J. H. Christenson, J. W. Cronin and R. Turlay. Evidence for the 2π decay of the k_2^0 meson. *Phys. Rev. Lett.*, Vol. 13, p. 138, 1964.

[50] K. Abe, et al. The T2K Experiment. *Nucl.Instrum.Meth.*, Vol. A659, pp. 106–135, 2011.

[51] J. Beringer, et al. Review of Particle Physics (RPP). *Phys.Rev.*, Vol. D86, p. 010001, 2012.

[52] A.K. Ichikawa. Design concept of the magnetic horn system for the t2k neutrino beam. *Nucl. Instrum. Meth.*, Vol. A690, pp. 27–33, 2012.

[53] Sampa Bhadra, et al. Optical Transition Radiation Monitor for the T2K Experiment. *Nucl. Instrum. Meth.*, Vol. A703, pp. 45–58, 2012.

[54] K. Matsuoka, et al. Design and performance of the muon monitor for the t2k neutrino oscillation experiment. *Nucl. Instrum. Meth.*, Vol. A624, pp. 591–600, 2010.

[55] M. Otani, N. Nagai, D. Orme, A. Minamino, K. Nitta, et al. Design and construction of INGRID neutrino beam monitor for T2K neutrino experiment. *Nucl.Instrum.Meth.*, Vol. A623, pp. 368–370, 2010.

[56] P.-A. Amaudruz, et al. The T2K fine-grained detectors. *Nucl. Instrum. Meth.*, Vol. A696, pp. 1–31, 2012.

[57] N. Abgrall, et al. Time Projection Chambers for the T2K Near Detectors. *Nucl. Instrum. Meth.*, Vol. A637, pp. 25–46, 2011.

[58] I. Giomataris, et al. Micromegas in a bulk. *Nucl. Instrum. Meth.*, Vol. A560, p. 405, 2006.

[59] S. Assylbekov, et al. The T2K ND280 off-axis pi-zero detector. *Nucl. Instrum. Meth.*, Vol. A686, pp. 48–63, 2012.

[60] D. Allan, et al. The electromagnetic calorimeter for the T2K near detector ND280. *JINST*, Vol. 8, p. P10019, 2013.

[61] S. Aoki, et al. The T2K Side Muon Range Detector (SMRD). *Nucl. Instrum. Meth.*, Vol. A698, pp. 135–146, 2013.

[62] Y. Fukuda, et al. The Super-Kamiokande detector. *Nucl.Instrum.Meth.*, Vol. A501, pp. 418–462, 2003.

[63] P. Baron, et al. AFTER, an ASIC for the readout of the large T2K time projection chambers. *IEEE Trans. Nucl. Sci.*, Vol. 55, p. 1744, 2008.

[64] M. Yokoyama, et al. Mass production test of Hamamatsu MPPC for T2K neutrino oscillation experiment. *Nucl. Instrum. Meth.*, Vol. A610, pp. 362–365, 2009.

[65] M. Hasegawa, et al. Measurement of Neutrino Oscillation Parameters with Neutrino-Nucleus Interaction Studies in the K2K Experiment. *Ph.D. thesis, Kyoto university*, 2005.

[66] A. Cervera-Villanueva, et al. "RecPack" a reconstruction toolkit. *Nucl. Instrum. Meth.*, Vol. A534, p. 180, 2004.

[67] H. Maesaka. *Evidence For Muon Neutrino Oscillation In An Accelerator-based Experiment.* PhD thesis, Kyoto University, 2005.

[68] R. O. Duda and P. E. Hart. Use of the hough transformation to detect lines and curves in pictures. *Comm. ACM*, Vol. 15, p. 11, 1972.

[69] Y. Hayato. NEUT. *Nucl. Phys. (Proc. Suppl.)*, Vol. B112, p. 171, 2002.

[70] D. Ashery, et al. True absorption and scattering of pions on nuclei. *Phys. Rev.*, Vol. C23, p. 2173, 1981.

[71] I. Navon, et al. True absorption and scattering of 50 MeV pions. *Phys. Rev.*, Vol. C28, p. 2548, 1983.

[72] E. Bellotti, et al. Positive-pion absorption by C nuclei at 130 MeV. *NUOVO CIMENTO*, Vol. 18A, p. 75, 1973.

[73] E. Bellotti, et al. The $(\pi^+, \pi N)$ Reactions on Carbon at 130 MeV: A Bubble-Chamber Experiment. *NUOVO CIMENTO*, Vol. 14A, p. 567, 1973.

[74] D. Ashery, et al. Inclusive pion single-charge-exchange reactions. *Phys. Rev.*, Vol. C30, p. 946, 1984.

[75] I. Navon, et al. True absorption and scattering of 125 MeV pions on nuclei. *Phys. Rev. Lett*, Vol. 42, p. 1465, 1979.

[76] M. K. Jones, et al. Pion absorption above the $\Delta(1232)$ resonance. *Phys. Rev.*, Vol. C48, p. 2800, 1993.

[77] K. Nitta, et al. The K2K scibar detector. *Nucl. Instrum. Meth.*, Vol. A535, p. 147, 2004.

[78] S. Ritt, P. Amaudruz, and K. Olchanski. *MIDAS (Maximum Integration Data Acquisition System.* `http://midas.psi.ch`, 2001.

[79] S. Agostinelli, et al. Geant4 − a simulation toolkit. *Nucl. Instrum. Meth.*, Vol. A506, p. 250, 2003.

[80] A. Heikkinen, et al. *Bertini intra-nuclear cascade implementation in Geant4.* `http://arxiv.org/abs/nucl-th/0306008`, 2003.

[81] M. A. Moinester, et al. Elastic scattering of positive pions on ^{12}C at 49.9 MeV. *Phys. Rev.*, Vol. C18, p. 2678, 1978.

[82] S. L. Leonard and D. H. Stork. Total cross section for positive ions in hydrogen. *Phys. Rev.*, Vol. 93, p. 568, 1954.

[83] H. L. Anderson, et al. Angular distribution of pions scattered by hydrogen. *Phys. Rev.*, Vol. 91, p. 155, 1953.

[84] H. L. Anderson and M. Glicksman. Scattering of pions by hydrogen at 165 MeV. *Phys. Rev.*, Vol. 100, p. 268, 1955.

[85] J. Ashkin, et al. Total cross sections for negative and positive pions in hydrogen and deuterium. *Phys. Rev.*, Vol. 96, p. 1104, 1954.

[86] S. J. Lindenbaum and Luke C. L. Yuan. Total cross section of hydrogen for 150- to 750-MeV positive and negative pions. *Phys. Rev.*, Vol. 100, p. 306, 1955.

[87] M. Blecher, et al. Positive pion-nucleus elastic scattering at 40 MeV. *Phys. Rev.*, Vol. C20, p. 1884, 1979.

[88] R. R. Johnson, et al. Elastic scattering of positive pions from ^{12}C at 30, 40 and 50 MeV. *Nucl. Phys.*, Vol. A296, p. 444, 1978.

[89] J. F. Amann, et al. Inelastic π^+ scattering from ^{12}C and Si at low energies. *Phys. Rev.*, Vol. C23, p. 1635, 1981.

[90] M. Blecher, et al. Isospin effects in $\pi^\pm$ elastic scattering from ^{12}C, ^{13}C and ^{14}C at 65 and 80 MeV. *Phys. Rev.*, Vol. C28, p. 2033, 1983.

[91] L. E. Antonuk, et al. Elastic and inelastic pion scattering on ^{12}C and ^{13}C at 100 MeV. *Nucl. Phys.*, Vol. A420, p. 435, 1984.

[92] Alden T. Oyer. The measurement of the elastic crosssection for positive pions on carbon at 142MeV. *LA-6599-T Thesis*, 1976.

[93] Michael John Devereux. The study of elastic pion scattering from ^{9}Be, ^{28}Si, ^{58}Ni, and ^{208}Pb at 162 MeV. *LA-7851-T Thesis*, 1979.

[94] F. Binon, et al. Scattering of negative pions on carbon. *Nucl. Phys.*, Vol. B17, p. 168, 1970.

[95] J. S. Frank, et al. Measurement of low-energy elastic $\pi^{\pm}$ differential cross sections. *Phys. Rev.*, Vol. D28, p. 1569, 1983.

[96] Ch. Joram, et al. Low-energy differential cross sections ef pion-proton ($\pi^{\pm}p$) scattering. II. Phase shifts at T_{π} = 32.2, 45.1, and 68.6 MeV. *Phys. Rev.*, Vol. C51, p. 2159, 1995.

[97] J. T. Brack, et al. πp elastic scattering from 67 to 139 MeV. *Phys. Rev.*, Vol. C34, p. 1771, 1986.

[98] J. T. Brack, et al. Forward angle $\pi^{\pm}$p elastic scattering differential cross sections at T_{π} = 87 to 139 Mev. *Phys. Rev.*, Vol. C51, p. 929, 1995.

[99] P. J. Bussey, et al. πp elastic scattering from 88 to 292 MeV. *Nucl. Phys.*, Vol. B58, p. 363, 1973.

[100] L. L. Salcedo, et al. Computer simulation of inclusive pion nuclear reactions. *Nucl. Phys.*, Vol. A484, p. 557, 1988.

[101] C. W. DE Jager, et al. Nuclear charge- and magnetization-density-distribution parameters from elastic electron scattering. *Atomic data and nuclear data tables*, Vol. 14, p. 479, 1974.

[102] A. Saunders, et al. Reaction and total cross sections for low energy π^{+} and π^{-} on isospin zero nuclei. *Phys. Rev.*, Vol. C53, p. 1745, 1996.

[103] S. M. Levenson, et al. Inclusive pion scattering in the $\delta(1232)$ region. *Phys. Rev*, Vol. C28, p. 326, 1983.

[104] H. Hilscher, et al. Charge exchange of 70 MeV π^{-} on C, Al, Cu and Pb. *Phys. Rev*, Vol. C28, p. 326, 1983.

[105] R. H. Miller, et al. Inelastic scattering of 150 MeV negative pions by carbon and lead. *NUOVO CIMENTO*, Vol. V1, p. 882, 1957.

[106] N Abgrall, et al. Measurements of cross sections and charged pion spectra in proton-carbon interactions at 31 GeV/c. *Phys. Rev. C*, Vol. 84, p. 034604, 2011.

[107] N. Abgrall, et al. Measurement of production properties of positively charged kaons in proton-carbon interactions at 31 GeV/c. *Phys. Rev. C*, Vol. 85, p. 035210, 2012.

[108] A. A. Aguilar-Arevalo, et al. First measurement of the muon neutrino charged current quasielastic double differential cross section. *Phys. Rev.*, Vol. D81, p. 092005, 2010.

[109] A. A. Aguilar-Arevalo, et al. Measurement of ν_{μ}-induced charged-current neutral pion production cross sections on mineral oil at $E_{\nu} \in 0.5\breve{}2.0$GeV. *Phys.Rev.*, Vol. D83, p. 052009, Mar 2011.

[110] A. A. Aguilar-Arevalo, et al. Measurement of neutrino-induced charged-current charged pion production cross sections on mineral oil at $E_{\nu} \sim$ 1GeV. *Phys.Rev.*, Vol. D83, p. 052007, Mar 2011.

[111] Alexis A. Aguilar-Arevalo, et al. Measurement of nu(mu) and anti-nu(mu) induced neutral current single pi0 production cross sections on mineral oil at E(nu) O(1- GeV). *Phys.Rev.*, Vol. D81, p. 013005, 2010.

[112] Alfredo Ferrari, Paola R. Sala, Alberto Fasso, and Johannes Ranft. FLUKA: A multi-particle transport code. *CERN-2005-010, SLAC-R-773, INFN-TC-05-11*, 2005.

[113] T. Eichten, et al. Particle production in proton interactions in nuclei at 24 GeV/c. *Nucl. Phys. B*, Vol. 44, , 1972.

[114] J. V. Allaby, et al. High-energy particle spectra from proton interactions at 19.2 GeV/c. Technical Report 70-12, CERN, 1970.

[115] R. Brun, F. Carminati, and S. Giani. GEANT detector description and simulation tool. *CERN-W5013*, 1994.

[116] C. Zeitnitz and T. A. Gabriel. GCALOR. *In Proc. of International Conference on Calorimetry in High Energy Physics*, 1993.

[117] C.H. Llewellyn Smith. Neutrino Reactions at Accelerator Energies. *Phys.Rept.*, Vol. 3, pp. 261–379, 1972.

[118] D. Rein and L.M. Sehgal. Neutrino-excitation of baryon resonances and single pion production. *Ann. Phys.*, Vol. 133, p. 79, 1981.

[119] R. P. Feynman, et al. Current matrix elements from a relativistic quark model. *Phys. Rev.*, Vol. D3, p. 2706, 1971.

[120] D. Rein and L.M. Sehgal. Coherent [pi]0 production in neutrino reactions. *Nucl. Phys.*, Vol. B223, No. 1, pp. 29 – 44, 1983.

[121] D. Rein and L.M. Sehgal. Pcac and the deficit of forward muons in [pi]+ production by neutrinos. *Phys.Lett.*, Vol. B657, No. 4-5, pp. 207 – 209, 2007.

[122] S.L. Adler. Tests of the conserved vector current and partially conserved axial-vector current hypotheses in high-energy neutrino reactions. *Phys.Rev.*, Vol. 135, p. B963, 1964.

[123] C. H. Albright and C. Jarlskog. Neutrino production of M^+ and E^+ heavy leptons. *Nucl. Phys.*, Vol. B84, p. 467, 1975.

[124] M. Gluck, et al. Dynamical parton distributions revisited. *Eur.Phys.J.*, Vol. C5, pp. 461–470, 1998.

[125] A. Bodek and U.K. Yang. Modeling neutrino and electron scattering cross-sections in the few GeV region with effective LO PDFs. *AIP Conf. Proc.*, Vol. 670, p. 110, 2003.

[126] M. Nakahata, et al. Atmospheric neutrino background and pion nuclear effect for kamioka nucleon decay experiment. *Journal of the Physical Society of Japan*, Vol. 55, No. 11, pp. 3786–3805, 1986.

[127] Torbjorn Sjostrand. High-energy-physics event generation with pythia 5.7 and jetset 7.4. *Computer Physics Communications*, Vol. 82, No. 1, pp. 74 – 89, 1994.

[128] R.A. Smith and E.J. Moniz. NEUTRINO REACTIONS ON NUCLEAR TARGETS. *Nucl.Phys.*, Vol. B43, p. 605, 1972.

[129] Cezary Juszczak, Jaroslaw A. Nowak, and Jan T. Sobczyk. Spectrum of outgoing nucleons in quasielastic neutrino nucleus interactions. *Arxiv preprint nucl-th*, 2003.

[130] S. K. Singh, M. J. Vicente-Vacas, and E. Oset. Nuclear effects in neutrino production of Δ at intermediate energies. *Phys.Lett.*, Vol. B416, pp. 23–28, 1998.

[131] M. Day and K. S. McFarland. Differences in quasielastic cross sections of muon and electron neutrinos. *Phys. Rev.*, Vol. D86, p. 053003, 2012.

[132] F. Dufour. *Precise Study of the Atmospheric Neutrino Oscillation Pattern Using Super-Kamiokande I and II.* PhD thesis, Boston University, `http://www-sk.icrr.u-tokyo.ac.jp/sk/pub/fdufour-thesis.pdf`, 2009.

[133] T. Barszczak. *The efficient discrimination of electron and pi-zero events in a water Cherenkov detector and the application to neutrino oscillation experiments.* PhD thesis, University of California, `http://www-sk.icrr.u-tokyo.ac.jp/sk/pub/Tomasz-thesis.pdf`, 2005.

[134] R.B. Patterson, et al. The extended-track event reconstruction for MiniBooNE. *Nucl. Instrum. Meth.*, Vol. A608, pp. 206–224, 2009.

[135] G.L. Fogli, E. Lisi, A. Marrone, A. Palazzo, and A.M. Rotunno. Evidence of $\theta_{13} > 0$ from global neutrino data analysis. *Phys.Rev.*, Vol. D84, p. 053007, 2011.

[136] K. Hagiwara, et al. The earth matter effects in neutrino oscillation experiments from tokai to kamioka and korea. *Arxiv preprint hep-ph*, 2011.

[137] R. Wendell. *Prob3++*.

[138] Gary J. Feldman and Robert D. Cousins. A Unified approach to the classical statistical analysis of small signals. *Phys.Rev.*, Vol. D57, pp. 3873–3889, 1998.

[139] P. Adamson, et al. Electron neutrino and antineutrino appearance in the full minos data sample. *Phys. Rev. Lett.*, Vol. 110, p. 171801, 2013.

[140] A. Himmel, et al. Recent atmospheric neutrino results from super-kamiokande. *Arxiv preprint hep-ex*, 2013.

[141] K. Abe, et al. Letter of intent: The hyper-kamiokande experiment — detector design and physics potential. *Arxiv preprint hep-ex*, 2011.

[142] G. A. P. Cirrone, et al. Validation of the geant4 electromagnetic photon cross-sections for elements and compounds. *Nucl. Phys.*, Vol. A618, p. 315, 2010.

[143] K. Abe, et al. T2K neutrino flux prediction. *Phys. Rev.*, Vol. D87, p. 012001, 2013.

[144] R. J. Abrams, et al. Total cross sections of $k^{\pm}$ mesons and antiprotons on nucleons up to 3.3 gev/c. *Phys. Rev. D*, Vol. 1, p. 1917, 1970.

[145] J. V. Allaby, et al. Total and absorption cross-sections of pi-, k- and anti-p in the momentum range 20-65 gev/c. *Yad. Fiz.*, Vol. 12, p. 538, 1970.

[146] B. W. Allardyce, et al. Inelastic electron scattering and the weak coupling model for ^{16}o and ^{18}o. *Nucl. Phys. A*, Vol. 209, p. 1, 1973.

[147] G. Bellettini, et al. Proton-nuclei cross sections at 20 GeV. *Nucl. Phys*, Vol. 79, No. 3, pp. 609 – 624, 1966.

[148] B. M. Bobchenko, et al. Measurement of total inelastic cross-sections from proton interactions with nuclei in the momentum range from 5-gev/c to 9-gev/c and pi- mesons with nuclei in the momentum range from 1.75-gev/c to 6.5-gev/c. *Sov. J. Nucl. Phys.*, Vol. 30, p. 805, 1979.

[149] A. S. Carroll, et al. Absorption cross-sections of $\pi^{\pm}$, $k^{\pm}$, p and $\overline{p}$ on nuclei between 60-GeV/c and 280-GeV/c. *Phys. Lett. B*, Vol. 80, p. 319, 1979.

[150] J. W. Cronin, et al. Cross sections of nuclei for high-energy pions. *Phys. Rev.*, Vol. 107, p. 1121, 1957.

[151] F. F. Chen, et al. Attenuation cross sections for 860-Mev protons. *Phys. Rev.*, Vol. 99, p. 857, 1955.

[152] S. P. Denisov, et al. Absorption cross sections for pions, kaons, protons and antiprotons on complex nuclei in the 6 to 60 Gev/c momentum range. *Nucl. Phys. B*, Vol. 61, p. 62, 1973.

[153] M. J. Longo and B. J. Moyer. Nucleon and nuclear cross sections for positive pions and protons above 1.4 Bev/c. *Phys. Rev.*, Vol. 125, p. 701, 1962.

[154] A. V. Vlasov, et al. Total inelastic cross-sections for pi mesons on nuclei in the 2-Gev/c to 6-Gev/c momentum range. *Sov. J. Nucl. Phys.*, Vol. 27, p. 222, 1978.

[155] V. Lyubushkin, et al. A study of quasi-elastic muon neutrino and antineutrino scattering in the NOMAD experiment. *Eur.Phys.J.*, Vol. C63, p. 355, 2009.

[156] M. Hasegawa, et al. Search for coherent charged pion production in neutrino-carbon interactions. *Phys. Rev. Lett.*, Vol. 95, p. 252301, 2005.

[157] K. Hiraide, et al. Search for charged current coherent pion production on carbon in a few-GeV neutrino beam. *Phys. Rev.*, Vol. D78, p. 112004, 2008.

[158] Y. Kurimoto, et al. Improved measurement of neutral current coherent π^0 production on carbon in a few-GeV neutrino beam. *Phys. Rev.*, Vol. D81, p. 111102, 2010.

[159] P. Adamson, et al. Neutrino and Antineutrino Inclusive Charged-current Cross Section Measurements with the MINOS Near Detector. *Phys.Rev.*, Vol. D81, p. 072002, 2010.